High-pressure studies of naphthalene, anthracene, pyrene, and benzo[a]pyrene using single-crystal X-ray diffraction in a diamond anvil cell

Doctoral Thesis

submitted to obtain the academic degree of Doctor of Natural Sciences
(Dr. rer. nat.)
of the Bayreuth Graduate School of Mathematical and Natural Sciences
(BayNAT)
of the University of Bayreuth

Wenju Zhou

from *Xi'an, China*

Bayreuth, 2024

This doctoral thesis was prepared at the Laboratory of Crystallography (Material Physics and Technology at Extreme Conditions Group) and the Bavarian Research Institute of Experimental Geochemistry and Geophysics (BGI) at the University of Bayreuth from April/2022 until September/2024 and was supervised by Prof. Dr. Dr. h.c. Natalia Dubrovinskaia and Prof. Dr. Dr. h.c. Leonid Dubrovinsky.

This is a full reprint of the thesis submitted to obtain the academic degree of Doctor of Natural Sciences (Dr. rer. nat.) and approved by the Bayreuth Graduate School of Mathematical and Natural Sciences (BayNAT) of the University of Bayreuth.

Form of the dissertation: cumulative thesis

Date of submission: 09.10.2024

Admission by the executive board: 10.10.2024

Date of defense: 28.11.2024

Acting director: Prof. Dr. Jürgen Köhler

Doctoral committee:

Prof. Dr. Natalia Dubrovinskaia (reviewer)

Prof. Dr. Sander van Smaalen (reviewer)

PD Dr. Gerd Steinle-Neumann (chairman)

Prof. Dr. Daniel Frost

Zusammenfassung

Polyzyklische aromatische Kohlenwasserstoffe (kurz PAK) sind komplexe organische Verbindungen, die aus zwei oder mehreren kondensierten Benzolringen bestehen. Aufgrund ihrer außergewöhnlichen Eigenschaften und ihren breit gefächerten Anwendungen haben diese Verbindungen großes Interesse bei Geowissenschaftlern, Chemikern und Physikern geweckt. Druck hat sich als ein sehr leistungsfähiger thermodynamischer Parameter erwiesen, der strukturelle Veränderungen induziert, die die Materialeigenschaften beeinflussen. Daher kann die Untersuchung des Verhaltens von PAK unter Druck Einblicke in strukturelle Übergänge und intermolekulare Wechselwirkungen dieser bedeutenden Klasse organischer Materialien geben. Darüber hinaus haben die Fortschritte in der Einkristall-Röntgenbeugung (*englisch*: single-crystal X-Ray diffraction, kurz SC-XRD) in Diamantstempelzellen (*englisch*: diamond anvil cells, kurz DACs) unter Verwendung weicher druckübertragender Medien wie Edelgase neue Möglichkeiten zur Untersuchung von Kristallstrukturen, Phasenumwandlungen, Transformationspfaden im thermodynamischen Gleich- oder Ungleichgewicht, Anordnungen von Molekülen und chemischen Bindungen organischer Kristalle unter bisher unerforschten Hochdruckbedingungen geschaffen. Trotz dieser Fortschritte sind strukturelle Studien von PAK mittels SC-XRD noch immer auf einen Druck von maximal 2,1 GPa beschränkt.

Diese kumulative Dissertation präsentiert die Ergebnisse der SC-XRD-Experimente zum Hochdruckverhalten von vier Vertretern der PAK, die in DACs am Synchrotron gemessen wurden: Naphthalin ($C_{10}H_8$), Anthracen ($C_{14}H_{10}$), Pyren ($C_{16}H_{10}$) und Benzo[a]pyren (B*a*P) ($C_{20}H_{12}$). Hierfür wurde die Veränderung von Struktur und chemischen Bindungen dieser PAK unter zunehmenden Druck untersucht und dabei deren Eigenschaften charakterisiert.

Im ersten Teil dieses Forschungsprojekts wurde der Fokus auf das Hochdruckverhalten von Naphthalin und Anthracen bis zu 50 GPa bzw. 43 Gpa gerichtet. Unsere Ergebnisse zeigen keine Phasenübergänge und belegen die bemerkenswerte Stabilität dieser Verbindungen unter extremen Bedingungen. Die erfolgreiche Anwendung von Hirshfeld-Atom-Verfeinerungen (*englisch*: Hirshfeld Atom Refinements, kurz HARs) unterstreicht die Eignung dieser Methode zur präzisen Bestimmung der Positionen von Wasserstoffatomen in organischen Materialien, selbst bei geringer Vollständigkeit der Daten.

Ferner wurde Pyren bis etwa 35 Gpa untersucht. Unsere Ergebnisse zeigen die Phasenübergänge von Pyren-I zu Pyren-II (0,7 GPa) und zu den bisher unbekannten Phasen

Pyren-IV (2,7 GPa) und Pyren-V (7,3 GPa). Die Struktur- und Bindungsanalyse zeigt, dass eine allmähliche Druckzunahme eine kontinuierliche Verdichtung der Molekülpackung bedingt, was schließlich zu einem bisher unbekannten Phänomen führt, der Krümmung der Moleküle. Große organische Moleküle weisen eine unerwartet hohe konformationelle Flexibilität auf, wodurch Pyren-V bis zu 35 GPa erhalten bleibt. Dichtefunktionaltheorie (DFT)-Berechnungen deuten darauf hin, dass die gefundenen Phasen thermodynamisch metastabil gegenüber der bei 0,3 und 0,5 Gpa in der Literatur bekannten Phase Pyren-III sind.

Abschließend wurde das Hochdruckverhalten von B*a*P bis 28 GPa untersucht, wobei mit B*a*P-II ($P2_1/c$) bei 4,8 GPa und B*a*P-III (P-1) bei 7,1 Gpa zwei bisher unbekannte Polymorphe bestimmt werden konnten. Der strukturelle Übergang von B*a*P-I ($P2_1/c$) zu B*a*P-II ($P2_1/c$) erweist sich als eine abrupte Änderung des intermolekularen Winkels und der Gitterparameter a und b, während die Umwandlung von B*a*P-II ($P2_1/c$) zu B*a*P-III (P-1) durch eine Symmetrieverringerung gekennzeichnet ist. Laut DFT-Berechnungen ist B*a*P-III oberhalb von 3,5 GPa die stabilste Phase.

Die in dieser Dissertation vorgestellten Arbeiten erweitern unser Verständnis des Verhaltens von PAK jenseits von Normalbedingungen, der Veränderung der chemischen Bindungen dieser relevanten Materialklasse sowie ihrer strukturellen Dynamik und Stabilität unter Hochdruck. Sie tragen zudem zum grundlegenden Verständnis des Polymorphismus von PAK bei und erfordern weitere theoretische Untersuchungen ihrer Struktur-Eigenschafts-Beziehungen.

Summary

Polycyclic aromatic hydrocarbons (PAHs) are complex organic compounds consisting of two or more condensed benzene rings. Due to their exceptional properties and widespread applications, these compounds have attracted significant attention from geoscientists, chemists and physicists. Pressure has been proven to be a very powerful thermodynamic parameter which induces structural transformations affecting materials’ properties, so that exploring the behavior of PAHs under pressure may provide insights into the structural transitions and intermolecular interactions for this important class of organic materials. Furthermore, the advancement of single-crystal X-ray diffraction (SC-XRD) techniques in diamond anvil cells (DACs) with the use of soft pressure-transmitting media, such as inert gases, has created new possibilities for investigating crystal structures, phase transitions, equilibrium and non-equilibrium transformation paths, molecular arrangements, and chemical bonding of organic crystals under previously unexplored high-pressure conditions. However, despite these advancements, structural studies of PAHs using SC-XRD have been limited to only up to 2.1 GPa.

This cumulative thesis presents the results of experimental investigation of the high-pressure behavior of four representatives of PAHs—naphthalene ($C_{10}H_8$), anthracene ($C_{14}H_{10}$), pyrene ($C_{16}H_{10}$), and benzo[a]pyrene (B*a*P) ($C_{20}H_{12}$)—using synchrotron SC-XRD in DACs. We analyzed their structure and bonding evolution under compression and characterized their properties.

In the first part of this research, we focused on exploring the high-pressure behavior of naphthalene and anthracene up to 50 GPa and 43 GPa, respectively. Our findings reveal no phase transitions and demonstrate the remarkable stability of these compounds under extreme conditions. The successful application of Hirshfeld Atom Refinements (HARs) highlights the method's viability for accurately refining hydrogen atom positions in organic materials even with low data completeness.

We further investigated pyrene up to ~35 GPa. Our findings reveal the phase transitions from pyrene-I to pyrene-II (0.7 GPa), and to the previously unreported pyrene-IV (2.7 GPa), and pyrene-V (7.3 GPa). The structure and bonding analysis show that gradual compression results in continuous compaction of molecular packing, eventually leading to curvature of

molecules, which has never been observed before. Large organic molecules exhibit unexpectedly high conformational flexibility preserving pyrene-V up to 35 GPa. Density Functional Theory (DFT) calculations suggest that the phases we found are thermodynamically metastable compared to pyrene-III previously reported at 0.3 and 0.5 GPa.

Finally, we also investigated the high-pressure behavior of B*a*P up to 28 GPa. We identified two previously unknown polymorphs, B*a*P-II ($P2_1/c$) at 4.8 GPa and B*a*P-III (P-1) at 7.1 GPa. The structural transformation from B*a*P-I ($P2_1/c$) to B*a*P-II ($P2_1/c$) manifests as an abrupt change in the intermolecular angle and in the unit cell parameters a and b, whereas the transformation from B*a*P-II ($P2_1/c$) to B*a*P-III (P-1) is characterized by a decrease in symmetry. According to DFT calculations, above 3.5 GPa, B*a*P-III is the most stable phase.

The work presented in this thesis enhances our understanding of the behavior of PAHs under non-ambient conditions, the evolution of chemical bonding in this important class of materials, and their structural dynamics and stability under high pressure. It also contributes to the fundamental understanding of the polymorphism of PAHs and calls for further theoretical exploration of their structure-property relationships.

Acknowledgments

Time has flown by, and the years of my PhD journey have passed like a flowing river. Now, the moment of graduation has finally arrived. Looking back on this unforgettable journey, I am filled with profound gratitude for the support and encouragement I have received along the way.

First and foremost, I would like to express my deepest gratitude to my supervisors, Prof. Dr. Natalia Dubrovinskaia and Prof. Dr. Leonid Dubrovinsky, for their dedicated guidance and immense support throughout my PhD studies, as well as for their patience and tolerance towards my stubbornness and shortcomings. Their rigorous attitude towards work and passion for research have deeply inspired me. I feel fortunate to have had the opportunity to work with them and to be a part of a group with such a great scientific atmosphere.

I would like to thank my colleagues, Dr. Yuqing Yin, Andrey Aslandukov, Alena Aslandukova, Dr. Fariia Iasmin Akbar, Xiang Li, Dr. Dominique Laniel, Dr. Elena Bykova, Dr. Maxim Bykov, and Dr. Akun Liang, for their support and friendship. We have shared many beamtime hours together at the synchrotron, and those experiences have been truly memorable.

Most of my experiments were performed on the synchrotron beamlines at ESRF and DESY, and I would like to acknowledge their staff for their support and assistance, especially Dr. Michael Hanfland, Dr. Anna Pakhomova, Dr. Tomasz Poreba, and Dr. Konstantin Glazyrin.

I would like to express my gratitude to all the members of the Laboratory of Crystallography, where I spent most of my time. Special thanks to Prof. Dr. Sander van Smaalen for the helpful discussions during the laboratory seminars. I am also grateful to our secretary, Denise Kelk-Huth, for her assistance with various administrative problems and questions. Additionally, I would like to thank my officemates, Surya Kotla and Claudio Eisele, for creating a pleasant and enjoyable daily environment. A special thanks goes to Claudio Eisele for helping me translate the summary into German.

I have also conducted many experiments at BGI, and I would like to thank everyone who has supported and assisted me. Special thanks to Dr. Alexander Kurnosov and Dr. Andreas Audétat for their support and assistance with my experiments. I am especially grateful to my friends Lianjie Man and Dr. Hu Tang for their help in both research and daily life.

Finally, I would like to thank my family. I am grateful to my parents for their support and love. Most of all, I want to thank my wife, Siyuan Wang, for your understanding, patience, and love. Without your support and help, it would have been very difficult for me to complete my PhD. Thank you for always being by my side!

Table of Contents

Chapter 1 Introduction

1.1 The importance of PAHs

PAHs constitute a common class of compounds, characterized by the presence of two or more fused aromatic rings. These compounds are uncharged, non-polar, and many are colorless. PAHs are widely distributed throughout the environment and have garnered significant attention due to their well-recognized carcinogenicity, teratogenicity, and genotoxicity, posing serious health risks to humans and wildlife [1] (Yang *et al.*, 2010). Beyond their environmental and health implications, PAHs also hold notable potential as organic semiconductors, exhibiting unique optical, electrical, and magnetic properties that arise from their extended conjugation and diverse molecular structures [2] (Li *et al.*, 2022).

In natural settings, many PAHs are found in coal and oil deposits [3] (Harvey 1991), while others are primarily generated through the incomplete combustion and pyrolysis of carbon- and hydrogen-containing materials, such as coal, oil, wood, and petroleum products, which predominantly occur under oxygen-deficient conditions [4] (Ravindra *et al.*, 2008). Furthermore, PAHs extend their significance beyond Earth, serving as an essential component of the interstellar medium (ISM). They play a crucial role in various astrophysical processes, with infrared spectroscopy indicating that more than 20% of the carbon in the universe can be attributed to PAHs [5-7] (Allamandola *et al.*, 1985; Ehrenfreund & Charnley, 2000; d'Hendecourt & Ehrenfreund, 1997).

The importance of PAHs is not limited to their ubiquitous presence in terrestrial and extraterrestrial environments, but also to their enormous potential for application. For example, the four representative PAHs studied in this work—naphthalene ($C_{10}H_8$), anthracene ($C_{14}H_{10}$), pyrene ($C_{16}H_{10}$), and B*a*P ($C_{20}H_{12}$)—demonstrate diverse properties. Naphthalene appears as a white crystalline solid with a distinctive odor. It has been used as a main ingredient of traditional mothballs. Additionally, molten naphthalene serves as an effective solubilizing medium for poorly soluble aromatic compounds, making it valuable in various chemical applications [8] (Collin *et al.*, 2000). As a wide band-gap organic semiconductor, anthracene is particularly notable for its use in blue fluorescence materials, which show promising potential for creating efficient and stable organic light-emitting diodes (OLEDs) for lighting applications [9] (Ho *et al.*, 2012). Pyrene and its derivatives are widely used as fluorescent dyes due to their high photostability and bright fluorescence, as well as fluorescent probes in various scientific applications [10] (Alidağı *et al.*, 2018).

Unlike other PAHs studied for their advanced material applications, B*a*P is primarily researched for its toxicological effects and environmental impact due to its significant carcinogenic properties [11] (Bukowska *et al.*, 2022).

1.2 Naphthalene, anthracene, pyrene, and B*a*P – the simplest representatives of PAHs – at ambient conditions

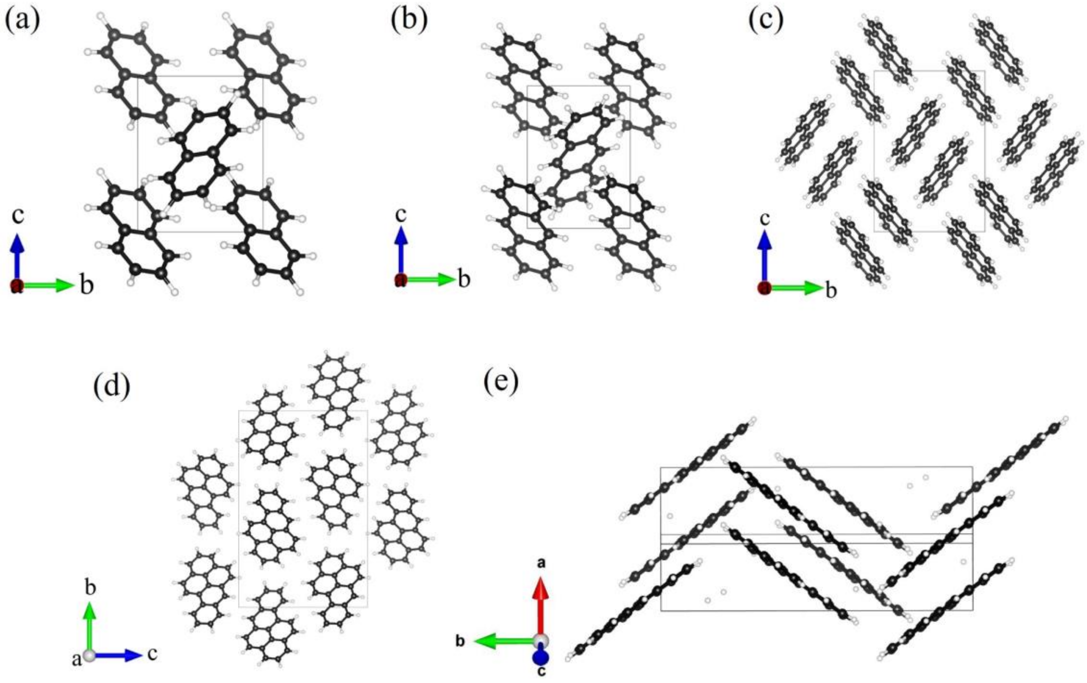

Figure 1.1 Crystal structures of naphthalene, anthracene, pyrene, and B*a*P. (a) Naphthalene, (b) anthracene, (c) pyrene, and (d) B*a*P viewed along the a-axis; (e) B*a*P viewed along [10 0 9]. C atoms are black, and H atoms are white.

Naphthalene ($C_{10}H_8$) is the simplest PAH, consisting of two fused aromatic rings. The crystal structure of naphthalene was first studied in the mid-20th century by Abrahams *et al.* [14] (Abrahams *et al.*, 1949), with using powder XRD to reveal that it crystallizes in the monoclinic space group $P2_1/a$. Later studies, including those by Natkaniec *et al.* [15] (Natkaniec *et al.*, 1983) using single-crystal neutron diffraction at 12 K, and Oddershede and Larsen [16] (Oddershede & Larsen, 2004) with SC-XRD at various temperatures, provided precise atomic coordinates and insights into the thermal vibrational behavior of the atoms within the crystal lattice. As shown in Fig.1.1a, the unit cell of naphthalene contains two molecules, with a molecular arrangement following a herringbone motif.

Anthracene ($C_{14}H_{10}$) is the second member in the series of PAHs, composed of three fused six-carbon rings. The crystal structure of anthracene was first refined in 1956 by Cruickshank [17] (Cruickshank, 1956) using powder XRD. This early study was followed by significant advancements in 1972, when Lehmann and Pawley [18] (Lehmann & Pawley, 1972) used single-crystal neutron diffraction at 12 K to investigate perdeuteroanthracene ($C_{14}D_{10}$). Their work provided a precise determination of the atomic coordinates of both carbon and deuterium atoms. As depicted in Fig.1.1b, the unit cell of anthracene includes two molecules, arranged in a herringbone motif similar to that observed in naphthalene.

Pyrene ($C_{16}H_{10}$) is another representative PAH, consisting of four fused benzene rings. The crystal structure of pyrene, known as pyrene-I, is characterized by a monoclinic structure in the $P2_1/c$ space group. This structure was first reported by Robertson and White in 1947 [19] (Robertson & White, 1947) using SC-XRD and later refined with neutron diffraction [20] (Hazell *et al.*, 1972) (CSD reference code PYRENE02). As shown in Fig.1.1c, the unit cell of pyrene contains four molecules, with two molecules forming pairs or "sandwiches." These molecular pairs are arranged in a sandwich herringbone motif, which differs from the packing motifs observed in naphthalene and anthracene.

B*a*P is one of the two isomeric species of benzopyrene ($C_{20}H_{12}$), formed by fusing a benzene ring to pyrene and it appears as a yellow solid under ambient conditions. Crystals of B*a*P were first described by John Iball in 1936 [21] (Iball, 1936), who obtained them from B*a*P solutions in the form of needles and plates and determined their symmetry and unit cell parameters using XRD. The needle-shaped crystals were monoclinic ($P2_1/c$), whereas plate-shaped – orthorhombic ($P2_12_12_1$). The crystal structure of the monoclinic B*a*P was later solved [22] (Iball & Young, 1956) and refined [23] (Iball *et al.*, 1976). Subsequently, one more orthorhombic B*a*P polymorph was reported [24] (Contag, 1978). However, it turned to be unstable and gradually, within 6 months, transformed into the known monoclinic B*a*P. Low-temperature SC-XRD measurements at 120 K [25] (Carrell *et al.*, 1997) enabled a more precise structure analysis. The crystal structure of B*a*P includes two molecules per unit cell, featuring a unique combination of herringbone (Fig.1.1d) and layered stacking (Fig.1.1e) arrangements, known as the γ structure [13] (Schatschneider *et al.*, 2011), which distinguishes it from the molecular arrangements of naphthalene, anthracene, and pyrene.

1.3 State of the art of high-pressure research for naphthalene, anthracene, pyrene, and B*a*P

Pressure has been proven to be a very powerful thermodynamic parameter which induces structural transformations affecting materials' properties, so that exploring the behavior of PAHs under pressure may provide insights into the structural transitions and intermolecular interactions for this important class of organic materials. However, so far, the information about the structural behavior of any organic crystals at pressures exceeding a few gigapascals is very limited. It is mainly due to studies at higher pressures that have been hindered by both the technical complexity of the experiments on fragile organic crystals and because of a common belief that the crystals are quickly destroyed under compression. The advancement of SC-XRD techniques in DACs with the use of soft pressure-transmitting media [26] (Dubrovinsky, 2013), such as inert gases, has created new possibilities for investigating crystal structures, phase transitions, equilibrium and non-equilibrium transformation paths, molecular arrangements, and chemical bonding of organic crystals under previously unexplored high-pressure conditions. For example, recently high-pressure polymorphism in L-threonine was studied between ambient pressure and 22 GPa [27] (Giordano *et al.*, 2019).

High-pressure experimental and theoretical studies of naphthalene and anthracene have been conducted by different methods. The first high-pressure experiments on naphthalene were carried out by Bridgman in 1938 [28] (Bridgman, 1938) to study the volume change of naphthalene under compression. He observed a small but noticeable volume discontinuity around 3 GPa, indicating a possible phase transition. Beyond 3 GPa, however, no further phase transitions were detected up to 5 GPa. Jones and Nicol [29] (Jones & Nicol, 1968) conducted fluorescence spectroscopy on naphthalene from ambient to 5 GPa and identified a new broad emission band at 3 GPa, indicative of an irreversible molecular structural change. Nonetheless, some studies, such as those by Vaidya and Kennedy [30] (Vaidya & Kennedy, 1971) and Nicol *et al.* [31] (Nicol *et al.*, 1975), which studied the volume change of naphthalene under compression and used Raman spectroscopy respectively, reported no evidence of phase transitions in similar pressure ranges. The existence of a phase transition in naphthalene under pressure remains debated. In 2013, Meletov [32] (Meletov, 2013) conducted experiments using powder XRD up to 20 GPa and did not observe any new diffraction peaks or significant changes in the existing peaks, further questioning the occurrence of a phase transition. Conversely, Likhacheva *et al.* [33] (Likhacheva *et al.*, 2014) reported using powder XRD that around ~2 GPa, a distinct bend in the pressure dependence of interlayer C–C distances curves was observed, suggesting a minor structural irregularity, indicating potential structural changes. However, beyond 2 GPa, no additional phase transitions were observed up to 6 GPa. Moreover, O'Bannon and Williams [34] (O'Bannon & Williams, 2016) performed infrared spectroscopy on naphthalene up to 54.5 GPa. Their data suggested a phase transition at 2–3 GPa, with a possible second transition around 30 GPa. Notably, the disappearance of spectral features associated with molecular naphthalene in the infrared spectra, coupled with the irreversibility of this transition, suggests that the material may become amorphous between approximately 30 and 45 GPa.

Phase transitions under high pressure in anthracene have been examined sporadically over the past several decades. Offen [35] (Offen, 1966) used fluorescence spectroscopy to study anthracene under pressures ranging from 0 to 2.5 GPa. His experiments revealed significant spectral changes, with diffuse bands at longer wavelengths appearing at pressures above 1 GPa. This irreversible change was thought to be associated with alterations in the crystal structure and molecular rearrangements of anthracene under high pressure. In a subsequent study, Adams and Tan [36] (Adams & Tan, 1981) utilized infrared spectroscopy to investigate anthracene under pressures up to 4.5 GPa. They identified several bands with clear breaks in slope at 2.4 GPa, indicating the existence of a phase change. Similarly, Leger and Aloualiti [37] (Leger & Aloualiti, 1991) conducted powder XRD experiments across pressures from 0 to 5.6 GPa. They observed non-linear changes in lattice parameters at 2.4 GPa, suggesting the occurrence of a phase transition, possibly a second-order transition. Further supporting evidence of a phase transition was provided by Zhao *et al.* [38] (Zhao *et al.*, 1999), who conducted Raman spectroscopy measurements up to 3.1 GPa and noted a significant increase in the full width at half maximum (FWHM) of the peaks at 2.4 GPa. Although the Raman frequencies did not show a clear discontinuous shift, the change in peak width supported the occurrence of a phase transition. In contrast, Oehzelt *et al.* [39] (Oehzelt *et al.*, 2003) conducted powder XRD experiments up to 27.8 GPa and observed no significant discontinuities in lattice parameters or notable changes in diffraction peaks, suggesting that no phase transition occurred under these conditions. More recently, O'Bannon and Williams [34] (O'Bannon & Williams, 2016) reported infrared data up to 19.9 GPa, documenting a transition at approximately 2 to 3 GPa and suggesting a possible second transition near 7 GPa.

Despite various investigations into the high-pressure behavior of naphthalene and anthracene, inconsistencies remain in the reported phase transitions. Previous studies using SC-XRD had only reached pressures up to 2.1 GPa [40] (Fabbiani *et al.*, 2006), leaving uncertainties regarding the structural behavior of these compounds at higher pressures. Fig. 1.2 summarizes representative high-pressure studies on naphthalene and anthracene, where green circles indicate reported phase transitions and blue circles indicate no observed phase transitions.

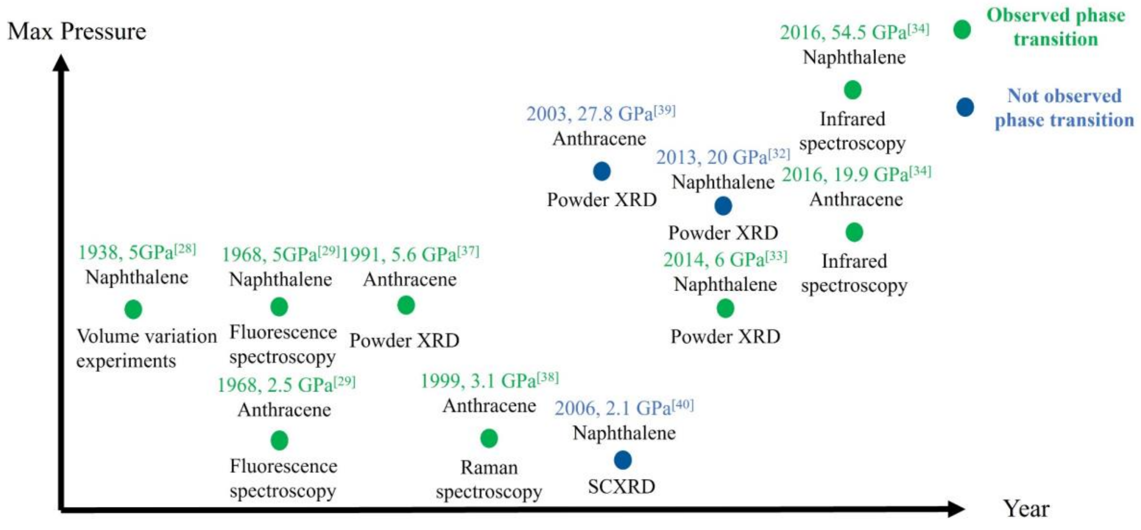

Figure 1.2 Schematic diagram of previous high-pressure studies on naphthalene and anthracene in this chapter. Blue solid circles represent studies where no phase transition was reported, while green solid circles indicate studies that observed phase transitions.

For pyrene, it has been observed that under high pressure, a new polymorph different from pyrene-I, called pyrene-III, was identified on single crystals of pyrene recrystallized from a dichloromethane solution at 0.3 and 0.5 GPa [40] (Fabbiani *et al.*, 2006). It was found to have a different molecular packing model and different intermolecular interactions. Although spectroscopic data do not provide explicit information about the structure of solid matter, it is worth noticing that vibrational spectroscopy investigation of pyrene up to about 1 GPa, pointing towards the existence of phase transformations in pyrene under pressure, was made as early as in 1976 [41] (Zallen *et al.*, 1976), when a transition was detected on an abrupt change of the Raman spectrum at ca. 0.4 GPa. Later Raman spectroscopy study [42] (Sun *et al.*, 2008) detected a transformation at 0.3 GPa on a crystal grown from a dichloromethane solution, and on a crystal pressurized in argon up to 0.6 GPa, interpreted in the both cases as observation of pyrene-III, similar to that described by Fabbiani et al [40] (Fabbiani *et al.*, 2006).

The behavior of B*a*P has been studied at high pressures. One notable investigation used Fourier Transform (FT) Raman spectroscopy to analyze B*a*P under pressures up to 40 kbar (4 GPa) with a DAC [43] (Warner *et al.*, 2003). The study reported a pressure-induced phase transition occurring at around 13 kbar (1.3 GPa) and identified two orthorhombic polymorphs at ambient pressure.

Despite numerous studies on the high-pressure behavior of these four PAHs, significant research gaps remain. For naphthalene and anthracene, while compression experiments have been conducted up to several tens of gigapascals, no definitive phase transitions have been directly observed. In the case of pyrene, although a new polymorph, pyrene-III, has been observed using high-pressure SC-XRD, with the highest pressure reaching only 0.7 GPa [40] (Fabbiani *et al.*, 2006), the evolution of the crystal structure of pyrene at higher pressures remains unknown. There is still a lack of detailed descriptions of molecular structural changes and the mechanisms driving phase transitions. As for B*a*P, no studies have yet been conducted on its structural behavior under high-pressure conditions.

To address the existing research gaps, I formulated questions that I wanted to address during my research. Our goal was to investigate the structural evolution of these four PAHs under compression, focusing on changes in their crystal structures, molecular packing, intermolecular interactions. We aimed to investigate whether new polymorphs of naphthalene and anthracene could be observed under high-pressure conditions. For pyrene, we aimed to confirm the presence of the pyrene-III polymorph at lower pressures (below 1 GPa), and to investigate whether a transition from pyrene-I to the low-temperature polymorph pyrene-II occurs under compression. Additionally, we sought to explore the structural evolution at higher pressures and observe any new polymorphs that may emerge. For B*a*P, this study represents the first exploration of its behavior under high-pressure conditions. Through this study of these four PAHs, we aim to enhance the fundamental understanding of the polymorphism of PAHs, their behavior under non-ambient conditions, and the evolution of chemical bonding that affect the structure-property relationships of this important class of organic materials.

To achieve our research objectives, we have systematically investigated the behavior of these four PAHs under high-pressure conditions using synchrotron SC-XRD in DACs. We explored pressures up to 50 GPa for naphthalene, 43 GPa for anthracene, 35.5 GPa for pyrene, and 35 GPa for B*a*P.

Chapter 2 Methods

2.1 Design of experiments

2.1.1 Working principles of DACs

Over the past 70 years, the DAC has been a crucial experimental tool for generating extremely high hydrostatic pressures, significantly impacting fields like Earth sciences and physics. The DAC is capable of reaching pressures from 0.1 GPa to 1 TPa [44,45] (Dubrovinskaia *et al.*, 2016; Dubrovinsky *et al.*, 2022). A schematic of the DAC is shown in Figure 2.1, and its structure can be divided into three main components: the diamond, the gasket, and the pressure application system.

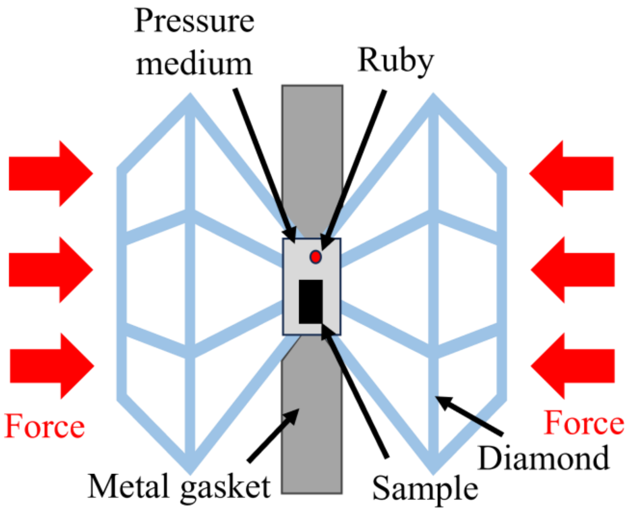

Figure 2.1 Schematic diagram of DAC loading.

The heart of the DAC is diamond, the hardest known natural material, with a Mohs hardness of 10 and a bulk modulus of approximately 440 GPa [46] (Occelli *et al.*, 2003). Diamond also has excellent thermal conductivity and is nearly transparent across a wide range of wavelengths, including X-rays, ultraviolet light, visible light, and infrared light, making it an ideal material for anvils. According to the definition of pressure, pressure is the force exerted per unit area ($P = F/S$). Thus, different pressure ranges can be achieved by varying the diamond culet size. Culets with diameters of 500, 250, and 120 μm are typically used for routine measurements up to 20, 80, and 160 GPa, respectively. For ultra-high-pressure experiments, smaller culet sizes are required. The highest achievable hydrostatic pressure in a DAC currently exceeds 1 TPa, made possible by a double-stage DAC design [44,45]

(Dubrovinskaia *et al.*, 2016; Dubrovinsky *et al.*, 2022). In this work, the pressure range we tested was below 60 GPa, and we selected a culet size of 250 μm for all high pressure experiments.

A gasket with an indentation and a hole is placed between the two opposing diamond anvils. Its primary function is to provide a space for the sample, as well as to transmit pressure and protect the diamonds from direct contact. The pressure application system classifies DACs into two major types based on the drive mechanism: screw-driven mechanical DACs and membrane DACs. In the mechanical type, the loading force is applied directly or through a mechanical system to the diamond anvils using screws. In membrane DACs, the pressure is controlled by adjusting the gas pressure within a metal membrane, which in turn controls the movement of the two diamond anvils. This method allows for a smoother pressurization process and more precise control over the pressure increments. For several synchrotron studies at the ESRF that required collecting SC-XRD diffraction data at a series of pressure points, we used a membrane driven Le Toullec type DAC [47] (Letoullec *et al.*, 1988). For the collection of diffraction data at just a few pressure points, we used the BX90 type [48] (Kantor *et al.*, 2012) DAC.

In addition, a large open angle is crucial for SC-XRD, as it provides higher resolution. The commercial Boehler-Almax [49] (Boehler, 2006) diamonds used in this study, supplied by Almax easyLab, offer the highest open angle of 4 theta = 80°.

2.1.2 Pressure transmitting medium

The pressure-transmitting medium plays a crucial role in high-pressure DAC experiments, as it transmits the pressure from squeezing diamonds to the sample. Due to the uniaxial compression design of the DAC, the presence of a pressure medium also helps to create a hydrostatic environment. This is particularly important in single crystal experiments, where good hydrostatic conditions can reduce shear strain within the sample, which would otherwise cause broadening of the diffraction peaks. Ideal pressure media are noble gases such as He, Ne, and Ar, as they have relatively high solidification pressures of around 10-15 GPa [50] (Jayaraman, 1983). In our room-temperature experiments, we chose He or Ne as the pressure medium because it has low X-ray absorption and provides a low background, which offers an additional advantage for XRD studies in DACs, especially when studying molecular crystals containing hydrogen atoms. In our high-temperature high-pressure experiments, we selected KCl as the pressure-transmitting medium. The main reason for this choice was to avoid potential issues with using gaseous pressure media in a DAC heated for extended periods in an oven. Under high temperatures, gases could expand significantly, which might cause the DAC to lose pressure or lead to the escape of the gas.

2.1.3 Pressure determination

In high-pressure experiments, accurate pressure calibration is crucial. In this study, in situ pressure measurements in DAC experiments were primarily conducted using two methods. For room temperature experiments, the first method involves measuring the R1 fluorescence peak position (694.2 nm) of Cr-doped Al_2O_3 (ruby). The following equation describes the relationship between the central position of the ruby R1 spectral peak and pressure [51] (Shen *et al.*, 2020):

$$P(GPa) = A \cdot \frac{\Delta\lambda}{\lambda_0} \cdot \left[1 + B \cdot \left(\frac{\Delta\lambda}{\lambda_0}\right)\right] \tag{2.1}$$

where A and B are the calibration constants (A=1.87(1) $\cdot$ 10^3, B=5.5) and λ_0 is the position of R1 peak at ambient pressure; $\Delta\lambda$ is the relative shift of R1 peak at pressure P. However, the ruby fluorescence method cannot measure pressures higher than ~100 GPa due to the weakening of the R1 peak signal.

The second method is in situ XRD to calibrate pressure by determining the unit cell parameters of a pressure marker material with a well-known equation of state (EOS). This pressure marker can be loaded into the DAC along with the sample and probed by X-rays. Common pressure markers include metals such as Au, Pt, and Mo, or simple binary compounds like MgO, NaCl, KCl, and KBr [52-55] (Dewaele *et al.*, 2012; Dewaele *et al.*, 2008; Fei *et al.*, 2007; Dorfman *et al.*, 2012). In this study, KCl was used as the pressure-transmitting medium and pressure marker for high-temperature high-pressure experiments.

2.2 XRD methods

2.2.1 Powder XRD and SC-XRD

In 1895, German physicist Wilhelm Röntgen first discovered X-rays. By 1912, Max von Laue, another German physicist, made two significant discoveries: (1) the wavelength of X-rays is of the same order of magnitude as the atomic spacing in many crystals, and (2) X-rays undergo diffraction when passing through crystals [56] (Taylor, 1961). Also in 1912, British physicists William Henry Bragg and William Lawrence Bragg successfully determined the structures of KCl, NaCl, and diamond using XRD. From this work, they formulated Bragg's Law of reflection [57] (Ladd *et al.*, 1977):

$$2d \cdot \sin\theta = n\lambda \tag{2.2}$$

Where d is the distance between crystal planes (also known as the interplanar spacing), θ is the angle of incidence (the angle between the incident X-rays and the crystal planes), n is the order of reflection (an integer, usually n=1 for the first-order diffraction), and λ is the wavelength of the X-rays. This discovery laid the foundation for the widespread application of X-ray crystallography in physics, chemistry, and materials science.

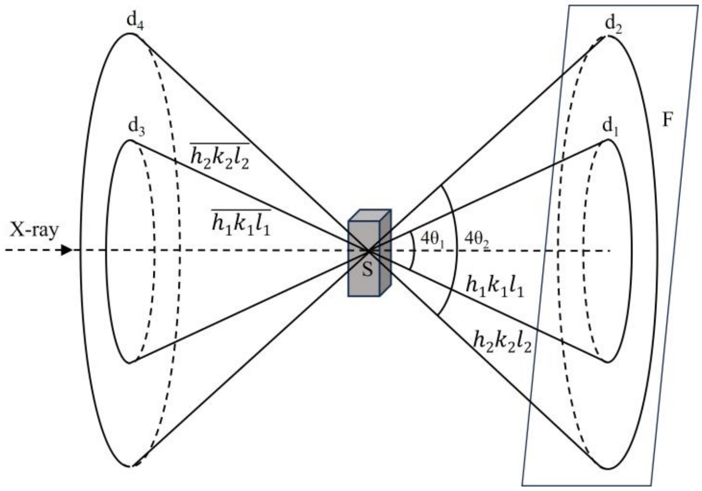

Figure 2.2 Powder XRD. The "S" represents the powder sample, and the "F" represents the 2D detector. d_1, d_2, d_3, and d_4 represent different lattice spacings corresponding to different crystallographic planes. The spacing d_1 corresponds to the plane $h_1k_1l_1$ and the diffraction angle θ_1. Similarly, d_2 corresponds to the plane $h_2k_2l_2$ with the diffraction angle θ_2. The other spacings d_3 and d_4 relate to different crystallographic planes $\overline{h_1k_1l_1}$ and $\overline{h_2k_2l_2}$. The relationship between the lattice spacing d, the diffraction angle θ, and the crystallographic plane *(hkl)* is governed by Bragg's Law.

The basic principle of a powder diffraction experiment can be described as follows: a monochromatic X-ray beam is directed onto small powder crystal particles. When a set of lattice planes (*hkl*) within the crystal satisfies Bragg's reflection condition, the incident X-rays form an angle θ with the (*hkl*) lattice planes, and the reflected beam forms an angle of 2θ with the incident beam. Since the orientations of the powder crystals are random, the diffraction lines corresponding to each set of (*hkl*) planes form conical surfaces with an apex angle of *4θ* and the incident direction as the axis, creating Debye–Scherrer cones. These cones intersect the 2D detector plane to form characteristic concentric rings. As long as the interplanar spacing is greater than *λ*/2 and satisfies Bragg's law, the lattice planes will generate corresponding diffraction cones, as illustrated in Figure 2.2. The different lattice spacings are associated with specific planes, and these planes are projected as distinct rings on the detector. All powder XRD methods include an X-ray source and a detection system to properly record the diffraction lines that satisfy Bragg's law [58] (Kaelble, 1967). In a powder XRD pattern, the structural information of the sample can be obtained from three parameters: diffraction peak shape, diffraction position, and diffraction intensity. The peak shape primarily aids in refining the crystal structure and identifying imperfections in the crystal, such as strain, defects, distortions, and grain size. The accurate measurement of diffraction positions provides information on the unit cell shape and size, while diffraction intensity is used to determine the atomic positions within the crystal structure.

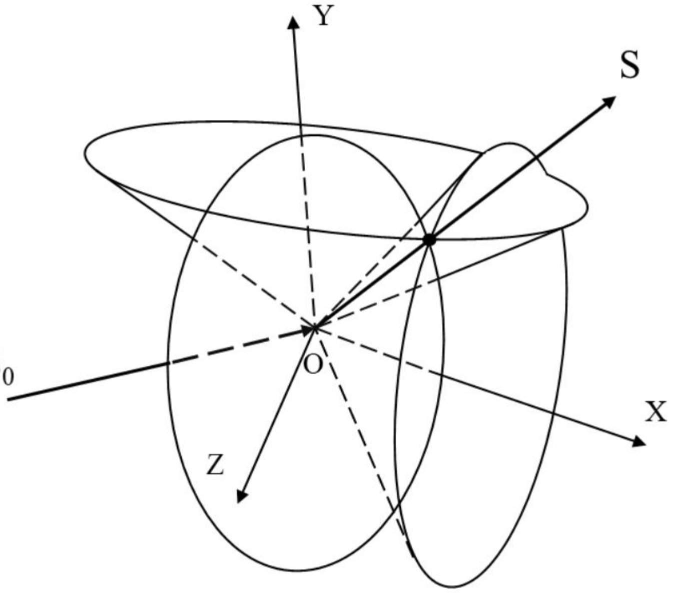

Figure 2.3 Diffraction cones of a three-dimensional atomic array. A schematic diagram satisfying the three-dimensional Laue condition.

The basic principle of SC-XRD can be described as follows: when X-rays pass through a material, coherent scattering occurs. The scattering of X-rays by atoms in the crystal is known as the diffraction effect. As the incident beam travels along a specific direction S_0 through the single crystal sample (as shown in Figure 2.3), diffraction may occur in a specific direction if the crystal lattice plane satisfies both Bragg's law and the Laue equations. This diffraction direction is represented by the Miller indices (*hkl*) for the corresponding reciprocal lattice point. SC-XRD analysis involves several key steps. The process begins with capturing diffraction signals using a 2D detector, recording both their geometric positions and intensities. By analyzing the positions of these diffraction spots, we can accurately calculate the crystal's lattice parameters. The next step is assigning correct Miller indices (*hkl*) to each diffraction spot. Using the calculated lattice parameters, Miller indices (*hkl*), and the intensity of diffraction spots (which helps determine extinction conditions), we can determine the symmetry of crystal, including its possible space group. Finally, we combine the Miller indices (*hkl*) and diffraction intensity data to determine an initial crystal structure. By refining the initial model, we obtained the final crystal structure. Compared to powder samples, the structure obtained from SC-XRD data is considered more reliable.

2.2.2 High-pressure XRD data collection strategy on synchrotron

Synchrotron radiation is electromagnetic radiation emitted when relativistic charged particles are accelerated perpendicular to their velocity. It was first discovered in a 70-MeV synchrotron equipped with a transparent vacuum tube [59] (Pollock, 1983). The experiments in this study were conducted at the ESRF-EBS (European Synchrotron Radiation Facility-Extremely Brilliant Source). The synchrotron beamlines involved were ID15b ($\lambda = 0.4100$ Å, beam size ~2.0×2.0 μm^2) and ID27 ($\lambda = 0.3738$ Å, beam size ~2.0×2.0 μm^2) at ESRF-EBS. Third-generation synchrotron facilities can provide brightness up to a billion times higher than laboratory X-ray sources, along with broad wavelength coverage and high collimation. This significantly compensates for the low data quality and completeness often caused by DAC experiments. Additionally, the micron-sized beam is essential for obtaining high-quality SC-XRD data in high-pressure experiments, as the sample chamber area becomes extremely limited due to the applied pressure.

Synchrotron-based SC-XRD experiments begin with the calibration of the diffractometer. This is done using standard powder samples such as LaB_6 or CeO_2, and a standard single crystal of enstatite ($(Mg_{1.93}Fe_{0.06})(Si_{1.93}Al_{0.06})O_6$, space group *Pbca*, $a = 8.8117(2)$ Å, $b = 5.1832(10)$ Å, $c = 18.2391(3)$ Å). Initial values for the sample-to-detector distance and goniometer angle offsets are obtained from the powder diffraction standard data, which are integrated using Dioptas software [60] (Prescher & Prakapenka, 2015). These parameters are then refined using the CrysAlisPro software [61] (Rigaku *et al.*, 2015), with the lattice parameters of enstatite providing precise calibration of the diffractometer.

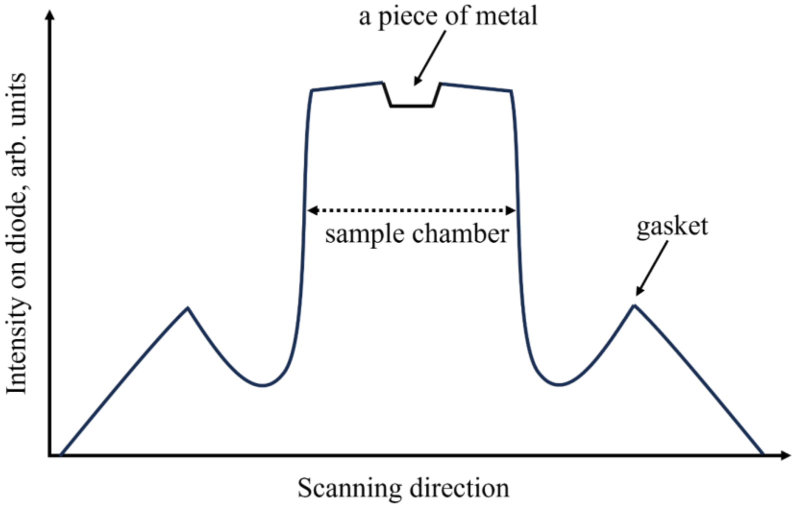

Figure 2.4 Schematic diagram of X-ray absorption curve for DAC alignment

Proper alignment of the sample in the DAC is essential for collecting high-quality XRD data. The general alignment procedure is usually based on the absorption of X-rays. The DAC is moved by the y- and z-motors, while a silicon diode is typically used to record the curve of X-ray intensity. When the DAC moves, the position of the X-ray beam spot shifts from the sample chamber to the metallic gasket. This causes a significant decrease in the recorded X-ray intensity due to the strong absorption by the gasket, allowing the location of the sample chamber to be identified, as shown in Fig. 2.4. The y- and z-axes are first adjusted to the center of the sample chamber. Then, the rotation center is corrected by comparing the absorption curves obtained by rotating the ω motor at positive and negative angles. In our study, when the DAC sample chamber is relatively thick (due to the maximum pressure being less than ~60 GPa), the correction of the rotation center should be done as precisely as possible using the sample itself, rather than the entire sample chamber. However, because PAHs have relatively weak X-ray absorption, we place a strongly absorbing metal (usually rhenium or gold) in the sample chamber to perform the rotation center correction. The final correction should be smaller than the beam size for optimal alignment.

After calibrating the rotation center, we used an on-site optical microscope to locate the sample, then aligned the X-ray beam onto the sample for data collection. The collection strategy was based on a vertical axis (ω-scan), and the rotation range was determined by the open angle of the DAC. In our work, at each pressure step, data were collected in step-scans of 0.5° while rotating the DAC from -34° to +34°. After acquiring the SC-XRD data, we immediately checked the data for intensity, overexposure, and potential misalignment of the sample relative to the rotation center. Based on these checks, necessary adjustments were made within the limited beamtime to ensure the highest possible data quality. In this study, the subsequent analysis of the SC-XRD data (including peak search, unit cell finding, and data integration) was carried out using the CrysAlisPro [61] (Rigaku *et al.*, 2015) software. The crystal structures were determined using SHELX [62] (Sheldrick, 2008) and refined with OLEX2 [63] (Dolomanov *et al.*, 2009). Visualization of the crystal structures was performed using VESTA software [64] (Momma & Izumi, 2008).

2.2.3 Crystal structure analysis

2.2.3.1 Single crystal structure analysis: HAR

Traditionally, crystal structure refinements have relied on the independent atom model (IAM), which assumes that the electron density of each atom is spherically symmetric. This assumption significantly affects the accuracy of describing the electron density around hydrogen atoms, as they possess only one valence electron. This electron density is often strongly shifted towards the atoms to which the hydrogens are bonded, leading to an underestimation of bond lengths involving hydrogen atoms. Recent studies have shown that HAR can provide C-H bond lengths that are within one standard uncertainty of those obtained from neutron diffraction measurements, offering comparable precision [65] (Woińska *et al.*, 2016).

HAR is a refinement method that utilizes molecular wavefunction calculations. It is based on the Hirshfeld partitioning scheme, which assigns electron density to individual atoms using quantum mechanically derived molecular wavefunctions, generating what are referred to as Hirshfeld atoms. A Fourier transformation of the electron density for Hirshfeld atoms is performed on the fly to generate the corresponding atomic form factors used in least-squares refinement. This process results in an improved structural model, and it is repeated iteratively—calculating a new wavefunction and new atomic form factors after each refinement cycle—until convergence is achieved. As a result, HAR is able to achieve more precise atomic positions compared to IAM.

In recent years, the HAR method has been integrated into the OLEX2 software, under the name NoSpherA2 Refinement [66] (Kleemiss *et al.*, 2020). In our work, we used the ORCA software [67] (Neese, F., 2022) via the OLEX2 plugin, employing the PBE0 hybrid functional and the def2-TZVPP pseudopotential basis set for molecular wavefunction calculations, as recommended in the relevant literature [66] (Kleemiss *et al.*, 2020).

2.2.3.2 Powder XRD data analysis: Lebail method

In our work, for samples that were subjected to heating, such as in pyrene's high-temperature and high-pressure experiments, the quality of the single crystals deteriorated, making it necessary to use the LeBail method for polymorph identification and fitting of peak shapes and primarily peak positions. The LeBail method, introduced by Armel Le Bail in 1988 [68] (Le Bail *et al.*, 1988), is an analytical technique used to extract diffraction peak shape information from X-ray powder diffraction data. The core concept of the LeBail method is to separate the positions and shapes of individual reflection peaks from powder diffraction data using known unit cell parameters and space group information, fitting their intensities. Unlike the Rietveld method, the LeBail method does not involve refining atomic positions or thermal parameters—it focuses solely on fitting peak shapes and intensities.

In our work, the steps for applying the LeBail method are as follows. First, we use Dioptas software to identify the phases from the obtained powder diffraction data and roughly estimate the corresponding unit cell parameters using the initial strong diffraction peaks. Then, we input the unit cell parameters and space group into the Jana2006 software [69] (Petříček *et al.*, 2014) for LeBail fitting. Using a Lorentzian function, the intensities of the diffraction peaks are iteratively fitted and corrected until the optimal fit is achieved, providing more accurate lattice parameters. We don't use the Rietveld method to refine atomic positions and thermal parameters due to the fact that the sample did not become a true powder, exhibiting strong anisotropy. Additionally, in the DAC, most diffraction peaks were blocked, further limiting the Rietveld method's applicability.

2.3 The equation of state calculation

The equation of state (EOS) is a mathematical model that describes the relationship between different state variables—such as temperature, pressure, and volume—under varying conditions. In thermodynamics and statistical mechanics, EOS is commonly used to describe the physical state of gases, liquids, and solids, as well as the behavior of these states as the system changes. In this thesis, we utilize the third-order Birch-Murnaghan isothermal EOS [70] (Birch, 1947) to measure the EOS at a constant (ambient) temperature of 293 K. The third-order Birch–Murnaghan isothermal EOS is given by:

$$\mathrm{P(V)} = \frac{3\mathrm{K_0}}{2}\left[\left(\frac{\mathrm{V_0}}{\mathrm{V}}\right)^{7/3} - \left(\frac{\mathrm{V_0}}{\mathrm{V}}\right)^{5/3}\right]\left\{1 + \frac{3}{4}(K' - 4)\left[\left(\frac{V_0}{V}\right)^{2/3} - 1\right]\right\} \tag{2.3}$$

where P is the pressure, V_0 is the reference volume, V is the volume, K_0 is the bulk modulus, and K' is the derivative of the bulk modulus with respect to pressure. The bulk modulus and its derivative are usually obtained from fits to experimental data and are defined as $K_0 = -V \cdot (\partial P/ \partial V)$ and $K' = (\partial K/ \partial P)$. In this work, we used Eosfit7c software [71] (Angel *et al.*, 2014) to fit experimental P-V data in order to determine the equations of state of the phases of interest.

2.4 The analysis of intermolecular interactions: Hirshfeld surface

Hirshfeld surface analysis is a method used to study intermolecular interactions, molecular crystal structures, and the molecular environment within a crystal [72-74] (McKinnon *et al.*, 2004; Spackman & Byrom, 1997; Spackman & Jayatilaka, 2009). By defining a surface around a molecule (the Hirshfeld surface), it allows for the visualization and quantitative analysis of the molecular environment and the interactions between molecules in a crystal. In this study, we used the CrystalExplorer program [75] (Spackman *et al.*, 2021) to construct the Hirshfeld surfaces. The Hirshfeld surface emerged from an attempt to define the space occupied by a molecule in a crystal for the purpose of partitioning the crystal electron density into molecular fragments [73] (Spackman & Byrom, 1997). Hirshfeld surfaces were named after F.L. Hirshfeld, whose 'stockholder partitioning' scheme for defining atoms in molecules [76] (Hirshfeld, 1977). Specifically, a weight function is used to define the Hirshfeld surface, as given by the following equation:

$$w_{\mathrm{A}}(r) = \frac{\sum_{\mathrm{i}\in\mathrm{molecule\ A}} \rho_{\mathrm{i}}^{\mathrm{at}}(r)}{\sum_{\mathrm{i}\in\mathrm{crystal}} \rho_{\mathrm{i}}^{\mathrm{at}}(r)} = \frac{\rho_{\mathrm{promolecule}}(r)}{\rho_{\mathrm{procrystal}}(r)} \tag{2.4}$$

where the $\rho_{\mathrm{promolecule}}(r)$ is the electron density of the molecule at a given point r and the $\rho_{\mathrm{procrystal}}(r)$ is the electron density of the entire crystal at same point. The Hirshfeld surface is defined as the isosurface where $w_{\mathrm{A}}(r)$=0.5. At any point on this surface, the electron density is contributed equally by the molecule of interest and its neighboring molecules, meaning that the contribution from the molecule itself is equal to the sum of contributions from all neighboring molecules. The Hirshfeld surfaces of adjacent molecules never overlap due to the nature of the weight function.

Hirshfeld surfaces can be visualized using various mapping techniques, including d_{norm}, d_{e}, d_{i}, shape index, and curvedness. Each of these mappings has its unique purpose and helps visualize the molecular surface and its interactions with the surrounding environment. Below is a detailed explanation of these five mapping methods and their meanings.

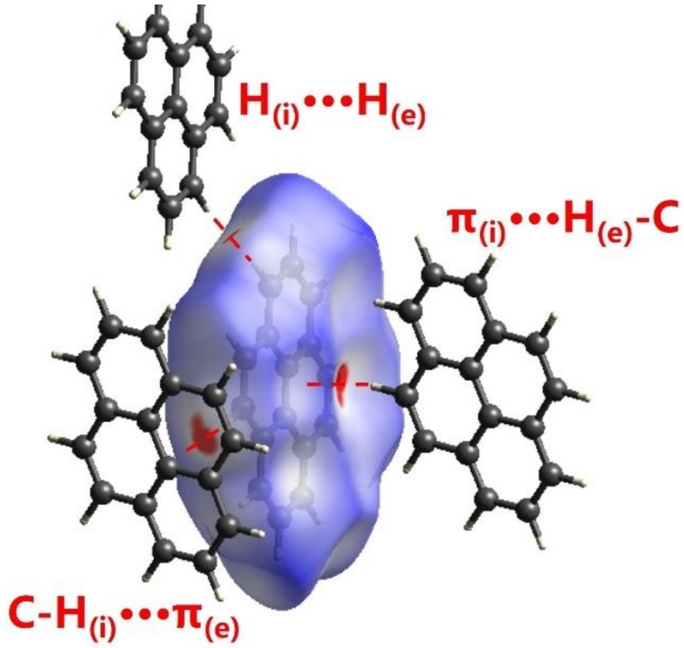

Figure 2.5 Hirshfeld surface of pyrene molecule in pyrene-I polymorph at ambient condition mapped with d_{norm} [77] (Zhou *et al.* 2024)**.** The (i) and (e) represent the atoms inside and outside the Hirshfeld surface, respectively.

d_{norm} is a normalized distance mapping that highlights the regions on the molecular surface where the closest intermolecular contacts occur. It is defined using the following formula:

$$d_{\mathrm{norm}} = \frac{d_{\mathrm{i}} - r_{\mathrm{vdW,i}}}{r_{\mathrm{vdW,i}}} + \frac{d_{\mathrm{e}} - r_{\mathrm{vdW,e}}}{r_{\mathrm{vdW,e}}} \tag{2.5}$$

In the formula, d_{i} represents the distance from a point on the Hirshfeld surface to the nearest atom inside the molecule, while d_{e} is the distance from the same point to the nearest atom outside the molecule. The terms $r_{\mathrm{vdW,i}}$ and $r_{\mathrm{vdW,e}}$ correspond to the van der Waals radii of the atoms inside and outside the molecule, respectively. Through d_{norm} mapping, we can efficiently identify regions of strong intermolecular interactions, such as hydrogen bonds.

This type of mapping allows for the rapid visualization of areas where molecules are in close contact. As shown in Figure 2.5, the red regions directly indicate C-H···π or H···H interactions between adjacent pyrene molecules.

d_e represents the distance from a point on the Hirshfeld surface to the nearest atom outside the molecule. Through d_e mapping, we can visualize how the molecular surface interacts with the external environment. On the other hand, d_i represents the distance from a point on the surface to the nearest atom inside the molecule. Unlike d_e, the d_i mapping is used to display the internal electron density distribution and intramolecular interactions. d_e mapping is typically employed to show the areas of closest contact between the molecular surface and the surrounding environment, making it particularly useful for analyzing short-range interactions such as van der Waals forces and hydrogen bonds. In contrast, d_i mapping reveals how the internal structure of the molecule interacts with its external surroundings, making it valuable for analyzing the molecule's internal geometry, bonding, and other structural aspects.

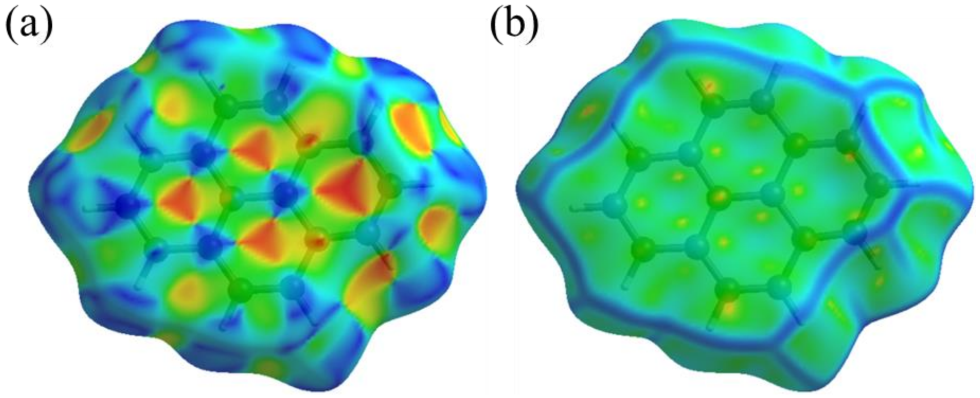

Figure 2.6 The back view of the Hirshfeld surface of the pyrene molecule in the pyrene-I polymorph at ambient condition, mapped with (a) shape index and (b) curvedness [77] (Zhou *et al.* 2024)**.**

The shape index is calculated based on the surface curvature, and different curvature forms on the surface can indicate how molecules pack and pair with each other. For example, positive and negative curvatures correspond to different types of contacts, where concave surfaces typically pair with the convex surfaces of neighboring molecules. This index is particularly useful for identifying complementary regions in molecular packing, such as

$\pi\cdots\pi$ stack interactions. For example, as shown in Fig. 2.6a, the alternating red and blue triangles in the back view of the Hirshfeld surface mapped with shape index indicate $\pi\cdots\pi$ stacking interactions that are characteristic of graphite-like layered packing [73] (Spackman & Byrom, 1997). The calculation of the shape index is based on the maximum curvature (k_1) and minimum curvature (k_2) of the surface, using the following formula:

$$S = \frac{1}{\pi} \arctan\left(\frac{k_1 + k_2}{k_1 - k_2}\right) \tag{2.6}$$

Curvedness is a quantitative measure of the degree of curvature on a surface, indicating the local bending at a specific point. Regions with high curvedness indicate areas where the surface bends sharply, while areas with low curvedness correspond to flatter regions. Curvedness mappings typically appear as large green regions (relatively flat), separated by dark blue edges (regions of high positive curvature), as illustrated in Fig. 2.6b. The calculation of curvedness is given by the following formula:

$$C = 2\sqrt{\frac{k_1^2 + k_2^2}{2}} \tag{2.7}$$

Through curvedness mapping, we can identify flat regions on the surface as well as highly curved areas.

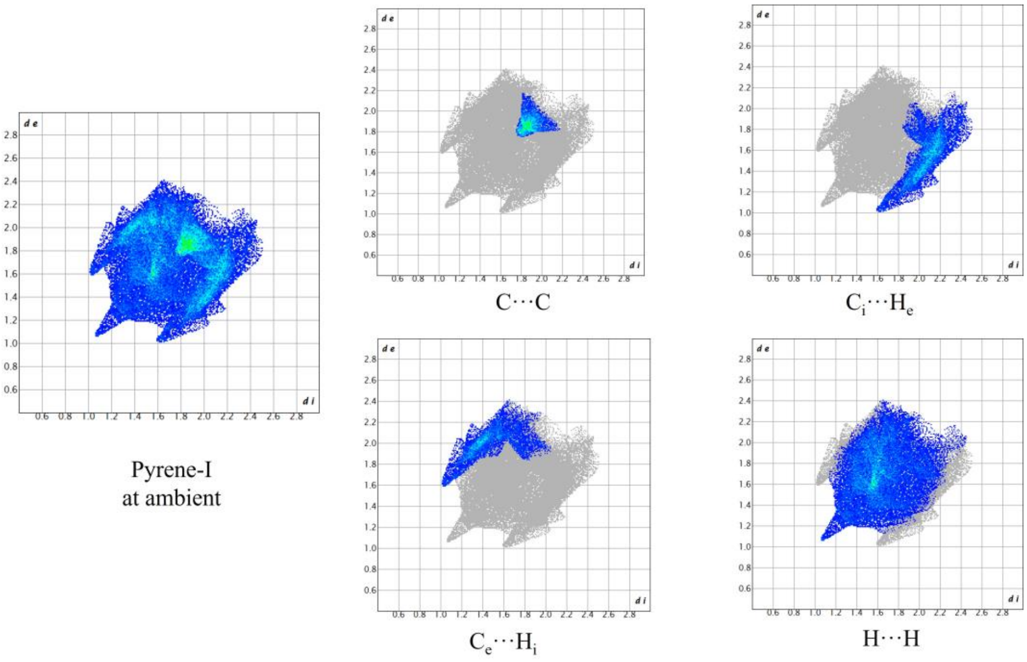

Pyrene-I
at ambient

C···C

$C_i \cdots H_e$

$C_e \cdots H_i$

H···H

Figure 2.7 Fingerprint plots for pyrene molecules in pyrene-I polymorph at ambient condition [77] (Zhou *et al.* 2024)**.** The four plots on the right represent the contributions of different specific interactions to the overall fingerprint plot. The "i" and "e " represent the atoms inside and outside the Hirshfeld surface, respectively.

The fingerprint plot is another important tool in Hirshfeld surface analysis, used to identify and quantitatively analyze various intermolecular interactions. Each point on the Hirshfeld surface is represented by its d_i and d_e values. These values correspond to the shortest distances from the surface point to atoms inside (d_i) and outside (d_e) the molecule. By mapping all the d_i and d_e values onto a two-dimensional plot, a fingerprint plot is generated. Typically, each point on the plot represents a specific combination of d_i and d_e values for a surface point.

The intensity of the color in the plot reflects the frequency of occurrence of that specific d_i and d_e combination. Darker colors indicate higher densities, meaning more surface points share that combination of d_i and d_e. In general, blue regions represent low point density (fewer interactions), green indicates medium density, and red signifies areas of high point density (usually corresponding to strong interactions or contacts). By simplifying the complex three-dimensional interaction information into a two-dimensional plot, the fingerprint plot allows for the quick identification of different types of intermolecular interactions. By examining the distribution in different regions of the plot, one can quantitatively analyze the relative contributions of various types of interactions. For example, four types of interactions and their contributions within the fingerprint plot for pyrene molecules in the pyrene-I polymorph at ambient conditions are shown in Fig. 2.7.

2.5 DFT calculations

DFT is a method that approximates the fundamental equations of quantum mechanics, reducing their complexity to a level where they can be solved numerically by computers. Since its development in the 1970s, DFT has become widely used in fields such as physics, chemistry, and materials science due to its ability to predict various material properties with reasonable accuracy at a computational cost that is feasible for many applications [78] (Jain *et al.*, 2016). The core idea of DFT is that the electron density of a system determines all of its ground state properties, without the need to solve the complex many-electron wavefunction, as required in traditional quantum mechanical methods like Hartree-Fock theory [79] (Slater, 1951). By solving the Kohn-Sham equations [80] (Kohn & Sham, 1965), the electron density of a system can be calculated, which can then be used to derive the system's energy, structure, and other physical and chemical properties.

In this thesis, first-principles calculations are performed within the framework of DFT using the Vienna Ab initio Simulation Package (VASP) [81] (Kresse & Furthmüller, 1996). The projector-augmented wave (PAW) method [82,83] (Blöchl, 1994; Kresse & Joubert, 1999) is employed to handle electron-ion interactions, simplifying the treatment of core electrons while maintaining high accuracy for valence electrons. In the Kohn-Sham DFT framework, the exchange-correlation energy is a crucial component of the total energy, describing the complex interactions between electrons. The generalized gradient approximation (GGA) is used, as it improves upon the local density approximation (LDA) by considering not only the electron density but also its gradient, leading to a more accurate description of systems with non-uniform electron densities. In this work, we primarily use the GGA functional parameterized by Perdew, Burke, and Ernzerhof [84] (Perdew *et al.*, 1996).

The valence electron configurations used for the PAW pseudopotentials were $2s^2 2p^2$ for C and $1s^1$ for hydrogen H. The plane-wave cutoff energy was set to 520 eV. To ensure an accurate description of the electronic structure of the system, the Brillouin zone was using the Monkhorst-Pack k-point grid [85] (Monkhorst & Pack, 1976). The specific k-point grids for the different crystal systems are detailed later in the text. Additionally, since standard DFT calculations, such as GGA-PBE, often fail to accurately describe weak interactions between molecules (e.g., van der Waals forces), we employed the DFT-D3 method proposed by Grimme *et al.* [86] (Grimme *et al.*, 2011). This method introduces an empirical dispersion correction, significantly improving the description of systems with weak interactions. In order to accurately describe the electronic density of states (eDOS) of the crystals, we used the PBE0 hybrid functional [87] (Adamo & Barone, 1999). PBE0 is widely used because it combines a portion of Hartree-Fock exchange energy with the exchange-correlation part of the PBE functional. Compared to pure PBE, PBE0 provides higher accuracy in describing certain electronic structures, particularly in predicting band gaps, electron densities, and properties related to excited states and localized electrons.

Chapter 3 Thesis synopsis

This section offers a brief summary of the results presented in Chapters 4-6, which have either been published or are being prepared for submission to peer-reviewed journals. In Chapter 4 we reported the results of behavior naphthalene and anthracene up to 50 GPa using SC-XRD. Our findings reveal no phase transitions and demonstrate the remarkable stability of these compounds under extreme conditions. In Chapter 5, we explored the high-pressure behavior of pyrene up to 35.5 GPa using SC-XRD. Several phase transitions were observed, revealing the transitions from pyrene-I to pyrene-II at 0.7 GPa, and to the previously unreported phases pyrene-IV at 2.7 GPa and pyrene-V at 7.3 GPa. Chapter 6 presents the results of investigations into the high-pressure behavior of B*a*P up to 28 GPa using SC-XRD. We identified two previously unknown polymorphs: B*a*P-II at 4.8 GPa and B*a*P-III at 7.1 GPa.

3.1 Studies of naphthalene and anthracene up to 50 GPa

Naphthalene was studied under high pressure up to 50.7 GPa using SC-XRD, revealing that it maintains its monoclinic structure (space group $P2_1/c$) throughout this range without undergoing any phase transitions, shown in Fig. 3.1a and b. The molecular arrangement of naphthalene, characterized by a herringbone packing motif, remains stable, with its lattice parameters a, b, c and β angle gradually decreasing under compression. Specifically, the b/b_0 parameter showed the least reduction, decreasing to 0.72 of its original value at 50.7 GPa, while the a/a_0 and c/c_0 reduced to 0.83 of their original values. The experimental pressure-volume data were analyzed using the third-order Birch-Murnaghan EOS, with the V_0 fixed at 182.2 Å^3, and fitting parameters $K_0 = 9.5(6)$ GPa, and $K' = 5.1(2)$ for naphthalene. Furthermore, the intermolecular angle of naphthalene shows a consistent decrease with increasing pressure, decreasing from 53.78° at ambient conditions to 40.6° at 50.7 GPa, indicating a densification of the molecular packing under high-pressure conditions.

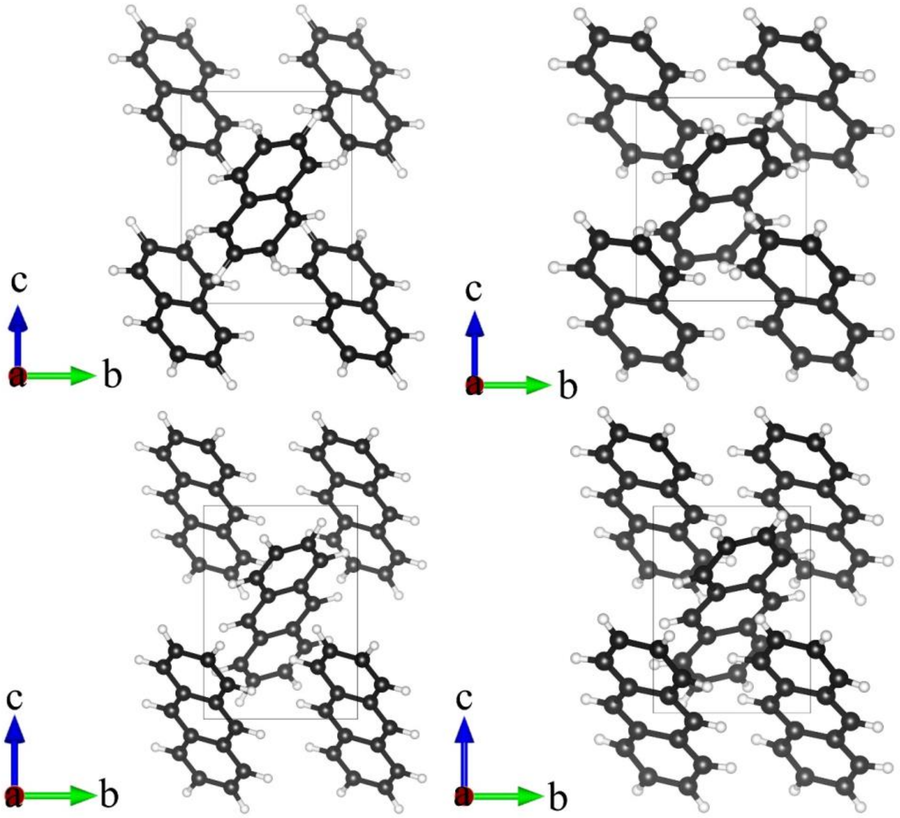

Figure 3.1 Crystal structures of naphthalene and anthracene viewed along the [1 0 0] direction. (a) Naphthalene at ambient conditions; (b) naphthalene at 50.7 GPa; (c) anthracene at ambient conditions; (d) anthracene at 42.3 GPa. C atoms are black. H atoms are white.

Anthracene also exhibits notable stability under high pressure, retaining its monoclinic structure (space group $P2_1/c$) up to 42.3 GPa, shown in Fig.3.1c and d, with no phase transitions observed. Like naphthalene, anthracene's lattice parameters decrease uniformly under pressure. The bulk modulus and first derivative obtained from experiments closely align with those of naphthalene, underscoring similar resistance to compression in both compounds. Despite some differences in the degree of compression, such as anthracene's higher bulk modulus values derived from DFT calculations, both compounds show a decrease in intermolecular angles under pressure, which results in denser molecular packing.

HAR was applied to analyze the C-H bond lengths of naphthalene and anthracene under high pressure. The HAR results for both compounds showed a strong correlation with neutron diffraction data and theoretical predictions, indicating that HAR can yield accurate C-H bond lengths even under extreme conditions. For naphthalene, the average C-H bond length at ambient pressure was 1.08(5) Å. Similarly, for anthracene, HAR produced an average C-H bond length of 1.09(2) Å, which is similar to that observed in previous neutron diffraction studies of perdeuteroanthracene [18] (Lehmann & Pawley, 1972). The uncertainty in anthracene measurements was smaller than in naphthalene, likely due to higher crystal quality. Despite the reduced completeness of the diffraction data, HAR provided bond lengths that aligned well with DFT-calculated values, confirming its potential as a robust tool for high-pressure crystallographic studies. This study highlights the effectiveness of HAR in providing detailed structural insights into complex systems at elevated pressures.

The C-C bonds in naphthalene and anthracene under compression were categorized into three types based on their bonding environments. While experimental data on C-C bond length changes were scattered with large uncertainties, theoretical data indicated that all types of C–C bonds generally decrease in length under compression.

The crystal structures of naphthalene and anthracene under high pressure, demonstrating their stability without phase transitions up to 50 GPa and 43 GPa, respectively. The successful application of HAR in high-pressure analysis provided accurate hydrogen positions, enhancing our understanding of PAHs' behavior under compression.

3.2 Studies of pyrene up to 35 GPa

This study focuses on the high-pressure behavior of pyrene polymorphs using synchrotron SC-XRD in a DAC with He as a quasi-hydrostatic pressure medium. By studying pyrene up to 35.5 GPa, the research revealed several phase transitions and previously unknown polymorphs, providing key insights into how pyrene's molecular structure responds to compression.

Upon initial compression of pyrene-I (Fig.3.2a, space group $P2_1/c$) to 0.7 GPa, a phase transition to pyrene-II (Fig.3.2b, $P2_1/c$) was observed. Despite having the same space group as pyrene-I, pyrene-II exhibited minor differences in its lattice parameters and packing motif. Notably, the β angle in pyrene-II was slightly larger than that in pyrene-I. The molecular arrangement in pyrene-II remained similar to pyrene-I, retaining the sandwich-herringbone packing motif. The observed transition is comparable to a previously reported low-temperature transition [88-90] (Jones *et al.*, 1978; Knight *et al.*, 1996; Frampton *et al.*, 2000), but this study marks the first structural analysis of pyrene-II under high pressure and room temperature.

Further compression led to the discovery of a previously unknown triclinic polymorph, pyrene-IV (Fig.3.2d, space group *P*-1), at 2.7 GPa. Pyrene-IV remained stable up to 4.3 GPa and displayed a more complex molecular arrangement. In pyrene-IV, there were two crystallographically distinct molecules forming different types of "sandwiches." One type consisted of almost flat molecules, while the other had curved molecules. Despite this transition, the overall molecular packing motif remained somewhat similar to the earlier polymorphs, though the reduction in symmetry and the more complex arrangement indicated significant changes in molecular interactions under pressure.

At 7.3 GPa, another phase transition occurred, leading to the formation of pyrene-V, which retained the same space group (Fig.3.2e, $P2_1/c$) as pyrene-I and pyrene-II. However, pyrene-V exhibited a change in molecular packing. The sandwich structure seen in the previous polymorphs collapsed, and the molecules became substantially curved and aligned along the crystallographic c-axis. This structural transformation marked a significant departure from the flat molecular configurations of earlier polymorphs. The molecular curvature in pyrene-V was a novel observation, as such curvature had not been reported for pyrene under pressure in previous studies. Pyrene-V remained stable up to 35.5 GPa, the highest pressure achieved in this study.

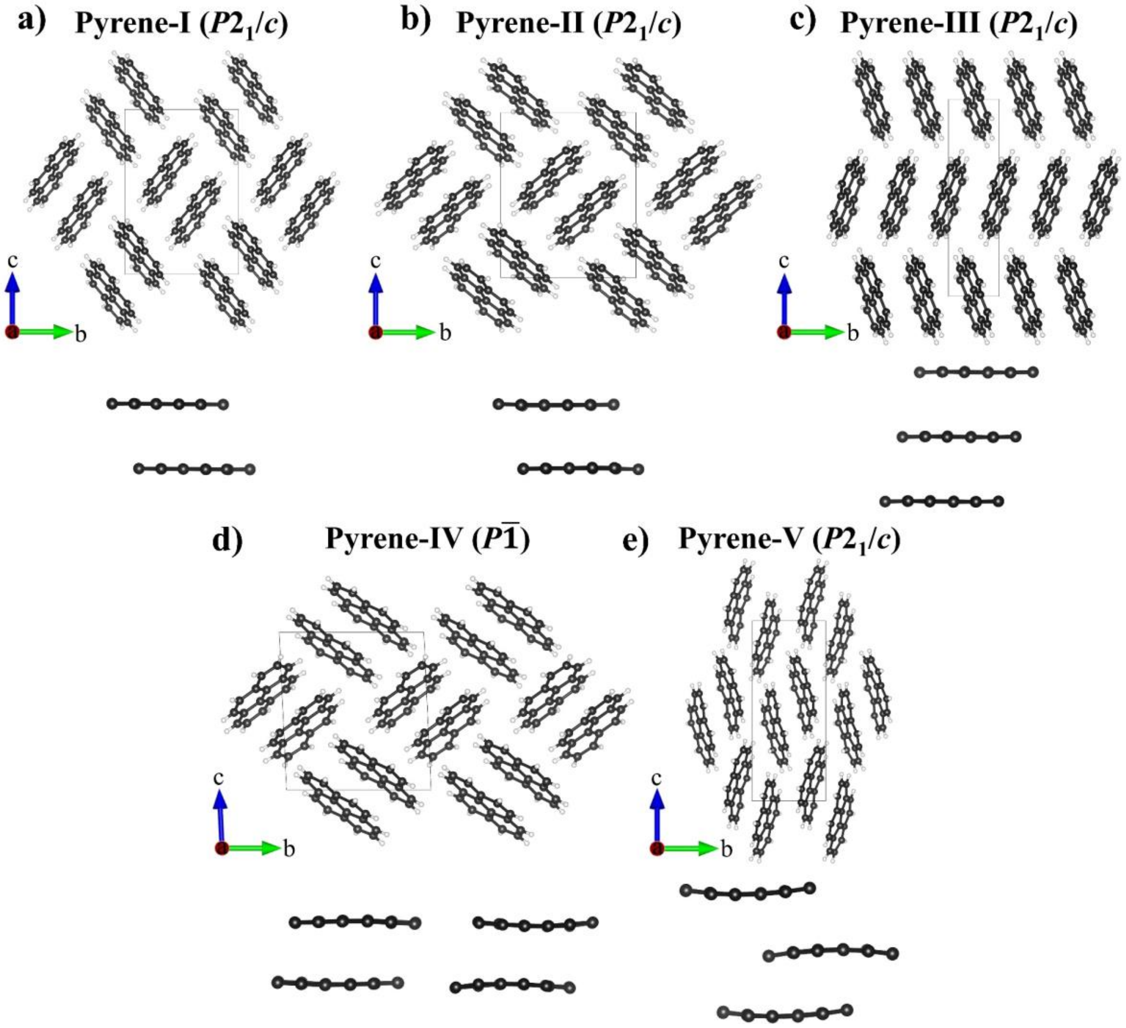

a) Pyrene-I ($P2_1/c$)

b) Pyrene-II ($P2_1/c$)

c) Pyrene-III ($P2_1/c$)

d) Pyrene-IV ($P\bar{1}$)

e) Pyrene-V ($P2_1/c$)

Figure 3.2. Crystal structures of pyrene polymorphs viewed along *a* axis. (a) Pyrene-I, ambient conditions; (b) pyrene-II, 0.7 GPa; (c) pyrene-III, 0.5 GPa [40] (Fabbiani *et al.*, 2006); (d) pyrene-IV, 2.7 GPa; (e) pyrene-V, 7.3 GPa. Pairs of molecules (sandwiches) determining the crystal-packing motif are shown in the bottom. Pyrene-IV has two types of sandwiches (sandwich 1- to the left, sandwich 2- to the right). Pyrene-III and V do not feature sandwiches in its crystal structure. C atoms are black, H atoms are white.

The compressional behavior of the various pyrene polymorphs was analyzed by fitting the pressure-volume data to the third-order Birch-Murnaghan EOS. The bulk modulus K_0 and its first derivative K' were determined to be 5.2(2) GPa and 10.6(4), respectively. These values were consistent with the results of theoretical calculations, which provided additional EOS parameters that agreed well with experimental data. DFT calculations also confirmed the experimental results, with both sets of data indicating continuous volume decreases as pressure increased. However, phase transitions were marked by abrupt changes in other structural parameters, such as lattice constants and interplanar angles.

The study's most significant finding was the gradual compaction of molecular structures in pyrene under pressure, leading to pronounced changes in molecular packing motifs. The progression from pyrene-I to pyrene-V showed a clear evolution in packing, with the structure shifting from a sandwich-herringbone arrangement in pyrene-I, pyrene-II, and pyrene-IV to a simple herringbone arrangement in pyrene-V. As the molecular packing compacted, the molecules themselves became increasingly curved, especially in pyrene-V, which was a novel observation in this context. The curvature of the molecules was analyzed using computational methods, which showed that the degree of curvature increased progressively with pressure. This phenomenon has not been previously observed in studies of organic materials under pressure.

To visualize these structural changes, a comprehensive geometrical analysis of the pyrene polymorphs was conducted. Using computational tools such as NumPy and SciPy libraries, we were able to accurately calculate intermolecular distances and interplanar angles. To analyze the intermolecular interactions in each polymorph, the Hirshfeld surface and fingerprint plots were used.

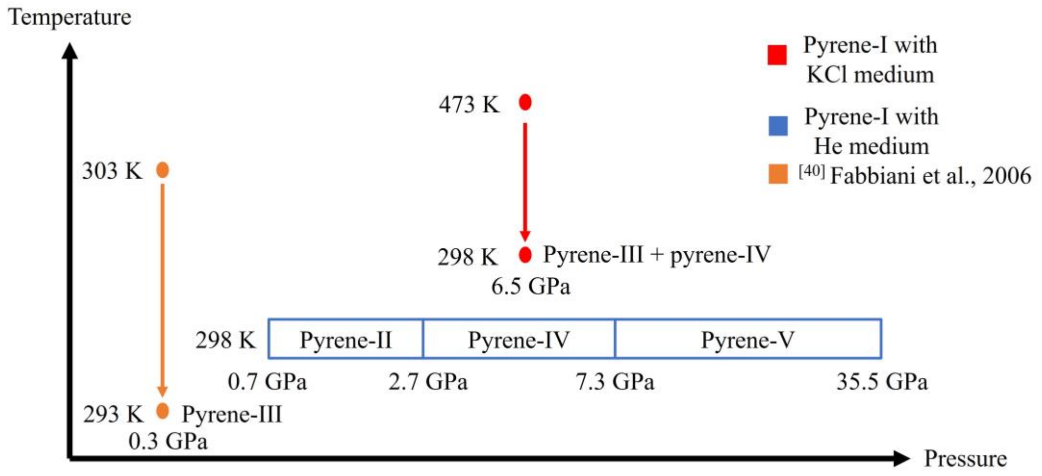

Figure 3.3. Overview of all high-pressure experiments on pyrene in this section. The red color represents high-temperature high-pressure experiments, where the sample was heated to 473 K and then quenched to 298 K at 6.5 GPa. The blue color denotes room-temperature high-pressure experiments. The orange color corresponds to the experiments conducted by Fabbiani *et al.* [40] (Fabbiani *et al.*, 2006), where Pyrene-III was observed, which recrystallized from a solution of pyrene in dichloromethane upon cyclic heating and cooling at 0.3 GPa.

Theoretical calculations provided further insights into the stability and transitions between polymorphs. The enthalpy differences (*ΔH*) for pyrene-II, pyrene-III, pyrene-IV, and pyrene-V relative to pyrene-I were calculated as a function of pressure up to 5 GPa. The results suggested that pyrene-II is more stable than pyrene-IV and pyrene-V at lower pressures, but above 2 GPa, pyrene-V becomes more stable. These findings align with the experimental observations, where pyrene-V was first detected at 7.3 GPa. Interestingly, pyrene-III (Fig 3.2c), which was synthesized in previous studies through recrystallization at 0.3 GPa [40] (Fabbiani *et al.*, 2006), was not observed in this room-temperature study, although it was predicted by DFT calculations to be stable under certain conditions. This discrepancy could be due to the experimental parameters or the metastable nature of pyrene-III under different conditions. However, in a subsequent high-temperature high-pressure experiment conducted at 473 K and 6.5 GPa, we successfully synthesized pyrene-III (Fig.3.3). This confirms that pyrene-III can indeed form under specific thermal conditions, supporting the theoretical prediction.

3.3 Studies of B*a*P up to 35 GPa

This study investigates the high-pressure behavior of B*a*P polymorphs using synchrotron SC-XRD in a DAC with He as the pressure medium. B*a*P-I, the ambient polymorph, undergoes a series of phase transitions as pressure increases. Upon compression to 4.8 GPa, B*a*P-I (space group $P2_1/c$) transforms into a previously unknown monoclinic polymorph, B*a*P-II, which retains the same space group ($P2_1/c$) but exhibits notable structural changes. At 7.1 GPa, B*a*P-II undergoes another phase transition into B*a*P-III, a triclinic polymorph (space group *P*-1), which remains stable up to 28 GPa. Beyond 28 GPa, the diffraction pattern disappeared, likely due to significant structural disorder.

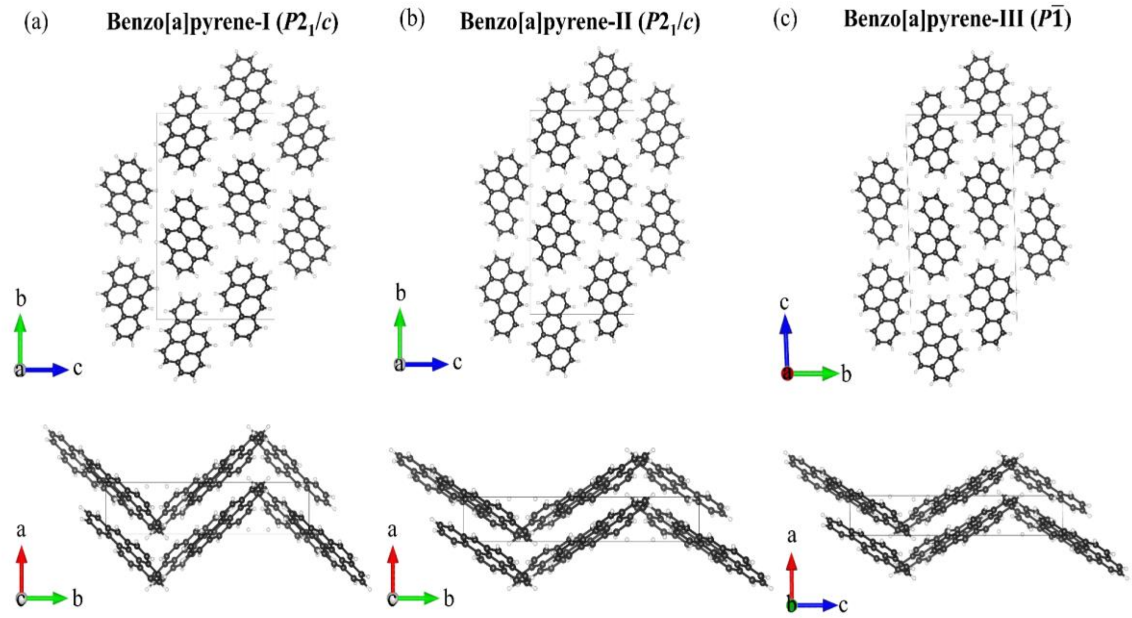

Figure 3.4. Crystal structures of B*a*P polymorphs. (a) B*a*P-I at ambient conditions, as viewed along the *a* axis (top figure) and *c* axis (bottom figure); (b) B*a*P-II at 4.8 GPa, viewed along the *a* axis (top) and *c* axis (bottom); (c) B*a*P-III at 7.1 GPa, as viewed along the *a* axis (top) and *b* axis (bottom); C atoms are black. H atoms are white.

The structure of B*a*P-I at ambient conditions (Fig. 3.4a) and 2.2GPa was similar to previously reported results. The monoclinic unit cell of B*a*P-I at ambient conditions has the parameters: a = 4.5384(3) Å, b =20.439(5) Å, c = 13.531(2) Å, β = 97.006(8) °, and volume V = 1245.8(4) Å^3. In comparison, B*a*P-II at 4.8 GPa has the unit cell parameters a = 3.59710(10) Å, b = 21.658(9) Å, c = 12.7908(9) Å, β = 95.339(5) °, and volume V = 992.2(4) Å^3. The arrangement of molecules in B*a*P-II is similar to that in B*a*P-I. In both structures, the molecules display a herringbone pattern in projection along the *a* direction (Figs. 3.4a, b, top), but the intermolecular angles in B*a*P-I and B*a*P-II are noticeably different (see the projections along the b axis in Figs. 3.4a, b, bottom). In our previous study of pyrene under pressure [77] (Zhou *et al.*, 2024), we also noticed that the phase transformation of pyrene-I to pyrene-II is accompanied by a change of the intermolecular angle, whereas the space group symmetry remains the same.

Further compression of B*a*P-II resulted in the formation of B*a*P-III at 7.1 GPa, with a triclinic structure (*P*-1). The unit cell parameters of B*a*P-III at this pressure are a = 3.4912(1) Å, b = 12.687(3) Å, c = 21.531(6) Å, α = 91.51(2) °, β = 90.434(9) °, γ = 95.820(8) °, and volume V = 911.5(2) Å^3. The lower symmetry of B*a*P-III compared to B*a*P-I and B*a*P-II leads to the disappearance of the herringbone molecular arrangement, as shown in Fig. 3.4c. Nevertheless, when viewed along the a- and b-axes, the structure of B*a*P-III still bears some resemblance to B*a*P-I and B*a*P-II.

The compressional behavior of B*a*P polymorphs up to 28 GPa was studied by analyzing the pressure-volume data for B*a*P-I, B*a*P-II, and B*a*P-III. These data were fitted using the third-order Birch-Murnaghan EOS. For B*a*P-I at ambient conditions, the initial volume V_0 was 311.45 Å^3, and the bulk modulus (K_0) and its first derivative (K') were determined to be 7.7(7) GPa and 10.10(10), respectively. The calculated data have also been fitted using the third-order Birch-Murnaghan EOS. The EOS parameters appeared to be as follows: V_0 = 295.92 Å^3, K_0 = 11.53(14) GPa, and K' = 8.28(9).

In addition to volume changes, the lattice parameters of the polymorphs were found to vary with pressure. The lattice parameters a, b, and c of B*a*P-I and B*a*P-II exhibited distinct changes during the phase transitions. Notably, a parameter shortened substantially upon the transition from B*a*P-I to B*a*P-II, decreasing from 4.2338(2) Å to 3.59710(10) Å, while the b parameter increased from 19.838(4) Å to 21.658(9) Å. The c parameter continuously decreased throughout the phase transitions. The β angle also decreased from 97.006° in B*a*P-I to 95.339° in B*a*P-II. For B*a*P-III, the lattice parameters followed a similar trend, with gradual compression as pressure increased to 28 GPa.

Theoretical calculations provided further insights into the stability of the polymorphs. The enthalpy differences (ΔH) between B*a*P-I, B*a*P-II, and B*a*P-III were calculated as a function of pressure up to 7.1 GPa. At ambient pressure, B*a*P-I was the most stable polymorph. However, B*a*P-II became more stable at pressures above 2.2 GPa. By 3.5 GPa, the atomic configuration of B*a*P-I relaxed into that of B*a*P-II. At pressures above 3.5 GPa, B*a*P-III emerged as the most stable phase. These findings agree with the experimental observations, where B*a*P-III was detected at 7.1 GPa.

A geometrical analysis of the B*a*P polymorphs was also conducted to study the changes in intermolecular distances and interplanar angles. Using computational tools (NumPy and SciPy libraries), the intermolecular distances and interplanar angles were calculated for B*a*P-I, B*a*P-II, and B*a*P-III. In B*a*P-I, the intermolecular angle changed only slightly from 72.9° at ambient pressure to 73.5° at 2.2 GPa. However, the transition to B*a*P-II caused an abrupt change in the intermolecular angle, decreasing from 73.5° at 2.2 GPa to 53.5° at 4.8 GPa. Further compression of B*a*P-II resulted in the transformation to B*a*P-III, where the interplanar angle gradually increased from 53.5° to 54.8° at 27.9 GPa. Unlike pyrene, which exhibited molecular curvature under high pressure, B*a*P did not show such a trend, maintaining flat molecular planes throughout the studied pressure range.

The analysis of the Hirshfeld surfaces of B*a*P polymorphs shows that the two sides of a molecule are involved in quite similar contacts with neighboring molecules, participating in a planar stacking arrangement of molecules (π···π stacking). Further analysis of fingerprint plot surface revealed that in all three polymorphs, the molecules are involved in similar contacts with neighboring molecules, participating in a planar stacking arrangement. A general trend is observed with an increase in the percentage contribution of C···C intermolecular contacts and a decrease in H···H contacts upon compression.

3.4 List of manuscripts and statement of authors' contribution

(1) W. Zhou (WZ), X. Li (XL), F. I. Akbar (FIA), A. Pakhomova (AP), M. Hanfland (MH), L. Dubrovinsky (LD) and N. Dubrovinskaia (ND). The behavior of naphthalene and anthracene under high pressure. To be submitted to *ChemEngineering* journal

LD and ND conceived the overall project. WZ prepared the high-pressure experiments. WZ, XL, FIA, AP and MH performed synchrotron X-ray diffraction experiments. WZ performed synchrotron X-ray diffraction data analysis and theoretical calculations. WZ, LD, and ND analyzed all the data. WZ, LD, and ND wrote the manuscript with input from all the other authors. All the authors discussed and contributed to the manuscript.

(2) W. Zhou (WZ), Y. Yin (YY), D. Laniel (DL), A. Aslandukov (AA), E. Bykova (EB), A. Pakhomova (AP), M. Hanfland (MH), T. Poreba (TP), M. Mezouar (MM), L. Dubrovinsky (LD) and N. Dubrovinskaia (ND). Polymorphism of pyrene on compression to 35 GPa in a diamond anvil cell. *Communications Chemistry*, 7(1), 209.

LD and ND conceived the overall project. WZ prepared the high-pressure experiments. WZ, YY, DL, AA, EB, AP, MH, TP, and MM performed synchrotron X-ray diffraction experiments. WZ performed synchrotron X-ray diffraction data analysis and theoretical calculations. WZ, LD, and ND analyzed all the data. WZ, LD, and ND wrote the manuscript with input from all the other authors. All the authors discussed and contributed to the manuscript.

(3) W. Zhou (WZ), A. Aslandukov (AA), A. Minchenkova (AM), M. Hanfland (MH), L. Dubrovinsky (LD) and N. Dubrovinskaia (ND). Structural transformations and stability of benzo[a]pyrene under high pressure. Under review, *IUCrJ*.

LD and ND conceived the overall project. WZ prepared the high-pressure experiments. WZ, AA, AM and MH performed synchrotron X-ray diffraction experiments. WZ processed the synchrotron X-ray diffraction data analysis and theoretical calculations. WZ, LD, and ND analyzed all the data. WZ, LD, and ND wrote the manuscript with input from all the other authors. All the authors discussed and contributed to the manuscript.

Reference

[1] Yang, F., Zhang, Q., Guo, H. *et al.* Evaluation of cytotoxicity, genotoxicity and teratogenicity of marine sediments from Qingdao coastal areas using in vitro fish cell assay, comet assay and zebrafish embryo test. *Toxicol In Vitro* **24**, 2003-2011 (2010).

[2] Li, Q., Zhang, Y., Xie, Z. *et al.* Polycyclic aromatic hydrocarbon-based organic semiconductors: ring-closing synthesis and optoelectronic properties. *Journal of Materials Chemistry C* **10**, 2411-2430 (2022).

[3] Harvey, R. G. *Polycyclic aromatic hydrocarbons*, (Wiley-VCH, 1991).

[4] Ravindra, K., Sokhi, R. and Vangrieken, R. Atmospheric polycyclic aromatic hydrocarbons: Source attribution, emission factors and regulation. *Atmospheric Environment* **42**, 2895-2921 (2008).

[5] Allamandola, L., Tielens, A. and Barker, J. Polycyclic aromatic hydrocarbons and the unidentified infrared emission bands-Auto exhaust along the Milky Way. *Astrophysical Journal, Part 2-Letters to the Editor (ISSN 0004-637X), vol. 290, March 1, 1985, p. L25-L28.* **290**, L25-L28 (1985).

[6] d'Hendecourt, L. and Ehrenfreund, P. Spectroscopic properties of polycyclic aromatic hydrocarbons (PAHs) and astrophysical implications. *Advances in Space Research* **19**, 1023-1032 (1997).

[7] Ehrenfreund, P. and Charnley, S. B. Organic molecules in the interstellar medium, comets, and meteorites: a voyage from dark clouds to the early Earth. *Annual Review of Astronomy and Astrophysics* **38**, 427-483 (2000).

[8] Collin, G., Höke, H. and Greim, H. Naphthalene and hydronaphthalenes. *Ullmann's Encyclopedia of Industrial Chemistry* (2000).

[9] Ho, M. H., Balaganesan, B. and Chen, C. H. Blue fluorescence and bipolar transport materials based on anthracene and their application in OLEDs. *Israel Journal of Chemistry* **52**, 484-495 (2012).

[10] Alidağı, H. A., Tümay, S. O., Şenocak, A. *et al.* Pyrene functionalized cyclotriphosphazene-based dyes: synthesis, intramolecular excimer formation, and fluorescence receptor for the detection of nitro-aromatic compounds. *Dyes and Pigments* **153**, 172-181 (2018).

[11] Bukowska, B., Mokra, K. and Michałowicz, J. Benzo [a] pyrene—Environmental occurrence, human exposure, and mechanisms of toxicity. *International journal of molecular sciences* **23**, 6348 (2022).

[12] Desiraju, G. R. and Gavezzotti, A. Crystal structures of polynuclear aromatic hydrocarbons. Classification, rationalization and prediction from molecular structure. *Acta Crystallographica Section B: Structural Science* **45**, 473-482 (1989).

[13] Schatschneider, B., Phelps, J. and Jezowski, S. A new parameter for classification of polycyclic aromatic hydrocarbon crystalline motifs: a Hirshfeld surface investigation. *CrystEngComm* **13** (2011).

[14]Abrahams, S., Robertson, J. M. and White, J. The crystal and molecular structure of naphthalene. I. X-ray measurements. *Acta Crystallographica* **2**, 233-238 (1949).

[15] Natkaniec, I., Dyck, W., Fuess, H. *et al.* The structure of perdeuteronaphthalene $C_{10}D_8$ at 12 K by neutron diffraction. *Zeitschrift für Kristallographie-Crystalline Materials* **163**, 285-294 (1983).

[16] Oddershede, J. and Larsen, S. Charge density study of naphthalene based on X-ray diffraction data at four different temperatures and theoretical calculations. *The Journal of Physical Chemistry A* **108**, 1057-1063 (2004).

[17]Cruickshank, D. W. J. A detailed refinement of the crystal and molecular structure of anthracene. *Acta Crystallographica* **9**, 915-923 (1956).

[18] Lehmann, M. and Pawley, G. S. Structure of perdeuterioanthracene by neutron diffraction. *ACTA CHEMICA SCANDINAVICA* **26**, 1996-& (1972).

[19] Robertson, J. M. and White, J. 72. The crystal structure of pyrene. A quantitative X-ray investigation. *Journal of the Chemical Society (Resumed)*, 358-368 (1947).

[20] Hazell, A., Larsen, F. and Lehmann, M. A neutron diffraction study of the crystal structure of pyrene, C16H10. *Acta Crystallographica Section B: Structural Crystallography and Crystal Chemistry* **28**, 2977-2984 (1972).

[21] Iball, J. The Crystal Structure of condensed Ring Compounds, III: Three carcinogenic hydrocarbons: 1: 2-Benzpvrene, Methylcholanthrene and 5: 6-cycloPenteno-I: 2-benzanthracene. *Zeitschrift für Kristallographie-Crystalline Materials* **94**, 7-21 (1936).

[22] Iball, J. and Young, D. Structure of 3: 4-benzpyrene. *Nature* **177**, 985-986 (1956).

[23] Iball, J., Scrimgeour, S. and Young, D. 3, 4-Benzopyrene (a new refinement). *Acta Crystallographica Section B: Structural Crystallography and Crystal Chemistry* **32**, 328-330 (1976).

[24] Contag, B. Die polymorphic von benzo [a] pyren. *Naturwissenschaften* **65**, 108-109 (1978).

[25] Carrell, C. J., Carrell, T. G., Carrell, H. *et al.* Benzo [a] pyrene and its analogues: structural studies of molecular strain. *Carcinogenesis* **18**, 415-422 (1997).

[26] Dubrovinsky, L. Single-crystal x-ray diffraction in the megabar pressure range. *High Press. Res.* **33**, 451-583 (2013).

[27] Giordano, N., Beavers, C. M., Kamenev, K. V. *et al.* High-pressure polymorphism in l-threonine between ambient pressure and 22 GPa. *CrystEngComm* **21**, 4444-4456 (2019).

[28] Bridgman, P. W. in *Proc. Am. Acad. Arts Sci.* 227-268 (1938).

[29] Jones, P. F. and Nicol, M. Excimer emission of naphthalene, anthracene, and phenanthrene crystals produced by very high pressures. *The Journal of Chemical Physics* **48**, 5440-5447 (1968).

[30] Vaidya, S. and Kennedy, G. Compressibility of 18 molecular organic solids to 45 kbar. *The Journal of Chemical Physics* **55**, 987-992 (1971).

[31] Nicol, M., Vernon, M. and Woo, J. T. Raman spectra and defect fluorescence of anthracene and naphthalene crystals at high pressures and low temperatures. *The Journal of Chemical Physics* **63**, 1992-1999 (1975).

[32] Meletov, K. Phonon spectrum of a naphthalene crystal at a high pressure: Influence of shortened distances on the lattice and intramolecular vibrations. *Physics of the Solid State* **55**, 581-588 (2013).

[33] Likhacheva, A. Y., Rashchenko, S. V. and Litasov, K. D. High-pressure structural properties of naphthalene up to 6 GPa. *Journal of Applied Crystallography* **47**, 984-991 (2014).

[34] O'Bannon, E. and Williams, Q. Vibrational spectra of four polycyclic aromatic hydrocarbons under high pressure: implications for stabilities of PAHs during accretion. *Physics and Chemistry of Minerals* **43**, 181-208 (2016).

[35] Offen, H. Fluorescence spectra of several aromatic crystals under high pressures. *The Journal of Chemical Physics* **44**, 699-703 (1966).

[36] Adams, D. M. and Tan, T.-K. Vibrational spectroscopy at high pressures. Part 37. —Infrared spectrum of anthracene. *Journal of the Chemical Society, Faraday Transactions 2: Molecular and Chemical Physics* **77**, 1711-1714 (1981).

[37] Leger, J. and Aloualiti, H. X-ray study of anthracene under high pressure. *Solid state communications* **79**, 901-904 (1991).

[38] Zhao, L., Baer, B. J. and Chronister, E. L. High-pressure Raman study of anthracene. *The Journal of Physical Chemistry A* **103**, 1728-1733 (1999).

[39] Oehzelt, M., Heimel, G., Resel, R. *et al.* High pressure x-ray study on anthracene. *The Journal of chemical physics* **119**, 1078-1084 (2003).

[40] Fabbiani, F. P., Allan, D. R., Parsons, S. *et al.* Exploration of the high-pressure behaviour of polycyclic aromatic hydrocarbons: naphthalene, phenanthrene and pyrene. *Acta Crystallographica Section B: Structural Science* **62**, 826-842 (2006).

[41] Zallen, R., Griffiths, C., Slade, M. *et al.* The solid state transition in pyrene. *Chemical Physics Letters* **39**, 85-89 (1976).

[42] Sun, B., Dreger, Z. and Gupta, Y. High-pressure effects in pyrene crystals: vibrational spectroscopy. *The Journal of Physical Chemistry A* **112**, 10546-10551 (2008).

[43] Warner S. D., Lau, E., Farant, J. P. *et al.* Benzo (a) pyrene: A high-pressure FT-Raman investigation. *Canadian journal of analytical sciences and spectroscopy*, **48(2)**, 153-156 (2003).

[44] Dubrovinskaia, N., Dubrovinsky, L., Solopova, N. A. *et al.* Terapascal static pressure generation with ultrahigh yield strength nanodiamond. *Science advances* **2**, e1600341 (2016).

[45] Dubrovinsky, L., Khandarkhaeva, S., Fedotenko, T. *et al.* Materials synthesis at terapascal static pressures. *Nature* **605**, 274-278 (2022).

[46] Occelli, F., Loubeyre, P. and LeToullec, R. Properties of diamond under hydrostatic pressures up to 140 GPa. *Nature materials* **2**, 151-154 (2003).

[47] Letoullec, R., Pinceaux, J. and Loubeyre, P. The membrane diamond anvil cell: a new device for generating continuous pressure and temperature variations. *International Journal of High Pressure Research* **1**, 77-90 (1988).

[48] Kantor, I., Prakapenka, V., Kantor, A. *et al.* BX90: A new diamond anvil cell design for X-ray diffraction and optical measurements. *Review of Scientific Instruments* **83** (2012).

[49] Boehler, R. New diamond cell for single-crystal x-ray diffraction. *Review of Scientific Instruments* **77** (2006).

[50] Jayaraman, A. Diamond anvil cell and high-pressure physical investigations. *Reviews of Modern Physics* **55**, 65 (1983).

[51] Shen, G., Wang, Y., Dewaele, A. *et al.* Toward an international practical pressure scale: A proposal for an IPPS ruby gauge (IPPS-Ruby2020). *High Pressure Research* **40**, 299-314 (2020).

[52] Dewaele, A., Belonoshko, A. B., Garbarino, G. *et al.* High-pressure–high-temperature equation of state of KCl and KBr. *Physical Review B—Condensed Matter and Materials Physics* **85**, 214105 (2012).

[53] Dewaele, A., Torrent, M., Loubeyre, P. *et al.* Compression curves of transition metals in the Mbar range: Experiments and projector augmented-wave calculations. *Physical Review B—Condensed Matter and Materials Physics* **78**, 104102 (2008).

[54] Fei, Y., Ricolleau, A., Frank, M. *et al.* Toward an internally consistent pressure scale. *Proceedings of the National Academy of Sciences* **104**, 9182-9186 (2007).

[55] Dorfman, S. M., Prakapenka, V. B., Meng, Y. *et al.* Intercomparison of pressure standards (Au, Pt, Mo, MgO, NaCl and Ne) to 2.5 Mbar. *Journal of Geophysical Research: Solid Earth* **117** (2012).

[56] Taylor, A. *X-ray Metallography*, (Wiley, 1961).

[57] Ladd, M. F. C., Palmer, R. A. and Palmer, R. A. *Structure determination by X-ray crystallography*, (Springer, 1977), Vol. 233.

[58] Kaelble, E. F. *Handbook of X-rays*, (McGraw-Hill, 1967).

[59] Pollock, H. C. The discovery of synchrotron radiation. *Am. J. Phys* **51**, 278 (1983).

[60] Prescher, C. and Prakapenka, V. B. DIOPTAS: a program for reduction of two-dimensional X-ray diffraction data and data exploration. *High Pressure Research* **35**, 223-230 (2015).

[61] Rigaku, O., CrysAlis P. R. O. Rigaku Oxford Diffraction. *Yarnton, England* (2015).

[62] Sheldrick, G. M. A short history of SHELX. *Acta Crystallographica Section A: Foundations of Crystallography* **64**, 112-122 (2008).

[63] Dolomanov, O. V., Bourhis, L. J., Gildea, R. J. *et al.* OLEX2: a complete structure solution, refinement and analysis program. *Journal of applied crystallography* **42**, 339-341 (2009).

[64] Momma, K. and Izumi, F. VESTA: a three-dimensional visualization system for electronic and structural analysis. *Journal of Applied crystallography* **41**, 653-658 (2008).

[65] Woińska, M., Grabowsky, S., Dominiak, P. M. *et al.* Hydrogen atoms can be located accurately and precisely by x-ray crystallography. *Science advances* **2**, e1600192 (2016).

[66] Kleemiss, F., Dolomanov, O. V., Bodensteiner, M. *et al.* Accurate crystal structures and chemical properties from NoSpherA2. *Chem Sci* **12**, 1675-1692 (2020).

[67] Neese, F. Software update: The ORCA program system—Version 5.0. *Wiley Interdisciplinary Reviews: Computational Molecular Science* **12(5)**, e1606.

[68] Le Bail, A., Duroy, H. and Fourquet, J. L. Ab-initio structure determination of $LiSbWO_6$ by X-ray powder diffraction. *Materials Research Bulletin* **23**, 447-452 (1988).

[69] Petříček, V., Dušek, M. and Palatinus, L. Crystallographic computing system JANA2006: general features. *Zeitschrift für Kristallographie-Crystalline Materials* **229**, 345-352 (2014).

[70] Birch, F. Finite elastic strain of cubic crystals. *Physical review* **71**, 809 (1947).

[71] Angel, R. J., Alvaro, M. and Gonzalez-Platas, J. EosFit7c and a Fortran module (library) for equation of state calculations. *Zeitschrift für Kristallographie-Crystalline Materials* **229**, 405-419 (2014).

[72] McKinnon, J. J., Spackman, M. A. and Mitchell, A. S. Novel tools for visualizing and exploring intermolecular interactions in molecular crystals. *Acta Crystallographica Section B: Structural Science* **60**, 627-668 (2004).

[73] Spackman, M. A. and Byrom, P. G. A novel definition of a molecule in a crystal. *Chemical physics letters* **267**, 215-220 (1997).

[74] Spackman, M. A. and Jayatilaka, D. Hirshfeld surface analysis. *CrystEngComm* **11**, 19-32 (2009).

[75] Spackman, P. R., Turner, M. J., McKinnon, J. J. *et al.* CrystalExplorer: a program for Hirshfeld surface analysis, visualization and quantitative analysis of molecular crystals. *Journal of Applied Crystallography* **54**, 1006-1011 (2021).

[76] Hirshfeld, F. L. Bonded-atom fragments for describing molecular charge densities. *Theoretica chimica acta* **44**, 129-138 (1977).

[77] Zhou, W., Yin, Y., Laniel, D. *et al.* Polymorphism of pyrene on compression to 35 GPa in a diamond anvil cell. *Communications Chemistry* **7**, 209 (2024).

[78] Jain, A., Shin, Y. and Persson, K. A. Computational predictions of energy materials using density functional theory. *Nature Reviews Materials* **1**, 1-13 (2016).

[79] Slater, J. C. A simplification of the Hartree-Fock method. *Physical review* **81**, 385 (1951).

[80] Kohn, W. and Sham, L. J. Self-consistent equations including exchange and correlation effects. *Physical review* **140**, A1133 (1965).

[81] Kresse, G. and Furthmüller, J. Efficient iterative schemes for ab initio total-energy calculations using a plane-wave basis set. *Physical review B* **54**, 11169 (1996).

[82] Blöchl, P. E. Projector augmented-wave method. *Physical review B* **50**, 17953 (1994).

[83] Kresse, G. and Joubert, D. From ultrasoft pseudopotentials to the projector augmented-wave method. *Physical review b* **59**, 1758 (1999).

[84] Perdew, J. P., Burke, K. and Ernzerhof, M. Generalized gradient approximation made simple. *Physical review letters* **77**, 3865 (1996).

[85] Monkhorst, H. J. and Pack, J. D. Special points for Brillouin-zone integrations. *Physical review B* **13**, 5188 (1976).

[86] Grimme, S., Ehrlich, S. and Goerigk, L. Effect of the damping function in dispersion corrected density functional theory. *Journal of computational chemistry* **32**, 1456-1465 (2011).

[87] Adamo, C. and Barone, V. Toward reliable density functional methods without adjustable parameters: The PBE0 model. *The Journal of chemical physics* **110**, 6158-6170 (1999).

[88] Jones, W., Ramdas, S. and Thomas, J. M. Novel approach to the determination of the crystal structures of organic molecular crystals: Low temperature form of pyrene. *Chemical Physics Letters* **54**, 490-493 (1978).

[89] Knight, K. S., Shankland, K., David, W. I. *et al.* The crystal structure of perdeuterated pyrene II at 4.2 K. *Chemical physics letters* **258**, 490-494 (1996).

[90] Frampton, C., Knight, K., Shankland, N. *et al.* Single-crystal X-ray diffraction analysis of pyrene II at 93 K. *Journal of Molecular Structure* **520**, 29-32 (2000).

Chapter 4 High-pressure study of naphthalene ($C_{10}H_8$) and anthracene ($C_{14}H_{10}$), up to 50 GPa using single-crystal X-ray diffraction

Wenju Zhou[a*], *Xiang Li*[c,e], *Fariia Iasmin Akbar*[a,b], *Anna Pakhomova*[c], *Michael Hanfland*[c], *Leonid Dubrovinsky*[b], *Natalia Dubrovinskaia*[a,d]*

[a]*Material Physics and Technology at Extreme Conditions, Laboratory of Crystallography, University of Bayreuth, 95440 Bayreuth, Germany*

[b]*Bayerisches Geoinstitut, University of Bayreuth, 95440 Bayreuth, Germany*

[c]*European Synchrotron Radiation Facility, CS 40220, 38043 Grenoble Cedex 9, France*

[d]*Department of Physics, Chemistry and Biology (IFM), Linköping University, SE-581 83, Linköping, Sweden*

[e]*Institut für Mineralogie, University of Münster, Corrensstr. 24, 48149 Münster, Germany.*

**Correspondence E-mails: Wenju.Zhou@uni-bayreuth.de, Natalia.Dubrovinskaia@uni-bayreuth.de*

To be submitted to *ChemEngineering* journal

4.1 Abstract

In this study, we explored the high-pressure behavior of naphthalene and anthracene up to 50 GPa and 43 GPa, respectively, using synchrotron single-crystal X-ray diffraction. Our findings reveal no phase transitions and demonstrate the remarkable stability of these compounds under extreme conditions. The successful application of Hirshfeld Atom Refinements (HARs) highlights the method's viability for accurately refining hydrogen atom positions in organic materials even with low data completeness. This work enhances our understanding of polycyclic aromatic hydrocarbons (PAHs), their behavior under non-ambient conditions, and the evolution of chemical bonding in this important class of materials.

4.2 Introduction

Naphthalene ($C_{10}H_8$) and anthracene ($C_{14}H_{10}$), the first and second members in a series of polycyclic aromatic hydrocarbons (PAHs), are among the representative compounds of this large class of organic materials and have long served as model solids. The crystal structure, molecular packing, and relative orientation of molecules within a molecular crystal can be significantly influenced by changes in temperature, pressure, and electric or magnetic fields. Due to the relatively weak intermolecular interactions in PAHs, the properties of these solids are highly responsive to applied pressure [1] (Tasch *et al.*, 1997).

Naphthalene was first investigated in the mid-20th century, with the first published crystal structure reported by Abrahams *et al.* [2] (1949) using powder X-ray diffraction. This study revealed that naphthalene crystallizes in the monoclinic space group $P2_1/a$, containing two molecules per primitive unit cell. Later, Natkaniec *et al.* [3] (1983) employed single-crystal neutron diffraction at 12 K to investigate perdeuteronaphthalene ($C_{10}D_8$), achieving a precise determination of the atomic coordinates of carbon and deuterium atoms. Oddershede and Larsen [4] (2004) further explored naphthalene using single-crystal X-ray diffraction (SC-XRD) at various temperatures, not only providing accurate atomic coordinates but also analysing the thermal vibrational behaviour of the atoms within the crystal lattice.

High-pressure experimental and theoretical studies of naphthalene and anthracene have been conducted by different methods. The first high-pressure experiments on naphthalene were carried out by Bridgman in 1938 [5] to study the volume change of naphthalene under compression. He observed a small but noticeable volume discontinuity around 3 GPa, indicating a possible phase transition. Beyond 3 GPa, however, no further phase transitions were detected up to 5 GPa. Jones and Nicol [6] (1968) conducted fluorescence spectroscopy on naphthalene from ambient to 5 GPa and identified a new broad emission band at 3 GPa, indicative of an irreversible molecular structural change. Nonetheless, some studies, such as those by Vaidya and Kennedy [7] (1971) and Nicol [8] (1975), using compressibility and Raman spectroscopy respectively, reported no evidence of phase transitions in similar pressure ranges. The existence of a phase transition in naphthalene under pressure remains debated. In 2013, Meletov [9] conducted experiments using powder X-ray diffraction up to 20 GPa and did not observe any new diffraction peaks or significant changes in the existing peaks, further questioning the occurrence of a phase transition. Conversely, Likhacheva *et al.* [10] (2014) reported using powder X-ray diffraction that around ~2 GPa, there was a notable stiffening of the inter-layer C–C distances and a shift in compression anisotropy, indicating potential structural changes. However, beyond 2 GPa, no additional phase transitions were observed up to 6 GPa. Moreover, O'Bannon and Williams [11] (2016) performed infrared spectroscopy on naphthalene up to 54.5 GPa. Their data suggested a phase transition at 2–3 GPa, with a possible second transition around 30 GPa. Notably, the disappearance of spectral features associated with molecular naphthalene in the infrared spectra, coupled with the irreversibility of this transition, suggests that the material may become amorphous between approximately 30 and 45 GPa.

The pure anthracene molecule consists of three benzene rings arranged in a herringbone manner similar to naphthalene. This structure was first refined using powder X-ray diffraction by Cruickshank in 1956 [12]. Later, in 1972, Lehmann & Pawley [13] employed single-crystal neutron diffraction at 12 K to study perdeuteroanthracene ($C_{14}D_{10}$). Their study achieved a precise determination of the atomic coordinates of both carbon and deuterium atoms.

Phase transitions under high pressure in anthracene have been examined sporadically over the past several decades. Offen [14] (1966) used fluorescence spectroscopy to study anthracene under pressures ranging from 0 to 2.5 GPa. His experiments revealed significant spectral changes, with diffuse bands at longer wavelengths appearing at pressures above 1 GPa. This irreversible change was thought to be associated with alterations in the crystal structure and molecular rearrangements of anthracene under high pressure. In a subsequent study, Adams and Tan [15] (1981) utilized infrared spectroscopy to investigate anthracene under pressures up to 4.5 GPa. They identified several bands with clear breaks in slope at 2.4 GPa, indicating the existence of a phase change. Similarly, Leger and Aloualiti [16] (1991) conducted powder X-ray diffraction experiments across pressures from 0 to 5.6 GPa. They observed non-linear changes in lattice parameters at 2.4 GPa, suggesting the occurrence of a phase transition, possibly a second-order transition. Further supporting evidence of a phase transition was provided by Zhao *et al.* [17] (1999), who conducted Raman spectroscopy measurements up to 3.1 GPa and noted a significant increase in the full width at half maximum (FWHM) of the peaks at 2.4 GPa. Although the Raman frequencies did not show a clear discontinuous shift, the change in peak width supported the occurrence of a phase transition. In contrast, Oehzelt *et al.* [18] (2003) conducted powder X-ray diffraction experiments up to 27.8 GPa and observed no significant discontinuities in lattice parameters or notable changes in diffraction peaks, suggesting that no phase transition occurred under these conditions. More recently, O'Bannon and Williams [11] (2016) reported infrared data up to 19.9 GPa, documenting a transition at approximately 2 to 3 GPa and suggesting a possible second transition near 7 GPa.

Despite various investigations into the high-pressure behavior of naphthalene and anthracene, inconsistencies remain in the reported phase transitions. Previous studies using single-crystal X-ray diffraction had only reached pressures up to 2.1 GPa [19] (Fabbiani *et al.*, 2006), leaving uncertainties regarding the structural behavior of these compounds at higher pressures. To address these gaps and explore the structural behavior under more extreme conditions, we conducted a study using synchrotron single-crystal X-ray diffraction (SC-XRD) in diamond anvil cells (DACs). Our experiments investigated naphthalene in the pressure range from ambient to 50 GPa and anthracene from ambient to 43 GPa. Throughout these experiments, we carefully monitored the structural evolutions to obtain accurate crystal structures under high pressure. Notably, no phase transitions were observed in either compound within these pressure ranges.

4.3 Experimental

4.3.1 Sample preparation

Crystalline powders of anthracene and naphthalene of >98% purity were purchased from Merck. Single crystals of anthracene and naphthalene were selected under an optical microscope and preselected for high-pressure XRD studies in DAC#1(with naphthalene) and DAC#3 (with anthracene) at ambient pressure (see Table S4.1 for the summary of all experiments). Two high-quality crystals of anthracene and two of naphthalene, each paired with a piece of ruby, were then loaded into membrane-type DAC#2 (with naphthalene) and DAC#4 (with anthracene), each equipped with Boehler-Almax type diamonds [20] (Boehler, 2006), with culet sizes of 250 μm, and a rhenium gasket with a hole of ~120 μm in diameter and a thickness of ~30 μm. Helium (He) was used as the pressure-transmitting medium (PTM). The DAC#2 was gradually pressurized from 6.2 GPa to 53 GPa, and DAC#4 from 1.5 GPa to 45 GPa.

4.3.2 Single-crystal XRD experiments

SC-XRD studies at room temperature were conducted in DAC #1 and DAC #2 on the ID27 beamline (λ= 0.3738 Å, ESRF) with a beam size of approximately 2 × 2 μm^2, and in DAC

#3 and DAC #4 on the ID15B beamline (λ= 0.4100 Å, ESRF) with a beam size of approximately 1.5 × 1.5 μm². In both experiments, a micro-grain of tungsten was placed in the center of the pressure chamber along with the sample. The strong X-ray absorption signal of tungsten was used to adjust the rotation center. The pressure was determined by the ruby luminescence method [21] (Mao *et al.*, 1986). At each pressure step, the data were collected in step-scans of 0.5° upon rotating the DAC from -34° to +34° about the vertical axis (ω-scan). For single-crystal data analysis (peak search, unit cell finding, and data integration), the CrysAlisPro Software [22] (Rigaku & CrysAlis, 2015) was employed, whereas the crystal structures were determined using SHELX [23] (Sheldrick, 2008) and refined utilizing the OLEX2 software [24] (Dolomanov, 2009). Hydrogen atoms were added using two different methods, the riding constraint (HFIX instructions) and Hirshfeld Atom Refinement (HAR) [25] (Kleemiss *et al.*, 2021), to automatically constrain their positions in OLEX2. A detailed analysis of these two modelling methods is presented separately in the discussion section. Crystal structure visualization was made with the VESTA software [26] (Momma & Izumi, 2011). EoSFIT7 software [27] (Angel *et al.*, 2014) was used to fit the pressure-volume data.

4.3.3 Theoretical calculations

Our density functional theory (DFT) calculations were performed using the Vienna ab initio simulation package (VASP) [28] (Kresse & Furthmüller, 1996) with the Projector-Augmented-Wave (PAW) method [29] (Blöchl, 1994). The Generalized Gradient Approximation (GGA) functional was used for calculating the exchange-correlation energy, as proposed by Perdew–Burke–Ernzerhof (PBE) [30] (Kresse & Joubert, 1999). Additionally, we employed the DFT-D3 method for dispersion correction [31] (Grimme *et al.*, 2011). The Brillouin zone was sampled with a 5×6×5 Monkhorst-Pack [32] (Monkhorst & Pack, 1976) special k-point grid for naphthalene, and 4×6×5 for anthracene. Furthermore, the valence states $2s^2 2p^2$ for C and $1s^1$ for H were used with the energy cutoff of 520 eV for the plane wave basis set. The geometries were optimized until the remaining atomic forces were less than 5×10^{-3} eV/Å and the energy convergence criterion was set at 10^{-5} eV.

4.4 Results and discussion

4.4.1 Naphthalene

4.4.1.1 Structure of naphthalene

The structure of naphthalene determined at ambient conditions (Fig. 4.1a) is similar to previously reported monoclinic structures. For a detailed comparison with the naphthalene single crystal refined by X-ray diffraction at 205 K [4] (Oddershede and Larsen, 2004) and with perdeuteronaphthalene ($C_{10}D_8$) single crystal refined by neutron diffraction at 12 K [3] (Natkaniec et. al, 1983), see Table S4.2. The structure of naphthalene (Fig. 4.1a) is monoclinic (space group #14, $P2_1/c$) with the following unit cell parameters: a = 8.147(6) Å, b = 6.0035(8) Å, c = 8.293(3) Å, β = 116.08(7) °, and V = 364.3(4) Å^3. The unit cell contains two naphthalene molecules, with the molecular arrangement characterized by a herringbone packing motif. This arrangement leads to C-H$\cdots\pi$ interactions between adjacent molecules, contributing to the stability of the crystal structure.

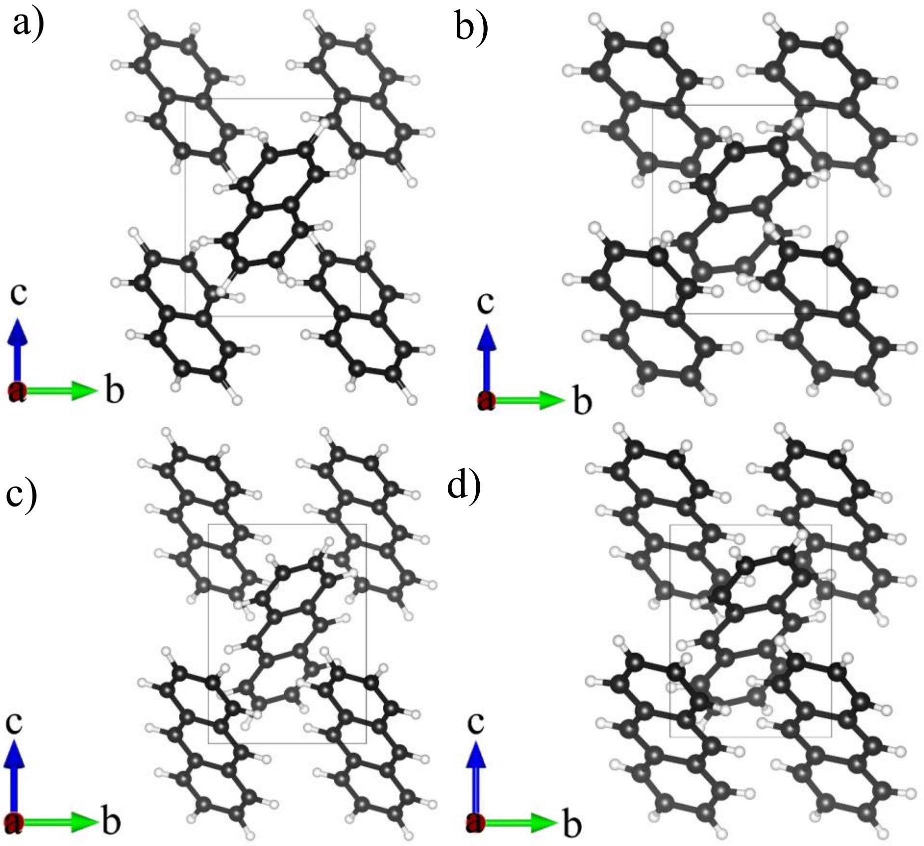

Figure 4.1 Crystal structures of naphthalene and anthracene viewed along the [1 0 0] direction. (a) Naphthalene at ambient conditions; (b) naphthalene at 50.7 GPa; (c) anthracene at ambient conditions; (d) anthracene at 42.3 GPa. C atoms are black. H atoms are white.

4.4.1.2 Compressional behaviour of naphthalene

Upon compression from 6.2 GPa to 50.7 GPa in a He pressure medium, we did not observe any phase transition. At the next pressure step of 53 GPa, the X-ray diffraction pattern disappeared. Full crystallographic and experimental data for naphthalene are provided in Table S4.3.

The dependences of the lattice parameters of naphthalene on pressure are shown in Fig. 4.2a (see Table S4.6 for numerical values). Upon compression of naphthalene the a, b, and c parameters, as well as the beta angle, gradually decrease. For naphthalene, the reduction in b/b_0 is the minimum, decreasing to 0.72 at 50.7 GPa, while the changes in a/a_0 and c/c_0 are nearly identical, both reducing to 0.83 at 50.7 GPa. Additionally, the β angle of naphthalene decreases from 116.08(7) ° at ambient pressure to 103.3(3) ° at 50.7 GPa.

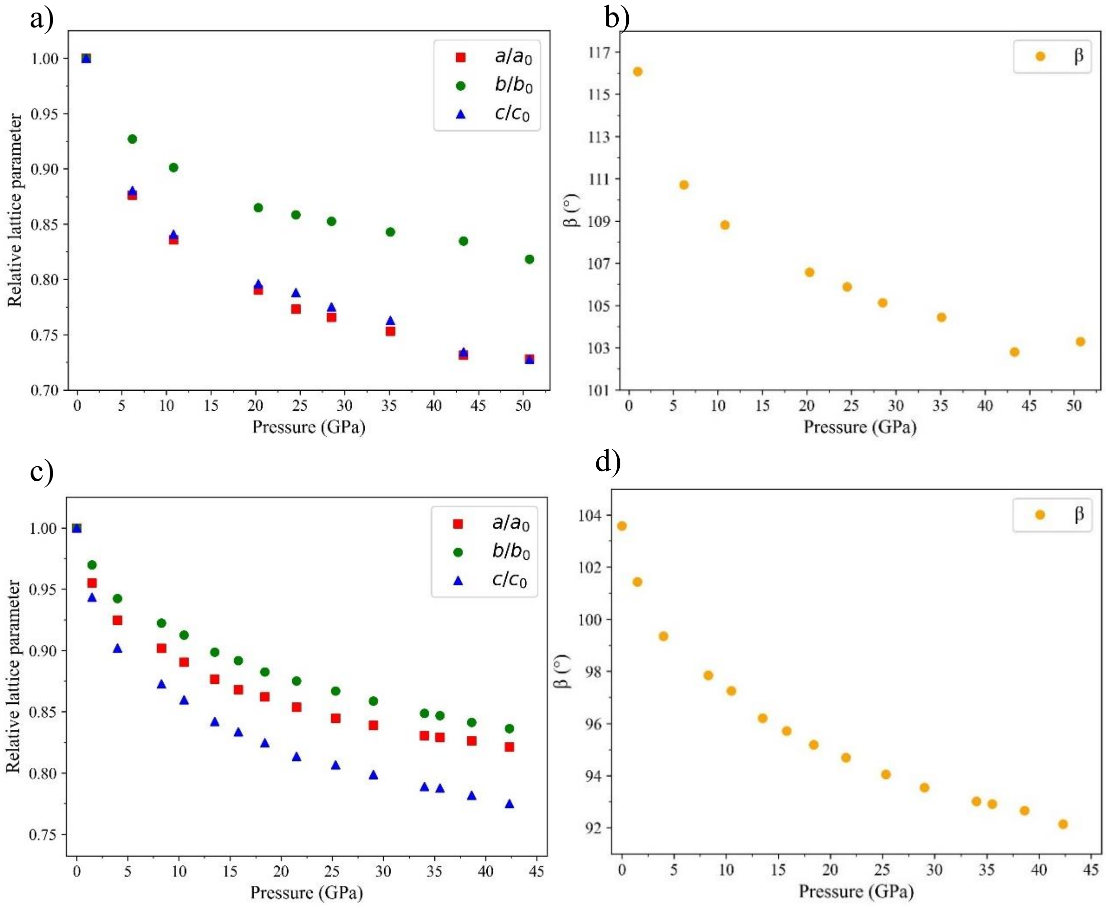

Figure 4.2 Pressure dependence of the lattice parameters of naphthalene and anthracene. (a) a/a_0, b/b_0, and c/c_0 of naphthalene up to 50.7 GPa; (b) β of naphthalene up to 50.7 GPa. (c) a/a_0, b/b_0, and c/c_0 of anthracene up to 42.3 GPa; (d) β of anthracene up to 42.3 GPa. a_0, b_0, and c_0 represent the lattice parameters a, b, and c at ambient pressure, respectively.

The values of the unit cell volume per formula unit for naphthalene as a function of pressure, obtained from our experiments (Table S4.7), are shown in Fig. 3a, illustrating the pressure dependence up to 50.7 GPa. These pressure-volume data were fitted using the third-order Birch-Murnaghan equation of state with the fixed unit cell volume per formula unit V_0 = 182.2 Å^3, which is the unit cell volume of naphthalene at ambient conditions. The bulk modulus, K_0, and its first derivative, K´, were determined to be 9.5(6) GPa and 5.1(2).

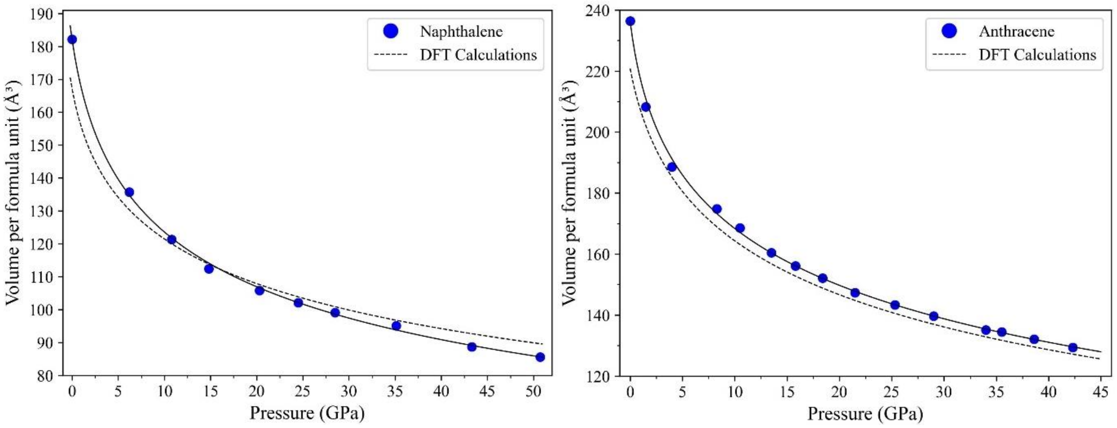

Figure 4.3 Pressure dependence of the unit cell volume per formula unit for naphthalene up to 50.7 GPa and anthracene up to 42.3 GPa. (a) Naphthalene; (b) Anthracene. The solid black lines show the fit of all pressure-volume experimental points using the third-order Birch-Murnaghan equation of state with V_0 fixed at 182.2 Å3, and fitting parameters K_0 = 9.5(6) GPa, and K´ = 5.1(2) for naphthalene; V_0 fixed at 236.5 Å3, and fitting parameters K_0 = 8.4(5) GPa, and K´ = 8.0(4) for anthracene. Dashed lines show the fit of DFT calculations data with V_0 fixed at 167.2 Å3, and fitting parameters K_0 = 10.8(2) GPa, and K´ = 6.99(13) for naphthalene; V_0 fixed at 222.3 Å3, and fitting parameters K_0 = 11.57(13) GPa, and K´ = 7.34(8) for anthracene.

The pressure-volume data points calculated using DFT for naphthalene are presented in Table S4.8. The crystal structure at ambient pressure was obtained by setting the pressure and performing ionic relaxation without any restrictions. For high-pressure data, the pressure values were derived from the external pressure calculated based on the fixed lattice volumes obtained from experiments. The calculated data have also been fitted using the third-order Birch-Murnaghan equation of state. The EOS parameters appeared to be as follows: V_0 = 167.2 Å^3, K_0 = 10.8(2) GPa, and K´ = 6.99(13).

4.4.1.3 Geometrical analysis of the structure of naphthalene under compression

Fig. 4.4a illustrates the structures of naphthalene viewed along the [5 0 4] direction, chosen to optimally display the topology of the molecular structures. To accurately calculate the interplanar angles (δ) in naphthalene, the molecules were approximated by mean molecular planes considering 10 carbon atoms in a molecule, using the NumPy and SciPy libraries in Python (red lines in Fig. 4.4a). They are listed in Table S4.9 and presented graphically in Fig. 4.4b as a function of pressure. The intermolecular angle of naphthalene shows an overall decrease with increasing pressure from 53.78° at ambient pressure to 40.6° at 50.7 GPa.

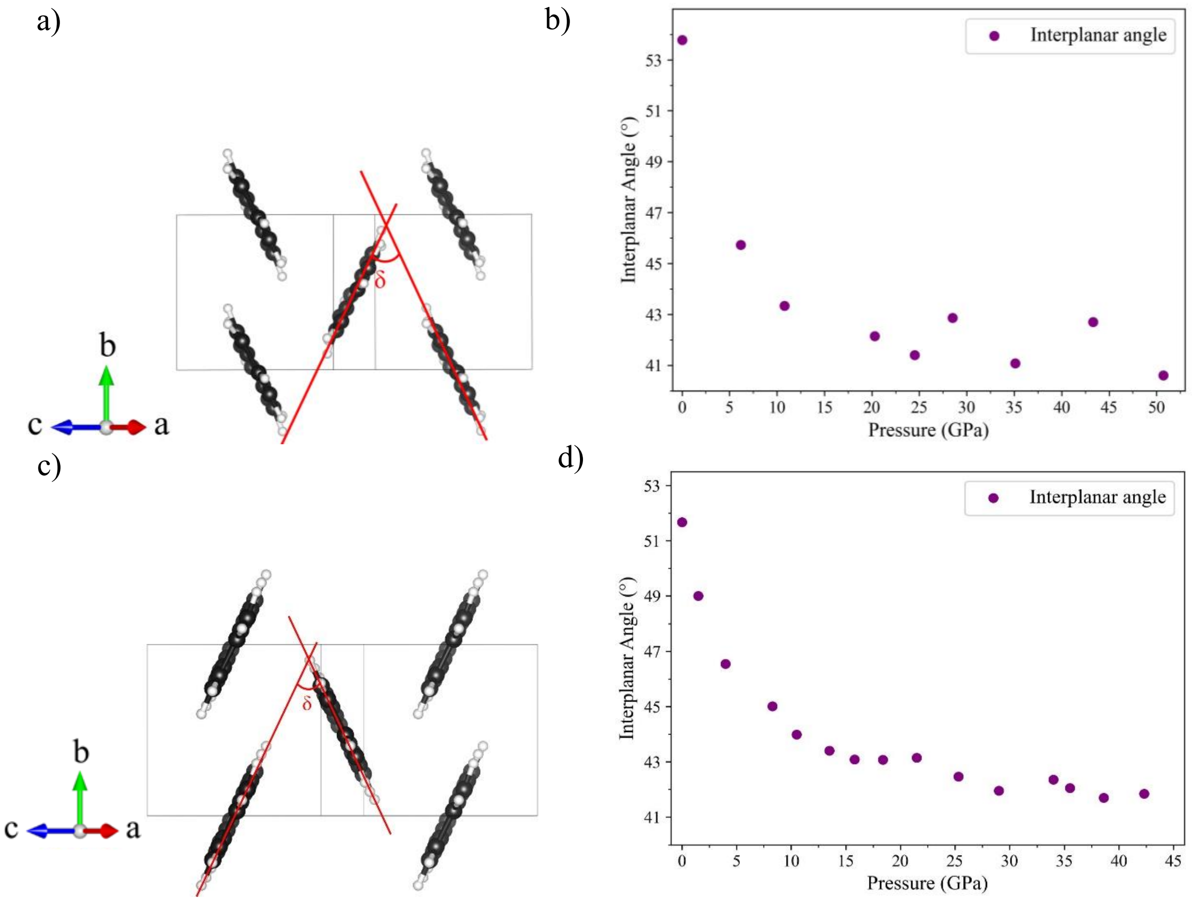

Figure 4.4 Interplanar angles for molecules in the naphthalene and anthracene structures. (a) Naphthalene structure as viewed along the [5 0 4] direction at ambient conditions. (b) Variation of interplanar angles of naphthalene up to 50.7 GPa. (c) Anthracene structure as viewed along the [5 0 4] direction at ambient conditions; (d) Variation of the interplanar angle in anthracene up to 42.3 GPa. C atoms are black, and H atoms are white; δ is the interplanar angle.

4.4.2 Anthracene

4.4.2.1 Structure of anthracene

The structure of anthracene (Fig. 4.1c) is monoclinic (space group #14, $P2_1/c$) with the following unit cell parameters at ambient conditions: a = 9.488(5) Å, b = 6.0253(3) Å, c = 8.5642(14) Å, β = 103.52(3) °, and V = 476.0(3) Å^3. These parameters are similar to those previously reported for perdeuteroanthracene, as determined by single crystal neutron diffraction. For a detailed comparison with perdeuteroanthracene ($C_{14}D_{10}$) at 293 K (Lehmann & Pawley, 1972), see Table S4.4. Like naphthalene, anthracene molecules also exhibit a herringbone packing motif if viewed along the [1 0 0] direction.

4.4.2.2 Compressional behaviour of anthracene

Upon compression from 1.5 GPa to 42.3 GPa in a He pressure medium, we did not observe any phase transition in anthracene. At the next pressure step of 45 GPa, the X-ray diffraction pattern disappeared. Full crystallographic and experimental data are provided in Table S4.5.

The dependences of the lattice parameters of anthracene on pressure are shown in Fig. 4.2c, d (see Table S4.6 for numerical values). Similar to the trend observed in naphthalene, all lattice parameters of anthracene decrease with increasing pressure.

The values of the unit cell volume per formula unit for anthracene as a function of pressure, obtained from our experiments (Table S4.7), are shown in Fig. 4.3b, illustrating the pressure dependence up to 42.3 GPa. These pressure-volume data were fitted with the fixed volume per formula unit V_0 = 236.5 Å^3, which is the volume of anthracene at ambient conditions. The bulk modulus, K_0, and its first derivative, K´, were determined to be 8.4(5) GPa and 8.0(4).

The pressure-volume data points calculated using DFT for anthracene are presented in Table S4.8. The EOS parameters appeared to be as follows: V_0 = 222.3 Å^3, K_0 = 11.57(13) GPa, and K´ = 7.34(8). They agree well with the EOS parameters obtained from the experimental data. However, the volume values from the calculated data fitting are consistently lower than those from the experimental data fitting. This observation can be attributed to the fact that DFT calculations simulate the structures at 0K.

4.4.2.3 Geometrical analysis of the structure of anthracene under compression

Fig. 4.4c illustrates the structures of anthracene viewed along the [5 0 4] direction as. The interplanar angles (δ) in anthracene were calculated using the same analysis method applied to naphthalene, approximating the molecules by mean molecular planes considering 14 carbon atoms. They are listed in Table S4.9 and presented graphically in Fig. 4.4d as a function of pressure. The intermolecular angle of anthracene shows an overall decrease with increasing pressure from 51.67° at ambient pressure to 41.93° at 42.3 GPa.

The comparison between the high-pressure behaviors of naphthalene and anthracene further highlights their structural similarities and differences under compression. Figs. 4.1b and 1d show the crystal structures of naphthalene at 50.7 GPa and anthracene at 42.3 GPa, respectively. From the figures, it can be observed that the intermolecular angles decrease under high pressure, and the molecular packing becomes significantly denser. At 50.7 GPa, the unit cell volume of naphthalene decreases from 364.3(4) Å^3 at ambient pressure to 171.2(8) Å^3. Likewise, at 42.3 GPa, the unit cell volume of anthracene decreases from 476.0(3) Å^3 at ambient pressure to 258.8(6) Å^3.

4.4.3 Hirshfeld atom refinement (HAR) for naphthalene and anthracene

Traditionally, crystal structure refinements have relied on the independent atom model (IAM). In the IAM, the lack of asphericity significantly affects the description of the electron density around hydrogen atoms, which have only one valence electron. This electron density is often strongly shifted towards the atoms to which the hydrogens are bonded. The most significant consequence of this approach is the underestimation of the bond lengths formed by hydrogen atoms. For example, in this work, all C-H bond lengths were constrained to 0.93 Å using the AFIX 43 instruction [33] (Sheldrick & Schneider, 1997) in OLEX2.

Recent studies have demonstrated that Hirshfeld atom refinement (HAR) can yield C-H bond lengths that are within one standard uncertainty of those obtained from neutron diffraction measurements, offering comparable precision [34] (Woińska et. al, 2016). Furthermore, using high-resolution, good-quality X-ray data can further improve the accuracy and precision of the bond length measurements, enhancing the overall quality of the refinement. With high-quality data, it is also possible to apply an anisotropic treatment of hydrogen atom thermal motions, although this approach may result in slightly lower accuracy compared to anisotropic displacement parameters (ADPs) derived from neutron diffraction or other structural methods. [34] [35] (Woińska et. al, 2016; Malaspina et. al, 2020). In 2021, Guńka *et al.* [36] attempted HAR for the α-$C_6H_{12}N_4$ (urotropine) polymorph using diffraction data collected under high pressure. This was the first attempt to apply HAR to molecular crystals at high pressure. Notably, the HAR of the C-H bond length, which was found to be 1.13(3) Å at 0.34(5) GPa, is consistent within one standard uncertainty with the value of 1.10(2) Å obtained from neutron diffraction experiments on urotropine single crystals conducted at around 0.25 GPa. [37] (Binns et.al, 2016) This example demonstrated that despite the lower completeness of diffraction data obtained for crystals in a DAC compared to ambient pressure conditions, HAR can still be performed on lower symmetry crystals under high pressure, provided the data quality is sufficiently high. However, due to the lower completeness, only isotropic refinement for hydrogen atoms can be successful. Subsequent studies on other molecular crystals under high pressure have also confirmed this conclusion, demonstrating the reliability of HAR in high-pressure crystallography, even for lower symmetry structures. [38] [39] (Olejniczak *et al.*, 2022; Zwolenik *et al.*, 2024)

We attempted HAR for naphthalene and anthracene using diffraction data collected with He as PTM. The completeness of the data for the maximum attained 2θ value ranged from 20% to 35%. The low completeness was due to the low symmetry of naphthalene and anthracene, as well as the limitations of the open angle (70°) of the DACs. Additionally, we aimed to check if the refined C-H bond lengths would agree with our DFT-calculated data.

Fig. 4.5a shows the average C-H bond lengths plotted as a function of pressure for naphthalene, with the experimental data plotted up to about 43 GPa (see Table S4.10 for numerical values) and calculations up to about 53 GPa (see Table S4.11 for numerical values), represented in different colors (red for experimental data and blue for calculations). At ambient pressure, the HAR value of the average C-H bond length is 1.08(5) Å, which compares closely with the average C-D bond length 1.093(3) Å determined from neutron diffraction experiments on perdeuteronaphthalene single crystals at 12 K. (Natkaniec et. al, 1983) While the average C-H bond lengths are similar, the uncertainties for the HAR values are significantly larger, with an average error of 0.067 Å across all pressure points in our experimental data. Therefore, there is a systematically reasonable agreement between the HAR and DFT data.

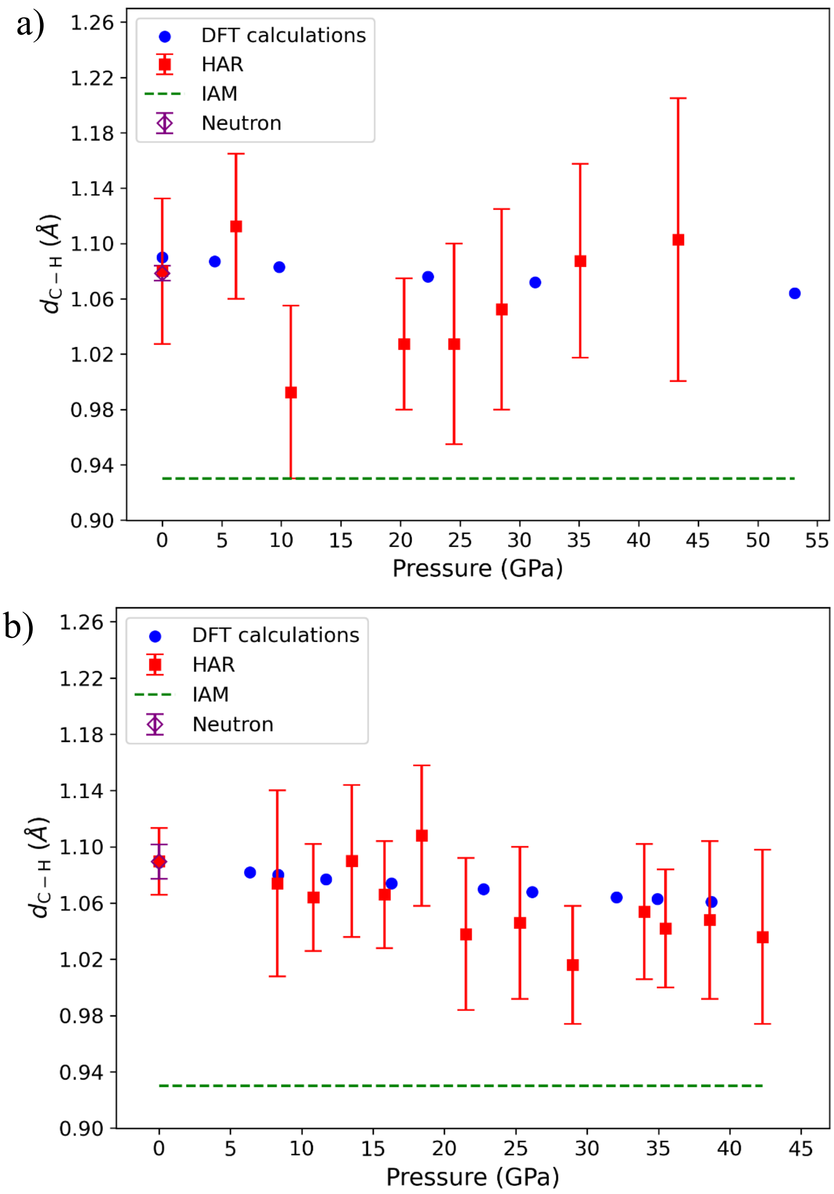

Figure 4.5 The average C-H bond lengths plotted as a function of pressure for naphthalene and anthracene molecules. (a) Naphthalene up to 43.3 GPa; (b) anthracene up to 42.3 GPa. Solid symbols of different colours represent the following: blue circles - DFT calculated values; red squares - the values obtained using Hirshfeld atom refinement (HAR); green dash - the values derived from the independent atom model (IAM), and a purple open diamond - the value acquired from neutron diffraction.

Fig. 4.5b shows the average C-H bond lengths plotted as a function of pressure for anthracene, with the experimental data plotted up to about 42 GPa (see Table S4.10 for numerical values) and calculations up to about 39 GPa (see Table S4.11 for numerical values), represented in different colours (red for experimental data and blue for calculations). Note that the HAR value of the average C-H bond length of 1.09(2) Å at ambient pressure is within one standard uncertainty from average C-D bond length of 1.104(2) Å, which was determined from neutron diffraction experiments on perdeuteroanthracene single crystals. (Lehmann & Pawley, 1972) The average error for the HAR value of the C-H bond length across all pressure points in the experimental data is 0.047 Å. This smaller uncertainty, in comparison to the larger uncertainties observed in naphthalene, can be attributed to the higher quality single crystals of anthracene used for measurement. Overall, the HAR data on the C-H bond lengths are in good agreement with the DFT results for both naphthalene and anthracene indicating that, compared to the IAM, the HAR provides values that are generally closer to theoretical predictions and more accurately reflects C-H bond lengths.

4.4.4 Intramolecular C-C bond lengths in naphthalene and anthracene crystals under compression

To better observe the changes in C-C bonds in naphthalene and anthracene crystals under compression, we categorize the C-C bonds within these molecules into three types based on their environments. Type-I denotes C-C bonds where the carbon atoms at both ends do not form C-H bonds with surrounding hydrogen atoms. Type-II refers to C-C bonds where one of the carbon atoms at the ends forms a C-H bond with a surrounding hydrogen atom. Type-III indicates C-C bonds where the carbon atoms at both ends form C-H bonds with surrounding hydrogen atoms. For example, a naphthalene molecule possesses one C-C bond of type-I, four of type-II, and six of type-III (Fig. 4.6a). The dependence of the C-C bond lengths in naphthalene and anthracene as a function of pressure is shown in Figs. 4.6b, c, and d (see Table S4.12 for numerical values). Unfortunately, the values obtained from experiment are scattered and the uncertainties are comparable with the variation of the values in the whole studied pressure interval. Therefore, we used theoretical data to see the trend. As seen in Figs. 6b-d all bonds are highly incompressible but tend to decrease with pressure.

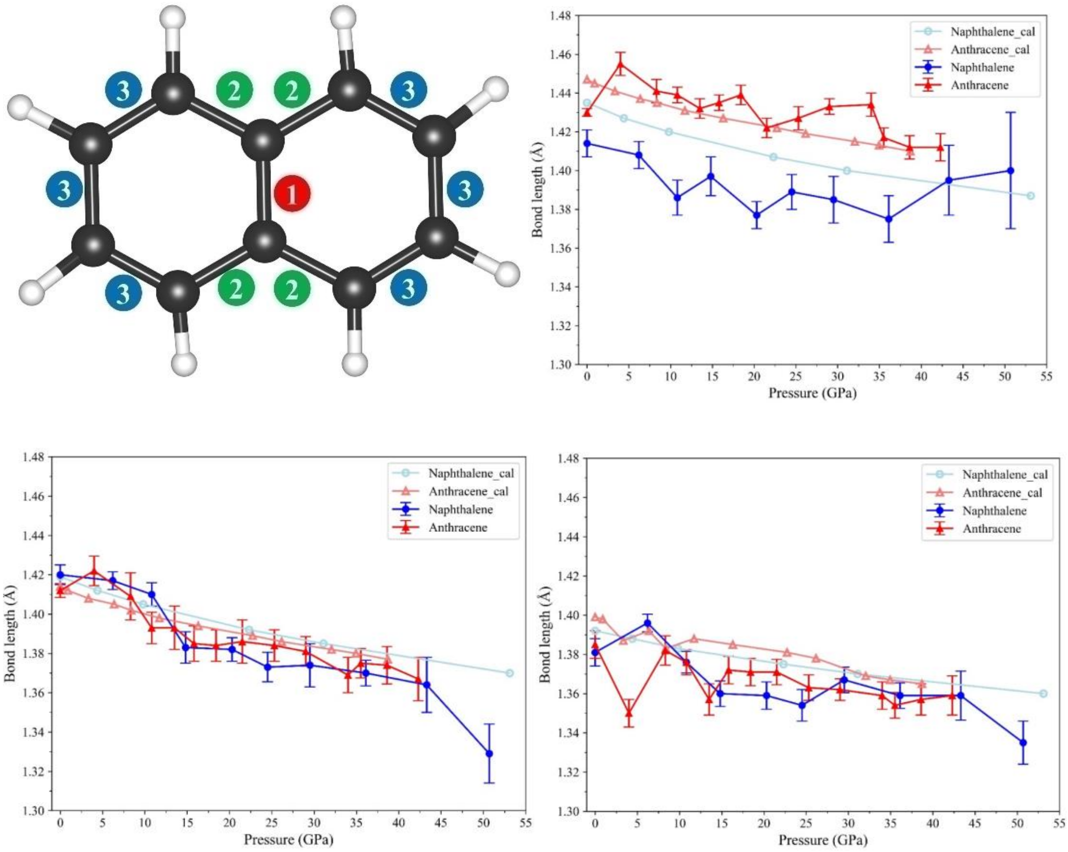

Figure 4.6 The dependence of different types of average C-C bond lengths in naphthalene and anthracene on pressure. (a) Different types of C-C bonds in naphthalene molecule. C atoms are black, and H atoms are white.; (b) type-I; (c) type-II; (d) type-III; Type-I denotes a type of C-C bond where the carbon atoms at both ends do not form C-H bonds with surrounding hydrogen atoms. Type-II denotes a type of C-C bond where one of the carbon atoms at the ends forms a C-H bond with a surrounding hydrogen atom. Type-III denotes a type of C-C bond where the carbon atoms at both ends form C-H bonds with surrounding hydrogen atoms. The blue circles represent the data points for naphthalene from ambient pressure to 50.7 GPa. The red triangles represent anthracene from ambient pressure to 42.3 GPa. The light blue circles represent the theoretical data points for naphthalene from ambient pressure to 53 GPa. The light red triangles represent the theoretical data points for anthracene from ambient pressure to 38 GPa.

4.5 Conclusion

In this study, we refined the crystal structures of naphthalene and anthracene under high pressures up to about 50 GPa and 43 GPa, respectively, using SC-XRD. Our experiments demonstrated that both compounds exhibit remarkable structural stability, with no observed phase transitions within these pressure ranges.

The implementation of HARs for both naphthalene and anthracene has shown that HARs can be effectively applied in high-pressure data analysis despite the data's lower completeness, provided that the diffraction data are of sufficient quality and resolution.

Our experimental research contributes to the fundamental understanding of the behavior of polycyclic aromatic hydrocarbons under high pressure and the mechanism of compression of the simple's members of a PAH series of compounds of the important class of organic materials.

4.6 Acknowledgements

The authors acknowledge the European Synchrotron Radiation Facility (ESRF) for the provision of beamtime at the ID15b and ID27 beamlines. Computations were performed at the Leibniz Supercomputing Center of the Bavarian Academy of Sciences and the Humanities, and the research center for scientific computing at the University of Bayreuth.

4.7 Supplementary materials

Table S4.1 Summary of the experiments conducted in this work.

DAC number	DAC type	Anvils type/ culet size, μm	Starting material/ pressure transmitting medium	Beamline/XRD wavelength, Å	Result	Pressure, GPa
1	Membrane-type	Boehler-Almax 250	Naphthalene/ No medium	ID27 ESRF, 0.3738	Naphthalene	ambient
2	Membrane-type	Boehler-Almax 250	Naphthalene/ Helium	ID27 ESRF, 0.3738	Naphthalene	6.2, 10.8, 20.3, 24.5, 28.5, 35.1, 43.3, 50.7
3	Membrane-type	Boehler-Almax 250	Anthracene/ No medium	ID15B ESRF, 0.4100	Anthracene	ambient
4	Membrane-type	Boehler-Almax 250	Anthracene/ Helium	ID15B ESRF, 0.4100	Anthracene	1.5, 4.0, 8.3, 10.8, 13.5, 15.8, 18.4, 21.5, 25.3, 29.0, 34.0, 35.5, 38.6, 42.3

Table S4.2 Experimental crystallographic data for Naphthalene at ambient conditions obtained by single-crystal X-ray diffraction in this work and in ref. and Perdeuteronaphthalene by neutron diffractionin refs.

	Naphthalene at ambient condition	Perdeuteronaphthalene at 12K
CCDC deposition number	2364321	1216820
Crystal data		
Chemical formula	$C_{10}H_8$	$C_{10}D_8$
M_r	128.175	136.212
Crystal system, space group	Monoclinic, $P2_1/c$	Monoclinic, $P2_1/c$
a, b, c (Å)	8.147(6), 6.0035(8), 8.293(3)	7.795(11), 5.941(5), 8.096(7)
α, β, γ (°)	90, 116.08(7), 90	90,114.09(13),
V (Å^3)	364.3(4)	342.3(11)
Z	2	2
Density (Mg/m^3)	1.169	1.244
Wavelength (Å)	0.3738	1.26
μ (mm^{-1})	0.029	0.948
Data collection		
Absorption correction	Multi-scan	
$T_{\min}$, $T_{\max}$	0.37, 1.00	
No. of measured, independent and observed reflections	890, 521, 191	1036, 907, 1036
R_{int}	0.0931	0.01
$\theta_{\max}$ (°)	17.24	
Refinement		
Refinement on	F^2	
$R[F^2>2\sigma(F^2)]$, $wR(F^2)$, S	0.0788, 0.1708, 0.8835	0.031, 0.031
Data / restraints / parameters	521/ 0/ 58	
H-atom treatment	Refined by non-spherical atomic form factors	
Weighting scheme	$w = 1/[\sigma^2(F_o^2) + (0.0320P)^2]$, where $P = (F_o^2 + 2F_c^2)/3$	
$\Delta\rho_{\max}$, $\Delta\rho_{\min}$ (e Å^{-3})	0.1579, -0.1451	
Crystal Structure		
Fractional atomic coordinates (x, y, z)	C1: (0.5354(6), 0.6029(4), 0.4880(5)) C2: (0.4224(8), 0.7457(4), 0.3471(6)) C3: (0.2792(8), 0.3428(5), 0.3970(6)) C4: (0.2478(9), 0.6865(5), 0.2350(5)) C5: (0.1748(8), 0.4820(5), 0.2599(6)) H2: (0.477(11), 0.897(5), 0.345(7)) H3: (0.228(9), 0.188(6), 0.416(6)) H4: (0.185(10), 0.796(6), 0.114(7)) H5: (0.027(10), 0.444(4), 0.175(7))	C1: (-0.32992, 0.01978, -0.24795) C2: (-0.22385, 0.16414, -0.11164) C3: (-0.03712, 0.10646, 0.01103) C4: (0.07552, 0.25342, 0.15193) C5: (-0.25501, -0.19085, -0.26917) D1: (-0.47167, 0.06896, -0.34013) D2: (-0.27971, 0.32721, -0.09414) D3: (0.01722, 0.41521, 0.16763) D4: (-0.33985, -0.30454, -0.37786)

Table S4.2 (continuation)

Naphthalene at 205K
233931
$C_{10}H_8$
128.175
Monoclinic, $P2_1/c$
7.9435(1), 5.9534(1), 8.1645(1)
90, 114.998(1), 90
349.93(1)
2
0.7107 (Mo Kα)
0.070
Multi-scan
0.970, 0.979
63300, 4250,
0.0321
27.5
F^2
0.037, 0.036, 0.952
4250/ 0
$w = 1/ [\sigma^2 (F_o^2)]$
C1: (-0.32771(2); 0.01801(3); -0.24400(2)) C2: (-0.22158(2); 0.16157(2); -0.10779(1)) C3: (-0.03688(1); 0.10432(1); 0.01133(1)) C4: (0.07573(2); 0.24971(2); 0.15240(1)) C5: (-0.25405(2); -0.18980(3); -0.26666(1)) H1: (-0.46765; 0.06860; -0.33321) H2: (-0.27416; 0.32213; -0.08760) H3: (0.01617; 0.40788; 0.16702) H4: (-0.33537; -0.30490; -0.37360)

Table S4.3 Experimental crystallographic data for Naphthalene obtained by single-crystal X-ray diffraction at room temperature in this work.

	Naphthalene at 6.2 GPa	Naphthalene at 10.8 GPa
CCDC deposition number	2364322	2364323
Crystal data		
Chemical formula	$C_{10}H_8$	$C_{10}H_8$
M_r	128.175	128.175
Crystal system, space group	Monoclinic, $P2_1/c$	Monoclinic, $P2_1/c$
a, b, c (Å)	7.140(6), 5.5654(5), 7.302(2)	6.811(12), 5.4101(11), 6.974(4)
α, β, γ (°)	90, 110.72(7), 90	90, 108.82(12), 90
V (Å^3)	271.4(3)	243.3(5)
Z	2	2
Density (Mg/m^3)	1.569	1.75
Wavelength (Å)	0.3738	0.3738
μ (mm^{-1})	0.038	0.043
Data collection		
Absorption correction	Multi-scan	Multi-scan
T_{min}, T_{max}	0.2263, 1.00	0.0736, 1.00
No. of measured, independent and observed reflections	644, 333, 189	505, 312, 191
R_{int}	0.0354	0.0381
θ_{max} (°)	17.22	20.97
Refinement		
Refinement on	F^2	F^2
$R[F^2>2\sigma(F^2)]$, $wR(F^2)$, S	0.0503, 0.1122, 0.9465	0.0755, 0.1916, 1.0141
Data / restraints / parameters	333/ 0/ 58	312/ 0/ 58
H-atom treatment	Refined by non-spherical atomic form factors	Refined by non-spherical atomic form factors
Weighting scheme	$w = 1/ [\sigma^2 (F_o^2) + (0.0765P)^2]$, where $P = (F_o^2 + 2F_c^2)/3$	$w = 1/ [\sigma^2 (F_o^2) + (0.1460P)^2]$, where $P = (F_o^2 + 2F_c^2)/3$
$\Delta\rho_{max}$, $\Delta\rho_{min}$ (e Å^{-3})	0.1424, -0.1487	0.1871, -0.2191
Crystal Structure		
Fractional atomic coordinates (x, y, z)	C1: (0.2666(10), 0.6783(4), 0.3843(5)) C2: (0.1535(9), 0.5236(4), 0.2405(4)) C3: (0.7686(10), 0.7056(4), 0.7811(5)) C4: (0.4615(9), 0.6138(3), 0.5098(4)) C5: (0.5792(9), 0.7736(3), 0.6571(4)) H1: (0.200(13), 0.856(6), 0.409(6)) H2: (0.004(13), 0.591(4), 0.151(5)) H3: (0.877(14), 0.829(5), 0.891(7)) H5: (0.505(13), 0.937(4), 0.673(5))	C1: (0.5830(12), 0.2196(4), 0.6572(6)) C2: (0.2616(11), 0.3171(5), 0.3827(6)) C3: (0.7729(14), 0.2921(5), 0.7845(7)) C4: (0.4633(12), 0.3829(4), 0.5101(6)) C5: (0.1489(11), 0.4733(5), 0.2358(5)) H1: (0.548(16), 0.048(7), 0.656(7)) H2: (0.220(15), 0.147(8), 0.390(8)) H3: (0.87(2), 0.181(9), 0.874(10)) H5: (0.000(18), 0.410(8), 0.144(8))

Table S4.3 (continuation)

Naphthalene at 20.3 GPa	Naphthalene at 24.5 GPa	Naphthalene at 28.5 GPa
2364324	2364325	2364326
$C_{10}H_8$	$C_{10}H_8$	$C_{10}H_8$
128.175	128.175	128.175
Monoclinic, $P2_1/c$	Monoclinic, $P2_1/c$	Monoclinic, $P2_1/c$
6.440(11), 5.1922(7), 6.6024(18)	6.299(12), 5.1533(7), 6.5364(18)	6.239(11), 5.1189(6), 6.429(2)
90, 106.57(8), 90	90, 105.89(9), 90	90, 105.13(10), 90
211.6(4)	204.1(4)	198.2(4)
2	2	2
2.012	2.086	2.147
0.3738	0.3738	0.3738
0.049	0.051	0.052
Multi-scan	Multi-scan	Multi-scan
0.1893, 1.00	0.2273, 1.00	0.2153, 1.00
548, 332, 227	434, 290, 191	463, 278, 169
0.0286	0.0202	0.0445
20.87	21.01	20.76
F^2	F^2	F^2
0.0751, 0.1721, 0.9604	0.0843, 0.1964, 0.9401	0.079, 0.2067, 0.9786
332/ 0/ 58	290/ 0/ 58	278/ 0/ 58
Refined by non-spherical atomic form factors	Refined by non-spherical atomic form factors	Refined by non-spherical atomic form factors
$w = 1/ [\sigma^2 (F_o^2) + (0.1384P)^2]$, where $P = (F_o^2 + 2F_c^2)/3$	$w = 1/ [\sigma^2 (F_o^2) + (0.1714P)^2]$, where $P = (F_o^2 + 2F_c^2)/3$	$w = 1/ [\sigma^2 (F_o^2) + (0.1691P)^2]$, where $P = (F_o^2 + 2F_c^2)/3$
0.2717, -0.2787	0.2827, -0.2417	0.2739, -0.2851
C1: (0.2258(13), 0.2855(4), 0.2089(4)) C2: (0.7422(12), 0.3112(4), 0.6180(4)) C3: (0.4163(12), 0.2111(4), 0.3416(4)) C4: (0.5408(11), 0.3798(4), 0.4895(4)) C5: (0.8543(12), 0.4709(5), 0.7705(4)) H1: (0.153(18), 0.164(7), 0.076(7)) H2: (0.779(17), 0.126(7), 0.610(7)) H3: (0.471(15), 0.027(7), 0.326(6)) H5: (0.991(15), 0.412(7), 0.879(7))	C1: (0.2247(16), 0.2846(5), 0.2072(5)) C2: (0.1438(15), 0.5293(5), 0.2273(5)) C3: (0.4152(15), 0.2091(5), 0.3421(4)) C4: (0.2558(14), 0.6902(5), 0.3808(5)) C5: (0.5422(14), 0.3778(5), 0.4893(4)) H1: (0.13(2), 0.167(8), 0.083(9)) H2: (0.01(2), 0.587(10), 0.106(9)) H3: (0.50(2), 0.048(11), 0.319(8)) H4: (0.19(3), 0.875(9), 0.387(10))	C1: (0.2234(19), 0.2812(7), 0.2042(7)) C2: (0.1425(18), 0.5290(7), 0.2273(7)) C3: (0.4220(18), 0.2057(6), 0.3387(7)) C4: (0.253(2), 0.6921(6), 0.3827(8)) C5: (0.5413(18), 0.3768(6), 0.4886(7)) H1: (0.09(2), 0.166(8), 0.095(10)) H2: (0.01(2), 0.627(12), 0.128(12)) H3: (0.46(2), 0.024(9), 0.334(9)) H4: (0.20(3), 0.892(10), 0.391(11))

Table S4.3 (continuation)

Naphthalene at 35.1 GPa	Naphthalene at 43.3 GPa	Naphthalene at 50.7 GPa
2364327	2364328	2364329
$C_{10}H_8$	$C_{10}H_8$	$C_{10}H_8$
128.175	128.175	128.175
Monoclinic, $P2_1/c$	Monoclinic, $P2_1/c$	Monoclinic, $P2_1/c$
6.136(14), 5.0604(12), 6.327(3)	5.96(4), 5.011(3), 6.091(9)	5.93(2), 4.913(2), 6.035(11)
90, 104.45(14), 90	90, 102.8(4), 90	90, 103.3(3), 90
190.2(5)	177.4(12)	171.2(8)
2	2	2
2.238	2.4	2.486
0.3738	0.3738	0.3738
0.055	0.059	0.061
Multi-scan	Multi-scan	Multi-scan
0.281, 1.00	0.185, 1.00	0.3356, 1.00
464, 234, 149	300, 171, 101	169, 121, 67
0.0272	0.0516	0.0122
18.14	16.42	14.83
F^2	F^2	F^2
0.0797, 0.1906, 1.0257	0.0867, 0.2363, 1.2027	0.0864, 0.2046, 1.0947
234/ 0/ 58	171/ 13/ 58	121/ 6/ 46
Refined by non-spherical atomic form factors	Refined by ride model	Refined by ride model
$w = 1/ [\sigma^2 (F_o^2) + (0.1609P)^2]$, where $P = (F_o^2 + 2F_c^2)/3$	$w = 1/ [\sigma^2 (F_o^2) + (0.1795P)^2]$, where $P = (F_o^2 + 2F_c^2)/3$	$w = 1/ [\sigma^2 (F_o^2) + (0.1874P)^2]$, where $P = (F_o^2 + 2F_c^2)/3$
0.2255, -0.2256	0.2073, -0.2028	0.2206, -0.2325
C1: (0.4187(18), 0.7978(6), 0.3399(8)) C2: (0.8575(18), 0.5293(7), 0.7753(8)) C3: (0.5400(18), 0.6252(6), 0.4905(8)) C4: (0.2214(17), 0.7205(6), 0.2029(7)) C5: (0.7477(18), 0.6945(6), 0.6179(9)) H1: (0.46(2), 0.982(10), 0.334(10)) H2: (1.02(2), 0.617(12), 0.873(14)) H4: (0.07(2), 0.846(11), 0.099(14)) H5: (0.75(2), 0.902(12), 0.635(14))	C1: (0.417(3), 0.7990(9), 0.3425(14)) C2: (0.868(3), 0.5292(11), 0.7700(15)) C3: (0.548(3), 0.6251(9), 0.4900(12)) C4: (0.223(3), 0.7237(11), 0.1979(15)) C5: (0.759(3), 0.6959(12), 0.6137(14)) H1: (0.507(14), 0.968(14), 0.285(11)) H2: (1.00(3), 0.651(16), 0.875(14)) H4: (0.07(4), 0.823(15), 0.110(12)) H5: (0.84(4), 0.892(13), 0.591(14))	C1: (0.418(4), 0.1978(17), 0.3402(17)) C2: (0.133(3), 0.5296(19), 0.2241(18)) C3: (0.217(4), 0.2834(13), 0.2014(17)) C4: (0.253(3), 0.6967(17), 0.3792(15)) C5: (0.449(4), 0.6253(12), 0.5146(16)) H1: (0.464(4), 0.0173(17), 0.3357(17)) H2: (-0.008(3), 0.5840(19), 0.1321(18)) H3: (0.136(4), 0.1677(13), 0.0885(17)) H4: (0.195(3), 0.8705(17), 0.3926(15))

Table S4.4 Experimental crystallographic data for Anthracene at ambient conditions obtained by single-crystal X-ray diffraction in this work and Perdeuteroanthracene by neutron diffraction in ref.

	Anthracene at ambient condition	Perdeuteroanthracene at 293 K
CCDC deposition number	2364306	1103075
Crystal data		
Chemical formula	$C_{14}H_{10}$	$C_{14}D_{10}$
M_r	178.235	188.280
Crystal system, space group	Monoclinic, $P2_1/c$	Monoclinic, $P2_1/c$
a, b, c (Å)	9.488(5), 6.0253(3), 8.5642(14)	9.451(10), 6.016(6), 8.542(5)
α, β, γ (°)	90, 103.52(3), 90	90, 103.49(9), 90
V (Å^3)	476.0(3)	472.3(7)
Z	2	2
Density (Mg/m^3)	1.243	1.253
Wavelength (Å)	0.3738	1.025
μ (mm^{-1})	0.03	0.9
Data collection		
Absorption correction	Multi-scan	
T_{min}, T_{max}	0.46, 1.00	
No. of measured, independent and observed reflections	935, 506, 347	1145, 1093, 1053
R_{int}	0.0046	0.02
θ_{max} (°)	15.46	
Refinement		
Refinement on	F^2	
R[$F^2 > 2\sigma(F^2)$], wR(F^2), S	0.0319, 0.0819, 1.1486	0.034, 0.034
Data / restraints / parameters	506/ 2/ 79	
H-atom treatment	Refined by non-spherical atomic form factors	
Weighting scheme	$w = 1/ [\sigma^2 (F_o^2) + (0.0466P)^2]$, where $P = (F_o^2 + 2F_c^2)/3$	
$\Delta\rho_{max}$, $\Delta\rho_{min}$ (e Å^{-3})	0.0735, -0.0659	
Crystal Structure		
Fractional atomic coordinates (x, y, z)	C1: (0.5466(5), 0.2913(2), 0.4593(3)) C2: (0.6364(5), 0.4183(2), 0.5778(3)) C3: (0.4096(6), 0.3688(2), 0.3795(3)) C4: (0.7779(7), 0.3448(3), 0.6606(4)) C5: (0.6833(6), 0.7578(3), 0.7434(4)) C6: (0.8167(8), 0.6799(4), 0.8197(5)) C7: (0.8668(7), 0.4708(3), 0.7787(4)) H1: (0.591(6), 0.130(3), 0.430(3)) H4: (0.825(6), 0.196(3), 0.632(3)) H5: (0.649(6), 0.916(3), 0.782(3)) H6: (0.891(4), 0.766(4), 0.921(2)) H7: (0.967(3), 0.393(4), 0.840(3))	C1: (0.31645, 0.18085, 0.32074) C2: (0.18304, 0.25914, 0.24299) C3: (0.08945, 0.13148, 0.12026) C4: (-0.04777, 0.20911, 0.03965) C5: (0.13875, -0.08145, 0.07972) C6: (0.27989, -0.15608, 0.16158) C7: (0.36574, -0.02942, 0.27879) D1: (0.38642, 0.27991, 0.41431) D2: (0.14527, 0.41971, 0.27421) D3: (-0.08531, 0.37035, 0.07234) D4: (0.31743, -0.31666, 0.12935) D5: (0.47369, -0.08826, 0.33967)

Table S4.5 Experimental crystallographic data for Anthracene obtained by single-crystal X-ray diffraction at room temperature in this work.

	Anthracene at 1.5 GPa	Anthracene at 4.0 GPa
CCDC deposition number	2364307	2364308
Crystal data		
Chemical formula	$C_{14}H_{10}$	$C_{14}H_{10}$
M_r	178.22	178.22
Crystal system, space group	Monoclinic, $P2_1/c$	Monoclinic, $P2_1/c$
a, b, c (Å)	8.0741(10), 5.8283(7), 9.032(11)	8.747(11), 5.6633(7), 7.718(2)
α, β, γ (°)	90, 101.44(4), 90	90, 99.35(7), 90
V (Å^3)	416.6(5)	377.3(5)
Z	2	2
Density (Mg/m^3)	1.421	1.569
Wavelength (Å)	0.3738	0.3738
μ (mm^{-1})	0.037	0.041
Data collection		
Absorption correction	Multi-scan	Multi-scan
T_{min}, T_{max}	0.66, 1.00	0.089, 1.00
No. of measured, independent and observed reflections	684, 311, 156	515, 285, 130
R_{int}	0.0713	0.0535
θ_{max} (°)	15.711	15.633
Refinement		
Refinement on	F^2	F^2
R[F^2>2σ(F^2)], wR(F^2), S	0.0545, 0.1262, 0.558	0.054, 0.1102, 0.923
Data / restraints / parameters	311/ 6/ 67	285/ 36/ 64
H-atom treatment	Refined by ride model	Refined by ride model
Weighting scheme	$w = 1/ [\sigma^2 (F_o^2)]$, where $P = (F_o^2 + 2F_c^2)/3$	$w = 1/ [\sigma^2 (F_o^2) + (0.0377P)^2]$, where $P = (F_o^2 + 2F_c^2)/3$
$\Delta\rho_{max}$, $\Delta\rho_{min}$ (e Å^{-3})	0.089, -0.107	0.133, -0.116
Crystal Structure		
Fractional atomic coordinates (x, y, z)	C1: (0.4072(19), 0.3611(8), 0.3792(6)) C2: (0.6487(19), 0.4126(7), 0.5836(7)) C3: (0.787(2), 0.3436(8), 0.6702(7)) C4: (0.8807(18), 0.4743(9), 0.7897(5)) C5: (0.309(2), 0.2296(9), 0.2536(7)) C6: (0.176(2), 0.3011(10), 0.1711(7)) C7: (0.5504(16), 0.2842(7), 0.4632(6)) H3: (0.826617, 0.198421, 0.652713) H4: (0.974(18), 0.407(8), 0.849(6)) H5: (0.348419, 0.084877, 0.233901) H6: (0.117468, 0.216242, 0.090200) H7: (0.588333, 0.139272, 0.442442)	C1: (0.445(2), 0.2778(12), 0.5365(13)) C2: (0.194(3), 0.3444(13), 0.3220(14)) C3: (0.1215(17), 0.4744(9), 0.2086(10)) C4: (0.399(3), 0.6477(12), 0.3736(15)) C5: (0.361(3), 0.4077(13), 0.4186(13)) C6: (0.167(3), 0.7042(13), 0.1651(16)) C7: (0.312(3), 0.7772(13), 0.2518(15)) H1: (0.405977, 0.132916, 0.565783) H2: (0.148787, 0.204455, 0.350737) H3: (0.029063, 0.416365, 0.146705) H6: (0.105031, 0.799555, 0.084443) H7: (0.349227, 0.923333, 0.222973)

Table S4.5 (continuation)

Anthracene at 8.3 GPa	Anthracene at 10.8 GPa	Anthracene at 13.5 GPa
2364309	2364310	2364311
$C_{14}H_{10}$	$C_{14}H_{10}$	$C_{14}H_{10}$
178.235	178.235	178.235
Monoclinic, $P2_1/c$	Monoclinic, $P2_1/c$	Monoclinic, $P2_1/c$
8.522(6), 5.5444(4), 7.4715(11)	8.421(5), 5.4845(4), 7.3579(8)	8.291(3), 5.4007(3), 7.2067(6)
90, 97.85(3), 90	90, 97.26(2), 90	90, 96.21(2), 90
349.7(3)	337.12(19)	320.81(14)
2	2	2
1.693	1.756	1.845
0.3738	0.3738	0.3738
0.044	0.046	0.048
Multi-scan	Multi-scan	Multi-scan
0.0085, 1.00	0.3268, 1.00	0.3578, 1.00
665, 354, 237	597, 402, 246	717, 446, 239
0.0407	0.019	0.0378
16.31	18.94	21.02
F^2	F^2	F^2
0.063, 0.1672, 0.9847	0.0425, 0.0886, 0.8806	0.0506, 0.1195, 0.988
354/ 6/ 79	402/ 0/ 79	446/ 0/ 79
Refined by non-spherical atomic form factors	Refined by non-spherical atomic form factors	Refined by non-spherical atomic form factors
$w = 1/ [\sigma^2 (F_o^2) + (0.1432P)^2]$, where $P = (F_o^2 + 2F_c^2)/3$	$w = 1/ [\sigma^2 (F_o^2) + (0.0638P)^2]$, where $P = (F_o^2 + 2F_c^2)/3$	$w = 1/ [\sigma^2 (F_o^2) + (0.0858P)^2]$, where $P = (F_o^2 + 2F_c^2)/3$
0.2877, -0.272	0.221, -0.1817	0.2328, -0.2657
C1: (0.4482(13), 0.2657(6), 0.5368(7)) C2: (0.2027(15), 0.3319(7), 0.3285(7)) C3: (0.3105(12), 0.7928(6), 0.2493(7)) C4: (0.3546(14), 0.4125(7), 0.4146(7)) C5: (0.4059(12), 0.6472(6), 0.3763(6)) C6: (0.1162(13), 0.4749(7), 0.2009(8)) C7: (0.1666(15), 0.7058(7), 0.1602(8)) H1: (0.422(11), 0.095(6), 0.562(6)) H2: (0.169(13), 0.156(6), 0.357(7)) H3: (0.335(10), 0.968(6), 0.237(5)) H6: (-0.019(17), 0.430(10), 0.163(10)) H7: (0.094(15), 0.845(8), 0.069(8))	C1: (0.3532(7), 0.4105(4), 0.4144(3)) C2: (0.4073(7), 0.6487(4), 0.3766(4)) C3: (0.4503(7), 0.2638(4), 0.5384(4)) C4: (0.2014(8), 0.3314(4), 0.3275(4)) C5: (0.3108(7), 0.7942(4), 0.2503(4)) C6: (0.1688(8), 0.7080(4), 0.1594(4)) C7: (0.1129(8), 0.4739(4), 0.2013(4)) H3: (0.411(6), 0.084(4), 0.574(3)) H4: (0.156(7), 0.147(4), 0.358(4)) H5: (0.338(7), 0.979(4), 0.227(3)) H6: (0.128(9), 0.824(4), 0.062(4)) H7: (0.002(8), 0.401(6), 0.130(4))	C1: (0.1985(9), 0.6707(5), 0.3278(5)) C2: (0.3064(9), 0.2014(5), 0.2485(5)) C3: (0.4043(9), 0.3492(5), 0.3755(4)) C4: (0.3532(9), 0.5918(5), 0.4148(4)) C5: (0.4481(9), 0.7396(5), 0.5375(5)) C6: (0.1679(10), 0.2898(5), 0.1564(5)) C7: (0.1144(10), 0.5259(6), 0.1992(5)) H1: (0.144(11), 0.847(6), 0.357(6)) H2: (0.341(8), 0.012(6), 0.225(5)) H5: (0.401(8), 0.919(6), 0.571(5)) H6: (0.104(10), 0.169(6), 0.054(6)) H7: (-0.009(14), 0.599(7), 0.141(6))

Table S4.5 (continuation)

Anthracene at 15.8 GPa	Anthracene at 18.4 GPa	Anthracene at 21.5 GPa
2364312	2364313	2364314
$C_{14}H_{10}$	$C_{14}H_{10}$	$C_{14}H_{10}$
178.235	178.235	178.235
Monoclinic, $P2_1/c$	Monoclinic, $P2_1/c$	Monoclinic, $P2_1/c$
8.209(5), 5.3592(4), 7.1344(9)	8.156(6), 5.3045(3), 7.0586(3)	8.075(5), 5.2590(4), 6.9637(9)
90, 95.72(3), 90	90, 95.183(13), 90	90, 94.70(3), 90
312.31(18)	304.1(2)	294.7(2)
2	2	2
1.895	1.946	2.008
0.3738	0.3738	0.3738
0.049	0.051	0.052
Multi-scan	Multi-scan	Multi-scan
0.6033, 1.00	0.3703, 1.00	0.0396, 1.00
527, 334, 214	495, 284, 228	617, 402, 241
0.0181	0.0206	0.0176
16.96	16.98	21.02
F^2	F^2	F^2
0.0314, 0.0566, 1.0137	0.0461, 0.1102, 1.052	0.061, 0.1466, 0.9458
334/ 0/ 79	284/ 24/ 79	402/ 30/ 79
Refined by non-spherical atomic form factors	Refined by non-spherical atomic form factors	Refined by non-spherical atomic form factors
$w = 1/ [\sigma^2 (F_o^2) + (0.0301P)^2]$, where $P = (F_o^2 + 2F_c^2)/3$	$w = 1/ [\sigma^2 (F_o^2) + (0.0864P)^2]$, where $P = (F_o^2 + 2F_c^2)/3$	$w = 1/ [\sigma^2 (F_o^2) + (0.1089P)^2]$, where $P = (F_o^2 + 2F_c^2)/3$
0.1563, -0.1422	0.1891, -0.1252	0.3176, -0.2259
C1: (0.1976(8), 0.3272(4), 0.3286(5))	C1: (0.1955(10), 0.3276(4), 0.3284(3))	C1: (0.6902(9), 0.8059(4), 0.7498(5))
C2: (0.3497(8), 0.4078(4), 0.4146(4))	C2: (0.4058(8), 0.6550(3), 0.3761(2))	C2: (0.5959(9), 0.6552(4), 0.6247(5))
C3: (0.5532(9), 0.7406(4), 0.4621(4))	C3: (0.3069(8), 0.8033(3), 0.2485(2))	C3: (0.8100(10), 0.3260(5), 0.6712(5))
C4: (0.4022(8), 0.6529(4), 0.3743(4))	C4: (0.3486(8), 0.4075(3), 0.4152(2))	C4: (0.6465(9), 0.4064(5), 0.5847(5))
C5: (0.3069(8), 0.8008(4), 0.2482(4))	C5: (0.5534(8), 0.7438(3), 0.4619(2))	C5: (0.5543(10), 0.2541(5), 0.4620(5))
C6: (0.1115(8), 0.4717(4), 0.1983(4))	C6: (0.1686(8), 0.7135(4), 0.1537(3))	C6: (0.8912(11), 0.4720(5), 0.8029(5))
C7: (0.1662(9), 0.7137(4), 0.1549(5))	C7: (0.1087(9), 0.4707(4), 0.1969(3))	C7: (0.8362(10), 0.7151(5), 0.8489(5))
H1: (0.156(7), 0.146(4), 0.367(4))	H1: (0.201(13), 0.152(5), 0.370(4))	H1: (0.659(10), 1.000(6), 0.771(5))
H3: (0.585(8), 0.916(4), 0.415(4))	H3: (0.357(10), 1.007(5), 0.216(3))	H3: (0.886(11), 0.159(6), 0.647(6))
H5: (0.339(7), 0.989(4), 0.215(4))	H5: (0.607(10), 0.942(5), 0.429(3))	H5: (0.584(10), 0.073(6), 0.442(6))
H6: (-0.008(12), 0.401(5), 0.134(6))	H6: (0.090(12), 0.837(4), 0.049(4))	H6: (1.000(12), 0.410(8), 0.867(7))
H7: (0.116(7), 0.823(5), 0.046(4))	H7: (-0.000(14), 0.404(5), 0.117(4))	H7: (0.883(11), 0.850(6), 0.944(7))

Table S4.5 (continuation)

Anthracene at 25.3 GPa	Anthracene at 29.0 GPa	Anthracene at 34.0 GPa
2364315	2364316	2364317
$C_{14}H_{10}$	$C_{14}H_{10}$	$C_{14}H_{10}$
178.235	178.235	178.235
Monoclinic, $P2_1/c$	Monoclinic, $P2_1/c$	Monoclinic, $P2_1/c$
7.989(10), 5.2110(4), 6.9048(5)	7.935(11), 5.1607(5), 6.8359(6)	7.854(16), 5.1011(9), 6.7534(8)
90, 94.05(2), 90	90, 93.54(2), 90	90, 93.02(3), 90
286.7(4)	279.4(4)	270.2(6)
2	2	2
2.064	2.119	2.191
0.3738	0.3738	0.3738
0.054	0.055	0.057
Multi-scan	Multi-scan	Multi-scan
0.2668, 1.00	0.206, 1.00	0.4722, 1.00
584, 333, 230	529, 324, 229	434, 279, 192
0.0193	0.0106	0.0135
20.53	20.98	21.21
F^2	F^2	F^2
0.0596, 0.1553, 1.0226	0.0447, 0.106, 1.0611	0.0419, 0.1, 0.9902
333/ 6/ 79	324/ 0/ 79	284/ 24/ 79
Refined by non-spherical atomic form factors	Refined by non-spherical atomic form factors	Refined by non-spherical atomic form factors
$w = 1/ [\sigma^2 (F_o^2) + (0.1235P)^2]$, where $P = (F_o^2 + 2F_c^2)/3$	$w = 1/ [\sigma^2 (F_o^2) + (0.0823P)^2]$, where $P = (F_o^2 + 2F_c^2)/3$	$w = 1/ [\sigma^2 (F_o^2) + (0.0835P)^2]$, where $P = (F_o^2 + 2F_c^2)/3$
0.1331, -0.1460	0.1222, -0.1482	0.1497, -0.141
C1: (0.4450(9), 0.7497(4), 0.5386(3)) C2: (0.6961(10), 0.8076(4), 0.7515(3)) C3: (0.1926(11), 0.6756(4), 0.3305(3)) C4: (0.3490(10), 0.5950(4), 0.4150(3)) C5: (0.5965(11), 0.6555(4), 0.6247(3)) C6: (0.1073(10), 0.5300(4), 0.1949(3)) C7: (0.8346(10), 0.7154(5), 0.8486(3)) H1: (0.419(13), 0.936(5), 0.573(4)) H2: (0.661(11), 0.993(6), 0.780(4)) H3: (0.155(12), 0.869(5), 0.374(5)) H6: (0.003(14), 0.602(6), 0.115(4)) H7: (0.904(14), 0.834(6), 0.946(5))	C1: (0.5940(8), 0.3425(3), 0.6246(3)) C2: (0.6966(8), 0.1901(3), 0.7519(2)) C3: (0.1907(8), 0.3229(3), 0.3298(3)) C4: (0.8352(8), 0.2832(3), 0.8504(2)) C5: (0.3473(8), 0.4036(3), 0.4151(2)) C6: (0.1053(8), 0.4690(3), 0.1943(3)) C7: (0.4452(8), 0.2487(3), 0.5386(2)) H2: (0.671(9), 0.010(5), 0.779(3)) H3: (0.133(10), 0.145(5), 0.371(4)) H4: (0.914(11), 0.161(4), 0.953(4)) H6: (0.011(12), 0.389(5), 0.128(4)) H7: (0.429(9), 0.065(4), 0.574(3))	C1: (0.3043(9), 0.8119(4), 0.2482(3)) C2: (0.5521(9), 0.7543(4), 0.4603(2)) C3: (0.4037(10), 0.6580(4), 0.3748(3)) C4: (0.8973(9), 0.5323(4), 0.8071(3)) C5: (0.6570(9), 0.5972(4), 0.5852(3)) C6: (0.8078(9), 0.6788(4), 0.6686(3)) C7: (0.1657(10), 0.7184(4), 0.1484(3)) H1: (0.336(10), 0.997(5), 0.215(3)) H2: (0.607(11), 0.938(5), 0.421(3)) H4: (0.998(13), 0.631(5), 0.878(4)) H6: (0.872(11), 0.873(5), 0.621(4)) H7: (0.109(15), 0.831(5), 0.043(4))

Table S4.5 (continuation)

Anthracene at 35.5 GPa	Anthracene at 38.6 GPa	Anthracene at 42.3 GPa
2364318	2364319	2364320
$C_{14}H_{10}$	$C_{14}H_{10}$	$C_{14}H_{10}$
178.235	178.235	178.235
Monoclinic, $P2_1/c$	Monoclinic, $P2_1/c$	Monoclinic, $P2_1/c$
7.843(16), 5.0901(9), 6.7422(8)	7.816(16), 5.0564(7), 6.6915(7)	7.769(19), 5.0266(9), 6.6325(8)
90, 92.91(3), 90	90, 92.66(3), 90	90, 92.14(4), 90
270.2(6)	264.2(5)	258.8(6)
2	2	2
2.202	2.241	2.287
0.3738	0.3738	0.3738
0.057	0.058	0.06
Multi-scan	Multi-scan	Multi-scan
0.1156, 1.00	0.3437, 1.00	0.5346, 1.00
498, 304, 209	470, 280, 193	451, 273, 169
0.0152	0.0134	0.0314
21.04	21.05	20.71
F^2	F^2	F^2
0.0359, 0.0801, 1.0394	0.0481, 0.1122, 1.0835	0.0491, 0.12, 1.2443
304/ 24/ 79	304/ 24/ 79	273/ 0/ 79
Refined by non-spherical atomic form factors	Refined by non-spherical atomic form factors	Refined by non-spherical atomic form factors
$w = 1/[\sigma^2(F_o^2) + (0.0835P)^2]$, where $P = (F_o^2 + 2F_c^2)/3$	$w = 1/[\sigma^2(F_o^2) + (0.0889P)^2]$, where $P = (F_o^2 + 2F_c^2)/3$	$w = 1/[\sigma^2(F_o^2) + (0.0174P)^2]$, where $P = (F_o^2 + 2F_c^2)/3$
0.1374, -0.1484	0.158, -0.1713	0.1424, -0.1595
C1: (0.3461(8), 0.4022(3), 0.4151(2))	C1: (0.3033(12), 0.8135(4), 0.2481(4))	C1: (0.3036(14), 0.1856(5), 0.2493(4))
C2: (0.5550(8), 0.7562(4), 0.4601(2))	C2: (0.1878(12), 0.3203(5), 0.3325(4))	C2: (0.1618(16), 0.2815(6), 0.1463(4))
C3: (0.4027(7), 0.6583(3), 0.3759(2))	C3: (0.6512(12), 0.5980(5), 0.5856(3))	C3: (0.8104(14), 0.3181(6), 0.6679(4))
C4: (0.3040(8), 0.8128(3), 0.2479(2))	C4: (0.4042(11), 0.6582(5), 0.3756(3))	C4: (0.5564(14), 0.2432(6), 0.4605(3))
C5: (0.1042(8), 0.4665(3), 0.1929(2))	C5: (0.5569(12), 0.7571(5), 0.4598(3))	C5: (0.8988(14), 0.4657(6), 0.8072(4))
C6: (0.1906(8), 0.3204(3), 0.3312(2))	C6: (0.1630(13), 0.7188(5), 0.1472(4))	C6: (0.4041(14), 0.3409(5), 0.3751(4))
C7: (0.1670(8), 0.7178(3), 0.1472(2))	C7: (0.1024(12), 0.4666(5), 0.1928(3))	C7: (0.6541(13), 0.4018(6), 0.5841(4))
H2: (0.583(10), 0.952(5), 0.421(3))	H1: (0.344(13), 1.005(7), 0.221(4))	H1: (0.349(15), -0.004(7), 0.221(4))
H4: (0.343(10), 1.000(5), 0.218(3))	H2: (0.161(16), 0.122(7), 0.360(6))	H2: (0.083(17), 0.165(6), 0.035(5))
H5: (-0.009(12), 0.378(5), 0.121(3))	H5: (0.582(15), 0.962(7), 0.424(4))	H3: (0.823(16), 0.132(7), 0.629(5))
H6: (0.158(8), 0.142(4), 0.367(3))	H6: (0.072(15), 0.832(6), 0.047(5))	H4: (0.591(15), 0.062(7), 0.422(5))
H7: (0.103(10), 0.839(4), 0.042(3))	H7: (0.008(15), 0.384(8), 0.116(5))	H5: (1.011(17), 0.380(7), 0.880(5))

Table S4.6 Lattice parameters for naphthalene up to 50.7 GPa and anthracene up to 42.3 GPa in this work.

Polymorph	Pressure, GPa	*a*, Å	*b*, Å	*c*, Å	*β*, °
Naphthalene	0	8.147(6)	6.0035(8)	8.293(3)	116.08(7)
Naphthalene	6.2	7.140(6)	5.5654(5)	7.302(2)	110.72(7)
Naphthalene	10.8	6.811(12)	5.4101(11)	6.974(4)	108.82(12)
Naphthalene	20.3	6.440(11)	5.1922(7)	6.6024(18)	106.57(8)
Naphthalene	24.5	6.299(12)	5.1533(7)	6.5364(18)	105.89(9)
Naphthalene	28.5	6.239(11)	5.1189(6)	6.429(2)	105.13(10)
Naphthalene	35.1	6.136(14)	5.0604(12)	6.327(3)	104.45(14)
Naphthalene	43.3	5.96(4)	5.011(3)	6.091(9)	102.8(4)
Naphthalene	50.7	5.93(2)	4.913(2)	6.035(11)	103.3(3)
Anthracene	0	9.488(5)	6.0253(3)	8.5642(14)	103.52(3)
Anthracene	1.5	8.0741(10)	5.8283(7)	9.032(11)	101.44(4)
Anthracene	4	8.747(11)	5.6633(7)	7.718(2)	99.35(7)
Anthracene	8.3	8.522(6)	5.5444(4)	7.4715(11)	97.85(3)
Anthracene	10.8	8.421(5)	5.4845(4)	7.3579(8)	97.26(2)
Anthracene	13.5	8.291(3)	5.4007(3)	7.2067(6)	96.21(2)
Anthracene	15.8	8.209(5)	5.3592(4)	7.1344(9)	95.72(3)
Anthracene	18.4	8.156(6)	5.3045(3)	7.0586(3)	95.183(13)
Anthracene	21.5	8.075(5)	5.2590(4)	6.9637(9)	94.70(3)
Anthracene	25.3	7.989(10)	5.2110(4)	6.9048(5)	94.05(2)
Anthracene	29	7.935(11)	5.1607(5)	6.8359(6)	93.54(2)
Anthracene	34	7.854(16)	5.1011(9)	6.7534(8)	93.02(3)
Anthracene	35.5	7.843(16)	5.0901(9)	6.7422(8)	92.91(3)
Anthracene	38.6	7.816(16)	5.0564(7)	6.6915(7)	92.66(3)
Anthracene	42.3	7.769(19)	5.0266(9)	6.6325(8)	92.14(4)

Table S4.7 Unit cell volume per formula unit for naphthalene up to 50.7 GPa and anthracene up to 42.3GPa in this work.

Polymorph/ pressure transmitting medium	Pressure, GPa	Volume per formula unit, Å^3
Naphthalene/ He	0	182.2(2)
Naphthalene/ He	6.2	135.70(15)
Naphthalene/ He	10.8	121.7(3)
Naphthalene/ He	20.3	105.8(2)
Naphthalene/ He	24.5	102.1(2)
Naphthalene/ He	28.5	99.1(2)
Naphthalene/ He	35.1	95.1(3)
Naphthalene/ He	43.3	88.7(6)
Naphthalene/ He	50.7	85.6(4)
Anthracene/ He	0	238.00(15)
Anthracene/ He	1.5	208.3(3)
Anthracene/ He	4	188.6(3)
Anthracene/ He	8.3	174.85(15)
Anthracene/ He	10.8	168.57(10)
Anthracene/ He	13.5	160.40(7)
Anthracene/ He	15.8	156.16(9)
Anthracene/ He	18.4	152.05(10)
Anthracene/ He	21.5	147.35(10)
Anthracene/ He	25.3	143.4(2)
Anthracene/ He	29	139.7(2)
Anthracene/ He	34	135.1(3)
Anthracene/ He	35.5	134.4(3)
Anthracene/ He	38.6	132.1(3)
Anthracene/ He	42.3	129.4(3)

Table S4.8 DFT-calculated unit cell volume per formula unit for naphthalene up to 50.7 GPa and anthracene up to 42.3 GPa.

Polymorph	Pressure (GPa)	Volume per formula unit (Å^3)
Naphthalene	0	167.17
Naphthalene	4.4	135.70
Naphthalene	9.8	121.62
Naphthalene	22.3	105.80
Naphthalene	31.3	99.10
Naphthalene	53.1	88.70
Anthracene	0	222.29
Anthracene	0.9	208.29
Anthracene	3.3	188.62
Anthracene	6.4	174.84
Anthracene	8.4	168.57
Anthracene	11.7	160.40
Anthracene	16.3	152.07
Anthracene	22.7	143.37
Anthracene	26.2	139.70
Anthracene	32.1	134.41
Anthracene	34.9	132.09
Anthracene	38.7	129.42

Table S4.9 Interplanar angles of naphthalene and anthracene from experiments.

Polymorph	Pressure, GPa	Interplanar angle, °
Anthracene	0	51.67
Anthracene	1.5	49
Anthracene	3.8	46.25
Anthracene	8.5	45.01
Anthracene	10.8	44.27
Anthracene	13.5	43.4
Anthracene	15.8	42.59
Anthracene	18.4	42.39
Anthracene	21.5	43.17
Anthracene	25.3	42.5
Anthracene	29	40.87
Anthracene	34	40.64
Anthracene	35.5	40.45
Anthracene	38.6	40.17
Anthracene	42.3	41.93
Naphthalene	0	53.78
Naphthalene	6.2	45.73
Naphthalene	10.8	43.33
Naphthalene	20.3	42.14
Naphthalene	24.5	41.4
Naphthalene	28.5	42.86
Naphthalene	35.1	41.08
Naphthalene	43.3	42.7
Naphthalene	50.7	40.6

Table S4.10 The experimental average C-H bond length in anthracene and naphthalene molecules.

Polymorph	**Pressure, GPa**	**C-H Avg, Å**
Naphthalene	0	1.08(5)
Naphthalene	6.2	1.11(5)
Naphthalene	10.8	0.99(6)
Naphthalene	20.3	1.03(5)
Naphthalene	24.5	1.03(7)
Naphthalene	28.5	1.05(7)
Naphthalene	35.1	1.09(7)
Naphthalene	43.3	1.10(10)
Anthracene	0	1.09(2)
Anthracene	8.3	1.07(7)
Anthracene	10.8	1.06(4)
Anthracene	13.5	1.09(5)
Anthracene	15.8	1.07(4)
Anthracene	18.4	1.11(5)
Anthracene	21.5	1.04(5)
Anthracene	25.3	1.05(5)
Anthracene	29	1.02(4)
Anthracene	34	1.05(5)
Anthracene	35.5	1.04(4)
Anthracene	38.6	1.05(6)
Anthracene	42.3	1.04(6)

Table S4.11 The calculation average C-H bond length in anthracene and naphthalene molecules.

Polymorph	**Pressure, GPa**	**C-H Avg, Å**
Naphthalene	0	1.09
Naphthalene	4.4	1.087
Naphthalene	9.8	1.083
Naphthalene	22.3	1.076
Naphthalene	31.3	1.072
Naphthalene	53.1	1.064
Anthracene	0	1.089
Anthracene	6.36	1.082
Anthracene	8.36	1.08
Anthracene	11.71	1.077
Anthracene	16.29	1.074
Anthracene	22.73	1.07
Anthracene	26.15	1.068
Anthracene	32.05	1.064
Anthracene	34.94	1.063
Anthracene	38.7	1.061

Table S4.12 Different types of average C-C bond lengths in naphthalene and anthracene from experiments.

Polymorph	**Pressure, GPa**	**Type-I, Å**	**Type-II, Å**	**Type-III, Å**
Naphthalene	0	1.414(7)	1.420(5)	1.381(7)
Naphthalene	6.2	1.408(7)	1.417(4)	1.396(4)
Naphthalene	10.8	1.386(9)	1.410(6)	1.376(6)
Naphthalene	14.8	1.397(10)	1.383(8)	1.360(6)
Naphthalene	20.3	1.377(7)	1.382(6)	1.359(7)
Naphthalene	24.5	1.389(9)	1.373(8)	1.354(8)
Naphthalene	29.5	1.385(12)	1.374(11)	1.367(6)
Naphthalene	36.1	1.375(12)	1.370(6)	1.359(6)
Naphthalene	43.3	1.395(18)	1.364(14)	1.359(12)
Naphthalene	50.7	1.40(3)	1.329(15)	1.335(11)
Anthracene	0	1.43(2)	1.412(4)	1.385(7)
Anthracene	4	1.455(6)	1.422(8)	1.350(7)
Anthracene	8.3	1.441(6)	1.409(12)	1.382(8)
Anthracene	10.8	1.439(4)	1.393(8)	1.376(6)
Anthracene	13.5	1.432(5)	1.393(11)	1.357(8)
Anthracene	15.8	1.435(4)	1.385(9)	1.372(7)
Anthracene	18.4	1.439(5)	1.384(8)	1.371(7)
Anthracene	21.5	1.422(5)	1.386(11)	1.371(6)
Anthracene	25.3	1.427(6)	1.384(8)	1.363(6)
Anthracene	29	1.433(4)	1.381(8)	1.362(6)
Anthracene	34	1.434(6)	1.369(9)	1.359(7)
Anthracene	35.5	1.417(5)	1.375(8)	1.354(6)
Anthracene	38.6	1.412(6)	1.374(10)	1.357(8)
Anthracene	42.3	1.412(7)	1.367(11)	1.359(10)

References

[1] Leising, G. Ü. N., Tasch, S., Brandstatter, C. *et al.* Red–green–blue light emission from a thin film electroluminescence device based on parahexaphenyl. *Advanced Materials* **9(1)**, 33-36 (1997).

[2] Abrahams, S. C., Robertson, J. M. and White, J. G. The crystal and molecular structure of naphthalene. I. X-ray measurements. *Acta Crystallographica* **2(4)**, 233-238 (1949).

[3] Natkaniec, I., Dyck, W., Fuess, H. *et al.* The structure of perdeuteronaphthalene $C_{10}D_8$ at 12 K by neutron diffraction. *Zeitschrift für Kristallographie-Crystalline Materials* **163(1-4)**, 285-294 (1983).

[4] Oddershede, J. and Larsen, S. Charge density study of naphthalene based on X-ray diffraction data at four different temperatures and theoretical calculations. *The Journal of Physical Chemistry A* **108(6)**, 1057-1063 (2004).

[5] Bridgman, P. W. Polymorphic transitions up to 50,000 kg/cm^2 of several organic substances. *Proc. Am. Acad. Arts Sci* **72**, 227-268 (1938).

[6] Jones, P. F. and Nicol, M. Excimer emission of naphthalene, anthracene, and phenanthrene crystals produced by very high pressures. *The Journal of Chemical Physics* **48(12)**, 5440-5447 (1968).

[7] Vaidya, S. N. and Kennedy, G. C. Compressibility of 18 molecular organic solids to 45 kbar. *The Journal of Chemical Physics* **55(3)**, 987-992 (1971).

[8] Nicol, M., Vernon, M. and Woo, J. T. Raman spectra and defect fluorescence of anthracene and naphthalene crystals at high pressures and low temperatures. *The Journal of Chemical Physics* **63(5)**, 1992-1999 (1975).

[9] Meletov, K. P. Phonon spectrum of a naphthalene crystal at a high pressure: Influence of shortened distances on the lattice and intramolecular vibrations. *Physics of the Solid State* **55**, 581-588 (2013).

[10] Likhacheva, A. Y., Rashchenko, S. V. and Litasov, K. D. High-pressure structural properties of naphthalene up to 6 GPa. *Journal of Applied Crystallography* **47(3)**, 984-991(2014).

[11] O'Bannon, E. and Williams, Q. Vibrational spectra of four polycyclic aromatic hydrocarbons under high pressure: implications for stabilities of PAHs during accretion. *Physics and Chemistry of Minerals* **43**, 181-208 (2016).

[12] Cruickshank, D. W. J. A detailed refinement of the crystal and molecular structure of anthracene. *Acta Crystallographica* **9(11)**, 915-923 (1956).

[13] Lehmann, M. S. and Pawley, G. S. The Structure of Perdeuterioanthracene by Neutron Diffraction. *Acta Chemica Scandinavica* **26(5)**, 1996 (1972).

[14] Offen, H. W. Fluorescence spectra of several aromatic crystals under high pressures. *The Journal of Chemical Physics* **44(2)**, 699-703 (1966).

[15] Adams, D. M. and Tan, T. K. Vibrational spectroscopy at high pressures. Part 37.—Infrared spectrum of anthracene. *Journal of the Chemical Society, Faraday Transactions 2: Molecular and Chemical Physics* **77(9)**, 1711-1714 (1981).

[16] Leger, J. M. Aloualiti, H. X-ray study of anthracene under high pressure. *Solid state communications* **79(11)**, 901-904 (1991).

[17] Zhao, L., Baer, B. J. and Chronister, E. L. High-pressure Raman study of anthracene. *The Journal of Physical Chemistry A* **103(12)**, 1728-1733 (1999).

[18] Oehzelt, M., Heimel, G., Resel, R. *et al.* High pressure x-ray study on anthracene. *The Journal of chemical physics* **119(2)**, 1078-1084 (2003).

[19] Fabbiani, F. P. A., Allan, D. R., Parsons, S. *et al.* Exploration of the high-pressure behaviour of polycyclic aromatic hydrocarbons: naphthalene, phenanthrene and pyrene. *Acta Crystallographica Section B: Structural Science* **62(5)**, 826-842 (2006).

[20] Boehler, R. New diamond cell for single-crystal x-ray diffraction. *Review of Scientific Instruments* **77(11)**, (2006).

[21] Mao, H. K., Xu, J-A., and Bell, P. M. Calibration of the ruby pressure gauge to 800 kbar under quasi-hydrostatic conditions. *Journal of Geophysical Research: Solid Earth* **91(B5)**, 4673-4676 (1986).

[22] Rigaku, O. D. Crysalis Pro. Rigaku Oxford Diffraction. *Yarnton, England* (2015).

[23] Sheldrick, G. M. A short history of SHELX. *Acta Crystallographica Section A: Foundations of Crystallography* **64(1)**, 112-122 (2008).

[24] Dolomanov, O.V., Bourhis, L. J., Gildea, R. J. *et al.* OLEX2: a complete structure solution, refinement and analysis program. *Journal of applied crystallography* **42(2)**, 339-341 (2009).

[25] Kleemiss, F., Dolomanov, O.V., Bodensteiner, M. *et al.* Accurate crystal structures and chemical properties from NoSpherA2. *Chemical Science* **12(5)**,1675-1692 (2021).

[26] Momma, K, and Izumi, F. VESTA 3 for three-dimensional visualization of crystal, volumetric and morphology data. *Journal of applied crystallography* **44(6)**, 1272-1276 (2011).

[27] Angel, R. J., Alvaro, M. and Gonzalez-Platas, J. EosFit7c and a Fortran module (library) for equation of state calculations. *Zeitschrift für Kristallographie-Crystalline Materials* **229(5)**, 405-419 (2014).

[28] Kresse, G., and Furthmüller, J. Efficiency of ab-initio total energy calculations for metals and semiconductors using a plane-wave basis set. *Computational materials science* **6(1)**, 15-50 (1996).

[29] Blöchl, P. E. Projector augmented-wave method. *Physical review B* **50(24)**, 17953 (1994).

[30] Kresse, G. and Joubert, D. From ultrasoft pseudopotentials to the projector augmented-wave method. *Physical review B* **59(3)**, 1758 (1999).

[31] Grimme, S., Ehrlich, S. and Goerigk, L. Effect of the damping function in dispersion corrected density functional theory. *Journal of computational chemistry* **32(7)**, 1456-1465 (2011).

[32] Monkhorst, H. J. and Pack, J. D. Special points for Brillouin-zone integrations. *Physical review B* **13(12)**, 5188 (1976).

[33] Sheldrick, G.M. and Schneider, T. R. "[16] SHELXL: High-resolution refinement." Methods in enzymology. *Academic Press* **277**, 319-343 (1997).

[34] Woińska, M., Grabowsky, S., Dominiak, P. M. *et al.* Hydrogen atoms can be located accurately and precisely by x-ray crystallography. *Science advances* **2(5)**, e1600192 (2016).

[35] Malaspina, Lorraine A. *et al.* Hydrogen atoms in bridging positions from quantum crystallographic refinements: Influence of hydrogen atom displacement parameters on geometry and electron density. *CrystEngComm* **22(28)**, 4778-4789 (2020).

[36] Guńka, P. A. *et al.* Crystal Structure and Non-Hydrostatic Stress-Induced Phase Transition of Urotropine Under High Pressure. *Chemistry–A European Journal* **27(3)**, 1094-1102 (2021).

[37] Binns, J., Kamenev, K. V. and McIntyre, G. J. *et al.* Use of a miniature diamond-anvil cell in high-pressure single-crystal neutron Laue diffraction. *IUCrJ* **3**, 168–179 (2016).

[38] Olejniczak, A., Katrusiak, A. and Podsiadło, M. Stochastic hydration of a high-nitrogen-content molecular compound recrystallized under pressure. *IUCrJ* **9(1)**, 49-54 (2022).

[39] Zwolenik, A., Tchoń, D. and Makal, A. Evolution of structure and spectroscopic properties of a new 1, 3-diacetylpyrene polymorph with temperature and pressure. *IUCrJ* **11(4)** (2024).

Chapter 5 Polymorphism of pyrene on compression to 35 GPa in a diamond anvil cell

Wenju Zhou[1], Yuqing Yin[3], Dominique Laniel[4], Andrey Aslandukov[1,2], Elena Bykova[5], Anna Pakhomova[6], Michael Hanfland[6], Tomasz Poreba[6], Mohamed Mezouar[6], Leonid Dubrovinsky[2], Natalia Dubrovinskaia[1,3]**

[1]Material Physics and Technology at Extreme Conditions, Laboratory of Crystallography, University of Bayreuth, 95440 Bayreuth, Germany

[2]Bayerisches Geoinstitut, University of Bayreuth, 95440 Bayreuth, Germany

[3]Department of Physics, Chemistry and Biology (IFM), Linköping University, SE-581 83, Linköping, Sweden

[4]Centre for Science at Extreme Conditions and School of Physics and Astronomy, University of Edinburgh, EH9 3FD Edinburgh, United Kingdom

[5]Institut für Geowissenschaften, Goethe-Universität Frankfurt, 60438 Frankfurt am Main, Germany

[6]European Synchrotron Radiation Facility, CS 40220, 38043 Grenoble Cedex 9, France

**Correspondence E-mails: Wenju.Zhou@uni-bayreuth.de, Natalia.Dubrovinskaia@uni-bayreuth.de*

Communications Chemistry **2024**, 7 (1), 209. https://doi.org/10.1038/s42004-024-01294-0

5.1 Abstract

Structural studies of pyrene have been limited to below 2 GPa. Here, we report on investigations of pyrene up to ~35 GPa using *in situ* single-crystal synchrotron X-ray diffraction in diamond anvil cells and *ab initio* calculations. They reveal the phase transitions from pyrene-I to pyrene-II (0.7 GPa), and to the previously unreported pyrene-IV (2.7 GPa), and pyrene-V (7.3 GPa). The structure and bonding analysis show that gradual compression results in continuous compaction of molecular packing, eventually leading to curvature of molecules, which has never been observed before. Large organic molecules exhibit unexpected high conformational flexibility preserving pyrene-V up to 35 GPa. *Ab initio* calculations suggest that the phases we found are thermodynamically metastable compared

to pyrene-III previously reported at 0.3 and 0.5 GPa. Our study contributes to the fundamental understanding of the polymorphism of polycyclic aromatic hydrocarbons and calls for further theoretical exploration of their structure-property relationships.

5.2 Introduction

Polycyclic aromatic hydrocarbons (PAHs) have long attracted interest as potential materials for various optical, optoelectronic, and electronic applications [1-3] (Pope & Swenberg, 1999; Silinsh, & Cápek, 1994; Farchioni, 2001). In addition to application-oriented research, much work has been done for understanding the fundamental processes associated with their structure-property relationships. For example, the electronic and excitonic processes in aromatic crystals have been strongly linked to both the number of aromatic rings in the molecular structure and the arrangement of molecules in the crystal [1,2] (Pope & Swenberg, 1999; Silinsh, & Cápek, 1994).

Pressure has been proven to be a very powerful thermodynamic parameter which induces structural transformations affecting materials' properties, so that exploring the behavior of PAHs under pressure may provide insights into the structural transitions and intermolecular interactions for this important class of organic materials. However, so far, the information about the structural behavior of any organic crystals at pressures exceeding a few gigapascals is very limited. It is mainly due to studies at higher pressures have been hindered by both the technical complexity of the experiments on fragile organic crystals and because of a common belief that the crystals are quickly destroyed under compression. The advancement of single-crystal X-ray diffraction (SC-XRD) techniques in diamond anvil cells (DACs) with the use of soft pressure-transmitting media [4] (Dubrovinsky, 2013), such as inert gases, has created new possibilities for investigating crystal structures, phase transitions, equilibrium and non-equilibrium transformation paths, molecular arrangements, and chemical bonding of organic crystals under previously unexplored high-pressure conditions. For example, recently high-pressure polymorphism in L-threonine was studied between ambient pressure and 22 GPa [5] (Giordano *et al.*, 2019). Nevertheless, large molecules of PAHs have long been supposed to have a low conformational flexibility under pressure and so far, have been studied using SC-XRD only up to 2.1 GPa [6] (Fabbiani, 2006).

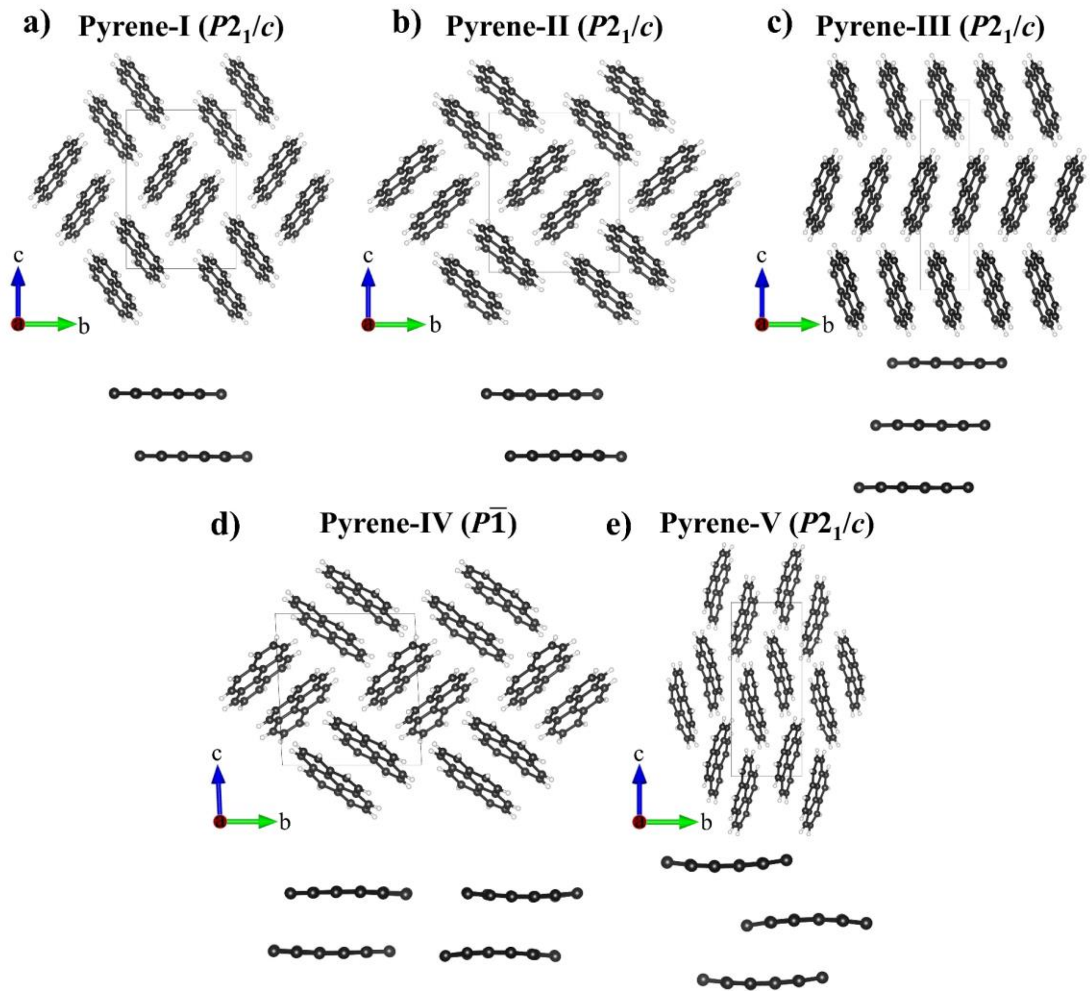

Figure 5.1 Crystal structures of pyrene polymorphs viewed along the *a* axis. a) Pyrene-I, ambient conditions; b) pyrene-II, 0.7 GPa; c) pyrene-III, 0.5 GPa [6]; d) pyrene-IV, 2.7 GPa; e) pyrene-V, 7.3 GPa. Pairs of molecules (sandwiches) determining the molecular packing sandwich-herringbone motif in pyrene-I, pyrene-II, and pyrene-IV are shown in the bottom. Pyrene-IV has two types of sandwiches (sandwich 1- to the left, sandwich 2- to the right). Pyrene-III and pyrene-V do not feature sandwiches. C atoms are black, H atoms are white.

Pyrene ($C_{16}H_{10}$) is a representative of PAHs. At ambient conditions, it is a solid with a monoclinic structure ($P2_1/c$ space group) [7] (Kai *et al.*, 1978) called pyrene-I. Flat pyrene molecules made of four fused benzene rings form pairs ("sandwiches") packed in a herringbone motif (Fig. 5.1a). Because of such molecular packing and the ring's conjugated π-system, pyrene crystals are of interest to study under pressure to examine pressure-induced structural transformations, changes in packing of molecular units, and chemical bond evolution in PAHs. Previous structural studies of pyrene, using diffraction methods, enabled to establish its two polymorphs. The first polymorph, pyrene-II (Fig. 5.1b), was identified upon a transition from pyrene-I at low temperature [8-10] (Jones *et al.*, 1978; Knight *et al.*,1996; Frampton *et al.*, 2000). Its structural motif is similar to that of pyrene-I. The other polymorph, pyrene III (Fig. 5.1c) was identified on single crystals of pyrene recrystallized from a dichloromethane solution at 0.3 and 0.5 GPa [6] (Fabbiani, 2006). It was found to have a different molecular packing model and different intermolecular interactions.

Although spectroscopic data do not provide explicit information about the structure of solid matter, it is worth noticing that vibrational spectroscopy investigation of pyrene up to about 1 GPa, pointing towards the existence of phase transformations in pyrene under pressure, was made as early as in 1976 [11] (Zallen, 1976), when a transition was detected on an abrupt change of the Raman spectrum at ca. 0.4 GPa. Later Raman spectroscopy study [12] (Sun *et al.*, 2008) detected a transformation at 0.3 GPa on a crystal grown from a dichloromethane solution, and on a crystal pressurized in argon up to 0.6 GPa, interpreted in the both cases as observation of pyrene-III, similar to that described by Fabbiani *et al.* (2006) [6] (Fabbiani, 2006).

In this work, we have investigated the behavior of pyrene in the pressure range from ambient to 35.5 GPa using synchrotron SC-XRD in DACs. We have observed three high-pressure polymorphs: pyrene-II, whose structure was known from low-temperature experiments at ambient pressure, but we solved and refined it at high pressure for the first time, and two new phases, pyrene-IV and pyrene-V. Here we report the results of the analysis of their structures and bonding evolution under pressure. Contrary to the previous belief that large organic molecules have low conformational flexibility under pressure, we have demonstrated that gradual compression results in continuous compaction of molecular packing, eventually leading to curvature of molecules, which has never been observed before. Our results reveal that pyrene-V can be preserved in He pressure medium up to ~35 GPa due to fully unexpected structure compaction accompanied by considerable deformation of molecules and their strong alignment along one crystallographic axis.

5.3 Results and discussion

5.3.1 Crystal structures of pyrene polymorphs

Upon compression of pyrene-I ($P2_1/c$) to 0.7 GPa in a He pressure medium, we observed a phase transition to pyrene-II ($P2_1/c$) (Fig. 5.1b), which was still preserved at 1.4 GPa. At the next pressure step (2.7 GPa), a previously unknown triclinic polymorph of pyrene, pyrene-

IV (P-1) (Fig. 5.1d), was identified. The next phase transition occurred at 7.3 GPa to pyrene-V (Fig. 5.1e) with a monoclinic structure ($P2_1/c$). Further we describe in detail the structures of all polymorphs observed in this work. Full crystallographic and experimental data are provided in Tables S5.2 through S5.5 and Supplementary Data 1 through 12.

The crystal structure of pyrene-I (Fig. 5.1a) was first reported in SC-XRD study of Robertson & White in 1947 [13] (Robertson *et al.*, 1947). It was later refined by means of neutron diffraction (CSD reference code PYRENE02) [14] (Hazell, *et al.*, 1972). The crystallographic data of pyrene-I obtained in this work based on synchrotron SC-XRD in comparison with neutron diffraction data of Hazell *et al.* (1972) [14] (Hazell, *et al.*, 1972) are provided in Table S5.2. The structure is monoclinic (space group #14, $P2_1/c$) with the following unit cell parameters at ambient conditions: a = 8.478(8) Å, b = 9.2562(12) Å, c = 13.655(7) Å, β = 100.31(8) ° and V = 1055.3(11) Å^3.

A transition from pyrene-I to pyrene-II below 110 K was first reported by Jones *et al.* (1978) [8] (Jones *et al.*, 1978), and the structure of pyrene-II was suggested on the basis of a combination of micro-electron diffraction and atom—atom, pairwise potential calculations. Knigt *et al.* (1996) [9] (Knight *et al.*,1996) confirmed and refined the pyrene-II structure from high-resolution neutron powder diffraction data collected from a fully deuterated sample at 4.2 K. First single-crystal XRD analysis of pyrene-II at 93 K and ambient pressure was reported by Frampton *et al.* (2000) [10] (Frampton *et al.*, 2000). Our work reports the first structural analysis of pyrene-II under pressure at room temperature using single-crystal XRD and provides crystallographic data for pyrene-II, which are in a very good agreement with those obtained at low temperature and ambient pressure [8-10] (Jones *et al.*, 1978; Knight *et al.*,1996; Frampton *et al.*, 2000).

We observed pyrene-II and solved and refined its structure at two pressure points (0.7. and 1.4 GPa) upon pressurizing crystals of pyrene-I in a helium pressure medium; see Table S5.3 for our crystallographic data in comparison with the low-temperature data of Frampton *et al.* (2000) [10] (Frampton *et al.*, 2000). It has the same space group as pyrene-I with the following unit cell parameters at 0.7 GPa: a = 8.1431(12) Å, b = 9.8639(7) Å, c = 12.1136(4) Å, β = 96.484(7) ° and V = 966.77(16) Å^3, and a similar sandwich-herringbone molecular packing motif if viewed along the a direction. The β angle in pyrene-II is about four degrees larger than in pyrene-I. Upon compression it slightly decreases.

The structures of the two polymorphs, pyrene-I and pyrene-II (Fig. 5.1a, b), are very similar. As underlined in previous studies [8, 10] (Jones *et al.*, 1978; Frampton *et al.*, 2000), “a small rotation of molecules around the *c*-axis [it corresponds to the *a*-axis in the standard setting $P2_1/c$ used in our paper for space group #14] of the pyrene-I unit cell generates a new structure that is very close in terms of cell dimensions and packing motif to pyrene-II” (cited from Frampton *et al.* (2000) [10]). Namely this rotation is responsible for considerable change in the molecules interplanar angle (see the analysis below).

Further compression of pyrene-II led to the formation of a previously unknown triclinic polymorph of pyrene, pyrene-IV (space group #2, *P*-1), which we observed at 2.7 GPa and 4.3 GPa. The unit cell parameters at 2.7 GPa are as follows: a = 7.593(3) Å, b = 10.223(3) Å, c = 11.192(2) Å, α = 92.536(19) °, β = 100.31(8) °, γ = 91.21(3) ° and V = 864.2(5) Å^3 (Fig. 5.1d). Table S5.4 provides the crystallographic data for pyrene-IV at 2.7 GPa and 4.3 GPa. In pyrene-IV, there are two crystallographically different molecules forming two kinds of sandwiches, one consisting of almost flat molecules and another of curved ones.

Strictly speaking, pyrene-IV does not possess the herringbone motif anymore, due to reducing the symmetry down to *P*-1 and lose of the *pgg* symmetry in the projection along the *a*-axis. However, due to the angles β and γ are so close to 90 degrees, it is practically invisible (Fig. 5.1d). So that we can say that compression up to 4.3 GPa doesn’t change much the molecular packing motif viewed along the *a* axis, it still remains sandwich-herringbone-like.

A new polymorph, pyrene-V, was first observed at 7.3 GPa (Fig. 5.1e). It has the same space group as pyrene-I and pyrene-II (space group #14, $P2_1/c$) with the following unit cell parameters at 7.3 GPa: a = 7.450(5) Å, b = 6.4503(12) Å, c = 16.096(2) Å, β = 100.65(3) ° and V = 760.1(5) Å^3. Table S5.5 provides detailed crystallographic data of pyrene-V for six pressure points in the range of 7.3 to 35.5 GPa.

As seen (Fig. 5.1e), the compression leads to the collapse of the sandwich structure in pyrene-V. The crystallographically equivalent molecules are aligned at a very low angle, they are substantially curved and shifted with respect to each other, forming a simple herringbone packing motif. A detailed geometrical analysis of the structures and shapes of molecules in different polymorphs is given in a separate section below.

5.3.2 Compressional behavior of the polymorphs of pyrene

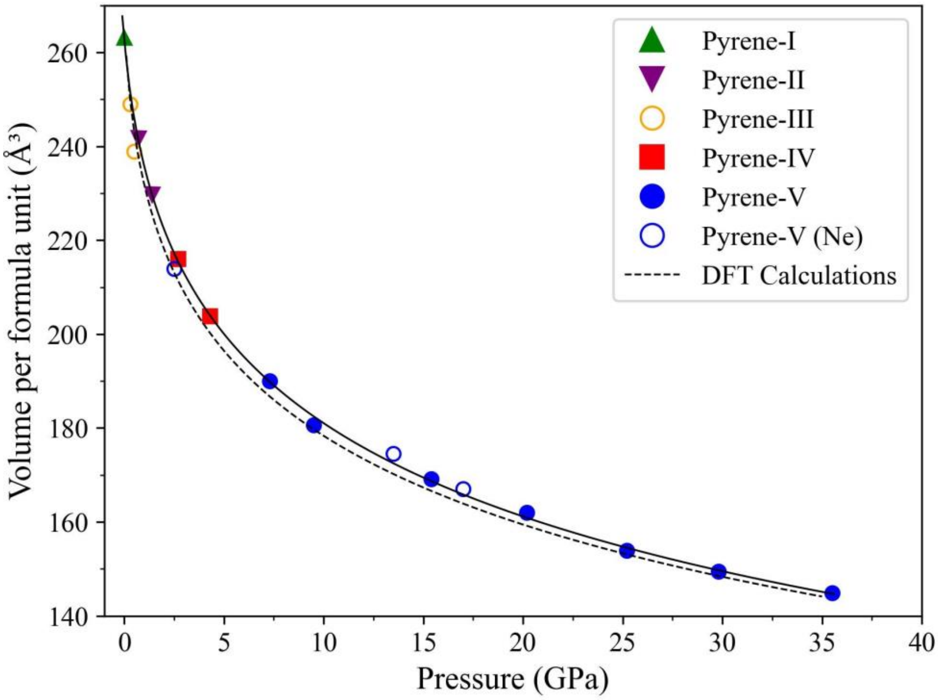

Figure 5.2 Compressional behaviour of the polymorphs of pyrene up to 35.5 GPa. The unit cell volume per formula unit as a function of pressure is presented for pyrene-II (purple solid inversed triangles), pyrene-IV (red solid squares), and pyrene-V (blue solid circles) as found in this work in experiments with He pressure medium. The green solid triangle corresponds to pyrene-I at ambient conditions. The solid black line shows the fit of all pressure-volume experimental points using the third-order Birch-Murnaghan equation of state with the parameters V_0 = 263.8(4) $Å^3$, K_0 = 5.2(2) GPa, and K′ = 10.6(4) (the EoSFit7 software was utilized). Open blue circles correspond to the pressure-volume data for pyrene-V in aNe pressure medium. Open orange circles correspond to the data for pyrene-III from ref. [6]. The dashed line presents the result of the fit of the DFT calculated pressure-volume points for each polymorph in the pressure interval in which these phases were observed experimentally. The fit parameters are as follows: V_0 = 261.0(8) $Å^3$, K_0 = 3.4(2) GPa, and K′ = 15.2(7).

The compressional behavior of the polymorphs of pyrene up to 35.5 GPa is presented in Fig. 5.2. Further pressurization led to the loss of the XRD signal. The values of the unit cell volume per formula unit for pyrene-I at ambient conditions and for pyrene-II, pyrene-IV, and pyrene-V as a function of pressure (in He pressure medium) were obtained from our experiments (Table S5.6). In Fig. 5.2 they are shown by solid symbols of different colors. These pressure-volume data were fitted using the third-order Birch-Murnaghan equation of state (EOS) with the fixed zero-pressure volume V_0 = 263.8 Å^3, which is the volume of pyrene-I at ambient conditions. The bulk modulus, K_0, and it's first derivative, K´, were determined to be 5.2(2) GPa and 10.6(4) (Figs. 5.2, 5.3) using EoSFIT7 software [15] (Angel *et al.*, 2014). The pressure-volume point for pyrene-V in Ne pressure medium, like also those for pyrene-III from ref. [6] (Fabbiani, 2006), were not included in the fit, although they are shown in the figure.

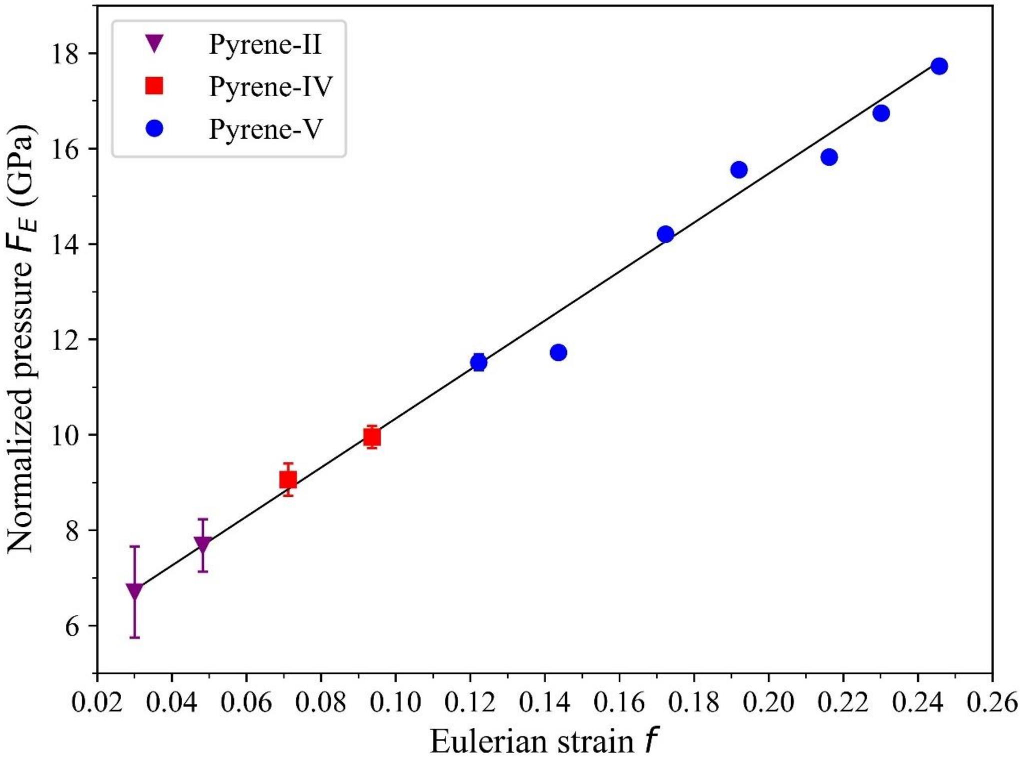

Figure 5.3 The Eulerian strain - normalized pressure (*f*-*F*) plot of the experimental data. In our experimental data, pyrene-II is depicted by purple inverted solid triangles, pyrene-IV is denoted by red squares, and pyrene-V are represented by blue solid circles. The solid line represents the linear fit.

The density functional theory (DFT) calculated pressure-volume points for each polymorph (Table S5.7) in the pressure interval, in which these phases were observed experimentally, have also been fitted using the third-order Birch-Murnaghan EOS. The EOS parameters appeared to be as follows: V_0 = 261.0(8) Å^3, K_0 = 3.4(2) GPa, and K´ = 15.2(7). They agree well with the EOS parameters obtained from the experimental data (Fig. 5.2).

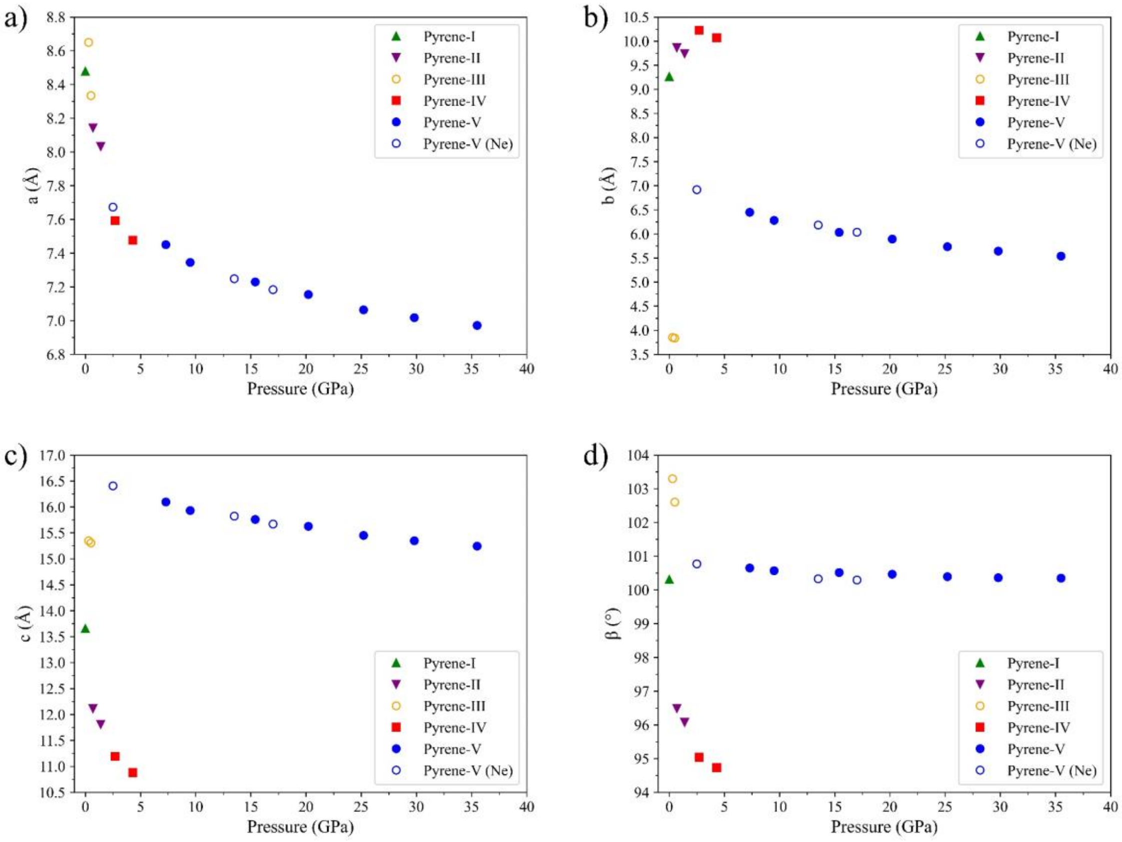

Figure 5.4 The dependence of the lattice parameters of pyrene polymorphs on pressure. a) *a*; b) *b*; c) *c*; d) *β*. Solid symbols correspond to the data points for the samples measured in He pressure transmitting medium: pyrene-I (green triangles), pyrene-II (purple inversed triangles), pyrene-IV (red squares), and pyrene-V (blue circles). Open blue circles are for pyrene-V in Ne pressure medium. Open orange circles correspond to the data for pyrene-III from ref. [6]. The pyrene-I-to- pyrene-II transition manifests in increase of the *b* parameter and decrease of the *β* angle; for the pyrene-II-to-pyrene-IV transition -in the decrease of the symmetry and increase of the *b* parameter; and for the pyrene-IV-to- pyrene-V – in the increase of the symmetry and the abrupt decrease of the *b* parameter and increase of the *β* angle.

The dependence of the lattice parameters of pyrene polymorphs on pressure is shown in Fig. 5.4 (see Table S5.8 for numerical values). In each polymorph, all parameters gradually decrease in response to pressurization. Phase transitions are manifested by abrupt changes in particular parameters. Whereas the *a* parameter always shortens (Fig. 5.4a), the value of b (Fig. 5.4b) increases upon the transition from pyrene-I to pyrene-II and from pyrene-II to pyrene-IV, but sharply decreases upon the transition from pyrene-IV to pyrene-V. The value of the c parameter (Fig. 5.4c) decreases upon the transition from pyrene-I to pyrene-II and from pyrene-II to pyrene-IV, but sharply increases (from 10.9 Å to 16.1 Å) upon the transition from pyrene-IV to pyrene-V. The variation in the β angle (Fig. 5.4d) shows a decrease from 100.3° in pyrene-I to 96.5° in pyrene-II, further reducing to 95.0° in pyrene-IV, and then increasing to the value of 100.7° in pyrene-V, similar to that in pyrene-I. Although the pressure-volume points of pyrene-III [6] (Fabbiani, 2006) fit the pressure-volume curve of other polymorphs (Fig. 5.2), the unit cell parameters of pyrene-III are quite different from those of pyrene-I and pyrene-II.

To summarize, we could describe the P-V behaviour for all pyrene polymorphs by a common continuous EOS, but in fact, the volume may change continuously with pressure, while other structural parameters abruptly change manifesting solid state transitions (Figs. 5.2 and 5.4).

5.3.3 Theoretical Calculations

The relaxed structural parameters of pyrene-I at ambient, pyrene-II at 1 GPa, pyrene-III at 1 GPa, pyrene-IV at 3 GPa and pyrene-V at 9 GPa are provided in Tables S5.9-13. The calculated unit cell volumes are slightly smaller than the experimental ones, likely due to the impact of temperature (0 K) on the results of calculations.

The enthalpy differences (ΔH) for the four polymorphs (pyrene-II, pyrene-III, pyrene-IV, and pyrene-V) relative to pyrene-I were calculated as a function of pressure up to 5 GPa at 0 K (Table S5.14, Fig. 5.5), as described in the Methods section. The calculations suggest that up to 2.07 GPa pyrene-II is relatively more stable than pyrene-IV and pyrene-V. We observed its formation at 0.7 and 1.4 GPa in our room temperature experiment that agrees with the calculations. Above 2.07 GPa pyrene-V is predicted to be more stable than other polymorphs except pyrene-III. This does not contradict to our observations, as we detected pyrene-V formation at 7.3 GPa at the pressure step from 4.3 GPa. It is known that formation of metastable phases is very sensitive to many parameters like stress, for example, which cannot be fully controlled in a DAC experiment, as we have shown previously in our work on high pressure phases of silica [16] (Bykova *et al.*, 2018).

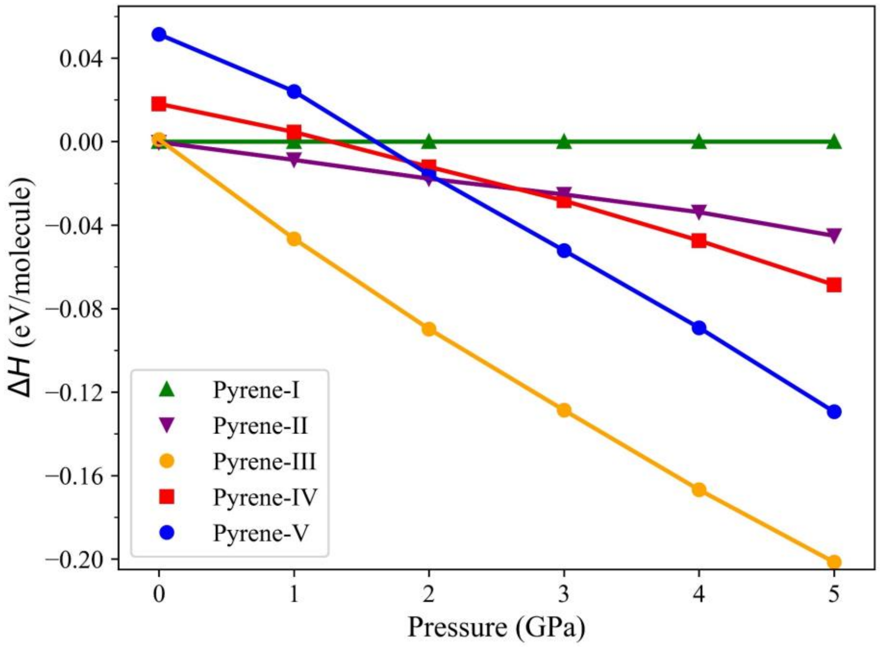

Figure 5.5 The enthalpy difference (*ΔH*) calculated for the four polymorphs (pyrene-II, pyrene-III, pyrene-IV, and pyrene-V) relative to pyrene-I as a function of pressure. All calculations were performed at 0 K. The data for different polymorphs are shown as follows: pyrene-I (green triangles); pyrene-II (purple inversed triangles), pyrene-III (orange circles), pyrene-IV (red squares), and pyrene-V (blue circles). Up to 2.07 GPa, pyrene-II is relatively more stable than pyrene-IV and pyrene-V, whereas above this pressure, pyrene-V is relatively more stable. Above 0.03 GPa and up to 5 GPa, pyrene-III appears to be the thermodynamically stable phase if compared to all other polymorphs.

As seen in Fig. 5.5, above 0.03 GPa and up to 5 GPa, pyrene-III appears to be the thermodynamically stable phase if compared to all other polymorphs. In our room temperature experiments, we did not observe pyrene-III described in the study of Fabbiani *et al.* (2006) [6], where it was synthesized through the recrystallisation from a 0.5 M solution of pyrene in dichloromethane after several temperature-annealing cycles (slow cooling and heating between 303 K and 293 K) at 0.3 GPa. This work and our computational result motivated us to conduct a high-pressure high-temperature experiment. This experiment was designed as described below.

A sample of pyrene-I was loaded into a DAC along with KCl as a pressure transmitting medium (DAC #4). The whole DAC (first pressurized to 4 GPa) was heated for two hours in an oven at 473 K. After heating pressure raised to 6.5 GPa and at this pressure the sample was investigated at the ID15B beamline at the ESRF (λ= 0.4100 Å). Dioptas program [17]

(Prescher *et al.*, 2015) and Jana2006 program [18] (Petříček *et al.*, 2014) were used for the data processing. The EOS of KCl was adopted from [19] (Dewaele *et al.*, 2012). The diffraction pattern of the sample featured SC-XRD reflections of two pyrene polymorphs (pyrene-III and pyrene IV) and continuous diffraction lines of the KCl pressure medium (Fig. 5.6). This observation suggests that pyrene-III is likely a thermodynamically stable phase at pressures above 0.3 GPa, whose synthesis requires heating to overcome the energy barrier.

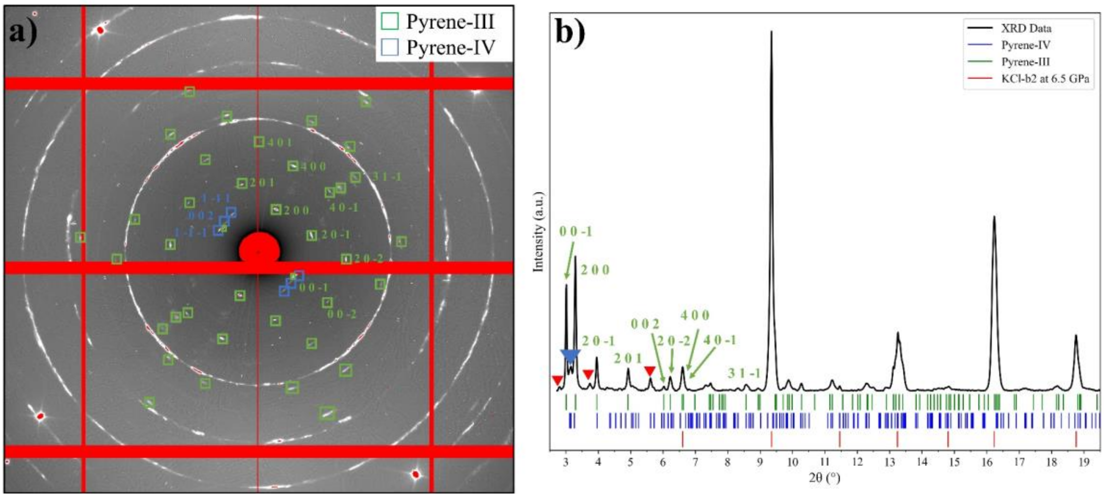

Figure 5.6 The XRD pattern obtained from a sample of pyrene in a KCl pressure medium at 6.5 GPa and room temperature after it was heated at 473 K for 20 min. a) A 2D XRD pattern resulted from merging individual frames obtained upon an omega scan (+- 34° degrees with a step of 0.5°) using the Dioptas program [17]. The diffraction spots from pyrene-III are highlighted by green boxes and those from pyrene-IV - by blue boxes. Continuous white circles are from KCl. b) Integrated X-ray diffraction pattern (λ=0.410 Å). Green ticks correspond to the positions of diffraction lines of pyrene-III at 6.5 GPa (a = 14.596(5) Å, b = 3.463(3) Å, c = 7.981(3) Å, β = 102.39(3) °, and V = 394.0(7) Å^3, lattice parameters refinement was performed using the Jana2006 program [18]); blue ticks – those of pyrene-IV (a = 7.467(6) Å, b = 10.057(6) Å, c = 10.865(7) Å, α = 92.43 °, β = 94.73 °, γ = 90.86 ° and V = 812.2(15) Å^3, all angles are fixed at the values of pyrene-IV at 4.3 GPa in this work); red ticks – those of B2-KCl [19] at 6.5 GPa. The peak marked with a blue solid inversed triangle results from overlapping of 002, 1-1-1, and 1-11 reflections of pyrene-IV. The peaks marked with red triangles are from non-identified spots.

Upon compression at room temperature, the visual appearance of the pyrene crystals changes: from colorless and transparent they become orange and eventually black (Fig. 5.7). Calculations of the electronic density of states (eDOS) for pyrene-I at 1 bar and 0 K and pyrene-V at 50 GPa and 0 K (Fig. 5.8) have shown that the band gap decreases from 3.3 eV to 0.9 eV. This explains the observed color change of the crystals.

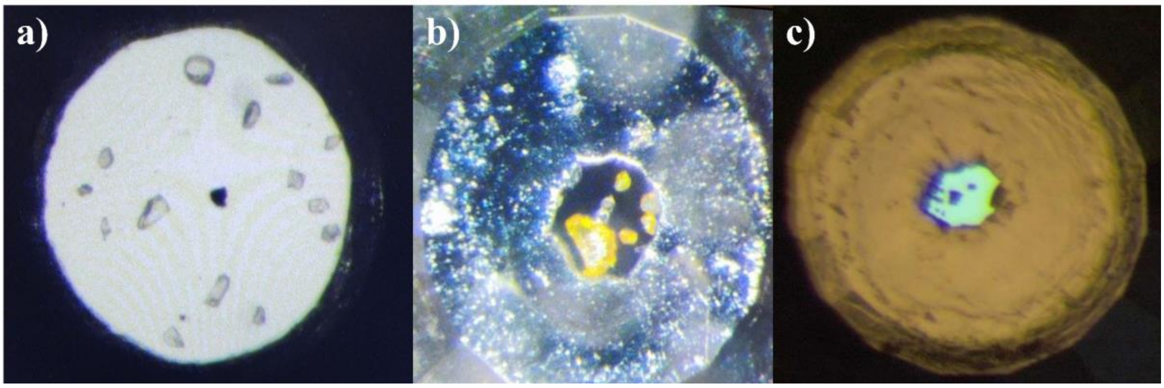

Figure 5.7 Images of pyrene crystals in DACs taken under an optical microscope at different pressures. a) numerous colorless transparent crystals of pyrene-I at ambient pressure (DAC#1), black triangular feature is due to a piece of tungsten used for the cell alignment in the X-ray beam); b) light orange crystals of pyrene-V at 2.5 GPa (DAC#2); c) non-transparent dark crystals of pyrene-V at ~35 GPa (DAC#3). The average size of the crystals is of about 10 μm.

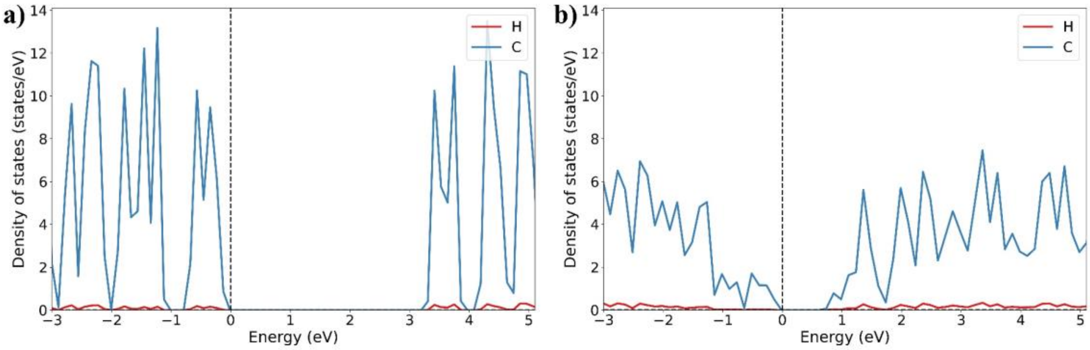

Figure 5.8 Electronic densities of states of pyrene polymorphs. a) pyrene-I at 1 bar; b) pyrene-V at 50 GPa. The partial density of states projected onto the C atoms is shown by blue curves, H atoms is shown by red curves and the Fermi energies - by the vertical dashed lines. The band gap of pyrene-I is 3.3 eV at ambient conditions and the band gap of pyrene-V is 0.9 eV at 50 GPa.

5.3.4 Geometrical analysis of the structures of the pyrene polymorphs

In order to accurately calculate the distances between pyrene molecules in pairs (sandwiches), pyrene molecules were approximated by mean molecular planes through performing planar fitting for 16 carbon atoms of pyrene molecules in each polymorph (Fig. 5.9) using the NumPy and SciPy libraries in Python. Blue lines in Fig. 5.9 highlight the mean molecular planes; the intermolecular distances (d) and interplanar angles (δ), which were determined using the same software, are designated. In Fig. 5.9 the structures of pyrene-I, II, IV are shown along the [4 0 1] direction (Fig. 5.9a, b, c), and that of pyrene-V in the [5 0 2] direction (Fig. 5.9d). The selection of these two specific orientations enables the best view of the topology of the molecular structures of the different polymorphs.

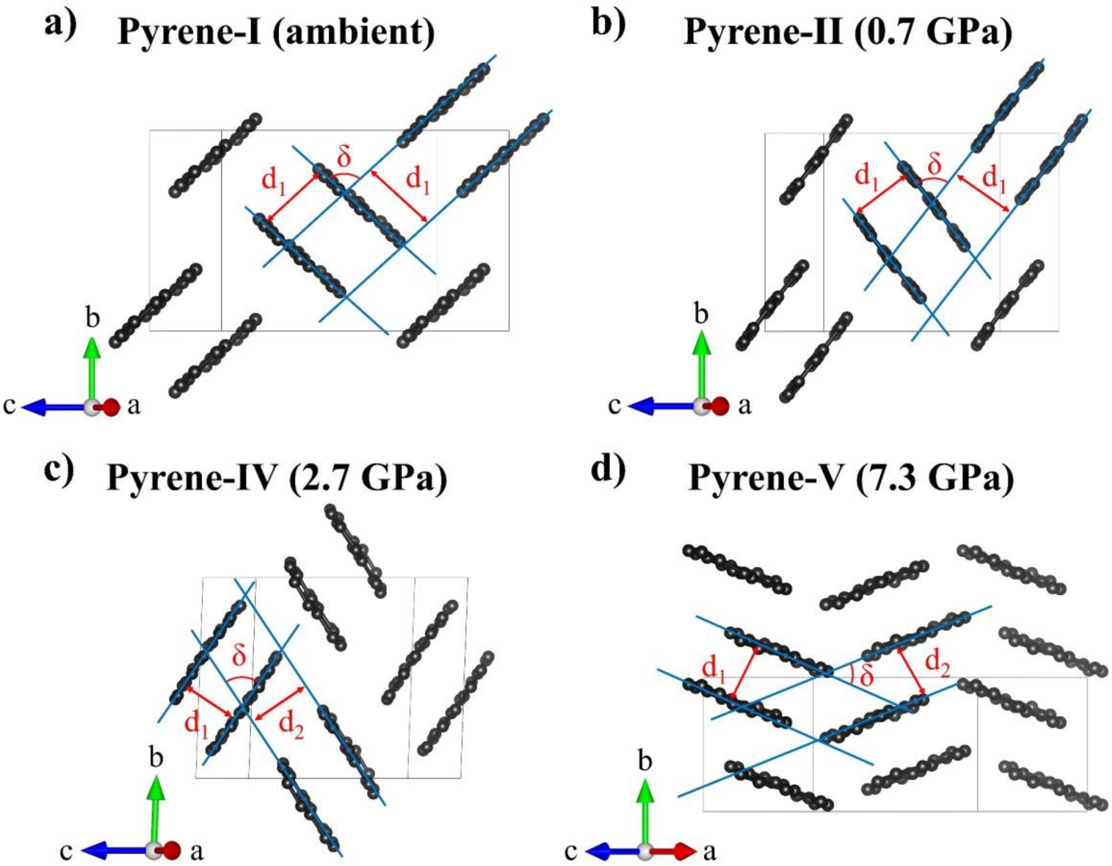

Figure 5.9 Visualization of intermolecular distances and interplanar angles in the structures of pyrene polymorphs. (a) Pyrene-I, (b) pyrene-II and (c) pyrene-IV, as viewed along the [4 0 1] direction, and (d) pyrene-V as viewed along the [5 0 2] direction. The blue lines represent the mean molecular planes determined on positions of carbon atoms in the molecules; d_1 and d_2 are the interplanar distances; δ is the interplanar angle. In pyrene-IV $d_1 < d_2$; in pyrene-V $d_1 > d_2$. C atoms are black. Hydrogen atoms are not shown.

Intermolecular distances and interplanar angles in pyrene polymorphs from experiments in the helium pressure medium are listed in Table S5.15 (for graphical representation of their pressure dependences see Fig. 5.10). As seen, the phase transitions from pyrene-I to pyrene-II and then to pyrene-IV result in the formation of more compact structures (with similar sandwich-herringbone molecular packing) due to a general shortening of intermolecular distances and decrease of interplanar angles (from 83.6 to 75.4, and 66.7 degrees in pyrene-I, pyrene-II, and pyrene-IV, respectively) (Table S5.15, Fig. 5.10), as well as due to a mutual shift of the molecules in sandwiches (Fig. 5.9). In pyrene-IV such compaction eventually leads to reduction of the symmetry to *P*-1, and the appearance of two crystallographically distinct molecules forming pairs with different intermolecular distances ($d_1 < d_2$, Figs. 5.9c, 5.10a). Such a "tension" in the structure of pyrene-IV is "released" in pyrene-V, which, like pyrene-I and pyrene-II, features crystallographically equivalent molecules. The latter, however, do not form pairs anymore, but shift with respect to each other and tightly align along the *c* direction (Fig. 5.1e) upon a drastic decrease of the δ angle down to 44.9° (Figs. 5.9d, 5.10b) that leads to the collapse of the sandwich structure. The symmetry of pyrene-V, compared to that of pyrene-IV, increases to $P2_1/c$. Interestingly, although twisted molecules in organic solids at ambient conditions are known (see for example, McKinnon *et al.* (2004) [20]), to the best of our knowledge, the phenomenon of the increase of the curvature upon gradual compression is reported here for the first time.

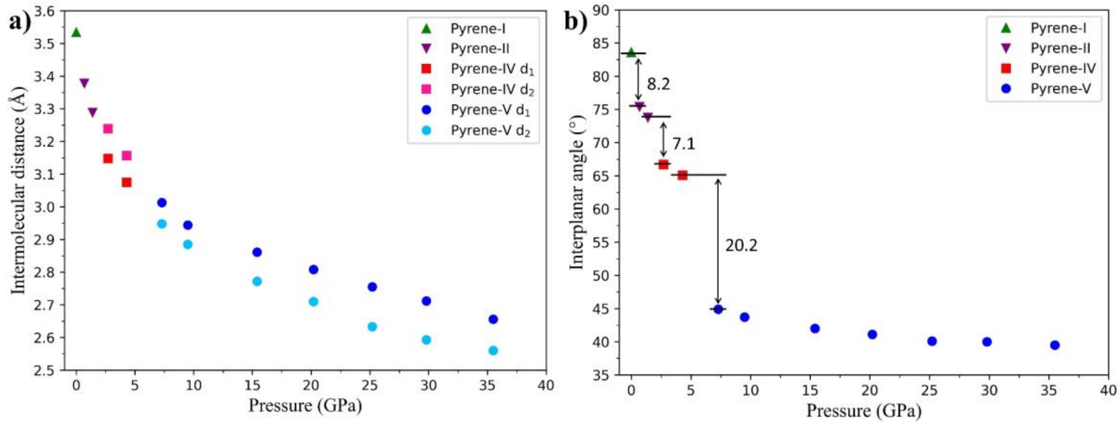

Figure 5.10 Variation of intermolecular distances and interplanar angles in pyrene polymorphs with pressure. a) Intermolecular distances see (Fig. 5 for d_1 and d_2); b) interplanar angles (see Fig. 5 for δ). Only the data obtained from pyrene in He pressure medium are presented.

Due to all molecules in pyrene-V being curved, there are two types of contacts between the molecules: each molecule has in its proximity both a convex and a concave neighbor at the distances of d_1 and d_2, respectively, so that $d_1 > d_2$. Such a geometrical arrangement results in a sharp raising of the *c* parameter (from 10.9 Å in pyrene-IV to 16.0 Å in pyrene-V) (Table S5.8, Fig. 5.4c) and a decrease of the *b* parameter (from 10.1 Å to 6.5 Å) (Fig. 5.4b), accompanied by a considerable expansion of the β angle to 100.5 degrees (Table S5.8, Figs. 5.4d, 5.9d) of the unit cell of pyrene-V.

To visualize changes in the curvature of the pyrene molecules under increasing pressure, we performed curved surface fitting using the NumPy and SciPy libraries in Python. We set the normal vector to the mean molecular plane described above. The height of the curved molecular surface, represented by the projection of each point on the normal axis, directly reflects the degree of curvature and the shape of the surface.

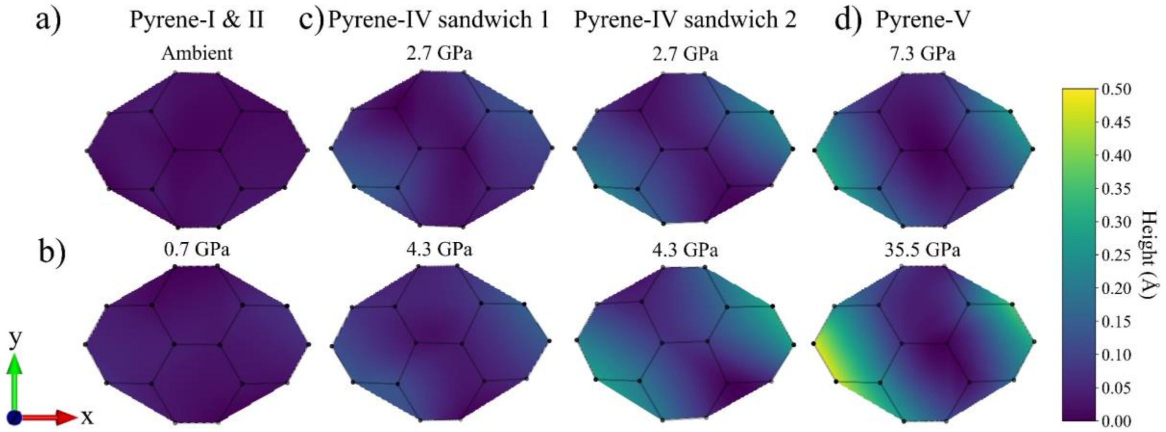

Figure 5.11 Curved surface plots for pyrene molecules in different polymorphs at selected pressures. a) Pyrene-I at ambient pressure; b) pyrene-II at 0.7 GPa; c) pyrene-IV at 2.7 GPa and 4.3 GPa with sandwich 1 and sandwich 2; d) pyrene-V at 7.3 and 35.5 GPa. The curved surface plots visualize the distribution of surface height variations, represented as the difference between the height at any given point on the surface and the minimum height of the surface. The range of height differences spans from 0 Å to 0.5 Å, with a corresponding color gradient ranging from purple to yellow (the color scale is given to the right of the figures). The plots were produced using matplotlib and NumPy libraries in python. C atoms are black spots.

The obtained curved surface plots (Fig. 5.11) visualize the distribution of surface height variations, represented as the difference between the height at any given point on the surface and the 0 Å (minimum) height of the surface. The range of height differences spans from 0 Å to 0.5 Å, with a corresponding color gradient ranging from purple to yellow. Fig. 5.12a shows the pressure dependence of the maximal surface height difference for all studied polymorphs.

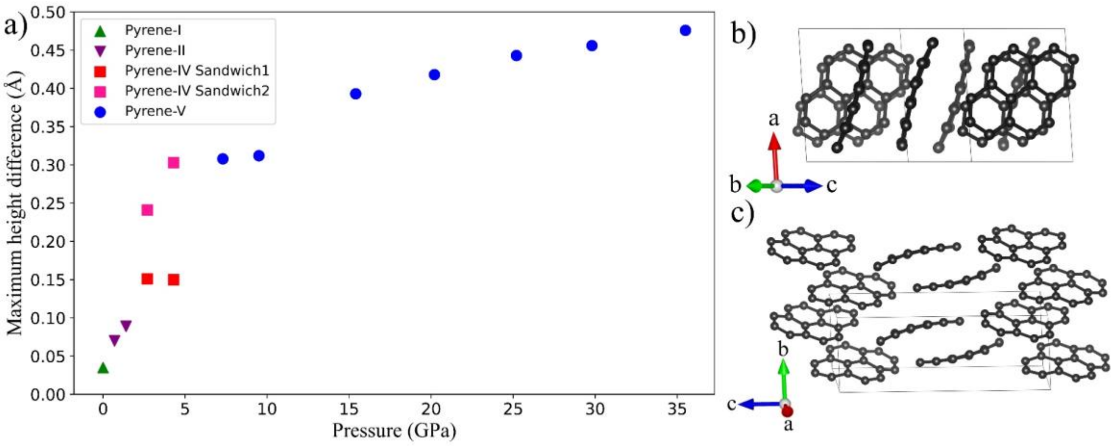

Figure 5.12 Scatter plot of the maximum surface height difference and crystal structures of pyrene-IV at 4.3 GPa and pyrene-V at 35.5 GPa. a) The pressure dependence of the maximal surface height difference for all studied polymorphs; b) the structure of pyrene-IV viewed along the [0 13 8] direction; c) the structure of pyrene-V viewed along the [31 10 1] direction. C atoms are black, H atoms are not shown.

As seen in Fig. 5.11a, b, molecules of pyrene-I and pyrene-II are flat. The molecules of pyrene-IV are different and form two kinds of sandwiches (Fig. 5.11c): sandwich 1 consists of almost flat molecules, whereas sandwich 2 consists of concave molecules. Their curvature is well seen in the [0 13 8] projection (Fig. 5.12b). Pyrene-V contains only curved molecules, whose curvature increases with pressure and is well seen in the [31 10 1] projection (Fig. 5.12c). The two concave molecules which formed sandwiches in pyrene-IV can still be recognized in pyrene-V, but they have a much larger offset with respect to each other.

5.3.5 Exploring intermolecular interactions using Hirshfeld surfaces and fingerprint plots

For visualizing and exploring intermolecular interactions in molecular crystals one uses Hirshfeld surfaces and fingerprint plots. This tool is described in detail in a comprehensive review by McKinnon *et al.* (2004) [20]. The molecular Hirshfeld surface envelops the molecule and defines the volume of space where the promolecule electron density exceeds that from all neighboring molecules [21,22] (Spackman *et al.*, 1997; Spackman & Jayatilaka, 2009). The Hirshfeld surface itself is defined by the molecule and the proximity of its nearest neighbors, and hence encodes information about intermolecular interactions.

The fingerprint plot represents in a 2D format two different but useful distance measures, the distances from the internal or external atoms (d_i or d_e) to the Hirshfeld surface. Thus, the fingerprint plots are highly sensitive to the immediate environment of the molecule [22] (Spackman & Jayatilaka, 2009). They are unique for a given molecule in a particular polymorphic form.

We used the CrystalExplorer program [23] (Spackman, 2021) to construct Hirshfeld surfaces, mapped with shape index, curvedness, and d_e (for details of various functions of distance and curvature mapped on Hirshfeld surfaces see Spackman and Jayatilaka (2009) [22]), as well as fingerprint plots for all pyrene polymorphs studied here. They are presented in Figs. 5.13-15. The fingerprint plots highlighting particular intermolecular contacts and interactions for crystallographically distinct molecules of all polymorphs are shown in Supplementary Figs. 5.1, 5.2. These two figures are described in detail in Supplementary Note 1.

Fig. 5.13a shows the crystal-packing diagram for molecules in pyrene-I. In pyrene-I, considering its sandwich herringbone structure, one side of each molecule in a pair is dominated by $\pi \cdots \pi$ stacking interactions (back side, turned to the other molecule in the pair), whereas the other (front) side is dominated by C-H$\cdots\pi$ contacts. The head-to-head H $\cdots$ H contacts of about 2 Å are very short [20] (McKinnon *et al.*, 2004). The Hirshfeld surfaces of the molecule in pyrene-I, as viewed from the front side (upper row) and back side (bottom row), are shown in Fig. 5.13b. The alternating red and blue triangles in the back view of the Hirshfeld surface mapped with shape index indicate $\pi\cdots\pi$ stacking interactions that are characteristic of graphite-like layered packing [20] (McKinnon *et al.*, 2004). The two molecules in the pair pack in offset. The blue color indicates convex curvatures. The large, red-colored regions of conclave curvature on the other side (front view) reflect the C—H$\cdots\pi$ interactions between pyrene molecules.

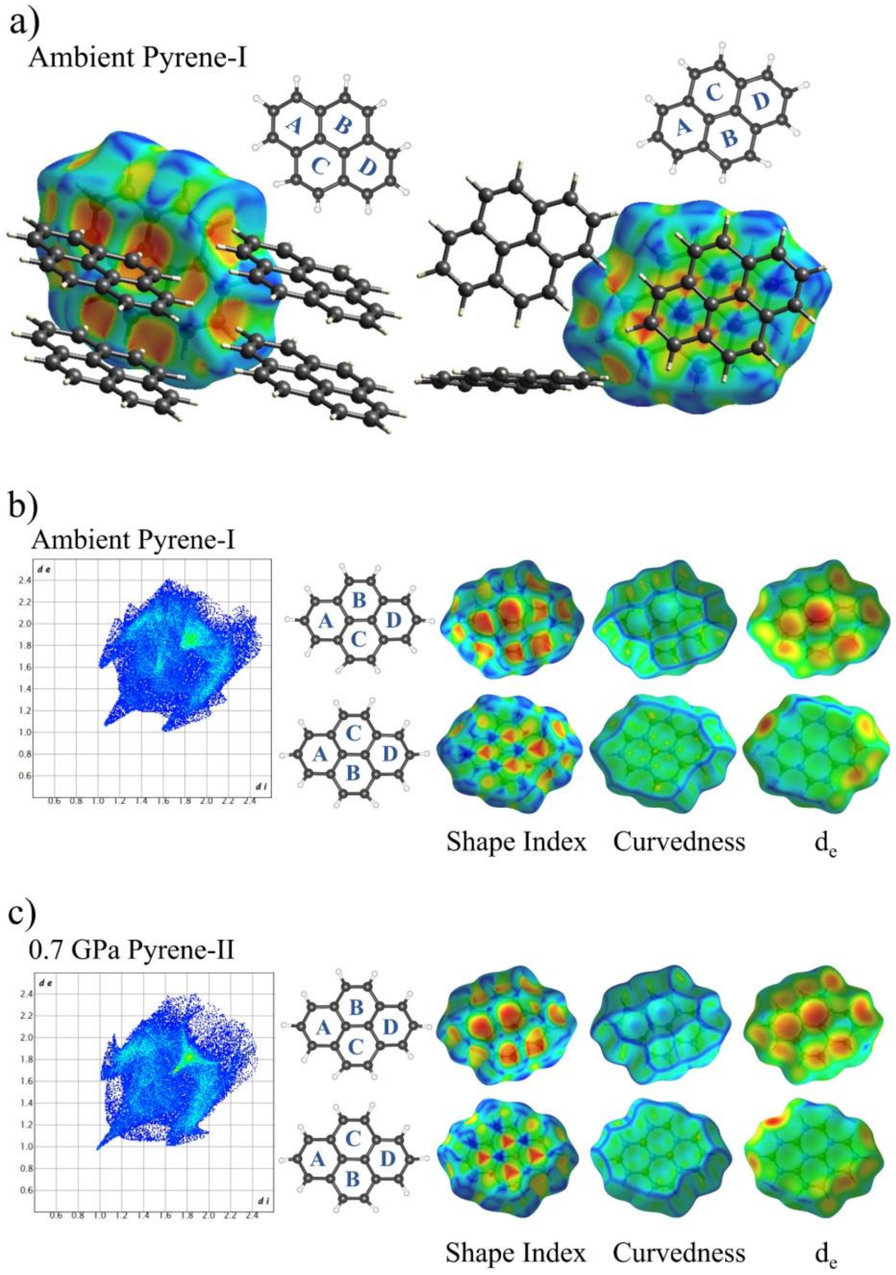

Figure 5.13 Fingerprint plot and Hirshfeld surfaces for pyrene-I at ambient and pyrene-II at 0.7GPa. a) Crystal-packing diagram in the front and back views of pyrene-I molecule at ambient, with the Hirshfeld surface of the central molecule mapped with shape index; Fingerprint plot and the front and back views of Hirshfeld surface for pyrene-I molecule at ambient (b) and pyrene-II molecule at 0.7 GPa (c), mapped with shape index, curvedness and d_e. The front view depicts the arrangement of the four carbon rings as ABCD, while the back view shows ACBD. Shape index is mapped from -1.0 (red) to 0.0 (green) to 1.0 (blue). Curvedness is mapped from -4.0 (red) to 0.0 (green) to 1.0 (blue). Distance external to the surface, d_e, is mapped over the range 1.0 (red) to 1.75 (green) to 2.5 (blue) Å. In Fingerprint plot, blue corresponds to the low frequency of occurrence of a (d_i, d_e) pair, while red points indicate the high frequency of the surface points with that (d_i, d_e) combination.

The π ··· π stacking motif is manifested in the two-dimensional fingerprint plot as a green triangular shaped region with the minimal $d_e \approx d_i$ at ~ 1.75 Å (Fig.5.13b, left), which is consistent with the previously mentioned interplanar distance of ~3.5 Å between the two molecules in a pair (Table S5.15). In pyrene-II at 0.7 GPa (Fig. 5.13c, left), due to compression, the corresponding $d_e \approx d_i$ point in the fingerprint plot is at ~ 1.65 Å that implies the decrease of the intermolecular distance in pyrene-II down to ~3.4 Å. The two pairs of wings represent two distinct main C-H ··· π (donor and acceptor) interactions. A sharp feature in the lower left corner of the fingerprint plot is a manifestation of a short head-to-head H ··· H contact. With the pressure increase (Fig. 5.13c), the two pairs of wings in the fingerprint plot of pyrene-II representing the main C-H ··· π interactions overlap, suggesting them to become less distinct with pressure.

Hirshfeld surfaces and fingerprint plots of pyrene-I at ambient conditions have been previously discussed by McKinnon *et al.* (2004) [20], and those of pyrene-I (with reference to the ambient-pressure structure at 113 K) and pyrene-II (with reference to the ambient-pressure structure at 93 K) by Fabbiani *et al.* (2006) [6]. Our observations are in accordance with the literature data.

Triclinic pyrene-IV possesses two crystallographically distinct molecules. Those in sandwich-1 (Fig. 5.14a), still almost flat, feature some asymmetry in the fingerprint plot clearly seen in its “wings” (Fig. S5.2), but preserve head-to-head H ··· H contacts. In sandwich-2 (Fig. 5.14b), the alternating red and blue triangles in the Hirshfeld surface mapped with shape index indicate graphite-like stacking, whereas that mapped with curvedness shows the decrease of the flat contact area on the back side reflecting a substantial curvature of the molecules. The two main C-H ··· π interactions mapped with d_e show their pronounced difference both in the back and front sides if compared with sandwich-1. In addition, the tip in the lower left corner of the fingerprint plot disappears in sandwich-2, indicating that there is no longer a short head-to-head H ··· H contact between the molecules.

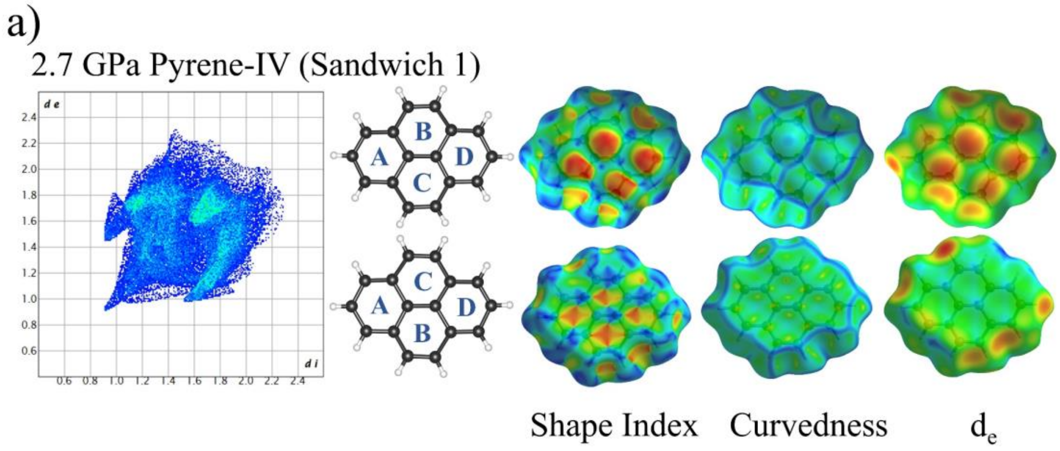
a)

2.7 GPa Pyrene-IV (Sandwich 1)

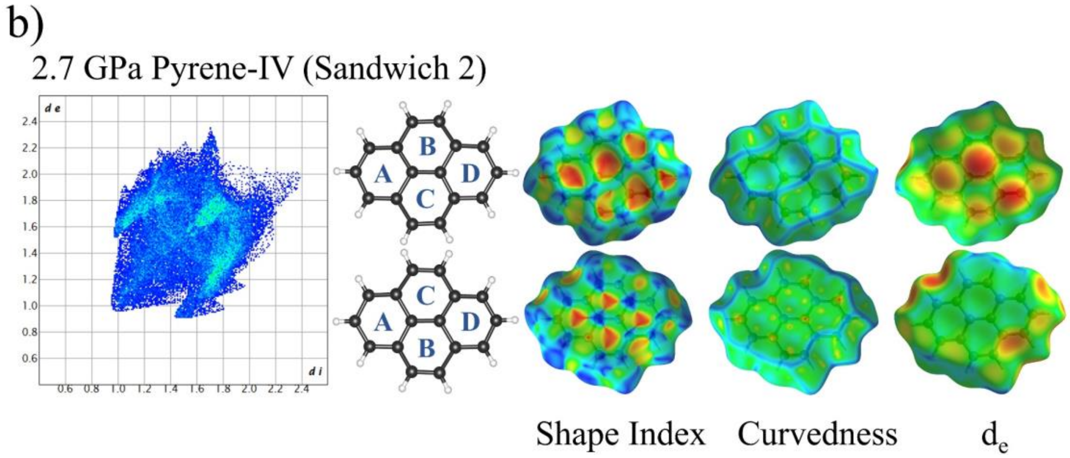
b)

2.7 GPa Pyrene-IV (Sandwich 2)

Figure 5.14 Fingerprint plot and Hirshfeld surfaces for pyrene-IV at 2.7GPa. Fingerprint plot and the front and back views of Hirshfeld surface for pyrene-IV sandwich1 molecule (a) and pyrene-IV sandwich2 molecule (b) at 2.7 GPa, mapped with shape index, curvedness and d_e. Distance external to the surface, d_e, is mapped over the range 0.9 (red) to 1.6 (green) to 2.3 (blue) Å.

In pyrene-V, the molecules are stacked in a simple herringbone motif that immediately reflects in the fingerprint plot and the Hirshfeld surfaces (Figs. 5.15, S5.2e, f). The $\pi \cdots \pi$ stacking interactions, manifesting as the alternating red and blue triangles in the Hirshfeld surface mapped with shape index [20] (McKinnon *et al.*, 2004), appear now on both back and front sides. Although crystallographically equivalent molecules in pyrene-V are related by an inversion centre, they do not form sandwiches. At 35.5 GPa, the size of the area of the fingerprint plot reduces considerably and the wings on both sides almost disappeared, suggesting a high density of molecular stacking (Fig. 5.15b). The regularity in the distribution of blue and red triangles in both front and back sides of the Hirschfeld surface (shape index) is lost, indicating a considerable departure from graphite-like stacking due to a large curvature of molecules.

a)
7.3 GPa Pyrene-V

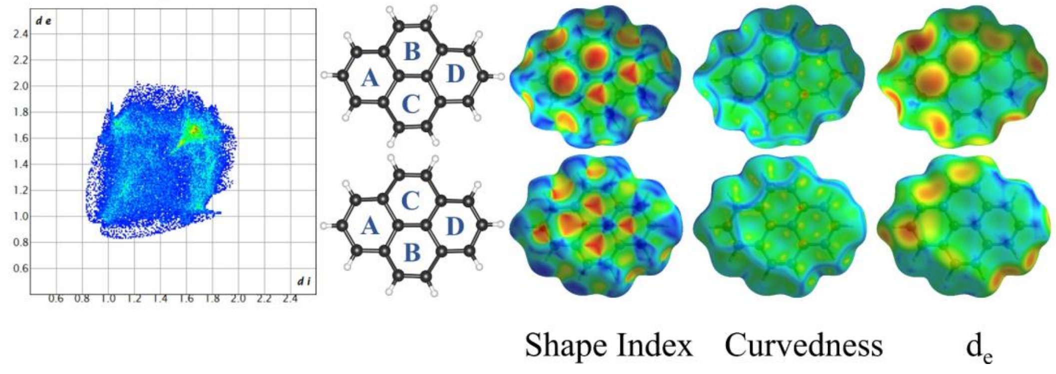

b)
35.5 GPa Pyrene-V

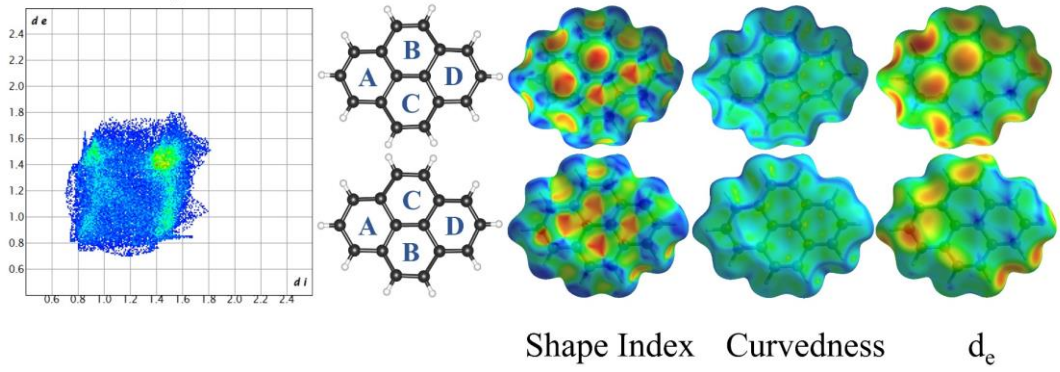

Figure 5.15 Fingerprint plot and Hirshfeld surfaces for pyrene-V at 7.3 GPa and 35.5 GPa. Fingerprint plot and the front and back views of Hirshfeld surface for pyrene-V molecule at 7.3 GPa (a) and 35.5 GPa (b), mapped with shape index, curvedness and d_e. Distance external to the surface, d_e, is mapped over the range 0.8 (red) to 1.5 (green) to 2.1 (blue) Å for pyrene-V molecule at 7.3 GPa and from 0.7 (red) to 1.3 (green) to 1.8 (blue) Å at 35.5 GPa.

For comparison with other polymorphs, we built fingerprint plots of pyrene-III at 0.3 GPa using the structure data from Fabbiani *et al.* (2006) [6] (Fig. S5.2g), as we did not have our own structural data for pyrene-III of sufficient quality. Interestingly, the fingerprint plot of pyrene-III (Fig. S5.2g) appeared to be substantially different from those of other polymorphs. However, the absence of head-to-head H ⋯ H contacts and large contribution of π ⋯ π interactions in the molecular bonding may be counted as similarities of pyrene-III and pyrene-V, sharing a common herringbone structural motif. A general glance at the evolution of Hirshfeld surfaces and fingerprint plots of metastable pyrene polymorphs allow to deduce that the change in molecular interactions under pressure is continuous and the dominating interactions are common for polymorphs with similar stacking motifs.

To summarize, our study represents a significant progress in high-pressure structural investigations of polycyclic aromatic hydrocarbons (PAHs) using single-crystal X-ray diffraction, which were previously limited to very low pressures of around 2 GPa (naphthalene was studied up to 2.1 GPa by Fabbiani *et al.* (2006) [6]. Here, the behavior of pyrene was studied under compression up to 35.5 GPa using synchrotron single-crystal X-ray diffraction in a diamond anvil cell with helium as a soft quasi-hydrostatic pressure transmitting medium. Previous structural investigations of pyrene were conducted on single crystals recrystallized from solution in dichloromethane under pressure, which are limited by the freezing pressure of dichloromethane of 1.33 GPa, leading to the deterioration of the single crystal [6] (Fabbiani *et al.*, 2006). Higher pressures in structural investigations of PAHs have never been explored before, because it was anticipated that large molecules have low conformational flexibility under pressure and the experience with direct compression of organic compounds with larger molecules showed this method to be ineffective [6] (Fabbiani *et al.*, 2006).

In our study it was found that at 0.7 GPa, pyrene-I transforms to metastable pyrene-II, whose structure under high pressure at room temperature is reported here for the first time. It is in good agreement with previous low temperature - ambient pressure data [8-10] (Jones *et al.*, 1978; Knight *et al.*,1996; Frampton *et al.*, 2000). Two other transformations to previously unknown metastable polymorphs, pyrene IV and pyrene V, were observed at 2.7 and 7.3 GPa, respectively. Pyrene-V was preserved in He pressure medium up to ~35 GPa due to fully unexpected structure compaction accompanied by considerable deformation of molecules and their alignment along the crystallographic *c*-axis, enabling avoiding direct H-H contacts. Our experiments reveal that gradual compression results in continuous compaction of molecular packing, eventually leading to curvature of molecules, which has never been observed before under pressure, although twisted organic molecules are known, for example, in diperinaphthyleneanthracene (NAPANT01), whose Hirshfeld surface reflects the significant twist in the molecular structure caused by repulsion between H atoms [20] (McKinnon *et al.*, 2004).

Upon compression, the molecules packing motif changed from sandwich-herringbone, distinctive for pyrene-I, pyrene-II, and pyrene-IV, to simple herringbone in pyrene-V.

Interestingly, the herringbone motif is characteristic for the structure of both low-pressure pyrene-III and high-pressure pyrene-V, whose molecules are drastically different in shape – they are flat in the former and substantially curved in the latter. Extending the pressure range of structural studies of an organic material to over 35 GPa enabled to demonstrate that compression of crystals of organic materials in a quasi-hydrostatic medium can lead to the formation of numerous unexpected metastable polymorphs.

To conclude, our experimental study contributes to the fundamental understanding of the polymorphism of polycyclic aromatic hydrocarbons, their behavior under none-ambient conditions, and the evolution of chemical bonding affecting the structure-property relationships of compounds of the important class of organic materials.

Our results highlight the need for a deeper understanding of the observed phases and phenomena using theoretical methods. This is particularly important given the proven potential of high-pressure techniques to alter material properties, as has been successfully demonstrated and exploited in the synthesis of inorganic materials like superhard diamond and cubic boron nitride. Our study indicates that similar potential exists for organic materials. Therefore, further research, including computational studies, aimed at exploring the capabilities of high pressure for synthesizing organic materials with unique properties, is highly warranted and timely.

5.4 Methods

5.4.1 Sample preparation

A crystalline powder of pyrene ($C_{16}H_{10}$) of 99.9 % purity was purchased from Merck. Single crystals were selected under an optical microscope and preselected for high-pressure XRD studies in DAC #1 at ambient pressure (see Table S5.1 for the summary of all experiments). The preselected crystals, averaging about 10 μm in size, and pieces of ruby, approximately 15 μm in size, were loaded in DACs equipped with diamonds with the culets size of 250 μm and a rhenium gasket with a thickness of 40 μm and a hole of ~120 μm in diameter. In all experiments, a gold micrograin was placed inside the center of pressure chamber along with the sample to facilitate locating the center of rotation. As a pressure transmitting medium, neon (Ne) or helium (He) were used. The DACs, BX90-type [24] (Kantor, *et al.*, 2012) (DAC #2) or membrane-type (DAC #3), were gradually pressurized to 17 GPa and to 35 GPa, respectively.

5.4.2 Single-crystal XRD

The SC-XRD studies at room temperature were carried out in DAC #1, DAC #2 at the ID15B beamline (λ= 0.4100 Å, ESRF) and DAC #3 at the ID27 beamline (λ= 0.3738 Å, ESRF). The pressure was determined by the ruby luminescence method [25] (Mao *et al.*, 1986). At each pressure step, the data were collected in step-scans of 0.5° upon rotating the DAC from -34° to +34° about the vertical axis (ω-scan). For single-crystal data analysis (peak search, unit cell finding, and data integration), the CrysAlisPro Software [26] (Rigaku & CrysAlis, 2015) was employed, whereas the crystal structures were determined using SHELX [27] (Sheldrick, 2008) and refined utilizing the OLEX2 software [28] (Dolomanov *et al.*, 2009). The high-pressure XRD data did not allow anisotropic refinement. All refinements were made in isotropic approximation. No twinning was observed. Hydrogen atoms were added using the riding constraint (HFIX instructions) to automatically constrain their positions in OLEX2.

5.4.3 Theoretical calculations

Structural relaxation, static enthalpy and electronic density of states were determined through first principles calculations employing the Kohn-Sham Density Functional Theory (DFT) framework with the generalized gradient approximation as proposed by Perdew-Burke-Ernzerhof [29] (Perdew *et al.*, 1996). This approximation was integrated within the projector augmented-wave method [30] (Blöchl, 1994) to describe the exchange and correlation within the Vienna Ab initio Simulation Package (VASP) [31] (Kresse & Furthmüller, 1996). Additionally, we employ the DFT-D3 method for dispersion correction [32] (Grimme *et al.*, 2011). For Brillouin zone sampling, we employed the Monkhorst-Pack scheme [33] (Monkhorst & Pack, 1976) with a k-point grid of 2×3×4 for pyrene-I and pyrene-II, 2×8×4 for pyrene-III, 4×3×3 for pyrene-IV and 4×2×2 for pyrene-V. Furthermore, an energy cutoff of 520 eV was applied to the plane-wave expansion. All structures were relaxed until the energy difference for the electronic self-consistent calculation was smaller than 10^{-5} eV/cell and the Hellman−Feynman forces became less than 2×10^{-3} eV/Å. Structural optimisations for all considered phases were performed with PBE. In order to accurately describe eDOSs of pyrene polymorphs, we used PBE0 [34] (Adamo & Barone, 1999).

5.5 Data Availability

CCDC number refers the supplementary crystallographic data for this paper. These data can be obtained free of charge from The Cambridge Crystallographic Data Centre via www.ccdc.cam.ac.uk/structures

5.6 Acknowledgments

The authors acknowledge the European Synchrotron Radiation Facility (ESRF) for the provision of beamtime at the ID15b and ID27 beamlines. Computations were performed at the Leibniz Supercomputing Center of the Bavarian Academy of Sciences and the Humanities, and the research center for scientific computing at the University of Bayreuth. N.D. and L.D. thank the Deutsche Forschungsgemeinschaft (DFG projects DU 945/15-1; LA 4916/1-1; DU 393–9/2, DU 393–13/1) for financial support. N.D. also thanks the Swedish Government Strategic Research Area in Materials Science on Functional Materials at Linköping University (Faculty Grant SFO-Mat-LiU No. 2009 00971). D.L. thanks the UKRI Future Leaders Fellowship (MR/V025724/1) for financial support. W.Z. thanks L. Man for helpful discussions. For the purpose of open access, the author has applied a Creative Commons Attribution (CC BY) license to any Author Accepted Manuscript version arising from this submission.

5.7 Supplementary materials

Table S5.1 Summary of the high-pressure experiments conducted in this work.

DAC number	DAC type	Anvils type/ culet size, µm	Starting material/ pressure transmitting medium	Beamline/XRD wavelength, Å	Result	Pressure, GPa
1	BX90	Boehler-Almax 500	Pyrene-I/ No medium	ID27 ESRF, 0.3738	Pyrene-I	ambient
2	BX90	Boehler-Almax 250	Pyrene-I/ Neon	ID15B ESRF, 0.4100	Pyrene-V	2.5 13.5 17.0
3	Membrane -type	Boehler-Almax 250	Pyrene-I/ Helium	ID27 ESRF, 0.3738	Pyrene-II	0.7 1.4
					Pyrene-IV	2.7 4.3
					Pyrene-V	7.3 9.5 15.4 20.2 29.8 35.5
4	BX90	Boehler-Almax 250	Pyrene-I/ KCl	ID15B ESRF, 0.4100	Pyrene-III Pyrene-IV	6.5

Table S5.2 Experimental crystallographic data for pyrene-I at ambient conditions obtained by single-crystal X-ray diffraction in this work and by neutron diffraction in ref. [14] (Hazell, *et al.*, 1972).

	Pyrene-I, this work	Pyrene-I, ref. [14]
CCDC deposition number*	2360694	1240736
Crystal data		
Chemical formula	$C_{16}H_{10}$	$C_{16}H_{10}$
M_r	202.24	202.24
Crystal system, space group	Monoclinic, $P2_1/c$	Monoclinic, $P2_1/c$
a, b, c (Å)	8.478(8), 9.2562(12), 13.655(7)	8.470(4), 9.253(5), 13.649(7)
α, β, γ (°)	90, 100.31(8), 90	90, 100.28(3), 90
V (Å^3)	1055.3(11)	1052.5(4)
Z	4	4
Density (Mg/m^3)	1.273	1.27
Wavelength (Å)	0.3738	1.025 (neutron radiation)
μ (mm^{-1})	0.031	0.155
Data collection		
Absorption correction	Multi-scan	Linear absorption coefficient
T_{min}, T_{max}	0.036, 1.00	
No. of measured, independent and observed reflections	2963, 1269, 456	3500, 1492, 1008
R_{int}	0.023	
θ_{max} (°)	18.32	34.67
Refinement		
Refinement on	F^2	F^2
$R[F^2>2\sigma(F^2)]$, $wR(F^2)$, S	0.049, 0.16, 0.92	0.034, 0.032, 0.89
Data / restraints / parameters	1269/ 0/ 145	1008/ 0/ 236
H-atom treatment	Refined by ride model	No restraints
Weighting scheme	$w = 1/[\sigma^2(F_o^2) + (0.0539P)^2]$, where $P = (F_o^2+2F_c^2)/3$	$w = 1/\sigma^2$, where $\sigma = 1/[\sigma_c(F^2) + (1+0.02) F^2 - F]$
$\Delta\rho_{max}$, $\Delta\rho_{min}$ (e Å^{-3})	0.08, -0.08	

*CCDC number refers to the supplementary crystallographic data for this paper. These data can be obtained free of charge from The Cambridge Crystallographic Data Centre via www.ccdc.cam.ac.uk/structures

Table S5.3 Experimental crystallographic data for pyrene-II obtained by single-crystal X-ray diffraction at room temperature and two different pressures in this work and at 93 K at ambient pressure in ref. [10] (Frampton *et al.*, 2000).

	Pyrene-II at 0.7 GPa	Pyrene-II at 1.4 GPa	Pyrene-II at 93 K, ref. [10]
CCDC deposition number	2360720	2360721	118728
Crystal data			
Chemical formula	$C_{16}H_{10}$	$C_{16}H_{10}$	$C_{16}H_{10}$
M_r	202.24	202.24	202.24
Crystal system, space group	Monoclinic, $P2_1/c$	Monoclinic, $P2_1/c$	Monoclinic, $P2_1/c$
a, b, c (Å)	8.1431(12), 9.8639(7), 12.1136(4)	8.0322(9), 9.7422(6), 11.8112(4)	8.260(4), 10.020(4), 12.358(6)
α, β, γ (°)	90, 96.484(7), 90	90, 96.074(7), 90	90, 96.48(4), 90
V (Å^3)	966.77(16)	919.05(12)	1016.3(8)
Z	4	4	4
Density (Mg/m^3)	1.389	1.462	1.322
Wavelength (Å)	0.3738	0.3738	0.71069
μ (mm^{-1})	0.035	0.035	0.075
Data collection			
Absorption correction	Multi-scan	Multi-scan	Multi-scan
T_{min}, T_{max}	0.20, 1.00	0.24, 1.00	
No. of measured, independent and observed reflections	1864, 1390, 830	2380, 1414, 832	10829, 2582, 1519
R_{int}	0.018	0.031	0.051
θ_{max} (°)	20.05	18.13	29.5
Refinement			
Refinement on	F^2	F^2	F^2
$R[F^2>2\sigma(F^2)]$, $wR(F^2)$, S	0.068, 0.208, 1.04	0.061, 0.182, 1.01	0.052, 0.091, 1.01
Data / restraints / parameters	1390/ 0/ 172	1414/ 0/ 175	1390/ 0/ 172
H-atom treatment	Refined by ride model	Refined by ride model	Refined by ride model
Weighting scheme	$w = 1/ [\sigma^2 (F_o^2) + (0.1448P)^2]$, where $P = (F_o^2 + 2F_c^2)/3$	$w = 1/[\sigma^2(F_o^2) + (0.1028P)^2]$, where $P = (F_o^2 + 2F_c^2)/3$	$w = 1/[\sigma^2(F_o^2) + (0.045P)^2 + 0.15P]$, where $P = (F_o^2 + 2F_c^2)/3$
$\Delta\rho_{max}$, $\Delta\rho_{min}$ (e Å^{-3})	0.17, -0.17	0.19, -0.17	0.34, -0.26

Table S5.4 Experimental crystallographic data for pyrene-IV obtained by single-crystal X-ray diffraction at room temperature in this work.

	Pyrene-IV at 2.7 GPa	Pyrene-IV at 4.3 GPa
CCDC deposition number	2360722	2360723
Crystal data		
Chemical formula	$C_{16}H_{10}$	$C_{16}H_{10}$
M_r	202.24	202.24
Crystal system, space group	Triclinic, *P*-1	Triclinic, *P*-1
a, b, c (Å)	7.593(3), 10.223(3), 11.192(2)	7.477(2), 10.070(2), 10.879(3)
α, β, γ (°)	92.536(19), 95.04(2), 91.21(3)	92.434(19), 94.73(2), 90.86(2)
V ($Å^3$)	864.2(5)	815.5(4)
Z	4	4
Density (Mg/m^3)	1.554	1.647
Wavelength (Å)	0.3738	0.3738
μ (mm^{-1})	0.038	0.040
Data collection		
Absorption correction	Multi-scan	Multi-scan
T_{min}, T_{max}	0.34, 1.00	0.18, 1.00
No. of measured, independent and observed reflections	657, 604, 415	1378, 1036, 558
R_{int}	0.015	0.034
θ_{max} (°)	14.43	14.83
Refinement		
Refinement on	F^2	F^2
$R[F^2>2\sigma(F^2)]$, $wR(F^2)$, S	0.098, 0.305, 1.07	0.134, 0.393, 1.40
Data / restraints / parameters	604/ 11/ 129	1036/ 0/ 129
H-atom treatment	Refined by ride model	Refined by ride model
Weighting scheme	$w = 1/[\sigma^2(F_o^2) + (0.1836P)^2 + 1.7101P]$, where $P = (F_o^2 + 2F_c^2)/3$	$w = 1/ [\sigma^2 (F_o^2) + (0.2P)^2]$, where $P = (F_o^2+2F_c^2)/3$
$\Delta\rho_{max}$, $\Delta\rho_{min}$ (e $Å^{-3}$)	0.18, -0.17	0.51, -0.38

Table S5.5 Experimental crystallographic data for pyrene-V obtained by single-crystal X-ray diffraction at room temperature in this work.

	Pyrene-V at 7.3 GPa	Pyrene-V at 9.5 GPa	Pyrene-V at 15.4 GPa
CCDC deposition number	2360724	2360725	2360726
Crystal data			
Chemical formula	$C_{16}H_{10}$	$C_{16}H_{10}$	$C_{16}H_{10}$
M_r	202.24	202.24	202.24
Crystal system, space group	Monoclinic, $P2_1/c$	Monoclinic, $P2_1/c$	Monoclinic, $P2_1/c$
a, b, c (Å)	7.450(5), 6.4503(12), 16.096(2)	7.345(4), 6.2802(8), 15.9325(19)	7.2292(3), 6.0333(14), 15.7590(6)
α, β, γ (°)	90, 100.65(3), 90	90, 100.57(3), 90	90, 100.516(5), 90
V ($Å^3$)	760.1(5)	722.5(4)	675.80(16)
Z	4	4	4
Density (Mg/m^3)	1.767	1.859	1.988
Wavelength (Å)	0.3738	0.3738	0.3738
μ (mm^{-1})	0.043	0.045	0.048
Data collection			
Absorption correction	Multi-scan	Multi-scan	Multi-scan
T_{min}, T_{max}	0.21, 1.00	0.15, 1.00	0.23, 1.00
No. of measured, independent and observed reflections	592, 488, 274	738, 595, 295	1021, 776, 632
R_{int}	0.063	0.075	0.051
θ_{max} (°)	13.50	14.06	29.5
Refinement			
Refinement on	F^2	F^2	F^2
$R[F^2>2\sigma(F^2)]$, $wR(F^2)$, S	0.087, 0.222, 0.99	0.12, 0.31, 1.16	0.078, 0.023, 1.12
Data / restraints / parameters	488/ 0/ 66	595/ 0/ 66	776/ 0/ 145
H-atom treatment	Refined by ride model	Refined by ride model	Refined by ride model
Weighting scheme	$w = 1/[\sigma^2(F_o^2) + (0.729P)^2]$, where $P = (F_o^2 + 2F_c^2)/3$	$w = 1/[\sigma^2(F_o^2) + (0.200P)^2]$, where $P = (F_o^2 + 2F_c^2)/3$	$w = 1/[\sigma^2(F_o^2) + (0.198P)^2]$, where $P = (F_o^2 + 2F_c^2)/3$
$\Delta\rho_{max}$, $\Delta\rho_{min}$ (e $Å^{-3}$)	0.20, -0.20	0.19, -0.17	0.53, -0.33

Table S5.5 (continuation)

Pyrene-V at 20.2 GPa	Pyrene-V at 25.2 GPa	Pyrene-V at 29.8 GPa	Pyrene-V at 35.5 GPa
2360727	2360728	2360729	2360730
$C_{16}H_{10}$	$C_{16}H_{10}$	$C_{16}H_{10}$	$C_{16}H_{10}$
202.24	202.24	202.24	202.24
Monoclinic, $\mathrm{P2_1/c}$	Monoclinic, $P2_1/c$	Monoclinic, $P2_1/c$	Monoclinic, $P2_1/c$
7.1550(3), 5.8939(13), 15.6277(6)	7.0634(3), 5.7352(14), 15.4503(6)	7.0174(5), 5.645(3), 15.3477(13)	6.9711(7), 5.541(4), 15.2471(16)
90, 100.467(5), 90	90, 100.395(5), 90	90, 100.363(8), 90	90, 100.349(10), 90
648.07(15)	615.62(15)	598.0(3)	579.4(4)
4	4	4	4
2.073	2.182	2.246	2.318
0.3738	0.3738	0.3738	0.3738
0.050	0.053	0.054	0.056
Multi-scan	Multi-scan	Multi-scan	Multi-scan
0.15, 1.00	0.01, 1.00	0.04, 1.00	0.34, 1.00
1004, 835, 654	990, 808, 630	760, 684, 521	560, 531, 403
0.016	0.018	0.017	0.060
19.95	20.25	20.41	19.84
$\mathrm{F^2}$	F^2	F^2	F^2
0.076, 0.231, 1.08	0.136, 0.338, 1.60	0.136, 0.345, 1.61	0.166, 0.392, 1.80
835/ 0/ 145	808/ 96/ 145	684/ 96/ 145	531/ 96/ 145
Refined by ride model	Refined by ride model	Refined by ride model	Refined by ride model
$\mathrm{w = 1/[\sigma^2(F_o^2) + (0.181P)^2 + 0.285P]}$, where $\mathrm{P = (F_o^2 + 2F_c^2)/3}$	$w = 1/ [\sigma^2 (F_o^2) + (0.2P)^2]$, where $P = (F_o^2 + 2F_c^2)/3$	$w = 1/[\sigma^2(F_o^2) + (0.2P)^2]$, where $P = (F_o^2 + 2F_c^2)/3$	$w = 1/[\sigma^2(F_o^2) + (0.2P)^2]$, where $P = (F_o^2 + 2F_c^2)/3$
0.46, -0.28	0.54, -0.59	0.41, -0.42	0.51, -0.54

Table S5.6 Unit cell volume per formula unit for pyrene polymorphs up to 35.5 GPa in this work and in ref. [6] (Fabbiani *et al.*, 2006).

Polymorph/ pressure transmitting medium	Pressure, GPa	Volume per formula unit, Å^3
Pyrene-I/ No medium	0	263.83(3)
Pyrene-II/ He	0.7	241.69(4)
Pyrene-II/ He	1.4	229.76(3)
Pyrene-III/ dichloromethane [6]	0.3	249(3)
Pyrene-III/ dichloromethane [6]	0.5	238.91(9)
Pyrene-IV/ He	2.7	216.05(16)
Pyrene-IV/ He	4.3	203.88(10)
Pyrene-V/ He	7.3	190.02(16)
Pyrene-V/ He	9.5	180.63(10)
Pyrene-V/ He	15.4	169.20(4)
Pyrene-V/ He	20.2	162.02(4)
Pyrene-V/ He	25.2	153.90(4)
Pyrene-V/ He	29.8	149.50(9)
Pyrene-V/ He	35.5	144.85(10)
Pyrene-V/ Ne	2.5	213.92(4)
Pyrene-V/ Ne	13.5	174.45(15)
Pyrene-V/ Ne	17	167.08(8)

Table S5.7 DFT-calculated unit cell volume per formula unit of pyrene polymorphs up to 36 GPa.

Polymorph	Pressure (GPa)	Volume per formula unit (Å^3)
Pyrene-I	0	247.71
Pyrene-II	1	229.64
Pyrene-II	2	219.12
Pyrene-IV	3	209.86
Pyrene-IV	4	203.54
Pyrene-V	6	191.04
Pyrene-V	9	180.58
Pyrene-V	13	170.96
Pyrene-V	17	163.82
Pyrene-V	21	158.07
Pyrene-V	24	154.41
Pyrene-V	27	151.19
Pyrene-V	30	148.28
Pyrene-V	33	145.80
Pyrene-V	36	143.37

Table S5.8 Lattice parameters of pyrene polymorphs up to 35.5 GPa determined in this work and in ref. [6] (Fabbiani *et al.*, 2006).

Polymorph/ pressure transmitting medium	Pressure, GPa	a, Å	b, Å	c, Å	α, °	β, °	γ, °
Pyrene-I/ no medium	0	8.478(8)	9.2652(12)	13.655(7)	90	100.31(8)	90
Pyrene-II/ He	0.7	8.1431(12)	9.8639(7)	12.1136(4)	90	96.484(7)	90
Pyrene-II/ He	1.4	8.0322(9)	9.7422(6)	11.8112(4)	90	96.074(7)	90
Pyrene-III/ dichloromethane [6]	0.3	8.65(7)	3.852(3)	15.35(9)	90	103.3(4)	90
Pyrene-III/ dichloromethane [6]	0.5	8.3341(16)	3.8375(5)	15.309(4)	90	102.606(19)	90
Pyrene-IV/ He	2.7	7.593(3)	10.223(3)	11.192(2)	92.536(19)	95.04(2)	91.21(3)
Pyrene-IV/ He	4.3	7.477(2)	10.070(2)	10.879(3)	92.434(19)	94.73(2)	90.86(2)
Pyrene-V/ He	7.3	7.450(5)	6.4503(12)	16.096(2)	90	100.65(3)	90
Pyrene-V/ He	9.5	7.345(4)	6.2802(8)	15.9325(19)	90	100.57(3)	90
Pyrene-V/ He	15.4	7.2292(3)	6.0333(14)	15.7590(6)	90	100.516(5)	90
Pyrene-V/ He	20.2	7.1550(3)	5.8939(13)	15.6277(6)	90	100.467(5)	90
Pyrene-V/ He	25.2	7.0634(3)	5.7352(14)	15.4503(6)	90	100.395(5)	90
Pyrene-V/ He	29.8	7.0174(5)	5.645(3)	15.3477(13)	90	100.363(8)	90
Pyrene-V/ He	35.5	6.9711(7)	5.541(4)	15.2471(16)	90	100.349(10)	90
Pyrene-V/ Ne	2.5	7.6733(13)	6.9186(3)	16.4075(9)	90	100.776(9)	90
Pyrene-V/ Ne	13.5	7.2481(7)	6.184(5)	15.8236(16)	90	100.331(12)	90
Pyrene-V/ Ne	17	7.1839(5)	6.034(3)	15.6713(8)	90	100.294(7)	90

Table S5.9a DFT-calculated crystallographic data for pyrene-I at ambient pressure.

Pyrene-I	
Chemical formula	$C_{16}H_{10}$
M_r	202.24
Crystal system, space group	Monoclinic, $P2_1/c$
a, b, c (Å)	8.309, 9.087, 13.358
α, β, γ (°)	90, 100.739, 90
V (Å^3)	990.849
Z	4

Table S5.9b Theoretical atomic coordinates for pyrene-I at ambient pressure.

Label	x	y	z	Occupancy
C1	0.07549	0.53393	0.21596	1
C2	0.48589	0.24487	0.00152	1
C3	0.36086	0.69108	0.00972	1
C4	0.78127	0.27446	0.05543	1
C5	0.21669	0.67255	0.36234	1
C6	0.07256	0.63621	0.29349	1
C7	0.63265	0.10517	0.14981	1
C8	0.4844	0.14166	0.08224	1
C9	0.2219	0.46774	0.20344	1
C10	0.63026	0.00299	0.23086	1
C11	0.52322	0.4403	0.25721	1
C12	0.66558	0.47554	0.32174	1
C13	0.33318	0.07738	0.0962	1
C14	0.18851	0.11693	0.02935	1
C15	0.19092	0.2836	0.45023	1
C16	0.3378	0.22	0.43605	1
H1	0.03831	0.00568	0.33541	1
H2	0.35957	0.61433	0.07224	1
H3	0.10308	0.82326	0.45523	1
H4	0.04235	0.18885	0.19866	1
H5	0.22367	0.38849	0.14215	1
H6	0.52383	0.3627	0.19519	1
H7	0.21897	0.57444	0.68816	1
H8	0.07324	0.06924	0.04095	1
H9	0.07701	0.25632	0.39874	1
H10	0.33987	0.1425	0.37386	1

Table S5.10a Theoretical crystallographic data for pyrene-II at 1 GPa.

Pyrene-II	
Chemical formula	$C_{16}H_{10}$
M_r	202.24
Crystal system, space group	Monoclinic, $P2_1/c$
a, b, c (Å)	7.998, 9.574, 11.966
α, β, γ (°)	90, 96.346, 90
V (Å^3)	910.681
Z	4

Table S5.10b Theoretical atomic coordinates for pyrene-II at 1 GPa.

Label	x	y	z	Occupancy
C1	0.30962	0.59097	0.07593	1
C2	0.38635	0.10838	0.36213	1
C3	0.1681	0.6432	0.00903	1
C4	0.22822	0.1766	0.36633	1
C5	0.53193	0.15805	0.42938	1
C6	0.21938	0.29121	0.4424	1
C7	0.30137	0.47303	0.14866	1
C8	0.74722	0.44303	0.27549	1
C9	0.60175	0.4906	0.20978	1
C10	0.35884	0.1618	0.00748	1
C11	0.44172	0.42468	0.21219	1
C12	0.08766	0.1279	0.2966	1
C13	0.51978	0.22522	0.00254	1
C14	0.66496	0.17731	0.06809	1
C15	0.10008	0.01203	0.22748	1
C16	0.81919	0.24246	0.06119	1
H1	0.04661	0.59363	0.01295	1
H2	0.09745	0.33949	0.44895	1
H3	0.18078	0.4208	0.15157	1
H4	0.73863	0.35194	0.32924	1
H5	0.34932	0.07539	0.06555	1
H6	0.4343	0.3334	0.26549	1
H7	0.03259	0.68077	0.20165	1
H8	0.65515	0.08935	0.12482	1
H9	0.01184	0.47484	0.32405	1
H10	0.06838	0.70508	0.38821	1

Table S5.11a Theoretical crystallographic data for pyrene-III at 1 GPa.

Pyrene-III	
Chemical formula	$C_{16}H_{10}$
M_r	202.24
Crystal system, space group	Monoclinic, $P2_1/c$
a, b, c (Å)	8.174, 3.701, 14.961
α, β, γ (°)	90, 102.437, 90
V (Å^3)	441.97
Z	2

Table S5.11b Theoretical atomic coordinates for pyrene-III at 1 GPa.

Label	x	y	z	Occupancy
C1	0.11509	0.55284	0.34116	1
C2	0.74033	0.18353	0.18261	1
C3	0.58503	0.16221	0.12051	1
C4	0.43347	0.29113	0.14258	1
C5	0.2842	0.27386	0.08086	1
C6	0.27334	0.37498	0.49144	1
C7	0.12168	0.39636	0.42645	1
C8	0.57773	0.00909	0.03217	1
H1	0.00465	0.07632	0.20723	1
H2	0.74604	0.30879	0.24926	1
H3	0.43973	0.40568	0.2102	1
H4	0.17013	0.37376	0.09898	1
H5	0.00814	0.29145	0.44391	1

Table S5.12a Theoretical crystallographic data for pyrene-IV at 3 GPa.

Pyrene-IV	
Chemical formula	$C_{16}H_{10}$
M_r	202.24
Crystal system, space group	Triclinic, *P*-1
a, *b*, *c* (Å)	7.512, 10.088, 11.129
α, *β*, *γ* (°)	92.825, 94.685, 90.639
V (Å^3)	839.45
Z	4

Table S5.12b Theoretical atomic coordinates for pyrene-IV at 3 GPa.

Label	x	y	z	Occupancy
C1	0.19644	0.04043	0.8431	1
C2	0.9842	0.1761	0.06727	1
C3	0.35799	0.02253	0.25269	1
C4	0.07558	0.2823	0.01779	1
C5	0.26603	0.11258	0.17824	1
C6	0.75675	0.44389	0.22391	1
C7	0.07993	0.09029	0.1456	1
C8	0.71091	0.04542	0.0858	1
C9	0.26162	0.30325	0.05197	1
C10	0.79736	0.15496	0.0366	1
C11	0.09219	0.51309	0.70171	1
C12	0.00927	0.02103	0.81143	1
C13	0.22027	0.58724	0.43434	1
C14	0.22335	0.46698	0.36084	1
C15	0.08855	0.89151	0.26036	1
C16	0.25498	0.31264	0.64076	1
C17	0.11391	0.15262	0.49011	1
C18	0.07132	0.41608	0.30006	1
C19	0.049	0.77516	0.51422	1
C20	0.02066	0.63634	0.06175	1
C21	0.05613	0.65572	0.4406	1
C22	0.79602	0.17843	0.4166	1
C23	0.09776	0.39082	0.63251	1
C24	0.39873	0.35568	0.7226	1
C25	0.62724	0.35889	0.49937	1
C26	0.29405	0.75925	0.04173	1
C27	0.35217	0.2237	0.13103	1
C28	0.26949	0.91387	0.29319	1

C29	0.25812	0.19292	0.56625	1
C30	0.2026	0.6565	0.09044	1
C31	0.60734	0.52368	0.21164	1
C32	0.63593	0.24513	0.42462	1
H1	0.26277	0.12582	0.8091	1
H2	0.50079	0.03632	0.27554	1
H3	0.76116	0.34998	0.17206	1
H4	0.56812	0.03137	0.06485	1
H5	0.32873	0.38522	0.01298	1
H6	0.34862	0.41518	0.35465	1
H7	0.02142	0.80408	0.28795	1
H8	0.1188	0.06164	0.43389	1
H9	0.07291	0.32185	0.24888	1
H10	0.04925	0.44337	0.89927	1
H11	0.80236	0.08824	0.35931	1
H12	0.48296	0.70531	0.26773	1
H13	0.49983	0.40567	0.50877	1
H14	0.43643	0.77561	0.06551	1
H15	0.49305	0.24243	0.15823	1
H16	0.65948	0.15496	0.64856	1
H17	0.37863	0.13356	0.57089	1
H18	0.27073	0.59214	0.1542	1
H19	0.49377	0.49074	0.15016	1
H20	0.51404	0.20757	0.37446	1

Table S5.13a Theoretical crystallographic data for pyrene-V at 9 GPa.

Pyrene-V	
Chemical formula	$C_{16}H_{10}$
M_r	202.24
Crystal system, space group	Monoclinic, $P2_1/c$
a, b, c (Å)	7.339, 6.292, 15.898
α, β, γ (°)	90, 100.28, 90
V (Å^3)	722.3
Z	4

Table S5.13b Theoretical atomic coordinates for pyrene-V at 9 GPa.

Label	x	y	z	Occupancy
C1	0.5488	0.09966	0.2072	1
C2	0.60866	0.19715	0.13618	1
C3	0.29593	0.15517	0.05236	1
C4	0.17771	0.3368	0.47309	1
C5	0.23743	0.07336	0.12659	1
C6	0.2603	0.66186	0.00997	1
C7	0.13868	0.61776	0.21429	1
C8	0.85721	0.33081	0.06621	1
C9	0.32011	0.55156	0.22022	1
C10	0.07992	0.71854	0.28208	1
C11	0.79753	0.25463	0.14121	1
C12	0.54986	0.21857	0.4832	1
C13	0.48383	0.21695	0.05792	1
C14	0.42838	0.22356	0.40515	1
C15	0.35871	0.04612	0.20096	1
C16	0.24544	0.28216	0.40039	1
H1	0.03344	0.37812	0.46939	1
H2	0.09401	0.02762	0.12313	1
H3	0.21018	0.61583	0.06737	1
H4	0.0393	0.58768	0.15656	1
H5	0.00176	0.37226	0.0694	1
H6	0.36218	0.46155	0.16885	1
H7	0.06411	0.26195	0.22244	1
H8	0.48002	0.19093	0.34722	1
H9	0.68841	0.48152	0.24344	1
H10	0.1579	0.29429	0.33819	1

Table S5.14 The enthalpy difference *ΔH* (e*V*/molecule) of the pyrene polymorphs up to 5 GPa calculated by DFT.

Pressure, GPa	Pyrene-I	Pyrene-II	Pyrene-III	Pyrene-IV	Pyrene-V
0	0	-0.0003	0.0010	0.0181	0.0514
1	0	-0.0088	-0.0465	0.0046	0.0241
2	0	-0.0178	-0.0898	-0.0121	-0.0158
3	0	-0.0253	-0.1287	-0.0283	-0.0521
4	0	-0.0338	-0.1668	-0.0474	-0.0891
5	0	-0.0451	-0.2015	-0.0686	-0.1294

Table S5.15 Intermolecular distances and interplanar angles of pyrene polymorphs up to 35.5 GPa from experiments in helium pressure medium.

Polymorph	Pressure, GPa	Intermolecular distance d_1, Å	Intermolecular distance d_2, Å	Interplanar angle, °
Pyrene-I	0	3.534	3.534	83.6
Pyrene-II	0.7	3.378	3.378	75.4
Pyrene-II	1.4	3.289	3.289	73.8
Pyrene-IV	2.7	3.148	3.239	66.7
Pyrene-IV	4.3	3.075	3.157	65.1
Pyrene-V	7.3	3.013	2.948	44.9
Pyrene-V	9.5	2.944	2.885	43.7
Pyrene-V	15.4	2.861	2.772	42
Pyrene-V	20.2	2.808	2.710	41.1
Pyrene-V	25.2	2.755	2.633	40.1
Pyrene-V	29.8	2.712	2.593	40
Pyrene-V	35.5	2.656	2.560	39.5

Supplementary Note 1. Fingerprint plot and Hirshfeld surface mapped with $\mathbf{d_{norm}}$

Pyrene molecules exhibit various interactions, including $\pi \cdots \pi$ stacking, C-H $\cdots$ π, and H $\cdots$ H contacts. As depicted in Fig. S5.1a, the $\pi \cdots \pi$ stacking motif is represented in the two-dimensional fingerprint plot as a green triangle region with $d_e \approx d_i$, starting at approximately 1.75 Å (indicated by Arrow 1). The letter indicates the minimal intermolecular distance in the pairs of pyrene-I molecules. This observation aligns with the intermolecular distance of ~3.5 Å based on geometrical consideration (see main text). On either side of the plot, two distinct pairs of 'wings' are observed, representing two different C-H(e)$\cdots\pi$(i) interactions (outlined in yellow) and two different C-H(i)$\cdots\pi$(e) interactions (outlined in purple), respectively. Fig. S5.1b illustrates the intermolecular interactions of pyrene-I molecules within their surrounding molecular environment. The Hirshfeld surface in this figure is mapped using d_{norm}, which incorporates both d_e and d_i values. Each is normalized by the vdW (van der Waals) radius corresponding to the atoms involved in the close contact near the surface. The advantage of using d_{norm} lies in its ability to provide a more balanced and symmetrical approach to analyze the distances between atoms. This method employs a distinct red-white-blue color scheme (differentiated from the red-green-blue scheme used for d_e and d_i) to map these distances. This design allows d_{norm} to impartially identify all close contacts, where contacts shorter than the vdW distance are displayed as red dots on a surface that is primarily blue. Fig. S5.1b displays three types of interactions: the primary C-H(e)$\cdots\pi$(i) interaction and the primary C-H(i)$\cdots\pi$(e) interaction, both represented by the lower pair of wings in the fingerprint plot, as well as the H(i)$\cdots$H(e) interaction. Other non-close contact interactions are not reflected in the d_{norm}.

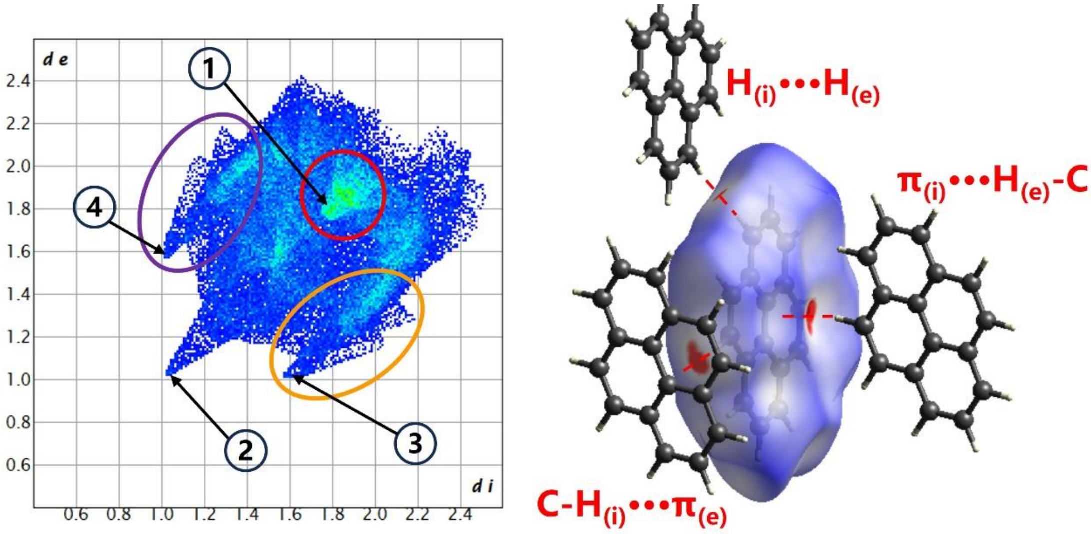

Figure S5.1 Intermolecular interactions for pyrene-I. a) Fingerprint plot: the green triangle within the red circle represents the range of the $\pi \cdots \pi$ stacking interaction; the two 'wings' within the yellow oval represent the ranges of two distinct C-$H_{(e)} \cdots \pi_{(i)}$ interactions, and the two 'wings' in the purple oval indicate the ranges of two different C-$H_{(i)} \cdots \pi_{(e)}$ interactions (in the figure b to the right, only one of each kind of C-H $\cdots$ π interactions is shown for the figure clarity); blue corresponds to the low frequency of occurrence of a (d_i, d_e) pair, while red points (if appear) indicate the high frequency of the surface points with that (d_i, d_e) combination; arrows numbered 1 through 4 point to the features corresponding to the shortest contacts for (1) the $\pi \cdots \pi$ stacking (represent the intermolecular distance), (2) $H_{(i)} \cdots H_{(e)}$ contacts, (3) C-$H_{(e)} \cdots \pi_{(i)}$, and (4) C-$H_{(i)} \cdots \pi_{(e)}$ interactions. (b) Hirshfeld surface mapped with d_{norm} from -0.12 (red) to 0 (white) to 1.46 (blue).

a)

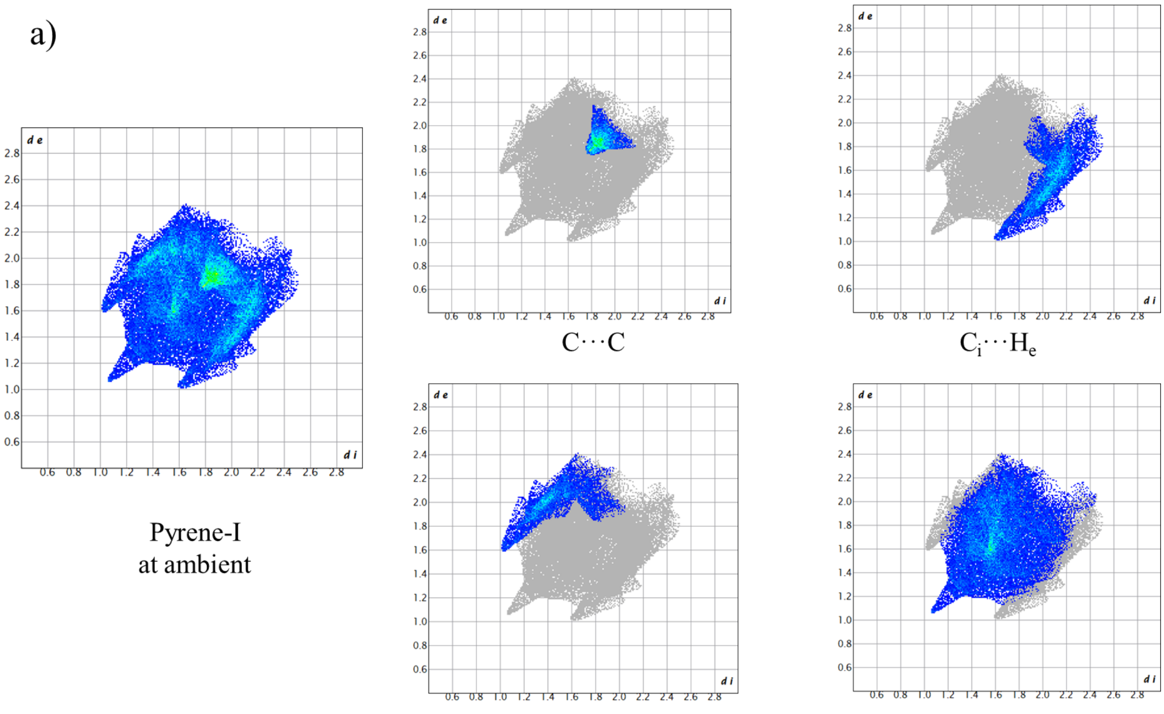

Pyrene-I
at ambient

C···C

C_i···H_e

C_e···H_i

H···H

b)

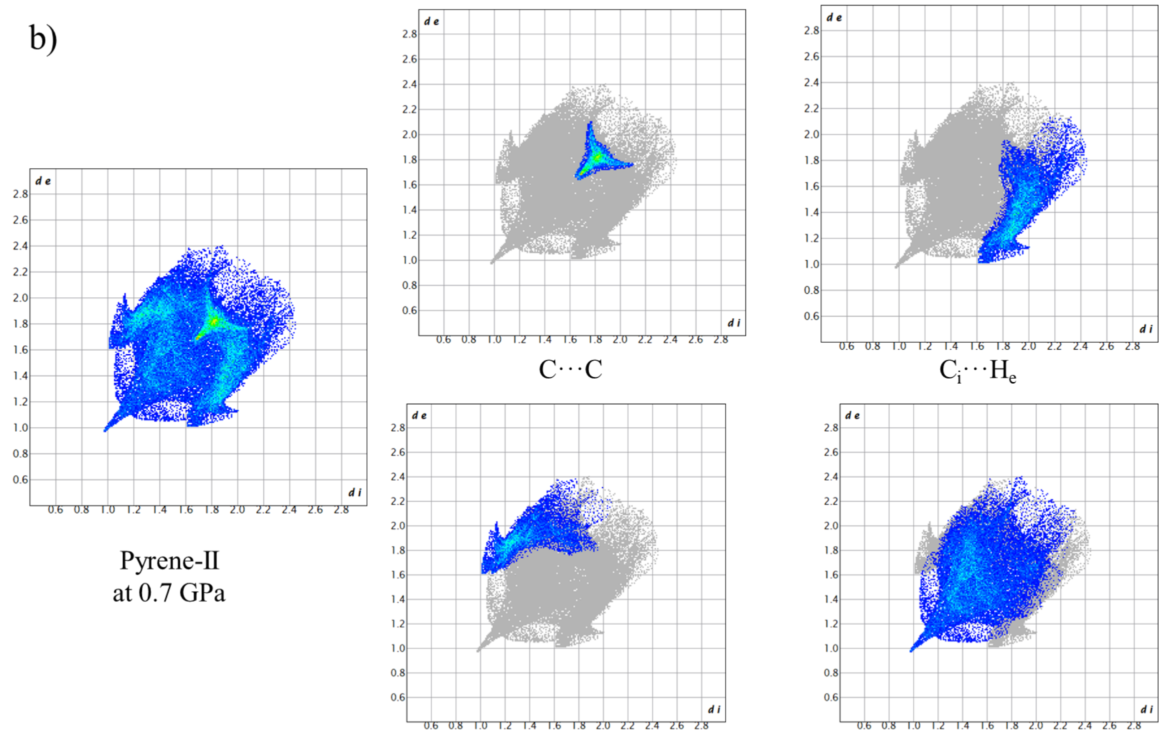

Pyrene-II
at 0.7 GPa

C···C

C_i···H_e

C_e···H_i

H···H

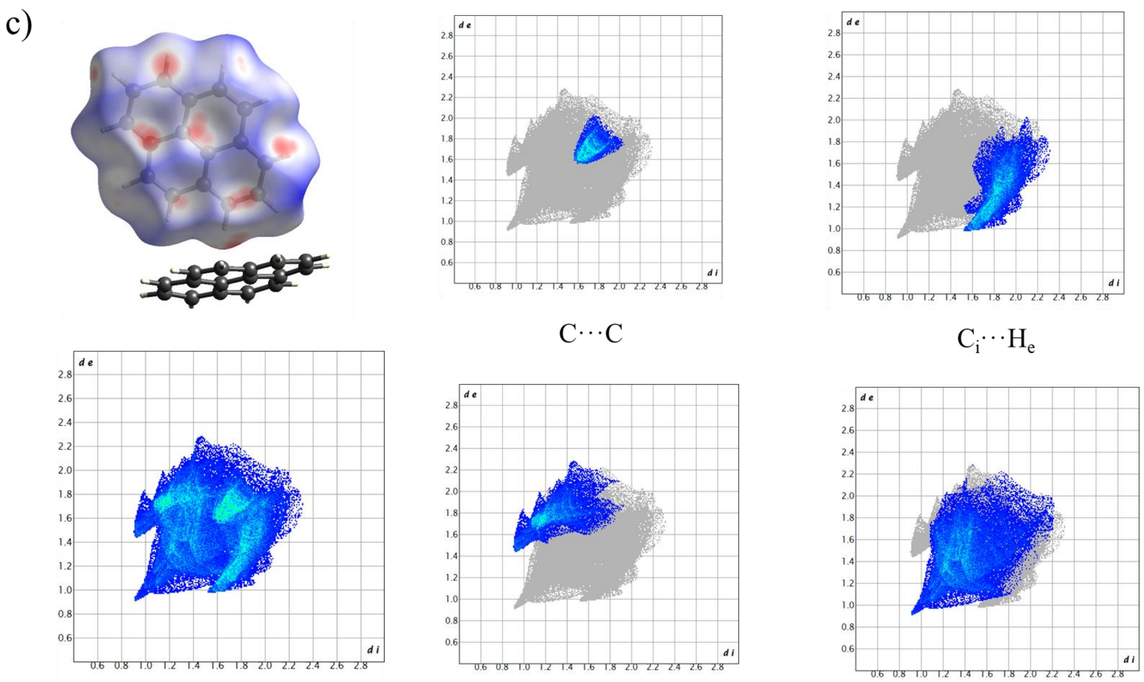

C···C

$C_i \cdots H_e$

Pyrene-IV Sandwich-I
at 4.3 GPa

$C_e \cdots H_i$

H···H

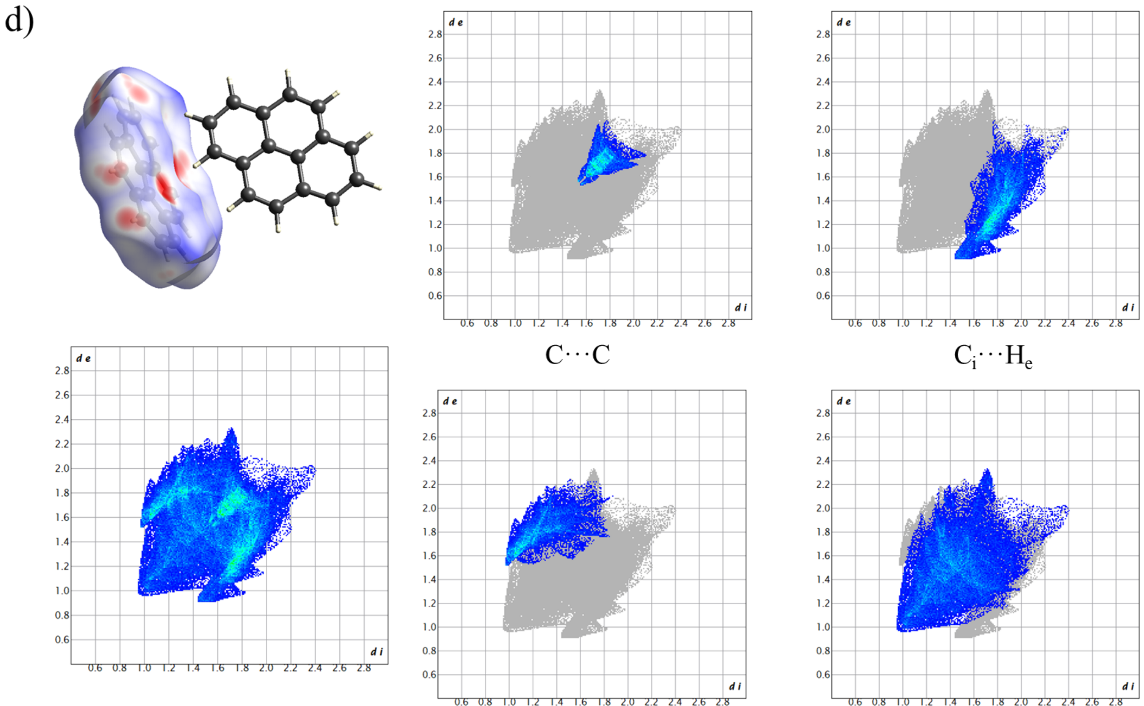

C···C

$C_i \cdots H_e$

Pyrene-IV Sandwich-II
at 4.3 GPa

$C_e \cdots H_i$

H···H

e)

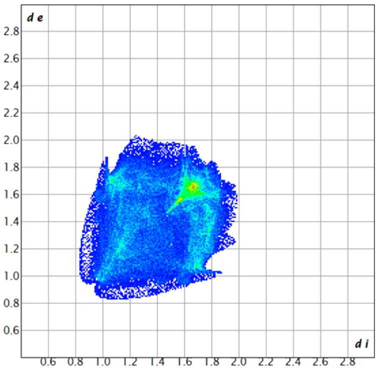

Pyrene-V
at 7.3 GPa

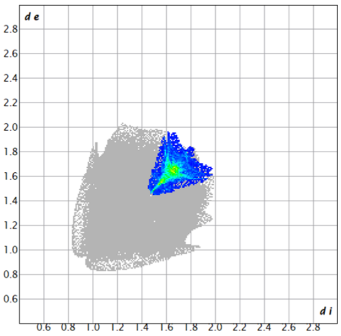

C···C

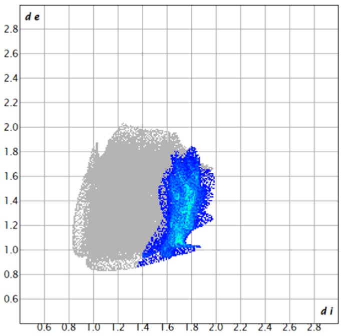

$C_i \cdots H_e$

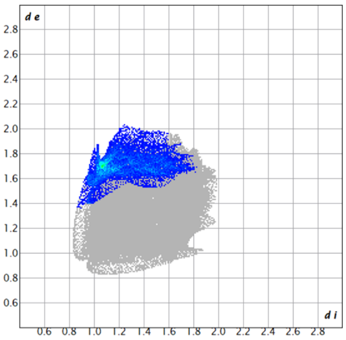

$C_e \cdots H_i$

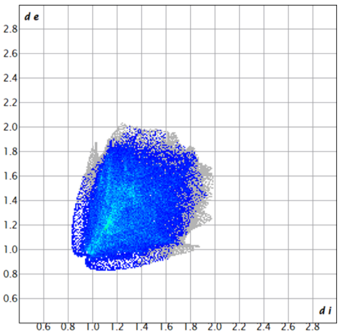

H···H

f)

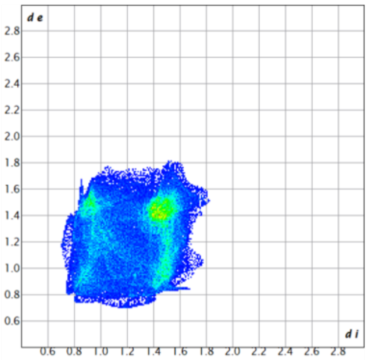

Pyrene-V
at 35.5 GPa

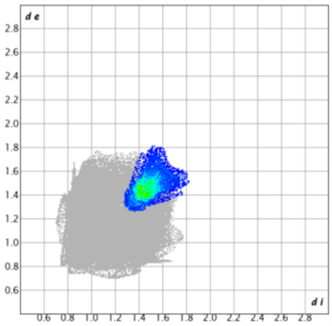

C···C

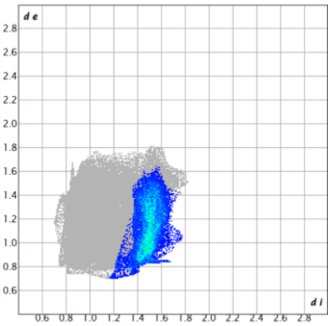

$C_i \cdots H_e$

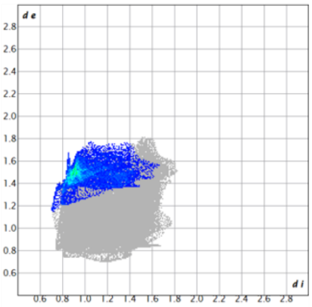

$C_e \cdots H_i$

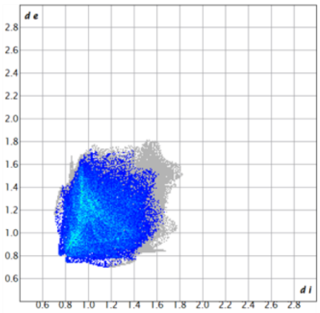

H···H

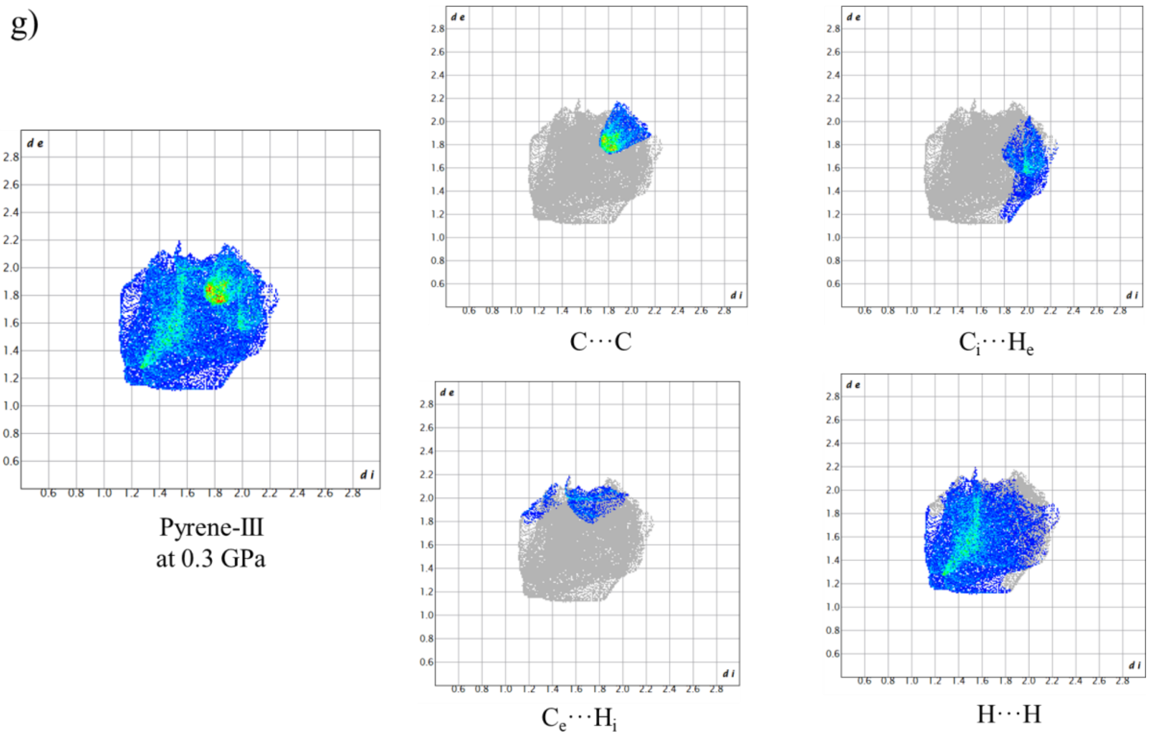

Pyrene-III
at 0.3 GPa

C···C

$C_i \cdots H_e$

$C_e \cdots H_i$

H···H

Figure S5.2 Fingerprint plots for pyrene molecules in pyrene polymorphs at different pressures. Different intermolecular interactions are highlighted in separate plots. a) Pyrene-I at ambient conditions; b) pyrene-II at 0.7 GPa; c) pyrene-IV: a molecule in sandwich-1 at 4.3 GPa, the Hirschfeld surface mapped in d_{norm} is given for clarity; d) pyrene-IV: a molecule in sandwich-2 at 4.3 GPa, the Hirschfeld surface mapped in d_{norm} is given for clarity; e) pyrene-V at 7.3 GPa; f) pyrene-V at 35.5 GPa; g) pyrene-III at 0.3 GPa, the structure data are from ref. [6] (Fabbiani *et al.*, 2006).

References

[1] Pope, M. and Swenberg, C. E. Electronic processes in organic crystals and polymers. *Oxford university press*, (1999).

[2] Silinsh, E. A. and Cápek, V. Organic molecular crystals: interaction, localization, and transport phenomena. *Oxford: Oxford University Press/American Institute of Physics,* (1994).

[3] Farchioni, R. Organic Electronic Materials: Conjugted Polymers and Low Molecular Weight Electronic Solids.*Springer Science & Business Media* **41** (2001).

[4] Single-crystal x-ray diffraction in the megabar pressure range. *High Pressure Research* **33(3)**, Editor Dubrovinsky, L., 451-583 (2013).

[5] Giordano, N., Beavers, C.M., Kamenev, K.V., *et al.* High-pressure polymorphism in L-threonine between ambient pressure and 22 GPa. *CrystEngComm*. **21**, 4444-4456 (2019).

[6] Fabbiani, F. P., Allan, D. R., Parsons, S. *et al.* Exploration of the high-pressure behaviour of polycyclic aromatic hydrocarbons: Naphthalene, phenanthrene and pyrene. *Acta Crystallographica Section B: Structural Science* **62**, 826-842 (2006).

[7] Kai, Y., Hama, F., Yasuoka, N. *et al.* Structural chemistry of layered cyclophanes. III. Molecular structures of [2.2] (2, 7) pyrenophane-1, 1'-diene and pyrene (redetermined) at–160° C. *Acta Crystallographica Section B: Structural Crystallography and Crystal Chemistry* **34**, 1263-1270 (1978).

[8] Jones, W., Ramdas, S. and Thomas, J. M. Novel approach to the determination of the crystal structures of organic molecular crystals: Low temperature form of pyrene. *Chemical Physics Letters* **54**, 490-493 (1978).

[9] Knight, K. S., Shankland, K., David, W. I. F. *et al.* The crystal structure of perdeuterated pyrene II at 4.2 K. *Chemical physics letters* **258(3-4)**, 490-494 (1996).

[10] Frampton, C. S., Knight, K. S., Shankland, N. *et al.* Single-crystal X-ray diffraction analysis of pyrene II at 93 K. *Journal of Molecular Structure* **520**, 29-32 (2000).

[11] Zallen, R., Griffiths, C., Slade, M. *et al.* The solid state transition in pyrene. *Chemical Physics Letters* **39**, 85-89 (1976).

[12] Sun, B., Dreger, Z. and Gupta, Y. High-pressure effects in pyrene crystals: vibrational spectroscopy. *The Journal of Physical Chemistry A* **112**, 10546-10551 (2008).

[13] Robertson, J. M. and White, J. G. 72. The crystal structure of pyrene. A quantitative X-ray investigation. *Journal of the Chemical Society (Resumed)*, 358-368 (1947).

[14] Hazell, A. C., Larsen, F. K. and Lehmann, M. S. A neutron diffraction study of the crystal structure of pyrene, $C_{16}H_{10}$. *Acta Crystallographica Section B: Structural Crystallography and Crystal Chemistry* **28**, 2977-2984 (1972).

[15] Angel, R. J., Alvaro, M. and Gonzalez-Platas, J. EosFit7c and a Fortran module (library) for equation of state calculations. *Zeitschrift für Kristallographie-Crystalline Materials* **229**, 405-419 (2014).

[16] Bykova, E., Bykov, M., Černok, A., *et al.* Metastable silica high pressure polymorphs as structural proxies of deep Earth silicate melts. *Nature communications* **9(1)**, 4789 (2018).

[17] Prescher, C. and Prakapenka, V. B. DIOPTAS: a program for reduction of two-dimensional X-ray diffraction data and data exploration. *High Pressure Research* **35**, 223-230 (2015).

[18] Petříček, V., Dušek, M. and Palatinus, L. Crystallographic computing system JANA2006: general features. *Zeitschrift für Kristallographie-Crystalline Materials* **229**, 345-352 (2014).

[19] Dewaele, A., Belonoshko, A. B., Garbarino, G. *et al.* High-pressure–high-temperature equation of state of KCl and KBr. *Physical Review B* **85**, 214105 (2012).

[20] McKinnon, J. J., Spackman, M. A. and Mitchell, A. S. Novel tools for visualizing and exploring intermolecular interactions in molecular crystals. *Acta Crystallographica Section B: Structural Science* **60**, 627-668 (2004).

[21] Spackman, M. A. and Byrom, P. G. A novel definition of a molecule in a crystal. *Chemical physics letters* **267**, 215-220 (1997).

[22] Spackman, M. A. and Jayatilaka, D. Hirshfeld surface analysis. *CrystEngComm* **11**, 19-32 (2009).

[23] Spackman, P. R., Turner, M. J., McKinnon, J. J. *et al.* CrystalExplorer: A program for Hirshfeld surface analysis, visualization and quantitative analysis of molecular crystals. *Journal of Applied Crystallography* **54**, 1006-1011 (2021).

[24] Kantor, I., Prakapenka, V., Kantor, A. *et al.* BX90: A new diamond anvil cell design for X-ray diffraction and optical measurements. *Review of Scientific Instruments* **83(12)**, (2012).

[25] Mao, H. K., Xu, J. A. and Bell, P. M. Calibration of the ruby pressure gauge to 800 kbar under quasi-hydrostatic conditions. *Journal of Geophysical Research: Solid Earth* **91(B5)**, 4673-4676 (1986).

[26] Rigaku, O. and CrysAlis, P. R. O. Rigaku Oxford Diffraction. *Yarnton, England* (2015).

[27] Sheldrick, G. M. A short history of SHELX. *Acta Crystallographica Section A: Foundations of Crystallography* **64**, 112-122 (2008).

[28] Dolomanov, O. V., Bourhis, L. J., Gildea, R. J., *et al.* OLEX2: a complete structure solution, refinement and analysis program. *Journal of applied crystallography* **42(2)**, 339-341 (2009).

[29] Perdew, J. P., Burke, K. and Ernzerhof, M. Generalized gradient approximation made simple. *Physical review letters* **77**, 3865 (1996).

[30] Blöchl, P. E. Projector augmented-wave method. *Physical review B* **50**, 17953 (1994).

[31] Kresse, G. and Furthmüller, J. Efficient iterative schemes for ab initio total-energy calculations using a plane-wave basis set. *Physical review B* **54**, 11169 (1996).

[32] Grimme, S., Ehrlich, S. and Goerigk, L. Effect of the damping function in dispersion corrected density functional theory. *Journal of computational chemistry* **32**, 1456-1465 (2011).

[33] Monkhorst, H. J. and Pack, J. D. Special points for Brillouin-zone integrations. *Physical review B* **13**, 5188 (1976).

[34] Adamo, C. and Barone, V. Toward reliable density functional methods without adjustable parameters: The PBE0 model. *The Journal of chemical physics* **110**, 6158-6170 (1999).

Chapter 6 Structural Transformations and Stability of Benzo[a]pyrene Under High Pressure

Wenju Zhou[a]**, Andrey Aslandukov*[a,b]*, Anastasiia Minchenkova*[b]*, Michael Hanfland*[c]*, Leonid Dubrovinsky*[b]*, Natalia Dubrovinskaia*[a,d]***

[a]*Material Physics and Technology at Extreme Conditions, Laboratory of Crystallography, University of Bayreuth, 95440 Bayreuth, Germany*

[b]*Bayerisches Geoinstitut, University of Bayreuth, 95440 Bayreuth, Germany*

[c]*European Synchrotron Radiation Facility, CS 40220, 38043 Grenoble Cedex 9, France*

[d]*Department of Physics, Chemistry and Biology (IFM), Linköping University, SE-581 83, Linköping, Sweden*

**Correspondence E-mails: Wenju.Zhou@uni-bayreuth.de, Natalia.Dubrovinskaia@uni-bayreuth.de*

Under review, *IUCrJ*

6.1 Abstract

Benzo[*a*]pyrene (B*a*P), $C_{20}H_{12}$, is a representative of polycyclic aromatic hydrocarbons (PAHs), which are ubiquitous in nature and the universe, where they undergo extreme conditions. This paper reports the results of investigations of the high-pressure behavior of B*a*P up to 28 GPa using *in situ* single-crystal synchrotron X-ray diffraction. We identified two previously unknown polymorphs, B*a*P-II ($P2_1/c$) at 4.8 GPa and B*a*P-III (P-1) at 7.1 GPa. The structural transformation from B*a*P-I ($P2_1/c$) to B*a*P-II ($P2_1/c$) manifests as an abrupt change in the intermolecular angle and in the unit cell parameters *a* and *b*, whereas the transformation from B*a*P-II ($P2_1/c$) to B*a*P-III (P-1) is characterized by a decrease in symmetry. According to DFT calculations, above 3.5 GPa, B*a*P-III is the most stable phase. These studies advance our understanding of the structural dynamics and stability of PAHs under high pressure.

Keywords: high-pressure crystallography; molecular crystals; polycyclic aromatic hydrocarbons; phase transition

6.2 Introduction

Polycyclic aromatic hydrocarbons (PAHs) are complex organic compounds consisting of two or more condensed benzene rings. Due to their exceptional properties and widespread applications, these compounds have attracted significant attention from geoscientists, chemists and physicists [1-3] (Silinsh & Cápek, 1997; Farchioni, 2001; Allamandola *et al.*, 1987). PAHs are ubiquitous in interstellar space, comprising 20% of the carbon of the universe and potentially representing the most abundant free organic molecules in space [4-6] (Allamandola *et al.*, 1985; Ehrenfreund & Charnley, 2000; d'Hendecourt & Ehrenfreund, 1997). It is thought that research into the evolution of PAHs under pressure may help to understand the origins of our universe [7,8] (Mimura *et al.*, 2005; Mimura & Toyama, 2005).

Benzo[*a*]pyrene (B*a*P) is one of the two isomeric species of benzopyrene ($C_{20}H_{12}$), a representative of PAHs, formed by a benzene ring fused to pyrene. The compound is abundant [9] (Bukowska *et al.*, 2022) and can be found, for example, in coal tar as a product of incomplete combustion of organic matter at high temperatures. It is a yellow solid at ambient conditions.

Crystals of B*a*P were first described by John Iball in 1936, who obtained them from B*a*P solutions in the form of needles and plates and determined their symmetry and unit cell parameters using X-ray diffraction (XRD). The needle-shaped crystals were monoclinic ($P2_1/c$), whereas plate-shaped – orthorhombic ($P2_12_12_1$) [10] (Iball, 1936). The crystal structure of the monoclinic B*a*P was later solved [11] (Iball & Young, 1956) and refined [12] (Iball *et al.*, 1976). Subsequently, one more orthorhombic B*a*P polymorph was reported [13] (Contag, 1978). However, it turned to be unstable and gradually, within 6 months, transformed into the known monoclinic B*a*P. Low-temperature single-crystal XRD (SC-XRD) measurements at 120 K [14] (Carrell *et al.*, 1997) enabled a more precise structure analysis.

In this work, we have investigated the behavior of B*a*P in the pressure range from ambient to 35 GPa using synchrotron SC-XRD in a diamond anvil cell (DAC). We have observed two previously unknown high-pressure polymorphs, B*a*P-II and B*a*P-III, and report the results of the analysis of their structures under pressure.

6.3 Experimental

6.3.1 Sample preparation

A crystalline powder of B*a*P of 96 % purity was purchased from Merck. Single crystals were selected under an optical microscope and preselected for high-pressure XRD studies in DAC #1 at ambient pressure (see Table S6.1 for the summary of all experiments). The preselected two crystals and a piece of ruby were loaded in a membrane-type DAC#2 equipped with Boehler-Almax type diamonds [15] (Boehler, 2006) with the culets size of 250 μm and a rhenium gasket with a hole of ~120 μm in diameter and a thickness of ~30 μm. As a pressure-transmitting medium, helium (He) was used. The DAC #2 was gradually pressurized from 2.2 GPa to 35 GPa.

6.3.2 Single-crystal XRD experiments

SC-XRD studies at room temperature were conducted in DAC #1 and DAC #2 on the ID15B beamline (λ= 0.4100 Å, ESRF) with a beam size of approximately 2 × 2 μm^2. In both experiments, a micro-grain of tungsten was placed at the center of the pressure chamber along with the sample. The strong X-ray absorption signal of tungsten was used to adjust the rotation center. The pressure was determined by the ruby luminescence method [16] (Mao *et al.*, 1986). At each pressure step, the data were collected in step-scans of 0.5° upon rotating the DAC from -34° to +34° about the vertical axis (ω-scan). For single-crystal data analysis (peak search, unit cell finding, and data integration), the CrysAlisPro Software [17] (Rigaku & CrysAlis, 2015) was employed, whereas the crystal structures were determined using SHELX [18] (Sheldrick, 2008) and refined utilizing the OLEX2 software [19] (Dolomanov, 2009). Crystal structure visualization was made with the VESTA software [20] (Momma & Izumi, 2011). EoSFIT7 software [21] (Angel *et al.*, 2014) was used to fit the pressure-volume data.

6.3.3 Theoretical calculations

Our density functional theory (DFT) calculations were performed using the Vienna *ab initio* simulation package (VASP) [22] (Kresse & Furthmüller, 1996) with the Projector-Augmented-Wave (PAW) method [23] (Blöchl, 1994) and the Generalized Gradient Approximation (GGA) functional was used for calculating the exchange-correlation energy, as proposed by Perdew–Burke–Ernzerhof (PBE) [24] (Kresse & Joubert, 1999). Additionally, we employed the DFT-D3 method for dispersion correction [25] (Grimme *et al.*, 2011). The Brillouin zone was sampled with a 7×1×2 Monkhorst-Pack [26] (Monkhorst

& Pack, 1976) special k-point grid for B*a*P-I and B*a*P-II, and 7×2×1 for B*a*P-III. Furthermore, the valence states $2s^22p^2$ for C and $1s^1$ for H were used with the energy cutoff of 520 eV for the plane wave basis set. The geometries were optimized until the remaining atomic forces were less than 5×10^{-3} eV/Å and the energy convergence criterion was set at 10^{-5} eV.

6.4 Result

Upon compression of B*a*P-I ($P2_1/c$) to 4.8 GPa in He pressure medium, we observed a phase transition to a previously unknown monoclinic polymorph B*a*P-II ($P2_1/c$). The next phase transition occurred at 7.1 GPa to B*a*P-III with a triclinic structure (P-1), which was preserved up to about 28 GPa. At the next pressure step of 35 GPa, the X-ray diffraction pattern disappeared. Below we describe in detail the structures of all B*a*P polymorphs observed in this work.

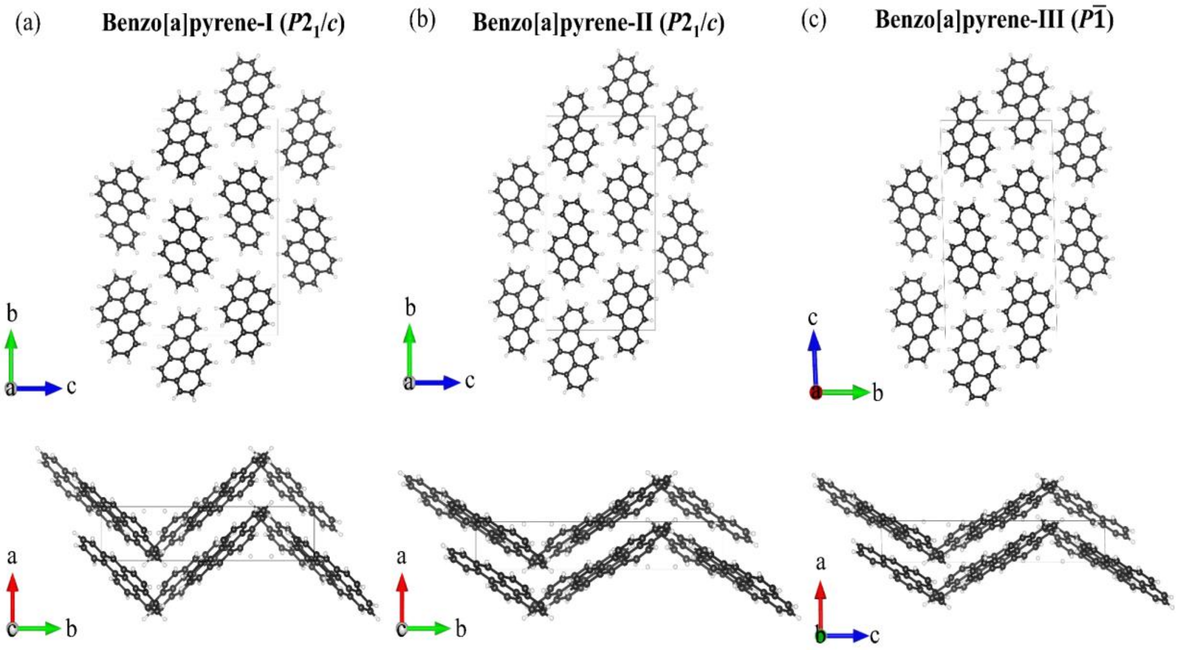

Figure 6.1 Crystal structures of B*a*P polymorphs. (a) B*a*P-I at ambient conditions, as viewed along the *a* axis (top figure) and *c* axis (bottom figure); (b) B*a*P-II at 4.8 GPa, viewed along the *a* axis (top) and *c* axis (bottom); (c) B*a*P-III at 7.1 GPa, as viewed along the *a* axis (top) and *b* axis (bottom); C atoms are black. H atoms are white.

The structure of B*a*P-I determined at ambient and 2.2 GPa (Fig. 6.1a) is similar to the previously reported monoclinic structure [14] (Carrell *et al.*, 1997). For a detailed comparison with B*a*P-I at 120 K, see Table S6.2. The structure is monoclinic (space group

#14, $P2_1/c$) with the following unit cell parameters at ambient conditions: *a* = 4.5384 (3) Å, *b* = 20.439(5) Å, *c* = 13.531(2) Å, *β* = 97.006(8) ° and V = 1245.8(4) Å^3.

The structure of the previously unknown monoclinic polymorph, B*a*P-II (space group #14, $P2_1/c$), was solved and refined at 4.8 GPa (Table S6.3, Fig. 6.1b). Its unit cell parameters are *a* = 3.59710 (10) Å, *b* = 21.658(9)Å, *c* = 12.7908(9) Å, *β* = 95.339(5) ° and V = 992.2(4) Å^3. The arrangement of molecules in B*a*P-II is similar to that in B*a*P-I. In both structures, the molecules display a herringbone pattern in projection along the *a* direction (Figs. 6.1a, b, top), but the intermolecular angles in B*a*P-I and B*a*P-II are noticeably different (see the projections along the *b* axis in Figs. 6.1a, b, bottom). In our previous study of pyrene under pressure [27] (Zhou *et al.*, 2024), we also noticed that the phase transformation of pyrene-I to pyrene-II is accompanied by a change of the intermolecular angle, whereas the space group symmetry remains the same.

Further compression of B*a*P-II led to the formation of a new triclinic polymorph, B*a*P-III (space group #2, *P*-1), which we first observed at 7.1 GPa (Fig. 6.1c). The unit cell parameters at 7.1 GPa are as follows: a = 3.4912(1) Å, b = 12.687(3) Å, c = 21.531(6) Å, α = 91.51(2) °, β = 90.434(9) °, γ = 95.820(8) ° and V = 911.5(2) Å^3. Table S6.4 provides detailed crystallographic data for B*a*P-III for six pressure points in the range of 7.1 to 27.9 GPa. As the *α* and *β* angles are very close to 90 degrees, the structure of B*a*P-III, if viewed along the *a* and *b* directions, looks very similar to those of B*a*P-I and B*a*P-II (Fig. 6.1). However, crystallographically, due to the lower symmetry, the molecular arrangement in B*a*P-III is missing the herringbone pattern. A detailed geometrical analysis of the structures in different polymorphs is given in the Discussion section below.

6.5 Discussion

6.5.1 Compressional behavior of the polymorphs of B*a*P

The compressional behaviour of the polymorphs of B*a*P up to 27.9 GPa is presented in Fig. 6.2. The values of the unit cell volume per formula unit for B*a*P-I, B*a*P-II and B*a*P-III as a function of pressure were obtained from our experiments (Table S6.5). In Fig. 6.2 they are shown by solid symbols of different colors. These pressure-volume data were fitted using the third-order Birch-Murnaghan equation of state with the volume V_0 = 311.45 Å^3, which is the volume of B*a*P-I at ambient conditions. The bulk modulus, K_0, and its first derivative, K´, were determined to be 7.7(7) GPa and 10.10(10).

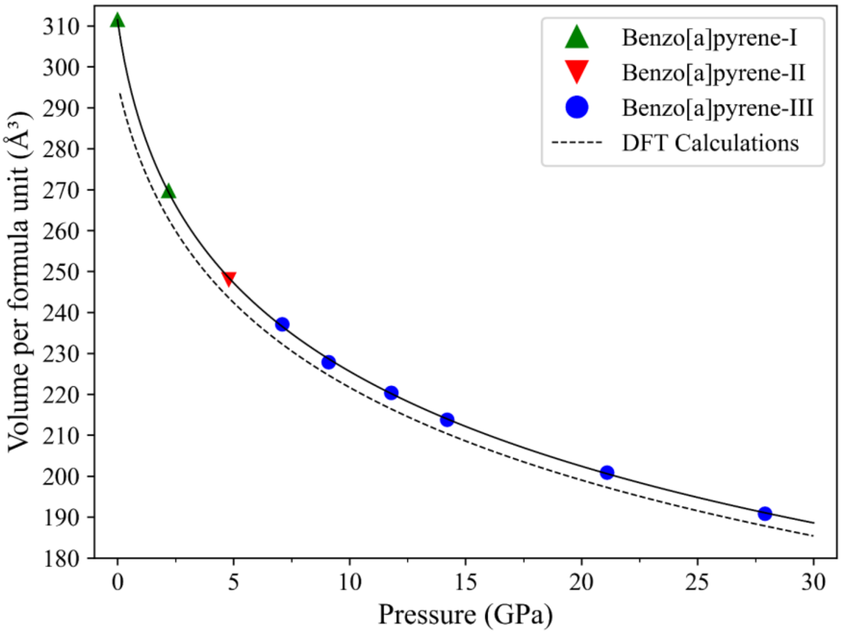

Figure 6.2 Pressure dependence of the unit cell volume per formula unit for polymorphs of B*a*P up to 27.9 GPa. The experimental data for B*a*P-I are shown by green solid triangles, for B*a*P-II - by red inversed solid triangle, and for B*a*P-III - by blue solid circles. The solid black line shows the fit of all pressure-volume experimental points using the third-order Birch-Murnaghan equation of state with the parameters V_0 = 311.45 Å^3, K_0 = 7.7(7) GPa, and K´ = 10.10(10). The dashed black line shows the fit of the calculated pressure-volume data points with the parameters V_0 = 295.92 Å^3, K_0 = 11.53(14) GPa, and K´ = 8.28(9).

The pressure-volume data points calculated using DFT for each polymorph (Table S6.6) are consistent with the pressure points at which the phases were observed experimentally. The calculated data have also been fitted using the third-order Birch-Murnaghan equation of state. The EOS parameters appeared to be as follows: V_0 = 295.92 Å^3, K_0 = 11.53(14) GPa, and K´ = 8.28(9). The volume values from the calculated data fitting are consistently lower than those from the experimental data fitting. This observation can be attributed to the fact that DFT calculations simulate the structures of polymorphs at 0K, where their volumes are always smaller than those obtained from experiments at room temperature.

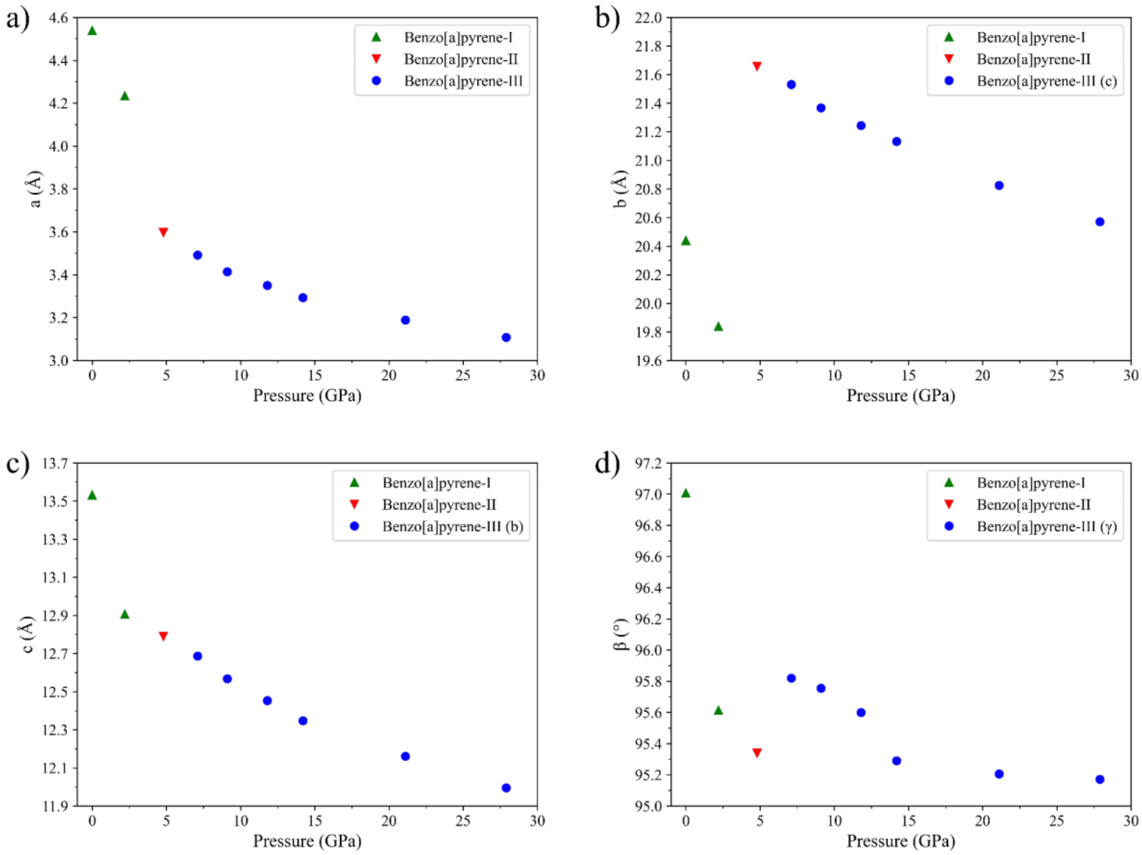

Figure 6.3 Lattice parameters of B*a*P polymorphs as a function of pressure up to 27.9 GPa. Lattice parameter *a* (a); *b* (b); *c* (c); and *β* (d) are designated in the *y* axes for the structures of B*a*P-I and B*a*P-II. For the triclinic structure of B*a*P-III the corresponding lattice parameters are given in brackets in the legend. (As α and β angles in the triclinic structure of B*a*P-III are very close to 90 degrees, then *b* of B*a*P-I and B*a*P-II corresponds to *c* in B*a*P-III and *vice versa*, while β corresponds to γ in B*a*P-III). Green solid triangles relate to B*a*P-I, red inversed solid triangle- to B*a*P-II, blue solid circles- to B*a*P-III.

The dependences of the lattice parameters of B*a*P polymorphs on pressure are shown in Fig. 6.3 (see Table S6.7 for numerical values). Upon compression of B*a*P-I, the *a* and *b* parameters gradually shorten, but they change substantially upon the transition from B*a*P-I to B*a*P-II: the value of the *a* parameter decreases from 4.2338(2) Å to 3.59710(10) Å, while the *b* parameter increases from 19.838(4) Å to 21.658(9) Å. The *c* parameter continuously shortens in all phases. The *β* angle decreases from 97.006(8) ° to 95.613(5) ° upon compression of B*a*P-I at pressures still below about 3 GPa. After a phase transition at 4.8 GPa it slightly rises to 95.820(8) ° in B*a*P-III and does not considerably change upon its compression to the maximum pressure of about 28 GPa.

6.5.2 Theoretical Calculations

DFT calculations were conducted at ten pressure points between 1 bar and 40 GPa. Relaxed structural parameters are detailed in Tables S6.8-S6.10, which include data for B*a*P-I at ambient pressure, B*a*P-II at 4.8 GPa, and B*a*P-III at 7.1 GPa.

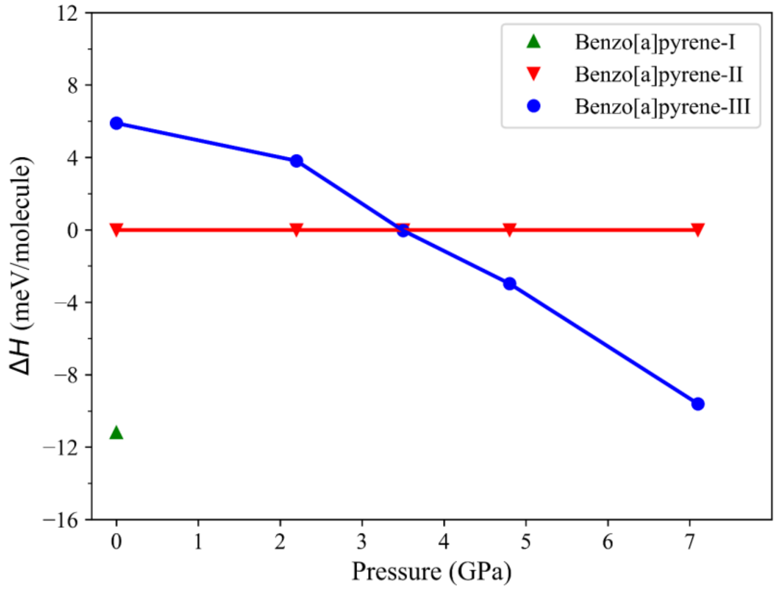

Figure 6.4 The enthalpy differences (ΔH) for the two polymorphs (B*a*P-I and B*a*P-III) relative to B*a*P-II calculated up to 7.1 GPa. Designations for different polymorphs are as follows: for B*a*P-I - green solid triangle, B*a*P-III - blue solid circles, B*a*P-II - red inversed solid triangles.

The enthalpy differences (ΔH) for the two polymorphs (B*a*P-I and B*a*P-III) relative to B*a*P-II were calculated as a function of pressure from ambient pressure up to 7.1 GPa at 0 K (Fig. 6.4) as described in Methods. They revealed that at ambient pressure, B*a*P-I is relatively more stable than B*a*P-II and B*a*P-III. We found that at 2.2 GPa, B*a*P-I relaxed into an atomic configuration with an enthalpy much higher than that of B*a*P-II and B*a*P-III. At 3.5 GPa, starting from the atomic configuration of B*a*P-I, atomic positions relaxed to those of B*a*P-II. According to the calculations, above 3.5 GPa, B*a*P-III is the most stable phase.

6.5.3 Geometrical analysis of the structures of B*a*P polymorphs

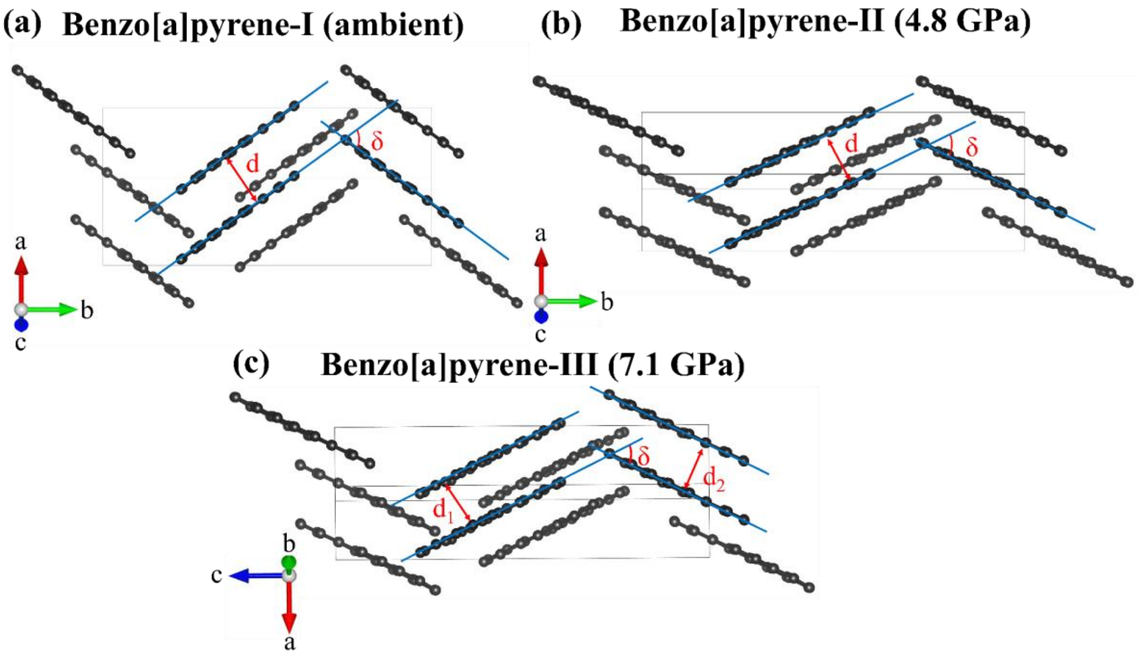

Figure 6.5 Visualization of intermolecular distances and interplanar angles in the structures of B*a*P polymorphs. (a) B*a*P-I and (b) B*a*P-II, as viewed along the [5 0 4] direction; (c) B*a*P-III, as viewed along the [5 4 0] direction. (H atoms are not shown. C atoms are black dots.) The blue lines represent the planes of the flat molecules; in B*a*P-I and B*a*P-II all intermolecular distances are equal (designated as d); d_1 and d_2 are the interplanar distances in B*a*P-III, which are almost equal; δ is the interplanar angle.

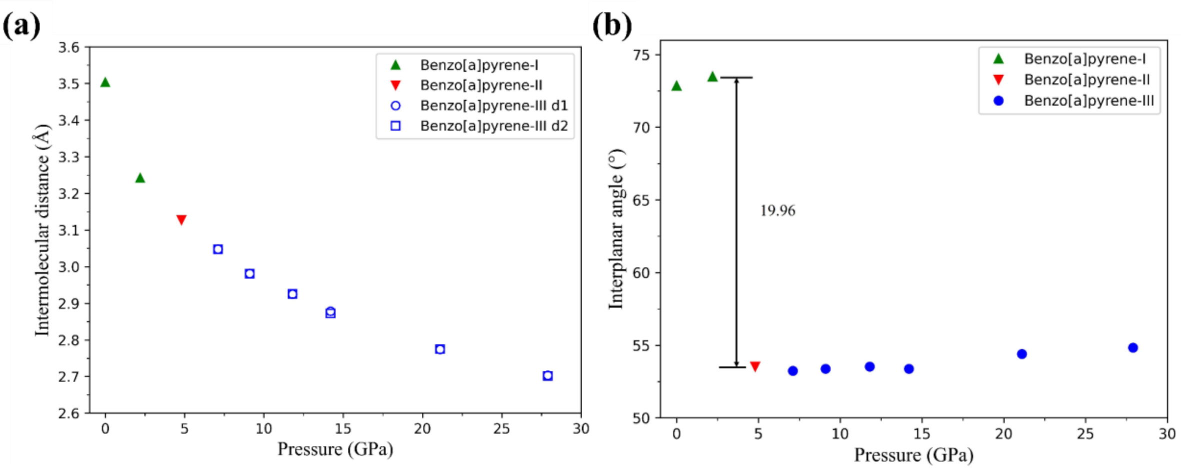

Figure 6.6 Variation of intermolecular distances and interplanar angles in B*a*P polymorphs with pressure. a) Intermolecular distances (see Fig. 6.5 for designations); b) interplanar angles (see Fig. 6.5 for δ).

Figure 6.5 illustrates the structures of B*a*P-I and B*a*P-II viewed along the [5 4 0] direction (Fig. 6.5a, b), and of B*a*P-III viewed along the [5 0 4] direction (Fig. 6.5c), chosen to optimally display the topology of the molecular structures of these different polymorphs. To accurately calculate the intermolecular distances in B*a*P polymorphs, the molecules were approximated by mean molecular planes considering 20 carbon atoms in a molecule, using the NumPy and SciPy libraries in Python (blue lines in Fig. 6.5). The intermolecular distances (d, d_1, and d_2) and interplanar angles (δ) were calculated using the same software. They are listed in Table S6.11 and presented graphically in Fig. 6.6 as a function of pressure. It is clear that the structure of B*a*P-I undergoes gradual compaction upon compression characterized by a gradual decrease of intermolecular distances (Fig. 6.6a). The intermolecular angle in B*a*P-I changes slightly from 72.9° at ambient pressure to 73.5° at 2.2 GPa, while upon the B*a*P-I to B*a*P-II transformation, the applied stress leads to an abrupt change in the intermolecular angle from 73.5° at 2.2 GPa in B*a*P-I to 53.5° at 4.8 GPa in B*a*P-II. Further compression of B*a*P-II to 7.1 GPa results in the decrease of symmetry to *P*-1, indicating a transformation to B*a*P-III. Upon further compression of B*a*P-III from 4.8 GPa to 27.9 GPa, the angle slowly rises to 54.8°. Interestingly, compared to the behaviour of pyrene molecules, which showed curvature with increasing pressure, as found in our previous study of pyrene [27] (Zhou *et al.*, 2024), in B*a*P polymorphs the molecules remain flat up to about 28 GPa, the highest pressure achieved in this study.

6.5.4 Evolution of intermolecular interactions upon compression

To visualize intermolecular interactions and explore their evolution upon compression, we constructed Hirshfeld surfaces for the three B*a*P polymorphs using the CrystalExplorer program [28] (Spackman *et al.*, 2021). Those mapped with shape index are shown in Fig. 6.7. Corresponding fingerprint plots are provided in Figure S6.1. The methodology of the Hirshfeld surface analysis is described in detail in a comprehensive review by McKinnon *et al.* (2004) [29] and in the paper by Spackman & Jayatilaka (2009) [30].

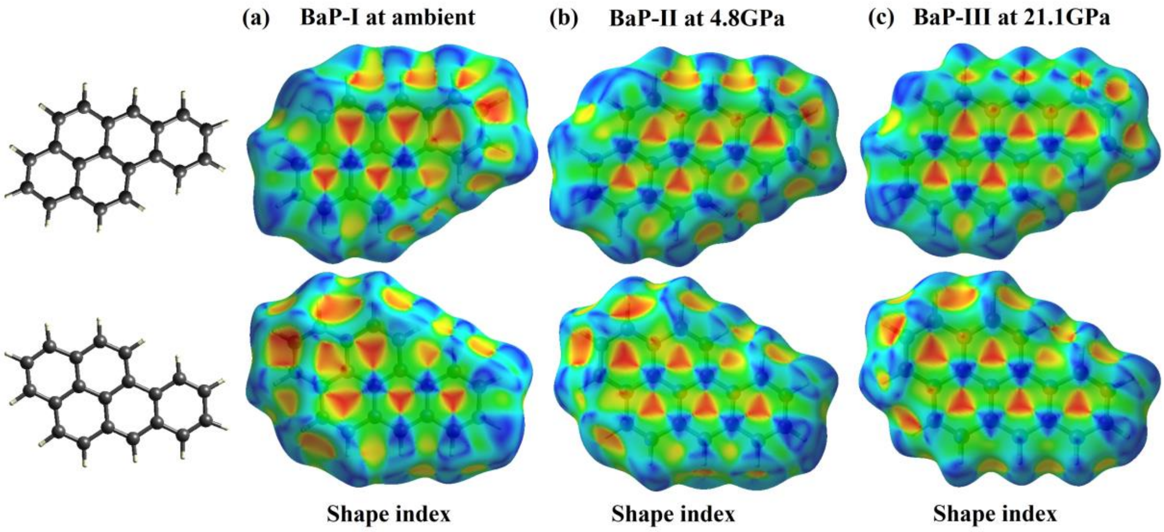

Figure 6.7 Hirshfeld surfaces of B*a*P polymorphs mapped with shape index. The front and back views of Hirshfeld surfaces for (a) B*a*P-I molecule at ambient, (b) B*a*P-II molecule at 4.8GPa, and (c) B*a*P-III molecule at 21.1 GPa. Shape index is mapped from -1.0 (red) to 0.0 (green) to 1.0 (blue).

The analysis of the Hirshfeld surfaces of B*a*P polymorphs— even based purely on visual inspection— shows that the two sides of a molecule are involved in quite similar contacts with neighboring molecules, participating in in a planar stacking arrangement of molecules ($\pi\cdots\pi$ stacking) showing up as the alternating red and blue triangles in both front and back sides of the Hirshfeld surfaces [29] [30] (McKinnon *et al.*, 2004; Spackman & Jayatilaka, 2009) (Fig. 6.7), as well as a red region near the centre of the fingerprint plot (Fig. S6.1). These features are quite obvious for all polymorphs (Figs. 6.7, S6.1). For B*a*P-I the red region in the fingerprint plot is in the vicinity of (d_i, d_e) ~ 1.8 - 2.0 Å, a range typical of the interplanar spacing of polycyclic aromatic hydrocarbons (d_i and d_e are the distances from the internal or external atoms to the Hirshfeld surface). With pressure this red feature is moving to lower (d_i, d_e) values, indicating a decrease of the intermolecular distances (see also Fig. 6.6a). The blue color specifies convex surface curvatures of the Hirshfeld surface corresponding to the direct H···H contacts. The red-colored regions of concave curvature reflect the C···H interactions between the molecules.

One can break down the Hirshfeld surface into patches associated with specific atom-type/atom-type pairs, to highlight just those regions on the surface, and sum the areas of surface patches associated with various contacts [30] (Spackman & Jayatilaka, 2009). We have made the calculations using the CrystalExplorer program for all B*a*P polymorphs as a function of pressure (Table S6.12). As seen, for B*a*P-I, H···H interactions are associated with nearly 60% of the surface area, whereas the contribution of C···C interactions is of about 20%, and the sum of all C···H interactions is also of about 20 %. Figure S6.2 presents percentage contributions to the Hirschfeld surface area for the various close intermolecular contacts (C···C, H···H, $\mathrm{C_e}\cdots\mathrm{H_i}$, and $\mathrm{C_i}\cdots\mathrm{H_e}$) as a function of pressure for molecules in B*a*P polymorphs. The percentage contribution of C···C intermolecular contacts increases with pressure, while that of H···H contacts decreases, showing an abrupt change upon B*a*P-I to B*a*P-II transition: While C···C contribution still shows increase (although nonmonotonic), the H···H contribution goes up, likely as a result of a sharp decrease of the interplanar angle by about 20 degrees. The C···H contribution decreases, as there is a decrease of the offset of stacked molecules upon B*a*P-I to B*a*P-II transition. Contrary, upon the B*a*P-II to B*a*P-III transition, there are no abrupt changes in the percentage contribution of direct H···H contacts (it continues to decrease monotonously), while that of C···C contacts monotonously increases, and the total C···H contribution almost does not change. The shortest H···H contacts considerably decrease in B*a*P-II compared to those in B*a*P-I, but do not noticeably decrease upon further compression (see the positions of the sharp features in the left lower corners of the fingerprint plots for B*a*P-I, and B*a*P-III in Fig. S6.1). To summarize, in all three polymorphs, the molecules are involved in similar contacts with neighboring molecules, participating in a planar stacking arrangement. A general trend is observed with an increase in the percentage contribution of C···C intermolecular contacts and a decrease in H···H contacts upon compression.

6.6 Conclusions

Here we presented the results of high-pressure studies of benzo[*a*]pyrene up to about 28 GPa. They provide insights into the structural transformations in a representative of a broad class of organic materials - polycyclic aromatic hydrocarbons. These studies combined *in situ* single-crystal synchrotron X-ray diffraction in a diamond anvil cell and *ab initio* calculations. At 4.8 GPa, B*a*P-I was found to transform to a previously unknown B*a*P-II phase with the same space group ($P2_1/c$). The transformation manifests as an abrupt change in the intermolecular angle and in the unit cell parameters. The second previously unknown polymorph, B*a*P-III, was detected at 7.1 GPa and preserved in He pressure medium up to 27.9 GPa. According to the DFT calculations, above 3.5 GPa, B*a*P-III is the most stable phase.

6.7 Related literature

The following references are cited in the supporting information: Carrell *et al.* [14] (1997).

6.8 Acknowledgements

The authors acknowledge the European Synchrotron Radiation Facility (ESRF) for the provision of beamtime at the ID15b beamline. Computations were performed at the Leibniz Supercomputing Center of the Bavarian Academy of Sciences and the Humanities, and the research center for scientific computing at the University of Bayreuth. N.D. and L.D. thank the Deutsche Forschungsgemeinschaft (DFG; projects LA 4916/1-1, DU 945–15-1, DU 393–9/2, DU 393–13/1) for financial support. N.D. also thanks the Swedish Government Strategic Research Area in Materials Science on Functional Materials at Linköping University (Faculty Grant SFO-Mat-LiU No. 2009 00971).

Financial support from the following funders is highly appreciated:

The Deutsche Forschungsgemeinschaft (DFG projects DU 945/15-1; LA 4916/1-1; DU 393–9/2, DU 393–13/1). The Swedish Government Strategic Research Area in Materials Science on Functional Materials at Linköping University (Faculty Grant SFO-Mat-LiU No. 2009 00971).

6.9 Supplementary materials

Table S6.1 Summary of the experiments conducted in this work.

DAC number	DAC type	Anvils type/ culet size, μm	Starting material/ pressure transmitting medium	Beamline/XRD wavelength, Å	Result	Pressure, GPa
1	Membrane-type	Boehler-Almax 250	B*a*P-I/ No medium	ID15B ESRF, 0.4100	B*a*P-I	ambient
2	Membrane-type	Boehler-Almax 250	B*a*P-I/ Helium	ID15B ESRF, 0.4100	B*a*P-I	2.2(3)
					B*a*P-II	4.8(3)
					B*a*P-III	7.1(3) 9.1(3) 11.8(3) 14.2(4) 21.1(3) 27.9(4)

Table S6.2 Experimental crystallographic data for B*a*P-I obtained by single-crystal X-ray diffraction at room temperature, at ambient pressure and at 2.2 GPa in this work and at low temperature at ambient pressure in ref. [14] (Carrell *et al.*, 1997).

	B*a*P-I at ambient	B*a*P-I at 2.2 GPa	B*a*P-I at 120 K
CCDC deposition number	2360829	2360830	1830498
Crystal data			
Chemical formula	$C_{20}H_{12}$	$C_{20}H_{12}$	$C_{20}H_{12}$
M_r	252.30	252.30	252.30
Crystal system, space group	Monoclinic, $P2_1/c$	Monoclinic, $P2_1/c$	Monoclinic, $P2_1/c$
a, b, c (Å)	4.5384(3), 20.439(5), 13.531(2)	4.2338(2), 19.838(4), 12.9059(10)	4.489(1), 20.309(6), 13.372(5)
α, β, γ (°)	90, 97.006(8), 90	90, 95.613(5), 90	90, 96.59(2), 90
V (Å^3)	1245.8(4)	1078.8(2)	1211.0(6)
Z	4	4	4
Density (Mg/m^3)	1.345	1.553	1.384
Wavelength (Å)	0.4100	0.4100	0.7107
μ (mm^{-1})	0.035	0.040	0.08
Data collection			
Absorption correction	Multi-scan	Multi-scan	
T_{min}, T_{max}	0.30, 1.00	0.08, 1.00	
No. of measured, independent and observed reflections	3094, 1877, 661	2644, 1646, 831	
R_{int}	0.035	0.013	
θ_{max} (°)	21.63	21.35	
Refinement			
Refinement on	F^2	F^2	
$R[F^2>2\sigma(F^2)]$, $wR(F^2)$, S	0.060, 0.145, 0.901	0.069, 0.218, 0.978	
Data / restraints / parameters	1877/ 0/ 181	1646/ 0/ 181	
H-atom treatment	Refined by ride model	Refined by ride model	
Weighting scheme	$w = 1/ [\sigma^2 (F_o^2) + (0.0949P)^2]$, where $P= (F_o^2+2F_c^2)/3$	$w = 1/ [\sigma^2 (F_o^2) + (0.1566P)^2]$, where $P= (F_o^2+2F_c^2)/3$	$w = 1/ [\sigma^2 (F_o^2)]$
$\Delta\rho_{max}$, $\Delta\rho_{min}$ (e Å^{-3})	0.08, -0.10	0.25, -0.20	

Table S6.3 Experimental crystallographic data for B*a*P-II obtained by single-crystal X-ray diffraction at room temperature at 4.8 GPa in this work.

	B*a*P-II at 4.8 GPa
CCDC deposition number	2360831
Crystal data	
Chemical formula	$C_{20}H_{12}$
M_r	252.30
Crystal system, space group	Monoclinic, $P2_1/c$
a, b, c (Å)	3.59710(10), 21.658(9), 12.7908(9)
α, β, γ (°)	90, 95.339(5), 90
V (Å^3)	992.2(4)
Z	4
Density (Mg/m^3)	1.689
Wavelength (Å)	0.4100
μ (mm^{-1})	0.044
Data collection	
Absorption correction	Multi-scan
T_{min}, T_{max}	0.19, 1.00
No. of measured, independent and observed reflections	2486, 1313, 796
R_{int}	0.020
θ_{max} (°)	21.49
Refinement	
Refinement on	F^2
$R[F^2>2\sigma(F^2)]$, $wR(F^2)$, S	0.052, 0.141, 0.959
Data / restraints / parameters	1313/ 0/ 181
H-atom treatment	Refined by ride model
Weighting scheme	$w = 1/ [\sigma^2 (F_o^2) + (0.1059P)^2]$, where $P = (F_o^2 + 2F_c^2)/3$
$\Delta\rho_{max}$, $\Delta\rho_{min}$ (e Å^{-3})	0.20, -0.16

Table S6.4 Experimental crystallographic data for B*a*P-III obtained by single-crystal X-ray diffraction at room temperature and a series of pressures in this work.

	B*a*P-III at 7.1 GPa	B*a*P-III at 9.1 GPa
CCDC deposition number	2360832	2360833
Crystal data		
Chemical formula	$C_{20}H_{12}$	$C_{20}H_{12}$
M_r	252.30	252.30
Crystal system, space group	Triclinic, *P*-1	Triclinic, *P*-1
a, b, c (Å)	3.49120(10), 12.687(3), 21.531(6)	3.41340(10), 12.5674(19), 21.367(5)
α, β, γ (°)	91.51(2), 90.434(9), 95.820(8)	91.675(15), 90.433(7), 95.755(6)
V ($Å^3$)	948.4(3)	911.5(2)
Z	4	4
Density (Mg/m^3)	1.767	1.838
Wavelength (Å)	0.4100	0.4100
μ (mm^{-1})	0.046	0.048
Data collection		
Absorption correction	Multi-scan	Multi-scan
T_{min}, T_{max}	0.16, 1.00	0.36, 1.00
No. of measured, independent and observed reflections	2260, 1531, 867	2374, 1617, 1036
R_{int}	0.031	0.017
θ_{max} (°)	20.99	21.30
Refinement		
Refinement on	F^2	F^2
$R[F^2>2\sigma(F^2)]$, $wR(F^2)$, S	0.063, 0.142, 0.942	0.051, 0.129, 0.949
Data / restraints / parameters	1534/ 84/ 361	1617/ 24/ 361
H-atom treatment	Refined by ride model	Refined by ride model
Weighting scheme	$w = 1/[\sigma^2(F_o^2) + (0.0973P)^2]$, where $P = (F_o^2 + 2F_c^2)/3$	$w = 1/ [\sigma^2 (F_o^2) + (0.1029P)^2]$, where $P= (F_o^2+2F_c^2)/3$
$\Delta\rho_{max}$, $\Delta\rho_{min}$ (e $Å^{-3}$)	0.20, -0.15	0.18, -0.19

Table S6.4 (continuation)

B*a*P-III at 11.8 GPa	B*a*P-III at 14.2GPa	B*a*P-III at 21.1 GPa	B*a*P-III at 27.9 GPa
2360834	2360835	2360836	2360837
$C_{20}H_{12}$	$C_{20}H_{12}$	$C_{20}H_{12}$	$C_{20}H_{12}$
252.30	252.30	252.30	252.30
Triclinic, *P*-1	Triclinic, *P*-1	Triclinic, P-1	Triclinic, P-1
3.35010(10), 12.453(2), 21.244(5) 91.709(18), 90.417(8), 95.599(7) 881.6(3)	3.2931(2), 12.347(4), 21.133(7) 91.42(3), 90.439(11), 95.290(11) 855.3(4)	3.1883(4), 12.1605(18), 20.825(6) 91.99(2), 90.297(18), 95.206(11) 803.6(3)	3.1077(4), 11.995(2), 20.571(8) 91.56(3), 89.92(3), 95.171(13) 763.4(3)
4	4	4	4
1.901	1.959	2.085	2.195
0.4100	0.4100	0.4100	0.4100
0.049	0.051	0.054	0.057
Multi-scan	Multi-scan	Multi-scan	Multi-scan
0.04, 1.00	0.02, 1.00	0.06, 1.00	0.04, 1.00
2203, 1482, 979	2119, 1448, 790	1711, 1242, 801	1034, 801, 446
0.023	0.022	0.023	0.066
21.32	21.30	21.17	16.08
F^2	F^2	F^2	F^2
0.057, 0.152, 0.972	0.076, 0.199, 1.005	0.063, 0.184, 0.986	0.125, 0.305, 1.584
1482/ 78/ 361	1448/ 90/ 361	1242/ 72/ 361	801/ 0/ 361
Refined by ride model	Refined by ride model	Refined by ride model	Refined by ride model
$w = 1/[\sigma^2(F_o^2) + (0.1282P)^2]$, where $P = (F_o^2 + 2F_c^2)/3$	$w = 1/ [\sigma^2 (F_o^2) + (0.1529P)^2]$, where $P = (F_o^2 + 2F_c^2)/3$	$w = 1/[\sigma^2(F_o^2) + (0.1784P)^2]$, where $P = (F_o^2 + 2F_c^2)/3$	$w = 1/[\sigma^2(F_o^2) + (0.2P)^2]$, where $P = (F_o^2 + 2F_c^2)/3$
0.21, -0.18	0.23, -0.20	0.18, -0.16	0.23, -0.23

Table S6.5 Unit cell volume per formula unit for B*a*P polymorphs up to 27.9 GPa in this work.

Polymorph/ pressure transmitting medium	Pressure, GPa	Volume per formula unit, Å^3
B*a*P-I/ No medium	0	311.45(10)
B*a*P-I/ He	2.2(3)	269.70(5)
B*a*P-II/ He	4.8(3)	248.05(10)
B*a*P-III/ He	7.1(3)	237.10(8)
B*a*P-III/ He	9.1(3)	227.88(5)
B*a*P-III/ He	11.8(3)	220.40(8)
B*a*P-III/ He	14.2(4)	213.83(10)
B*a*P-III/ He	21.1(3)	200.90(8)
B*a*P-III/ He	27.9(4)	190.85(8)

Table S6.6 DFT-calculated unit cell volume per formula unit of B*a*P polymorphs up to 40 GPa.

Polymorph	Pressure (GPa)	Volume per formula unit (Å^3)
B*a*P-I	0	295.92
B*a*P-I	2.2	263.06
B*a*P-II	4.8	243.28
B*a*P-III	7.1	231.74
B*a*P-III	11.8	216.64
B*a*P-III	14.2	210.16
B*a*P-III	21.1	197.29
B*a*P-III	27.9	187.86
B*a*P-III	40	175.72

Table S6.7 Lattice parameters of B*a*P polymorphs up to 35.5 GPa determined in this work.

Polymorph/ pressure transmitting medium	Pressure , GPa	a, Å	b, Å	c, Å	α, °	β, °	γ, °
B*a*P-I/No medium	0	4.5384(3)	20.439(5)	13.531(2)	90	97.006(8)	90
B*a*P-I/ He	2.2(3)	4.2338(2)	19.838(4)	12.9059(1)	90	95.613(5)	90
B*a*P-II/ He	4.8(3)	3.5971(1)	21.658(9)	12.7908(9)	90	95.339(5)	90
B*a*P-III/ He	7.1(3)	3.4912(1)	12.687(3)	21.531(6)	91.51(2)	90.434(9)	95.820(8)
B*a*P-III/ He	9.1(3)	3.4134(1)	12.5674(19)	21.367(5)	91.675(15)	90.433(7)	95.755(6)
B*a*P-III/ He	11.8(3)	3.3501(1)	12.453(2)	21.244(5)	91.709(18)	90.417(8)	95.599(7)
B*a*P-III/ He	14.2(4)	3.2931(2)	12.347(4)	21.133(7)	91.42(3)	90.439(11)	95.290(11)
B*a*P-III/ He	21.1(3)	3.1883(4)	12.1605(18)	20.825(6)	91.99(2)	90.297(18)	95.206(11)
B*a*P-III/ He	27.9(4)	3.1077(4)	11.995(2)	20.571(8)	91.56(3)	89.92(3)	95.171(13)

Table S6.8a DFT-calculated crystallographic data for B*a*P-I at ambient pressure.

B*a*P-I	
Chemical formula	$C_{20}H_{12}$
M_r	252.30
Crystal system, space group	Monoclinic, $P2_1/c$
a, b, c (Å)	4.444, 20.315, 13.195
α, β, γ (°)	90, 96.396,90
V (Å^3)	1183.690
Z	4

Table S6.8b Theoretical atomic coordinates for B*a*P-I at ambient pressure.

Label	x	y	z
C1	0.6790	0.4583	0.6470
C2	0.2430	0.6537	0.5536
C3	0.3121	0.6115	0.7308
C4	0.5244	0.6632	0.7563
C5	0.2424	0.5656	0.8060
C6	0.5900	0.6233	0.9325
C7	0.5948	0.7092	0.6804
C8	0.8901	0.5094	0.6748
C9	0.1693	0.6064	0.6277
C10	0.0304	0.5134	0.7781
C11	0.3868	0.5737	0.9074
C12	0.9631	0.5562	0.6023
C13	0.6678	0.6693	0.8581
C14	0.9531	0.4648	0.8478
C15	0.8799	0.7201	0.8819
C16	0.4469	0.7027	0.5783
C17	0.7480	0.4154	0.8185
C18	0.8063	0.7591	0.7076
C19	0.9482	0.7642	0.8073
C20	0.6076	0.4122	0.7170
H1	0.1299	0.6491	0.4763
H2	0.5027	0.7379	0.5207
H3	0.0582	0.4660	0.9264
H4	0.6927	0.3788	0.8739
H5	0.8628	0.7940	0.6498
H6	0.6977	0.6281	0.0107
H7	0.3346	0.5398	0.9669
H8	0.5747	0.4562	0.5683
H9	0.8549	0.5526	0.5241
H10	0.9920	0.7240	0.9595
H11	0.4427	0.3736	0.6951
H12	0.1155	0.8028	0.8256

Table S6.9a Theoretical crystallographic data for B*a*P-II at 4.8 GPa.

B*a*P-II	
Chemical formula	$C_{20}H_{12}$
M_r	252.30
Crystal system, space group	Monoclinic, $P2_1/c$
a, b, c (Å)	3.537, 21.750, 12.695
α, β, γ (°)	90, 94.906, 90
V (Å^3)	973.124
Z	4

Table S6.9b Theoretical atomic coordinates for B*a*P-II at 4.8 GPa.

Label	x	y	z
C1	0.9537	0.4918	0.2184
C2	0.4973	0.3363	0.2351
C3	0.6992	0.3909	0.2639
C4	0.0468	0.4521	0.3997
C5	0.7517	0.4368	0.1873
C6	0.7902	0.3520	0.4469
C7	0.4095	0.3734	0.0532
C8	0.3502	0.3272	0.1287
C9	0.1017	0.4987	0.3260
C10	0.3051	0.5526	0.3568
C11	0.2096	0.5923	0.1801
C12	0.2403	0.2371	0.2816
C13	0.8489	0.3991	0.3715
C14	0.3600	0.5985	0.2858
C15	0.1463	0.2734	0.1017
C16	0.0955	0.2288	0.1770
C17	0.5881	0.3007	0.4191
C18	0.6034	0.4260	0.0814
C19	0.4397	0.2905	0.3124
C20	0.0121	0.5401	0.1475
H1	0.1593	0.4584	0.4813
H2	0.9128	0.3590	0.5274
H3	0.2942	0.3663	0.9719
H4	0.4168	0.5568	0.4387
H5	0.2528	0.6288	0.1237
H6	0.1950	0.2020	0.3403
H7	0.5264	0.6388	0.3101
H8	0.0264	0.2675	0.0207
H9	0.9324	0.1878	0.1559
H10	0.5351	0.2662	0.4778
H11	0.6449	0.4602	0.0214
H12	0.8967	0.5365	0.0658

Table S6.10a Theoretical crystallographic data for B*a*P-III at 7.1 GPa.

B*a*P-III	
Chemical formula	$C_{20}H_{12}$
M_r	252.30
Crystal system, space group	Triclinic, *P*-1
a, *b*, *c* (Å)	3.434, 12.608, 21.532
α, *β*, *γ* (°)	91.558, 90.403, 95.870
V (Å^3)	926.940
Z	4

Table S6.10b Theoretical atomic coordinates for B*a*P-III at 7.1 GPa.

Label	x	y	z
C1	0.9737	0.2128	0.4938
C2	0.0462	0.2785	0.9915
C3	0.5217	0.2449	0.3370
C4	0.5244	0.2695	0.8356
C5	0.7295	0.2685	0.3936
C6	0.3165	0.2371	0.8895
C7	0.1062	0.3977	0.4615
C8	0.9709	0.0960	0.9478
C9	0.7678	0.1874	0.4366
C10	0.2520	0.3128	0.9370
C11	0.8464	0.4557	0.3630
C12	0.2402	0.0531	0.8460
C13	0.4083	0.0586	0.3660
C14	0.5889	0.4527	0.8764
C15	0.3607	0.1389	0.3227
C16	0.6626	0.3782	0.8288
C17	0.1448	0.3194	0.5054
C18	0.9053	0.1688	0.9961
C19	0.3546	0.3447	0.5613
C20	0.6975	0.1351	0.0495
C21	0.2144	0.1651	0.5944
C22	0.7814	0.3129	0.0935
C23	0.2689	0.3011	0.2389
C24	0.8076	0.2277	0.7361
C25	0.8992	0.3753	0.4067
C26	0.1743	0.1272	0.8952
C27	0.3864	0.2697	0.6052
C28	0.6326	0.2051	0.0971
C29	0.1522	0.1171	0.2670
C30	0.8722	0.4091	0.7758
C31	0.1126	0.1968	0.2254
C32	0.9430	0.3349	0.7300
C33	0.6248	0.4336	0.3109

C34	0.4447	0.0850	0.7949
C35	0.6033	0.0824	0.4209
C36	0.3908	0.4211	0.9285
C37	0.4695	0.3271	0.2948
C38	0.5943	0.1937	0.7880
C39	0.0145	0.1373	0.5398
C40	0.9820	0.3482	0.0416
H1	0.2360	0.4782	0.4721
H2	0.8647	0.0128	0.9524
H3	0.9817	0.5359	0.3734
H4	0.1201	0.9706	0.8507
H5	0.2821	0.9776	0.3550
H6	0.6952	0.5359	0.8706
H7	0.4892	0.4253	0.5694
H8	0.5919	0.0515	0.0523
H9	0.2455	0.1054	0.6291
H10	0.7380	0.3680	0.1320
H11	0.2308	0.3634	0.2061
H12	0.8671	0.1697	0.6999
H13	0.5524	0.2902	0.6475
H14	0.4605	0.1780	0.1367
H15	0.0188	0.0367	0.2573
H16	0.9822	0.4924	0.7718
H17	0.9462	0.1793	0.1828
H18	0.1113	0.3588	0.6895
H19	0.5623	0.4965	0.2801
H20	0.4970	0.0284	0.7579
H21	0.6350	0.0194	0.4532
H22	0.3370	0.4804	0.9639
H23	0.8827	0.0560	0.5326
H24	0.0964	0.4312	0.0396

Table S6.11 Intermolecular distances and interplanar angles of B*a*P polymorphs up to 27.9 GPa from experiments in helium pressure medium.

Polymorph	Pressure, GPa	Intermolecular distance d_1, Å	Intermolecular distance d_2, Å	Interplanar angle, °
B*a*P-I	0	3.503	3.503	72.85
B*a*P-I	2.2	3.242	3.242	73.49
B*a*P-II	4.8	3.127	3.127	53.53
B*a*P-III	7.1	3.048	3.047	53.24
B*a*P-III	9.1	2.981	2.981	53.38
B*a*P-III	11.8	2.925	2.926	53.53
B*a*P-III	14.2	2.878	2.873	53.38
B*a*P-III	21.1	2.774	2.775	54.40
B*a*P-III	27.9	2.703	2.701	54.83

Table S6.12 Percentage contributions to the Hirschfeld surface area for the various close intermolecular contacts ($C\cdots C$, $H\cdots H$, $C_e\cdots H_i$, $C_i\cdots H_e$) as a function of pressure for molecules in B*a*P polymorphs.

Polymorph	Pressure, GPa	$C\cdots C$, %	$H\cdots H$, %	$C_e\cdots H_i$, %	$C_i\cdots H_e$, %
B*a*P-I	0	20.9	57.9	7.6	13.6
B*a*P-I	2.2	22.4	54.2	8.4	15.1
B*a*P-II	4.8	27.3	55.7	5.4	11.6
B*a*P-III	7.1	27.6	54.6	5.7	12.1
B*a*P-III	9.1	28.5	53.9	5.6	12.0
B*a*P-III	11.8	29.0	53.3	5.5	12.1
B*a*P-III	14.2	29.8	52.8	5.5	11.9
B*a*P-III	21.1	30.5	51.5	5.6	12.5

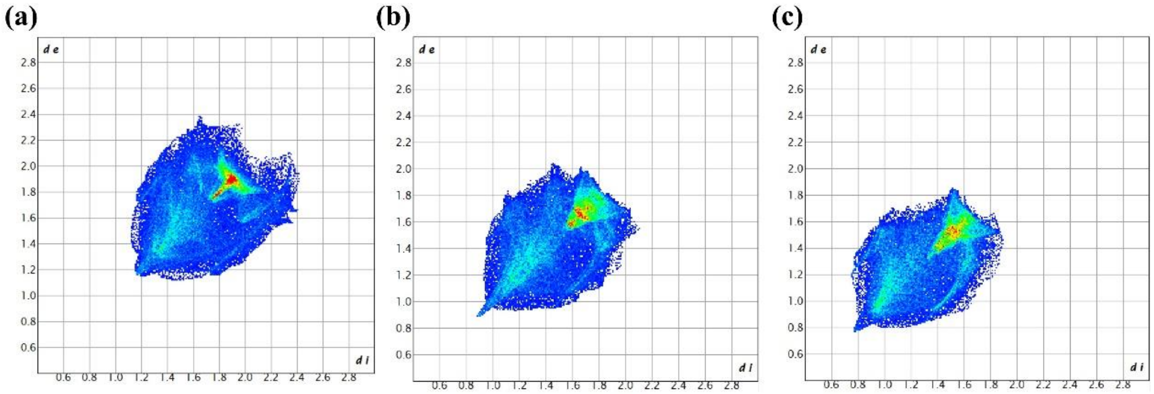

B*a*P-I at ambient **B*a*P-II at 4.8GPa** **B*a*P-III at 21.1GPa**

Figure S6.1 Fingerprint plots for B*a*P polymorphs. (a) B*a*P-I molecule at ambient, (b) B*a*P-II molecule at 4.8 GPa, and (c) B*a*P-III molecule at 21.1GPa.

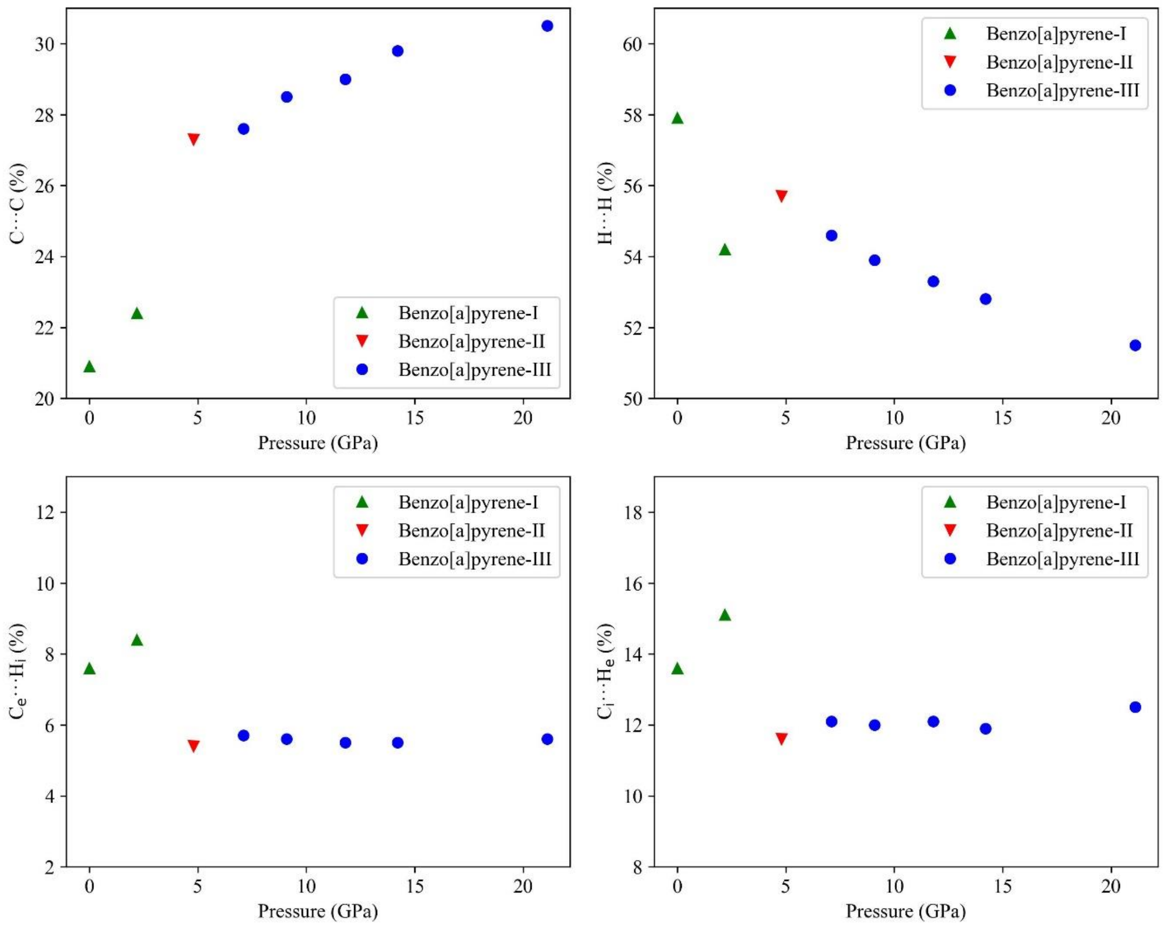

Figure S6.2 Percentage contribution to the Hirschfeld surface area for the various close intermolecular contacts (C···C, H···H, $C_e \cdots H_i$, $C_i \cdots H_e$) as a function of pressure for molecules in B*a*P polymorphs.

References

[1] Silinsh, E. A. and Cápek, V. Organic Molecular Crystals: Interaction, Localization, and Transport Phenomena. *(No Title)* (1997).

[2] Farchioni, R. Organic Electronic Materials: Conjugted Polymers and Low Molecular Weight Electronic Solids. *Springer Sci & Business Media* **41** (2001).

[3] Allamandola, L. J., Sandford, S. A. and Wopenka, B. *Science* **237(4810)**, 56-59 (1987).

[4] Allamandola, L. J., Tielens, A. G. G. M. and Barker, J. Polycyclic aromatic hydrocarbons and the unidentified infrared emission bands-Auto exhaust along the Milky Way. *Astrophys. J., Part 2-Letters to the Editor (ISSN 0004-637X)*, vol. 290, March 1, 1985, p. L25-L28., **290**, L25-L28 (1985).

[5] Ehrenfreund, P. and Charnley, S. B. Organic molecules in the interstellar medium, comets, and meteorites: a voyage from dark clouds to the early Earth. *Annu. Rev. Astron. Astrophys.* **38(1)**, 427-483 (2000).

[6] d'Hendecourt, L. and Ehrenfreund, P. Spectroscopic properties of polycyclic aromatic hydrocarbons (PAHs) and astrophysical implications. *Adv. Space Res.* **19(7)**, 1023-1032 (1997).

[7] Mimura, K., Toyama, S. and Sugitani, K. Shock-induced dehydrogenation of polycyclic aromatic hydrocarbons with or without serpentine: Implications for planetary accretion. *Earth Planet. Sci. Lett.* **232(1-2)**, 143-156 (2005).

[8] Mimura, K. and Toyama, S. Behavior of polycyclic aromatic hydrocarbons at impact shock: Its implication for survival of organic materials delivered to the early Earth. *Geochim. Cosmochim. Acta* **69(1)**, 201-209 (2005).

[9] Bukowska, B., Mokra, K. and Michałowicz, J. Benzo [a] pyrene—Environmental occurrence, human exposure, and mechanisms of toxicity. *Int. J. Mol. Sci.* **23(11)**, 6348 (2022).

[10] Iball, J. The Crystal Structure of condensed Ring Compounds, III: Three carcinogenic hydrocarbons: 1: 2-Benzpvrene, Methylcholanthrene and 5: 6-cycloPenteno-I: 2-benzanthracene. *Z. Kristallogr.* **94**, 7-21 (1936).

[11] Iball, J. and Young, D. W. Structure of 3: 4-benzpyrene. *Nature* **177(4517)**, 985-986 (1956).

[12] Iball, J., Scrimgeour, S. N., & Young, D. W. 3, 4-Benzopyrene (a new refinement). *Acta Cryst. B* **32(1)**, 328-330 (1976).

[13] Contag, B. Die polymorphic von benzo [a] pyren. *Naturwissenschaften* **65**, 108-109 (1978).

[14] Carrell, C. J., Carrell, T. G., Carrell, H. L., *et al.* Benzo [a] pyrene and its analogues: structural studies of molecular strain. *Carcinogenesis*, **18(2)**, 415-422 (1997).

[15] Boehler, R. New diamond cell for single-crystal x-ray diffraction. *Rev. Sci. Instrum.*, **77(11)** (2006).

[16] Mao, H. K., Xu, J. A. and Bell, P. M. Calibration of the ruby pressure gauge to 800 kbar under quasi-hydrostatic conditions. *Journal of Geophysical Research: Solid Earth* **91(B5)**, 4673-4676 (1986).

[17] Rigaku, O. D. Crysalis Pro. Rigaku Oxford Diffraction. *Yarnton, England* (2015).

[18] Sheldrick, G. M. A short history of SHELX. *Acta Cryst.* **A64(1)**, 112-122 (2008).

[19] Dolomanov, O. V., Bourhis, L. J., Gildea, R. J., *et al.* Crystal structure refinement with SHELXL. *J. Appl. Crystallogr.* **42(2)**, 339-341 (2009).

[20] Momma, K. and Izumi, F. VESTA 3 for three-dimensional visualization of crystal, volumetric and morphology data. *J. Appl. Crystal.* **44(6)**, 1272-1276 (2011).

[21] Angel, R. J., Alvaro, M. and Gonzalez-Platas, J. EosFit7c and a Fortran module (library) for equation of state calculations. *Z. Kristallogr.* **229(5)**, 405-419 (2014).

[22] Kresse, G. and Furthmüller, J. Efficiency of ab-initio total energy calculations for metals and semiconductors using a plane-wave basis set. *Comput. Mater. Sci.* **6(1)**, 15-50 (1996).

[23] Blöchl, P. E. Projector augmented-wave method. *Phys. Rev. B* **50(24)**, 17953 (1994).

[24] Kresse, G. and Joubert, D. From ultrasoft pseudopotentials to the projector augmented-wave method. *Phys. Rev. B* **59(3)**, 1758 (1999).

[25] Grimme, S., Ehrlich, S. and Goerigk, L. Effect of the damping function in dispersion corrected density functional theory. *J. Comput. Chem.* **32(7)**, 1456-1465 (2011).

[26] Monkhorst, H. J. and Pack, J. D. Special points for Brillouin-zone integrations. *Phys. Rev. B*, **13(12)**, 5188 (1976).

[27] Zhou, W., Yin, Y., Laniel, D., *et al.* Polymorphism of pyrene on compression to 35 GPa in a diamond anvil cell. *Communications Chemistry* **7(1)**, 209 (2024).

[28] Spackman, P. R., Turner, M. J., McKinnon, J. J., *et al.* CrystalExplorer: a program for Hirshfeld surface analysis, visualization and quantitative analysis of molecular crystals. *J. Appl. Cryst.* **54(3)**, 1006-1011 (2021).

[29] McKinnon, J. J. Novel tools for visualizing and exploring intermolecular interactions in molecular crystals. *Acta Cryst. B* ***60*****(6)**, 627-668 (2004).

[30] Spackman, M. A. and Jayatilaka, D. Hirshfeld surface analysis. *CrystEngComm.* **11**, 19-32 (2009).

List of all the author's publications

[1] Y. Yin, A. Aslandukov, M. Bykov, D. Laniel, A. Aslandukova, A. Pakhomova, T. Fedotenko, **W. Zhou**, F. I. Akbar, M. Hanfland, K. Glazyrin, C. Giacobbe, E. L. Bright, G. Garbarino, Z. Jia, N. Dubrovinskaia, L. Dubrovinsky, Polytypism of incommensurately modulated structures of crystalline bromine upon molecular dissociation under high pressure. Physical Review B. 110 (2024) 104111. doi: 10.1103/PhysRevB.110.104111.

[2] **W. Zhou**, Y. Yin, D. Laniel, A. Aslandukov, E. Bykova, A. Pakhomova, M. Hanfland, T. Poreba, M. Mezouar, L. Dubrovinsky, N. Dubrovinskaia, Polymorphism of pyrene on compression to 35 GPa in a diamond anvil cell. Communications Chemistry. 7 (2024) 209. doi: 10.1038/s42004-024-01294-0.

[3] Y. Yin, L. Dubrovinsky, A. Aslandukov, A. Aslandukova, F. I. Akbar, **W. Zhou**, M. Hanfland, I. A. Abrikosov, N. Dubrovinskaia, High-Pressure Synthesis of the Iodide Carbonate $Na_5(CO_3)_2I$. Solids. 5 (2024) 333-340. doi: 10.3390/solids5020022.

[4] L. Ye[#], **W. Zhou**[#], D. Huang, X. Jiang, Q. Guo, X. Cao, S. Yan, X. Wang, D. Jia, D. Jiang, Y. Wang, X. Wu, X. Zhang, Y. Li, H. Lei, H. Gou, B. Huang, Manipulation of nonlinear optical responses in layered ferroelectric niobium oxide dihalides. Nature Communications. 14 (2023) 5911. doi: 10.1038/s41467-023-41383-7. (# Contribute equally)

[5] Q. Guo, X. Qi, L. Zhang, M. Gao, S. Hu, **W. Zhou**, W. Zang, X. Zhao, J. Wang, B. Yan, M. Xu, Y. Wu, G. Eda, Z. Xiao, S. A. Yang, H. Gou, Y. P. Feng, G. Guo, W. Zhou, X. Ren, C. Qiu, S. J. Pennycook, A. T. S. Wee, Ultrathin quantum light source with van der Waals $NbOCl_2$ crystal. Nature. 613 (2023) 53-59. doi: 10.1038/s41586-022-05393-7.

[6] X. Li, H. Su, W. Liang, **W. Zhou**, A. Rahman, Z. Xu, C. Zhong, D. Mai, R. Dai, H. Gou, Z. Wang, X. Zheng, Q. Wu, Z. Zhang, Inference of a “Hot Ice” Layer in Nitrogen-Rich Planets: Demixing the Phase Diagram and Phase Composition for Variable Concentration Helium–Nitrogen Mixtures Based on Isothermal Compression. The Journal of Physical Chemistry A. 126 (2022) 3745-3757. doi: 10.1021/acs.jpca.2c02132.

[7] S. Zhao, **W. Zhou**, X. Xiang, X. Cao, N. Chen, W. Chen, X. Yu, B. Yan, H. Gou, Structure Determination, Mechanical Properties, Thermal Stability of Co_2MoB_4 and Fe_2MoB_4. Materials. 15 (2022) 3031. doi: 10.3390/ma15093031.

[8] Q. Wang, **W. Zhou**, W. Dong, H. Wen, B. Wang, Q. Yao, J. Li, J. Wang, $Rb_{21.89}W_{32.66}O_{108}$: An Excellent Mid-and Far-IR Nonlinear-Optical Material with a Wide Band Gap. Inorganic Chemistry. 59 (2020) 4601-4607. doi: 10.1021/acs.inorgchem.9b03711.

[9] H. Tang, X. Gao, J. Zhang, B. Gao, **W. Zhou**, B. Yan, X. Li, Q. Zhang, S. Peng, D. Huang, L. Zhang, X. Yuan, B. Wan, C. Peng, L. Wu, D. Zhang, H. Liu, L. Gu, F. Gao, T. Irifune, R. Ahuja, H.-K. Mao, H. Gou, Boron-rich molybdenum boride with unusual short-range vacancy ordering, anisotropic hardness, and superconductivity. Chemistry of Materials. 32 (2019) 459-467. doi: 10.1021/acs.chemmater.9b04052

[10] B. Wan, S. Xu, X. Yuan, H. Tang, D. Huang, **W. Zhou**, L. Wu, J. Zhang, H. Gou, Diversities of stoichiometry and electrical conductivity in sodium sulfides. Journal of Materials Chemistry A. 7 (2019) 16472-16478. doi: 10.1039/C9TA05907E.

(Eidesstattliche) Versicherungen und Erklärungen

(§ 9 Satz 2 Nr. 3 PromO BayNAT)

Hiermit versichere ich eidesstattlich, dass ich die Arbeit selbstständig verfasst und keine anderen als die von mir angegebenen Quellen und Hilfsmittel benutzt habe (vgl. Art. 97 Abs. 1 Satz 8 BayHIG).

(§ 9 Satz 2 Nr. 3 PromO BayNAT)

Hiermit erkläre ich, dass ich die Dissertation nicht bereits zur Erlangung eines akademischen Grades eingereicht habe und dass ich nicht bereits diese oder eine gleichartige Doktorprüfung endgültig nicht bestanden habe.

(§ 9 Satz 2 Nr. 4 PromO BayNAT)

Hiermit erkläre ich, dass ich Hilfe von gewerblichen Promotionsberatern bzw. -vermittlern oder ähnlichen Dienstleistern weder bisher in Anspruch genommen habe noch künftig in Anspruch nehmen werde.

(§ 9 Satz 2 Nr. 7 PromO BayNAT)

Hiermit erkläre ich mein Einverständnis, dass die elektronische Fassung meiner Dissertation unter Wahrung meiner Urheberrechte und des Datenschutzes einer gesonderten Überprüfung unterzogen werden kann.

(§ 9 Satz 2 Nr. 8 PromO BayNAT)

Hiermit erkläre ich mein Einverständnis, dass bei Verdacht wissenschaftlichen Fehlverhaltens Ermittlungen durch universitätsinterne Organe der wissenschaftlichen Selbstkontrolle stattfinden können.

…………………………………………………………………………………….

Ort, Datum, Unterschrift